

Observing the Distribution of Atmospheric Methane from Space

Thesis submitted for the degree of
Doctor of Philosophy at the
University of Leicester

by

Diane S. Knappett
Department of Physics and Astronomy
University of Leicester

June 11, 2012

© Diane S. Knappett, June 11, 2012

This thesis is copyright material and no quotation from it may be published without proper acknowledgement.

Declaration

I hereby declare that no part of this thesis has been previously submitted to this or any other University as part of the requirement for a higher degree. The work within this document has been conducted by the undersigned except for contributions where acknowledged in the text.

Diane S. Knappett

June 11, 2012

Abstract

Methane (CH_4) is a potent greenhouse gas with a radiative forcing efficiency 21 times greater than that of carbon dioxide (CO_2) and an atmospheric lifetime of approximately 12 years. Although the annual global source strength of CH_4 is fairly well constrained, the temporal and spatial variability of individual sources and sinks is currently less well quantified. In order to constrain CH_4 emission estimates, inversion models require satellite retrievals of XCH_4 with an accuracy of $< 1\text{--}2\%$. However, satellite retrievals of XCH_4 in the shortwave infrared (SWIR) are often hindered by the presence of atmospheric aerosols and/or thin ice (cirrus) clouds which can lead to biases in the resulting trace gas total column of comparable magnitude. This thesis aims to quantify the magnitude of retrieval errors caused by aerosol and cirrus cloud induced scattering for the Full Spectral Initiation Weighting Function Modified Differential Optical Absorption Spectroscopy (FSI WFM-DOAS) retrieval algorithm.

A series of sensitivity tests have been performed which reveal that a) for scenes of high optical depth, accurate aerosol a priori data is required to reduce retrieval errors, b) retrieval errors due to aerosol and ice cloud scattering are highly dependent on surface albedo, SZA and the altitude at which scattering occurs and c) errors induced in global retrievals by the presence of ice clouds (up to $\sim 35\%$) are significantly greater than those owing to aerosols ($\sim 1\text{--}2\%$). Cloud filtering is therefore important even when employing proxy methods. Furthermore, the original FSI WFM-DOAS V2 algorithm (OFSI) has been successfully modified with improved a priori albedo and aerosol, resulting in two new versions of the retrieval: MFSI and GFSI. Initial comparison of OFSI, MFSI and GFSI retrievals of XCH_4 over North America show minor improvements in retrieval error, however further comparison over regions of high optical depth are required.

Acknowledgments

Firstly I would like to thank my primary supervisor, Paul Monks, for his continued support and advice over the course of my PhD. Paul has been the embodiment of encouragement and motivation whilst keeping a watchful eye on my progress. I would also like to thank my secondary supervisor Hartmut Bösch who has spent many hours explaining retrieval theory, discussing results and suggesting new directions for my work; his enthusiasm for climate science has been a true inspiration.

Secondly I'd like to thank my colleague Rob Parker who, often entirely unprompted, has offered his help and support. This has been particularly true in recent months during which he has regularly given up valuable time to assist me with problem solving and proof reading. Thanks also to my colleagues Austin Cogan and Alan Hewitt, with whom I have often exchanged knowledge and ideas over the course of my PhD. I would also like to thank my good friend and graphic artist Austin Durose for his creative flair (and patience!) in turning several of my simple scientific sketches into beautiful illustrations.

I would like to acknowledge Michael Buchwitz for the creation of the WFM-DOAS retrieval algorithm, and Michael Barkley for the subsequent development of FSI WFM-DOAS on which this thesis is based. I must also acknowledge Alexi Rozanov for creation of the SCIATRAN radiative transfer model, Sander Houweling for producing the CH₄ climatology used in this work, Debra Wunch for the use of TCCON data, Angela Benedetti and Jean-Jacques Morcrette for their correspondence regarding GEMS data and the use of data from ECMWF and NOAA.

Finally I would like to thank my parents, who have been consistently supportive and encouraging throughout my university career. Without their love and support I wouldn't be where I am today.

Table of Contents

Chapter 1: Introduction	20
1.1 Climate Change	20
1.1.1 Radiative Forcing and Global Warming Potential	23
1.1.2 The Intergovernmental Panel on Climate Change	23
1.2 Radiative Equilibrium of the Earth	24
1.2.1 Blackbody Radiation	24
1.2.2 A Basic Model of the Earth	24
1.3 The Greenhouse Effect	25
1.3.1 A Model of the Greenhouse Effect	27
1.4 The Role of CH ₄ in the Atmosphere	28
1.4.1 CH ₄ Sources and Sinks	28
1.4.2 Trends in Atmospheric CH ₄ Concentrations	30
1.4.3 Ground Based Remote Sensing	31
1.4.4 Satellite Retrievals of Total Column CH ₄	32
1.5 Thesis Overview	38
Chapter 2: Remote Sensing of CH₄	40
2.1 Introduction	40
2.2 Satellite Remote Sensing	40
2.3 Molecular Spectroscopy in the SWIR	43
2.3.1 Vibration-Rotation Transitions	44
2.3.2 CO ₂ and CH ₄ Absorption Bands	45
2.4 Basic Radiative Transfer and DOAS Retrieval Theory	45
2.4.1 Basic Radiative Transfer	46
2.4.2 Differential Optical Absorption Spectroscopy (DOAS)	48
2.4.3 Spectral Fitting	49
2.4.4 Implementing DOAS in the SWIR	51

2.4.5	Weighting Function Modified Differential Optical Absorption Spectroscopy (WFM-DOAS)	51
2.4.6	Full Spectral Initiation (FSI) WFM-DOAS	54
2.5	Scattering by Aerosols in the SWIR	54
2.5.1	Defining Atmospheric Aerosol	54
2.5.2	Sources	55
2.5.3	Sinks	56
2.5.4	Scattering Properties of Aerosols	56
2.6	Scattering by Clouds in the SWIR	60
2.6.1	Scattering Properties of Clouds	60
Chapter 3: FSI for the Retrieval of CH₄ from SCIAMACHY		63
3.1	The SCIAMACHY Instrument	63
3.1.1	Introducing SCIAMACHY	63
3.1.2	Orbit and Viewing Geometry	64
3.1.3	Spectral Coverage	66
3.2	Calibration of SCIAMACHY L1B Data	67
3.2.1	Non-Linearity in the SWIR Channels	67
3.2.2	Dark Signal and Leakage	69
3.2.3	Pixel To Pixel Gain	70
3.2.4	Dead and Bad Pixels	70
3.3	FSI WFM-DOAS for the Retrieval of CH ₄	70
3.3.1	An Overview of FSI WFM-DOAS V2	71
3.3.2	The Proxy Approach for CH ₄ Column Normalisation	71
3.3.3	Trace Gas Climatologies	73
3.3.4	Albedo	74
3.3.5	Spectroscopy	75
3.3.6	ECMWF Meteorology	75
3.3.7	Radiative Transfer using SCIATRAN 2.2	78
3.4	Sources of Retrieval Error	79
3.4.1	Instrument Noise	79
3.4.2	Spectroscopy	80
3.4.3	Albedo	80
3.4.4	SZA	81
3.4.5	Aerosols and Cirrus Clouds	81
3.4.6	Quantifying Error Sensitivity	82

Chapter 4: The Effect of Aerosols and Cirrus Clouds on Atmospheric

Retrievals of CH₄	84
4.1 Introduction	84
4.2 Simulation 1: Quantifying the Effects of Inaccurate A Priori Data	85
4.2.1 Simulated SCIAMACHY Spectra	85
4.2.2 FSI Retrieval Aerosol Scenarios	88
4.2.3 Results	88
4.2.4 Summary of Simulation 1	94
4.3 Simulation 2: Effect of a Basic Aerosol/Cloud Layer	95
4.3.1 Defining a Simple Scattering Layer	95
4.3.2 Determining the Angstrom Exponent	96
4.3.3 Results	97
4.3.4 Discussion	98
4.3.5 Summary of Simulation 2	107
4.4 Simulation 3: Global Aerosol and Cloud Sensitivity Tests	108
4.4.1 Simulation of Atmospheric Aerosol	109
4.4.2 Simulation of Ice Clouds	111
4.4.3 Trace Gas Profiles	115
4.4.4 Surface Albedo	116
4.4.5 UTC Time Zones	117
4.4.6 Results	118
4.4.7 Summary of Simulation 3	130
4.5 Summary	131

Chapter 5: FSI WFM-DOAS Retrievals of CH₄ over North America 133

5.1 Introduction	133
5.1.1 MODIS Albedo Modifications	134
5.1.2 GEMS Aerosol Modifications	136
5.2 FSI WFM-DOAS Retrievals over North America for 2004	137
5.2.1 Data Filtering	137
5.2.2 Gridded Monthly Mean CH ₄ over North America	141
5.2.3 Monthly Mean Retrieved CH ₄ Comparison	148
5.3 Validation with TCCON FTS from Park Falls	149
5.4 Summary	152

Chapter 6: Conclusions	154
6.1 Thesis Achievements	154
6.1.1 FSI WFM-DOAS V2 Algorithm Modifications	154
6.1.2 Outcome and Impact of Sensitivity Tests	155
6.1.3 FSI WFM-DOAS V2 Retrievals	156
6.2 Future CH ₄ Satellite Missions	158
A Basic Molecular Spectroscopy	160
A1 Rotational Transitions	161
A2 Vibrational Transitions	162
A3 Vibration-Rotation Transitions	162
B SCIATRAN 2.2	163
C Retrieval Parameters and Data	165
References	174

List of Tables

1.1	Spectral classification schemes for the infrared (IR) spectral region. The three schemes presented here are the German Institute for Standardization (DIN) IR scheme, the Sensor Response scheme described by Miller (1994) and the French International Organization for Standardization (ISO) scheme 20473. *MWIR and LWIR are often referred to as thermal infrared (TIR)	26
1.2	Natural and anthropogenic sources of methane listed in order of magnitude [Denman et al. (2007)]. *Biogenic processes.	29
1.3	Details of space-based instruments from which retrievals of atmospheric CH ₄ have been performed. *Instruments which are sensitive to the troposphere. †IASI and TES retrievals are weighted towards the mid-troposphere however IASI has the potential to determine near-surface information also.	33
2.1	Parameters characterizing 9 GEMS aerosol types, including minimum and maximum radii (r_{\min} and r_{\max}), mode r_g and standard deviation σ_g of the log-normal distribution of radii. The source of each aerosol type and suitable refractive index (RI) profiles (for use in Mie calculations) are also provided for each case. Parameter values were obtained via personal correspondence with J-J. Morcrette from the GEMS project.	57
3.1	Spectral coverage and resolution of SCIAMACHY's eight channels. .	66
3.2	Calibration options available in the SciaL1c tool for the calibration of SCIAMACHY L1b data along with a description of each correction. If available, maximum errors have been given in binary units (BU) [Lichtenberg (2006); Scherbakov (2009); Kleipool (2002)].	68
3.3	Details of measurement states during which dark signal measurements are performed, along with their corresponding PET values.	69

3.4	The range of acceptable values of the SCIAMACHY signal, dark current (DC), standard deviation of the dark current σ_{DC} and shot noise, that constitute the manual bad pixel mask. For a given spectral point, if any of the stated thresholds are exceeded the point is classified as a bad pixel and subsequently ignored in the retrieval.	70
3.5	Summary of meteorological and trace gas climatologies used by the FSI WFM-DOAS V2 retrieval.	74
3.6	Percentage difference between the unperturbed retrieved XCH_4 and true XCH_4 (1774 ppb) for eight different scenarios.	82
3.7	Pressure profile error budget. Difference in XCH_4 [%] between retrievals where the a priori pressure profile was scaled by the amount shown at the top of each column and an unperturbed case.	83
3.8	Temperature profile error budget. Difference in XCH_4 [%] between retrievals where the a priori temperature profile was scaled by the amount shown at the top of each column and an unperturbed case.	83
4.1	Parameters used to define 64 atmospheric scenarios for the simulation of SCIAMACHY spectra; a priori XCH_4 , SZA, surface albedo and aerosol properties (boundary layer (BL) visibility, tropospheric (TR) visibility and humidity).	86
4.2	Parameters used to define aerosol scenarios for the 80 FSI WFM-DOAS V2 retrievals performed for each of the 64 simulated SCIAMACHY spectra defined in Table 4.1.	88
4.3	Physical and optical properties of a simple aerosol/cloud layer for the simulation of spectra using SCIATRAN 2.2. The layer was simulated as 1 km thick in all cases, therefore for the scenario where the aerosol layer top altitude is 1 km, the scattering layer occupies the entire atmospheric region from 1 km down to the Earth's surface.	96
4.4	Comparison of the set-up of Simulation 3 detailed in this section with an existing study by Butz et al. (2010).	129
5.1	Filter 1; thresholds for SZA, albedo, latitude and longitude used to filter out anomalous FSI WFM-DOAS V2 retrievals of CH_4	137
5.2	The error [%] incurred in CO_2 and CH_4 retrieved VCDs for SCIAMACHY scenes corresponding to low/high SZA and albedo. The resulting combined error on XCH_4 , given by $\sigma_{XCH_4} = \left[\left(\frac{\sigma_{CO_2}}{VCD_{CO_2}} \right)^2 + \left(\frac{\sigma_{CH_4}}{VCD_{CH_4}} \right)^2 \right]^{\frac{1}{2}}$, is shown in the final column.	139

B1 Description of specialised parameters required as input into SCIA-
TRAN. 164

List of Figures

1.1	Periodic variations in deuterium (δD ; black), a proxy for local temperature, and the concentrations of atmospheric trace gases CO ₂ (red), CH ₄ (blue) and N ₂ O (green) over the last 650 kyrs determined primarily from ice core measurements (figure taken from [Jansen et al. (2007)]). Benthic $\delta^{18}\text{O}$ from marine records (grey; a proxy for changes in global ice volume) is also shown.	21
1.2	Atmospheric concentrations of the three main anthropogenic GHGs over the last 2000 years (figure taken from Forster et al. (2007)). The sharp increase in all three species from around 1750 onwards is due to the rise in anthropogenic emissions resulting from industrialisation. Concentrations are stated in parts per million (ppm) for CO ₂ and N ₂ O and parts per billion (ppb) for CH ₄	22
1.3	A simple model of the radiation exchange between the Sun and Earth (figure produced by A. Durose and D. Knappett).	25
1.4	A simple model of the Greenhouse Effect (figure produced by A. Durose and D. Knappett).	27
1.5	Growth rate of CH ₄ over the last two decades as determined from the assimilation of air flask measurements from NOAA into an inversion model (figure taken from Bousquet et al. (2006)). Black indicates the global growth rate, whilst the southern hemisphere is shown in blue, the tropics in red and the northern hemisphere in green. El Niño events are indicated in light grey whereas dark grey highlights the period following the eruption of Mount Pinatubo in 1991.	30
1.6	TCCON observation sites accurate as of 30/04/2010 (figure obtained from https://tccon-wiki.caltech.edu/).	32
1.7	2004 yearly average of methane total column XCH ₄ retrieved using WFM-DOAS version 1.0 (figure taken from Schneising et al. (2009)).	36

1.8	Two-year mean total column XCH ₄ retrieved from SCIAMACHY data from 2003–2004 using IMAP-DOAS (figure taken from Frankenberg et al. (2006)). Data is shown on a 0.5° × 0.5° grid.	37
1.9	Yearly average of total column XCH ₄ retrieved using IMAP-DOAS with (top) an updated H ₂ O spectroscopy and (bottom) the corresponding difference between retrievals performed both with and without the spectroscopic update applied (figures taken from Frankenberg et al. (2008a)).	38
2.1	Typical atmospheric pressure and temperature profiles derived from the US standard atmosphere (figure taken from Gottwald et al. (2006)). Note the log scale on the x-axis, indicating that pressure decreases exponentially with altitude.	42
2.2	Energy level diagram for vibrational (ν) and rotational (J) transitions, showing the P, Q and R branches of coupled vibration-rotation transitions (figure produced by A. Durose and D. Knappett).	44
2.3	Absorption spectra for CO ₂ (top) and CH ₄ (bottom), focusing on the wavelength windows used for trace gas retrievals within this thesis. In each case, atmospheric transmission was obtained by running the SCIATRAN radiative transfer model both with and without the trace gas present and then calculating the difference.	46
2.4	Ensemble averaged extinction cross-section per particle $\langle\sigma_e\rangle$, single scattering albedo ω and asymmetry parameter g derived from Mie theory for the 9 GEMS aerosol types. Parameters are given for wavelengths corresponding to the centre of the CO ₂ and CH ₄ retrieval windows (1570 nm and 1650 nm respectively) as well as for a reference wavelength of 550 nm.	58
3.1	Spectral regions observed by both GOME and SCIAMACHY (figure taken from BREMEN). Note that CO ₂ and CH ₄ were originally intended to be retrieved from the SWIR ($\sim 2 \mu\text{m}$) however due to problems with the detectors covering this spectral range, these retrievals are instead performed using spectral windows around 1.57 μm and 1.65 μm respectively.	64
3.2	The three observational modes of SCIAMACHY; nadir(1), limb (2) and solar(/moon) occultation (3) (figure taken from Gottwald et al. (2006)).	65

- 3.3 Spectra from various stages of a typical FSI WFM-DOAS V2 spectral fit. Spectral panels in order from the top: SCIAMACHY manually calibrated signal; High resolution FSI reference spectrum simulated by SCIATRAN overlaid with the same spectrum convolved with the SCIAMACHY instrument slit function; WFM-DOAS fit (with the original SCIAMACHY spectrum for comparison); WFM-DOAS fit residual. Gaps in the spectra indicate where spectral points have been omitted due to either being flagged as dead pixels in the SCIAMACHY L1b product, or removed by the manual bad pixel mask (see Section 3.2.4). 72
- 3.4 Flowchart portraying the progression of the FSI WFM-DOAS V2 retrieval algorithm. Fully calibrated spectra are required to obtain mean spectral intensity which is used in conjunction with SZA to determine the albedo of a scene; the manually calibrated SCIAMACHY signal is used for retrievals since a better dark correction is achieved. 73
- 3.5 Diagram to illustrate the improved interpolation of ECMWF profiles to an observed location. Geometric heights were added to original ECMWF altitude profiles corresponding to a regular grid (indicated in black) in order to create profiles of altitude that were relative to sea level (shown in red). A new altitude profile was then created for the observed location (with surface geometric height A_{obs}) onto which the corner profiles could then be correctly interpolated (figure produced by A. Durose and D. Knappett). 77
- 4.1 AVIRIS surface albedo profiles for the wavelength range 0.4–2.5 μm . Right hand side panel shows the wavelength region encompassing both the CO_2 and CH_4 retrieval windows. 87
- 4.2 SCIATRAN extinction profiles for a BL visibility of 23 km and a TR visibility of 50 km, spanning the BL (0–2 km) and TR (3–10 km) for both rural (solid line) and urban (dotted line) BL aerosol types. The top panel shows extinction profiles for the four different humidity values (0%, 70%, 80% and 99%) whereas the lower panel shows the *difference* between the extinction in each case minus the extinction at 0% humidity. 87
- 4.3 Sensitivity tests for a low aerosol loading scenario (rural aerosol, $\tau_{\text{sim}} = 0.0385$) as a function of τ_{ret} (optical depth for FSI reference spectrum), for SZAs of 20°, 60° and 70°. 91

(a)	a=0.27, SZA = 20°	91
(b)	a=0.34, SZA = 20°	91
(c)	a=0.27, SZA = 60°	91
(d)	a=0.34, SZA = 60°	91
(e)	a=0.27, SZA = 70°	91
(f)	a=0.34, SZA = 70°	91
4.4	Sensitivity tests for a moderate aerosol loading scenario (urban aerosol, $\tau_{\text{sim}} = 0.235$) as a function of τ_{ret} (optical depth for FSI reference spectrum), for SZAs of 20°, 60° and 70°.	92
(a)	a=0.15, SZA = 20°	92
(b)	a=0.23, SZA = 20°	92
(c)	a=0.15, SZA = 60°	92
(d)	a=0.23, SZA = 60°	92
(e)	a=0.15, SZA = 70°	92
(f)	a=0.23, SZA = 70°	92
4.5	Sensitivity tests for a high aerosol loading scenario (urban aerosol, $\tau_{\text{sim}} = 1.11$) as a function of τ_{ret} (optical depth for FSI reference spectrum), for SZAs of 20°, 60° and 70°.	93
(a)	a=0.15, SZA = 20°	93
(b)	a=0.23, SZA = 20°	93
(c)	a=0.15, SZA = 60°	93
(d)	a=0.23, SZA = 60°	93
(e)	a=0.15, SZA = 70°	93
(f)	a=0.23, SZA = 70°	93
4.6	Aerosol basic layer XCH ₄ plotted against optical depth for (a) grassland/bare and (b) wetland/evergreen needleleaf forest albedo scenarios. The control run in each case is denoted by a red cross. For reference, a red dotted line indicates where $\Delta\text{XCH}_4 = 0\%$	102
(a)	ΔXCH_4 for aerosol scenarios of high albedo.	102
(b)	ΔXCH_4 for aerosol scenarios of low albedo.	102
4.7	Cirrus cloud basic layer XCH ₄ plotted against optical depth for (a) grassland/bare and (b) wetland/evergreen needleleaf forest albedo scenarios. The control run in each case is denoted by a red cross. For reference, a red dotted line indicates where $\Delta\text{XCH}_4 = 0\%$	103
(a)	ΔXCH_4 for cirrus cloud scenarios of high albedo.	103
(b)	ΔXCH_4 for cirrus cloud scenarios of low albedo.	103

4.8	Aerosol basic layer σ_{XCH_4} plotted against optical depth for (a) grassland/bare and (b) wetland/evergreen needleleaf forest albedo scenarios. The control run in each case is denoted by a red cross. For reference, a red dotted line indicates where $\sigma_{\text{XCH}_4} = 0\%$	104
	(a) σ_{XCH_4} for aerosol scenarios of high albedo.	104
	(b) σ_{XCH_4} for aerosol scenarios of low albedo.	104
4.9	Cirrus cloud basic layer σ_{XCH_4} plotted against optical depth for (a) grassland/bare and (b) wetland/evergreen needleleaf forest albedo scenarios. The control run in each case is denoted by a red cross. For reference, a red dotted line indicates where $\sigma_{\text{XCH}_4} = 0\%$	105
	(a) σ_{XCH_4} for cirrus cloud scenarios of high albedo.	105
	(b) σ_{XCH_4} for cirrus cloud scenarios of low albedo.	105
4.10	Spectral comparison for an aerosol layer simulated at altitudes of (a) 1 km, (b) 3 km, (c) 6 km and (d) 9 km. In all cases $\tau = 1$, $\text{SZA} = 20^\circ$ and surface albedo = 0.34 (AVIRIS grassland). In each plot, the top panel shows the high resolution simulated SCIAMACHY spectrum, the high resolution FSI reference spectrum and the convolution of the reference spectrum with the SCIAMACHY instrument line shape. The second panel shows the difference between the high resolution simulated and reference spectra. The third panel shows the convolved simulated and reference spectra along with the WFM-DOAS fit (the simulated spectrum is overlaid by the WFM-DOAS fit). The fourth panel shows the RMSE residual of the WFM-DOAS fit. In each case the proxy method normalised XCH_4 is given, along with the surface pressure normalised XCH_4 in brackets.	106
	(a) 1 km: $\text{XCH}_4 = 1787$ ppb (1797 ppb).	106
	(b) 3 km: $\text{XCH}_4 = 1909$ ppb (1541 ppb).	106
	(c) 6 km: $\text{XCH}_4 = 2181$ ppb (1068 ppb).	106
	(d) 9 km: $\text{XCH}_4 = 2656$ ppb (742 ppb).	106
4.11	AOD simulated at 1650 nm, calculated from GEMS aerosol MMR for the first day of months January, April, July and October 2004. Data is given on a $1.125^\circ \times 1.125^\circ$ grid.	110
	(a) Simulated AOD (01/01/2004)	110
	(b) Simulated AOD (01/04/2004)	110
	(c) Simulated AOD (01/07/2004)	110
	(d) Simulated AOD (01/10/2004)	110

4.12	Simulated ice COD calculated from GEMS cloud ice MMR. Data is gridded on a $1.125^\circ \times 1.125^\circ$ scale.	115
(a)	Simulated ice COD (01/01/2004)	115
(b)	Simulated ice COD (01/04/2004)	115
(c)	Simulated ice COD (01/07/2004)	115
(d)	Simulated ice COD (01/10/2004)	115
4.13	Ice COD corresponding to user defined SCIATRAN 2.2 cloud profiles. Data is gridded on a $1.125^\circ \times 1.125^\circ$ scale.	116
(a)	Ice COD for SCIATRAN (01/01/2004)	116
(b)	Ice COD for SCIATRAN (01/04/2004)	116
(c)	Ice COD for SCIATRAN (01/07/2004)	116
(d)	Ice COD for SCIATRAN (01/10/2004)	116
4.14	Global XCO ₂ calculated from CarbonTracker profiles used for the simulation of SCIAMACHY spectra for January, April, July and October 2004. Data is gridded on a $1.125^\circ \times 1.125^\circ$ scale.	117
(a)	Simulated XCO ₂ (01/01/2004)	117
(b)	Simulated XCO ₂ (01/04/2004)	117
(c)	Simulated XCO ₂ (01/07/2004)	117
(d)	Simulated XCO ₂ (01/10/2004)	117
4.15	Global XCH ₄ calculated from TM3 profiles used for the simulation of SCIAMACHY spectra for January, April, July and October 2004. Data is gridded on a $1.125^\circ \times 1.125^\circ$ scale.	118
(a)	Simulated XCH ₄ (01/01/2004)	118
(b)	Simulated XCH ₄ (01/04/2004)	118
(c)	Simulated XCH ₄ (01/07/2004)	118
(d)	Simulated XCH ₄ (01/10/2004)	118
4.16	Retrieved XCH ₄ (left) and Δ XCH ₄ (right) for a background scenario, simulated for the first day of months January, April, July and October 2004 (top to bottom). Data is gridded on a $1.125^\circ \times 1.125^\circ$ scale.	119
(a)	FSI retrieved XCH ₄ (01/01/2004)	119
(b)	Δ XCH ₄ (01/01/2004)	119
(c)	FSI retrieved XCH ₄ (01/04/2004)	119
(d)	Δ XCH ₄ (01/04/2004)	119
(e)	FSI retrieved XCH ₄ (01/07/2004)	119
(f)	Δ XCH ₄ (01/07/2004)	119
(g)	FSI retrieved XCH ₄ (01/10/2004)	119

(h)	ΔXCH_4 (01/10/2004)	119
4.17	Retrieved XCH_4 (left) and ΔXCH_4 (right) for the aerosol scenario, simulated for the first day of months January, April, July and October 2004 (top to bottom). Data is gridded on a $1.125^\circ \times 1.125^\circ$ scale.	120
(a)	FSI retrieved XCH_4 (01/01/2004)	120
(b)	ΔXCH_4 (01/01/2004)	120
(c)	FSI retrieved XCH_4 (01/04/2004)	120
(d)	ΔXCH_4 (01/04/2004)	120
(e)	FSI retrieved XCH_4 (01/07/2004)	120
(f)	ΔXCH_4 (01/07/2004)	120
(g)	FSI retrieved XCH_4 (01/10/2004)	120
(h)	ΔXCH_4 (01/10/2004)	120
4.18	Retrieved XCH_4 (left) and ΔXCH_4 (right) for a cirrus cloud scenario, simulated for the first day of months January, April, July and October 2004 (top to bottom). Data is gridded on a $1.125^\circ \times 1.125^\circ$ scale.	121
(a)	FSI retrieved XCH_4 (01/01/2004)	121
(b)	ΔXCH_4 (01/01/2004)	121
(c)	FSI retrieved XCH_4 (01/04/2004)	121
(d)	ΔXCH_4 (01/04/2004)	121
(e)	FSI retrieved XCH_4 (01/07/2004)	121
(f)	ΔXCH_4 (01/07/2004)	121
(g)	FSI retrieved XCH_4 (01/10/2004)	121
(h)	ΔXCH_4 (01/10/2004)	121
4.19	Retrieved XCH_4 (left) and ΔXCH_4 (right) for a combined aerosol and cirrus cloud scenario, simulated for the first day of months January, April, July and October 2004 (top to bottom). Data is gridded on a $1.125^\circ \times 1.125^\circ$ scale.	122
(a)	FSI retrieved XCH_4 (01/01/2004)	122
(b)	ΔXCH_4 (01/01/2004)	122
(c)	FSI retrieved XCH_4 (01/04/2004)	122
(d)	ΔXCH_4 (01/04/2004)	122
(e)	FSI retrieved XCH_4 (01/07/2004)	122
(f)	ΔXCH_4 (01/07/2004)	122
(g)	FSI retrieved XCH_4 (01/10/2004)	122
(h)	ΔXCH_4 (01/10/2004)	122

4.20	Histograms for the altitude of peak optical depth for simulated (a) aerosols and (b) ice clouds for January, April, July and October 2004 (from the combined aerosol and cirrus cloud run). Note the y-axis utilises a log scale for altitude.	125
	(b) Aerosol peak altitude	125
	(c) Ice cloud peak altitude	125
4.21	Scatter plots of ΔXCH_4 from Oct 2004 against SZA for (a) background, (b) aerosol, (c) ice cloud and (d) aerosol + ice cloud simulation scenarios.	126
	(a) Background	126
	(b) Aerosol	126
	(c) Ice cloud	126
	(d) Aerosol + ice cloud	126
4.22	Scatter plots of ΔXCH_4 against CH_4 surface albedo estimation error for (a) background, (b) aerosol, (c) ice cloud and (d) aerosol + ice cloud simulation scenarios for Jan 2004.	127
	(a) Background	127
	(b) Aerosol	127
	(c) Ice cloud	127
	(d) Aerosol + ice cloud	127
4.23	Scatter plots of ΔXCH_4 against AOD [(a), (c), (e) and (g)] and ice COD [(b), (d), (f) and (h)] for the months January, April, July and October of 2004 respectively.	128
	(a) AOD (01/01/2004)	128
	(b) Ice COD (01/01/2004)	128
	(c) AOD (01/04/2004)	128
	(d) Ice COD (01/04/2004)	128
	(e) AOD (01/07/2004)	128
	(f) Ice COD (01/07/2004)	128
	(g) AOD (01/10/2004)	128
	(h) Ice COD (01/10/2004)	128
4.24	XCH_4 error [%] (equivalent to ΔXCH_4) for proxy based retrievals using simulated SCIAMACHY spectra for an ensemble of aerosol and cirrus cloud scenarios (figure taken from Butz et al. (2010)).	130

5.1	Flowchart portraying the progression of the FSI WFM-DOAS V3 retrieval algorithm. In this version aerosol extinction profiles calculated from GEMS MMR are used as a priori aerosol and a priori albedo is obtained from MODIS. Cloud flagging of cirrus clouds using data from MERIS is mentioned as a future modification.	134
5.2	MODIS retrieved 16 day mean albedo at $1.64 \mu\text{m}$ for 01/10/2004. Black areas over land indicate consistently cloudy regions or inland water.	135
5.3	MODIS albedo scaled to the central wavelengths of retrieval windows for (a) CO_2 and (b) CH_4 at $1.57 \mu\text{m}$ and $1.65 \mu\text{m}$ respectively.	135
	(a) MODIS albedo at $1.57 \mu\text{m}$	135
	(b) MODIS albedo at $1.65 \mu\text{m}$	135
5.4	Distributions of the retrieval fit error σ_{XCH_4} , retrieved XCH_4 and a priori albedo for the OFSI (top), MFSI (centre) and GFSI (bottom) retrievals. Unfiltered data is shown in green and data filtered by Filter 1 (thresholds defined in Table 5.1) are shown in red. The median and median absolute deviation of the Filter 1 distribution of σ_{XCH_4} have been used to plot a robust gaussian (shown in blue) from which the thresholds of Filter 2 (shown in yellow) have been defined.	138
5.5	Density correlation plots of σ_{CO_2} , σ_{CH_4} and σ_{XCH_4} from the OFSI retrieval once filtered by Filter 1.	140
	(a) CO_2 VCD against σ_{CO_2}	140
	(b) CH_4 VCD against σ_{CH_4}	140
	(c) XCH_4 against σ_{XCH_4}	140
5.6	Density correlation plots of σ_{CO_2} , σ_{CH_4} and σ_{XCH_4} from the OFSI retrieval once filtered by Filter 2.	140
	(a) CO_2 VCD against σ_{CO_2}	140
	(b) CH_4 VCD against σ_{CH_4}	140
	(c) XCH_4 against σ_{XCH_4}	140
5.7	Monthly averaged OFSI retrievals of CH_4 over North America for the period Jan-Dec 2004.	143
5.8	Monthly averaged MFSI retrievals of CH_4 over North America for the period Jan-Dec 2004.	144
5.9	Monthly averaged GFSI retrievals of CH_4 over North America for alternate months from Jan-Nov 2004.	145

5.10	Total column XCH ₄ from TM3 (used as a priori XCH ₄ in the FSI WFM-DOAS V2 retrieval) for the first day of months May–August of 2004 gridded to 3.8°×5°	146
5.11	Monthly averaged XCH ₄ retrieved by WFM-DOAS version 1.0, for the period May–August 2004, gridded to 1°×10° (figure taken from Buchwitz (2007)).	146
5.12	Anthropogenic CH ₄ emission estimates from EDGAR for 2005 and the increase in emissions over the period 2000–2005 (both figures taken from Frankenberg et al. (2011)).	147
	(a) EDGAR CH ₄ emission estimates for 2005 (log scale)	147
	(b) Increase in anthropogenic emissions from 2000–2005	147
5.13	Comparison of OFSI, MFSI and GFSI distributions for matching scenes only.	148
5.14	Comparison of OFSI, MFSI and GFSI monthly mean retrieved XCH ₄ for matching scenes only (with 1σ error bars).	148
5.15	Comparison of TCCON FTS retrieved XCH ₄ with SCIAMACHY retrieved XCH ₄ over Park Falls, Wisconsin.	150
	(a) TCCON XCH ₄ with OFSI XCH ₄	150
	(b) TCCON XCH ₄ with MFSI XCH ₄	150
	(c) TCCON XCH ₄ with GFSI XCH ₄	150
5.16	Comparison of monthly mean XCH ₄ (filtered by both Filter 1 and 2) retrieved using OFSI, MFSI and GFSI with data from TCCON over Park Falls, Wisconsin.	151
5.17	Comparison of monthly mean XCH ₄ (filtered by both Filter 1 and 2) retrieved using OFSI, MFSI and GFSI with data from TCCON over Park Falls, Wisconsin, for GEMS matching scenes only.	151
6.1	Timeline of present and planned space based missions sensitive to CH ₄ in the planetary boundary layer (figure adapted from Ciaïis et al. (2010)). Note: CarbonSat and GOSAT-2 are currently both <i>proposed</i> missions and, only if confirmed, are likely to be launched around 2018.	158
C1	Value of α for 9 GEMS aerosol types computed by taking the mean of α values computed for one days worth of global GEMS data (corresponding to 01/10/2004). Calculations were based on a reference optical depth of τ = 1 at 1650 nm.	165

C2	Mass extinction coefficients (ω) for the RH dependent GEMS sea salt particle size bin 1. The upper plot displays ω for all RH and λ values whereas the lower plot shows ω interpolated to a specific λ , for all values of RH.	165
C3	Mass extinction coefficients (ω) for RH dependent GEMS sea salt particle size bins 2 and 3. The upper plot in each panel displays ω for all RH and λ values; the lower plot shows ω interpolated to a specific λ , for all values of RH.	166
C4	Mass extinction coefficients (ω) for RH dependent aerosols; organic matter (top panel), sulphate (bottom panel).	167
C5	Mass extinction coefficients (ω) for non-RH dependent aerosols; desert dust (top) and black carbon (bottom).	167
C6	Scatter plots of ΔXCH_4 against SZA for all simulation cases (from top to bottom; background, aerosol, cirrus, aerosol + cirrus) in each of the four months January, April, July and October 2004 (left to right).	168
C7	ALL CASES: Scatter plots of ΔXCH_4 against the error on CH_4 and CO_2 albedo estimation using the FSI look-up table method	169
C8	Density correlation plots of σ_{CO_2} , σ_{CH_4} and σ_{XCH_4} from the MFSI retrieval once filtered by Filter 1.	170
	(a) CO_2 VCD against σ_{CO_2}	170
	(b) CH_4 VCD against σ_{CH_4}	170
	(c) XCH_4 against σ_{XCH_4}	170
C9	Density correlation plots of σ_{CO_2} , σ_{CH_4} and σ_{XCH_4} from the MFSI retrieval once filtered by Filter 2.	170
	(a) CO_2 VCD against σ_{CO_2}	170
	(b) CH_4 VCD against σ_{CH_4}	170
	(c) XCH_4 against σ_{XCH_4}	170
C10	Density correlation plots of σ_{CO_2} , σ_{CH_4} and σ_{XCH_4} from the GFSI retrieval once filtered by Filter 1.	171
	(a) CO_2 VCD against σ_{CO_2}	171
	(b) CH_4 VCD against σ_{CH_4}	171
	(c) XCH_4 against σ_{XCH_4}	171
C11	Density correlation plots of σ_{CO_2} , σ_{CH_4} and σ_{XCH_4} from the GFSI retrieval once filtered by Filter 2.	171
	(a) CO_2 VCD against σ_{CO_2}	171

(b)	CH ₄ VCD against σ_{CH_4}	171
(c)	XCH ₄ against σ_{XCH_4}	171
C12	Total column CH ₄ for the first day of each month of 2004 gridded to 3.8° × 5°	172
C13	Monthly averaged total column CH ₄ retrieved by WFM-DOAS ver- sion 1.0, gridded to 1° × 10° [Buchwitz (2007)].	173

Chapter 1

Introduction

1.1 Climate Change

The “weather” characterises relatively short term fluctuations in meteorological conditions as opposed to the “climate”, which describes long term variations in the meteorological state and is therefore often referred to as “average weather”. Although the definition of climate refers specifically to atmospheric processes, the atmosphere is not an isolated entity but is instead linked via complex interactions with the oceans, cryosphere, biosphere and land surface; all of which collectively make up the Earth’s coupled climate system. Due to these interdependencies, perturbations to one aspect of the climate system tend to instigate knock-on effects in other areas of the system.

In addition to the complex internal interactions between different components of the climate system, the climate also reacts to external forcings which can be either natural or anthropogenic (man-made) in nature. Natural climate forcing occurs, for example, as a result of changes in solar insolation (resulting from variations in solar output or the Earth’s orbit), ice sheet coverage and volcanic activity [Jansen et al. (2007)]. In contrast, anthropogenic climate forcing results mainly from changes in atmospheric composition owing to anthropogenic emissions of so called “greenhouse gases” (GHGs; see Section 1.3) as well as changes in land use, particularly deforestation [Ciais et al. (2010)]. Although natural climate forcing can result in substantial climate change, such changes are generally either potent, yet relatively short lived (such as volcanic eruption), or subtle yet prolonged over geological timescales (such as changes in solar insolation). Figure 1.1 shows the variation in levels of deuterium, a strong indicator of atmospheric temperature, over the last 650 kyrs [Jansen et al.

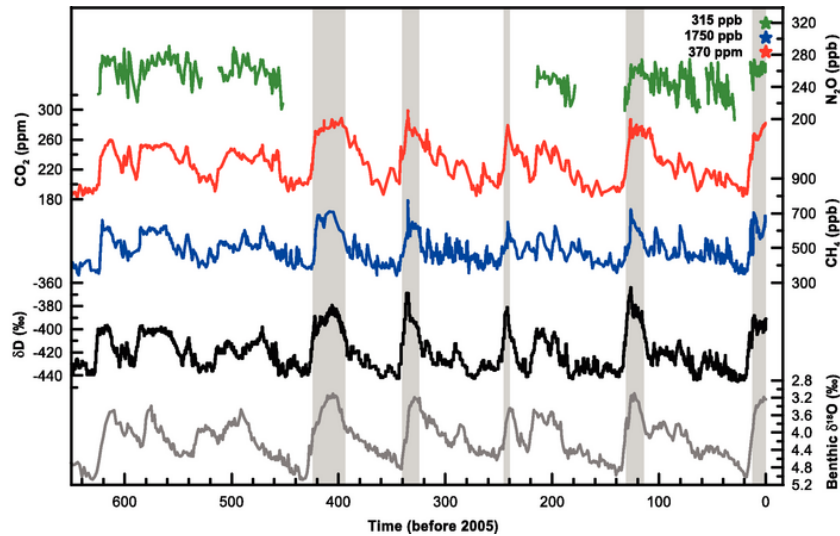


Figure 1.1: Periodic variations in deuterium (δD ; black), a proxy for local temperature, and the concentrations of atmospheric trace gases CO_2 (red), CH_4 (blue) and N_2O (green) over the last 650 kyrs determined primarily from ice core measurements (figure taken from [Jansen et al. (2007)]). Benthic $\delta^{18}\text{O}$ from marine records (grey; a proxy for changes in global ice volume) is also shown.

(2007)] determined from ice core measurements and reveals the long-term, periodic nature of natural variations in climate. Corresponding atmospheric concentrations of the main GHGs, carbon dioxide (CO_2), methane (CH_4) and nitrous oxide (N_2O), are also shown and tend to follow the same peaks and troughs as those of deuterium. High resolution ice core records indicate that a temperature rise generally precedes an increase in CO_2 by a few hundred years, nevertheless, the striking similarity in variations of temperature and GHG concentrations over the extended time period shown in Figure 1.1 implies that the two are closely related.

The modern perception of climate change refers to recent, rapid changes in the climate system which have occurred since the early 1700s. Scientific consensus in Section 1.1.2 attributes these relatively recent deviations from the natural climate cycle to anthropogenic activity, particularly the burning of fossil fuels and subsequent emission of GHGs [Forster et al. (2007)] since the onset of the industrial revolution. The dramatic increase in anthropogenic GHG emissions over this time, caused by the emergence of large-scale industrial activity, can be clearly seen in Figure 1.2 which shows the variation in concentrations of CO_2 , CH_4 and N_2O over the last 2000 years.

The predicted detrimental social and economic repercussions of climate change (such

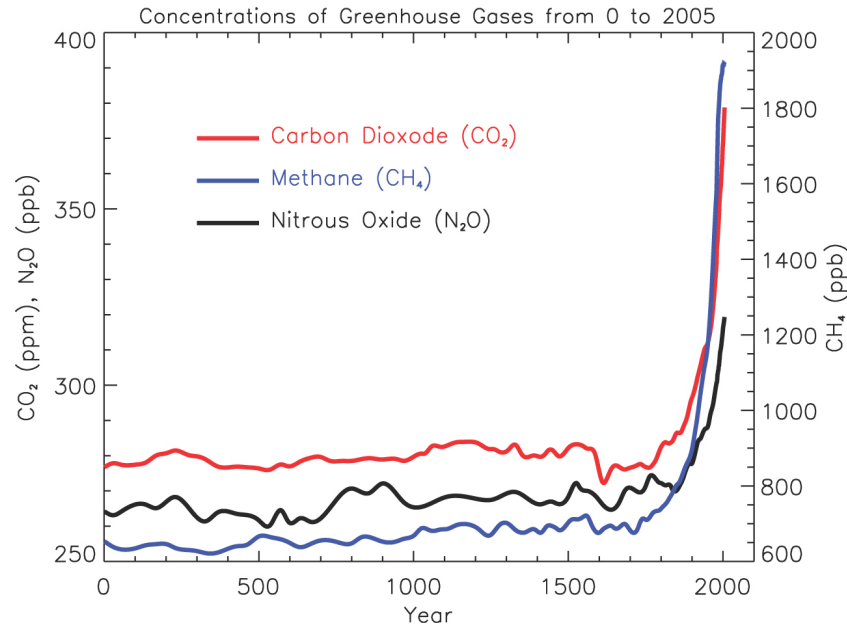


Figure 1.2: Atmospheric concentrations of the three main anthropogenic GHGs over the last 2000 years (figure taken from Forster et al. (2007)). The sharp increase in all three species from around 1750 onwards is due to the rise in anthropogenic emissions resulting from industrialisation. Concentrations are stated in parts per million (ppm) for CO₂ and N₂O and parts per billion (ppb) for CH₄.

as those outlined in the Stern review [Stern (2006)] have prompted the international community to agree legally binding targets for the reduction of GHG emissions. The United Nations Framework Convention on Climate Change (UNFCCC) is an international treaty which recognises the need for an international effort to mitigate climate change and encourages the reduction of GHG emission by the supporting 194 states (as of 2011). Although the UNFCCC does not impose mandatory restrictions on GHG emissions, scope exists for subsequent updates to the treaty to do so. The most successful of these to date has been the Kyoto Protocol [UNFCCC (1998)], which committed 37 participating countries to reducing emissions of four main GHGs (CO₂, CH₄, N₂O and sulphur hexafluoride (SF₆)) by 5% from 1990 levels over the period 2008–2012. More recently, in December 2009, the UNFCCC presented the Copenhagen Accord [UNFCCC (2010)] which recommends the continuation of targets set out in the Kyoto Protocol, but does not set any legally binding limitations.

1.1.1 Radiative Forcing and Global Warming Potential

Radiative forcing (RF) is defined by Ramaswamy et al. (2001) as “the change in net (down minus up) irradiance (solar plus longwave; in W m^{-2}) at the tropopause after allowing for stratospheric temperatures to readjust to radiative equilibrium, but with surface and tropospheric temperatures and state held fixed at the unperturbed values”. RF is therefore a useful metric for assessing the contribution of GHGs and other atmospheric constituents, such as clouds and aerosols, to climate change. CH_4 is responsible for an RF of $0.48 \pm 0.05 \text{ W m}^{-2}$ compared to $1.66 \pm 0.17 \text{ W m}^{-2}$ for CO_2 [Forster et al. (2007)].

The integrated RF of 1 kg of an atmospheric constituent over a given period of time, with respect to that of CO_2 , gives its global warming potential (GWP) [Ramaswamy et al. (2001)]. Over a period of 100 years, CH_4 has a GWP of 21 and is therefore a highly potent GHG. However, the atmospheric lifetime of CH_4 is limited to around 12 years owing to chemical reactions with tropospheric hydroxyl radical (OH; the main sink of atmospheric CH_4). As a result, CH_4 does not accumulate in the atmosphere as readily as CO_2 and subsequently its overall climatic impact is not as severe.

1.1.2 The Intergovernmental Panel on Climate Change

The Intergovernmental Panel on Climate Change (IPCC) is a collaborative effort of 152 lead authors from 30 countries which draws on state of the art climate science from experts around the world to provide a comprehensive overview of the key aspects of climate change for scientists, policy makers, the media and the general public. The findings of the IPCC thus represent the scientific consensus of the climate science community. The IPCC Fourth Assessment Report concluded with greater than 95% certainty that anthropogenic activities have contributed a positive radiative forcing (warming effect) of $+1.6 \text{ W m}^{-2}$ to the climate system since the industrial revolution [Forster et al. (2007)]. Furthermore, the IPCC provides a range of estimates of the projected rise in mean surface air temperature (SAT) resulting from six main model atmospheric scenarios in which GHG emissions remain unmitigated at different levels. Model scenarios reveal that if atmospheric CO_2 concentrations were to double, the mean SAT is likely to rise by between 2°C – 4.5°C by the end of the century [Meehl et al. (2007)]. Warming on this scale is expected to significantly perturb the climate system and possibly trigger climate feedback loops, such as the emission of CH_4 from thawing permafrost regions [Walter et al. (2007);

Zimov et al. (2006)], which can lead to runaway warming.

1.2 Radiative Equilibrium of the Earth

1.2.1 Blackbody Radiation

A blackbody is an idealised object which absorbs all incident radiation and is therefore a perfect absorber (i.e. no incident radiation is reflected). The Planck function B_ν describes the spectral radiance (power per unit area, per unit solid angle, per unit frequency [$\text{W m}^{-2} \text{sr}^{-1} \text{Hz}^{-1}$]) emitted by a blackbody:

$$B_\nu = \frac{2h\nu^3}{c^2 \exp\left(\frac{h\nu}{k_B T}\right) - 1}, \quad (1.1)$$

where $h = 6.63 \times 10^{-34} \text{ J s}$ is Planck's constant, ν is the frequency of radiation, $c = 3.0 \times 10^8 \text{ m s}^{-1}$ is the speed of light in a vacuum, $k_B = 1.38 \times 10^{-23} \text{ J K}^{-1}$ is Boltzmann's constant and T is the temperature of the blackbody in K. In reality, objects tend to fall short of the blackbody idealisation, however, it is a useful approximation. For example, the Sun and Earth can be modelled by blackbodies at temperatures of 5800 K and 288 K, respectively. Integrating B_ν over all solid angles and frequencies gives the emitted flux F [W m^{-2}], which is proportional to the fourth power of T , as described by the Stefan-Boltzmann law:

$$F = \sigma T^4. \quad (1.2)$$

1.2.2 A Basic Model of the Earth

In the absence of an atmosphere the approximate temperature of the Earth due to incident radiation from the Sun can be calculated using the simple model (example adapted from Andrews (2000) and Zender (2010)) depicted in Figure 1.3 and the following simplifying assumptions:

1. The Earth can be approximated by a blackbody of temperature T_e
2. The flux of solar radiation F_\odot ($\sim 1370 \text{ W m}^{-2}$) incident on the Earth can be considered approximately parallel
3. The albedo A of the Earth is ~ 0.3 (i.e. only $(1 - A)$ of the incident solar radiation is absorbed by the Earth)

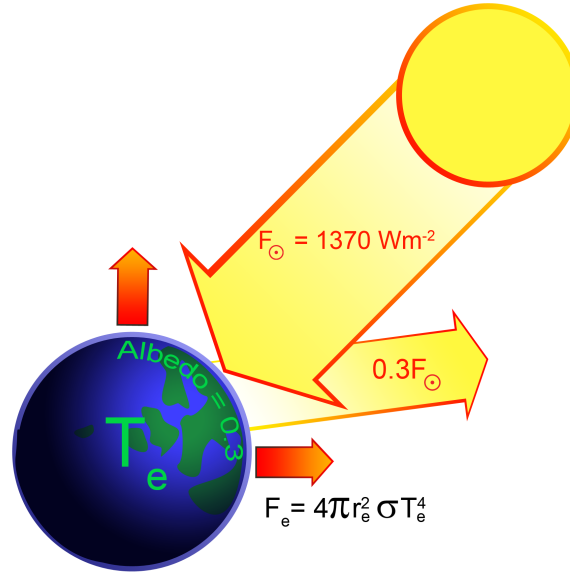


Figure 1.3: A simple model of the radiation exchange between the Sun and Earth (figure produced by A. Durose and D. Knappett).

4. The Earth (of radius r_e) intercepts an area πr_e^2 of F_\odot

From assumptions 3 and 4, the solar radiation absorbed by the Earth F_e is given by $(1 - A)F_\odot\pi r_e^2$. Owing to planetary rotation, F_\odot is distributed over the Earth's entire surface ($4\pi r_e^2$) hence the Earth reradiates over the same area. Using Equation 1.2 the temperature of the Earth can be expressed as $T_e = (F_e/\sigma)^{\frac{1}{4}}$, therefore the total outgoing radiation from the Earth is $4\pi r_e^2\sigma T_e^4$. Assuming the Earth to be in radiative equilibrium, the incoming and outgoing radiation can be equated and rearranged for T_e :

$$T_e = \left(\frac{(1 - A)F_\odot}{4\sigma} \right)^{\frac{1}{4}}. \quad (1.3)$$

Substituting values for F_\odot and A gives $T_e = 255$ K, which is significantly smaller than the empirical mean value of 288 K.

1.3 The Greenhouse Effect

The Earth's atmosphere is a thin gaseous layer which envelops the planet and consists of approximately 78% nitrogen, 21% oxygen, 1% argon (by concentration) and a mixture of various other gases such as CO_2 and CH_4 in trace amounts [Baede et al. (2001)]. Solar radiation incident at the top of the atmosphere (TOA) is predom-

Classification	Abbreviation	Classification scheme and spectral range (nm)		
		DIN	Sensor Response	ISO
Near Infrared	NIR	0.75–1.4	0.7–1.0	0.78–3.0
Short-wave Infrared	SWIR	1.4–3.0	1.0–3.0	-
Mid-wave Infrared*	MWIR	3.0–8.0	3.0–5.0	3.0–50
Long-wave Infrared*	LWIR	8.0–15	7.0–14	-
Far Infrared	FIR	15–1000	-	50–1000

Table 1.1: Spectral classification schemes for the infrared (IR) spectral region. The three schemes presented here are the German Institute for Standardization (DIN) IR scheme, the Sensor Response scheme described by Miller (1994) and the French International Organization for Standardization (ISO) scheme 20473.

*MWIR and LWIR are often referred to as thermal infrared (TIR)

inantly in the ultra-violet (UV) and visible regions of the spectrum since the Sun closely resembles a blackbody at a temperature of ~ 5800 K. The majority of visible radiation from the Sun passes unhindered down to the Earth’s surface as the atmosphere is relatively transparent (i.e. little absorption occurs) at these wavelengths; absorption by ozone and aerosols/clouds however can be significant in this spectral region. The Earth reflects a certain fraction of incident solar radiation, dependent on the localised albedo (reflectivity) of the surface, whilst the rest is absorbed and subsequently reradiated at considerably lower wavelengths in the thermal infrared (TIR), consistent with the Earth as a blackbody at ~ 288 K. A number of atmospheric trace gases, such as CO_2 and CH_4 , are strongly absorbing in the TIR spectral region, leading to warming of the Earth-atmosphere system. This process is known as the Greenhouse Effect and atmospheric trace gases which absorb strongly in the TIR (particularly CO_2 , CH_4 and N_2O) are known as GHGs.

It should be noted that several different schemes exist for the classification of the IR spectral region. Table 1.1 lists the spectral ranges of three schemes which are commonly encountered in Earth observation literature. For the purposes of this work, terminology corresponding to the ‘Sensor Response’ IR classification scheme will be adopted for consistency with the definition of spectral channels of the Scanning Imaging Absorption Spectrometer for Atmospheric Chartography (SCIAMACHY), referred to throughout this thesis.

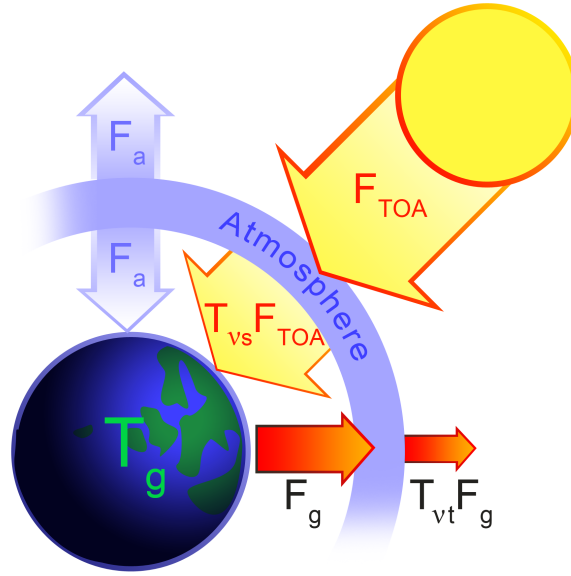


Figure 1.4: A simple model of the Greenhouse Effect (figure produced by A. Durose and D. Knappett).

1.3.1 A Model of the Greenhouse Effect

The introduction of a thin atmospheric layer to the example described in Section 1.2.2 (as depicted in Figure 1.4) can be used to demonstrate the role of the atmosphere in raising the mean temperature of the Earth by way of the Greenhouse Effect (example adapted from Andrews (2000) and Barkley (2007)). The atmosphere transmits radiation by varying amounts, dependent on the transmission T_ν at a given wavelength. Employing subscripts s and t to denote solar and thermal radiation respectively, the flux at the top of the atmosphere (TOA) F_{TOA} and at the Earth's surface F_g can be expressed as follows:

$$F_{\text{TOA}} = F_a + T_{vt}F_g, \quad (1.4)$$

$$F_g = F_a + T_{vs}F_{\text{TOA}}, \quad (1.5)$$

where F_a is the flux emitted by the atmosphere. Combining Equations 1.4 and 1.5 and rearranging for F_g gives:

$$F_g = F_{\text{TOA}} \frac{1 + T_{vs}}{1 + T_{vt}}. \quad (1.6)$$

A concept crucial to the Greenhouse Effect is that $T_{vs} > T_{vt}$, hence, whilst solar

radiation penetrates the atmosphere relatively easily, the longer wavelength, thermal radiation emitted by the Earth’s surface is more readily absorbed. Consequently, heat becomes “trapped” in the Earth-atmosphere system. By assuming the ground can be approximated by a blackbody of temperature T_g the surface flux becomes $F_g = \sigma T_g^4$ hence:

$$T_g = \left(\frac{F_g}{\sigma} \right)^{\frac{1}{4}}. \quad (1.7)$$

F_{\odot} corresponds to radiation impinging on a cross-sectional area πr^2 . Since however, this is redistributed over the whole globe (i.e. $4\pi r^2$), the intensity at the TOA is reduced by a factor of 4: $F_{\text{TOA}} = \frac{1}{4}F_{\odot}$. Selecting reasonable transmission values of $T_{\nu s} \sim 0.8$ and $T_{\nu t} = 0.2$, the resulting temperature at the Earth’s surface is $T_g = 286$ K. In practice, T_{ν} is dependent on atmospheric composition, therefore the extent of warming that occurs differs according to the relative concentrations of absorbing GHGs.

Despite its negative connotations, the Greenhouse Effect is actually crucial to life on Earth. Without the absorbing properties of the atmosphere the TIR blackbody radiation emitted by the Earth would simply be lost to space, leaving the planet at an average temperature of 255 K, as demonstrated in Section 1.2.2. The problem faced by the modern world is that the natural stability of the greenhouse effect has been disrupted by continuously increasing emissions of anthropogenic GHGs during the last three centuries.

1.4 The Role of CH₄ in the Atmosphere

1.4.1 CH₄ Sources and Sinks

The production of CH₄ occurs under anaerobic conditions (i.e. without oxygen) and generally results from the activity of methane-forming bacteria known as methanogens, which thrive in water logged environments. Table 1.2 lists key sources of present day CH₄ emission, which have been classified as being either natural or anthropogenic in origin. Although a number of the sources given in Table 1.2 can be classified as non-biogenic, they can usually be traced back to biogenic origins. For example, natural gas is classified as an inorganic source, however, its formation occurs as a result of methanogen activity during the decay and sequestration of ancient organic material. Wetlands are by far the largest natural source of CH₄, however the mag-

nitude of wetland emissions is highly changeable from year to year, since flooding and drought cause substantial variation in wetland coverage. Subsequently, significant variation is imposed upon multi-year emission records [Bousquet et al. (2006)].

Natural (40%)	Anthropogenic (60%)
Wetlands*	Ruminant animals*
Termites*	Rice cultivation*
Ocean*	Gas, oil and industry
Wild animals*	Landfill*
Geological sources	Waste management
Hydrates	Biomass burning
Wildfires	Coal mining

Table 1.2: Natural and anthropogenic sources of methane listed in order of magnitude [Denman et al. (2007)].

*Biogenic processes.

The primary sink of atmospheric CH₄ is oxidation by tropospheric OH:



The reaction of CH₄ with OH in the troposphere accounts for approximately 90% of the overall sink [Bergamaschi and Bousquet (2008)] and leads to the creation of CO and CO₂ in subsequent chemical reactions. Oxidation by dry soil, stratospheric loss and reactions with chlorine in the marine boundary layer make up the remainder of the CH₄ sink [Bergamaschi and Bousquet (2008)]. Since CO also reacts with OH there is a connection between the lifetimes of CH₄ and CO.

Estimations from a variety of studies collectively place the magnitude of global pre-industrial methane emissions in the range of 200–250 Tg yr⁻¹ [Denman et al. (2007)], with the vast proportion of emissions resulting from natural processes. In comparison, global emissions of CH₄ during 2005 were estimated to be around 582 Tg yr⁻¹, corresponding to an estimated atmospheric loading of 4932 Tg [Denman et al. (2007)]. Although the total global source strength of CH₄ is well constrained by measurements of OH [Frankenberg et al. (2006)], the temporal and spatial variability of individual CH₄ sources and sinks is currently not well known [Chen and Prinn (2006); Bousquet et al. (2006)].

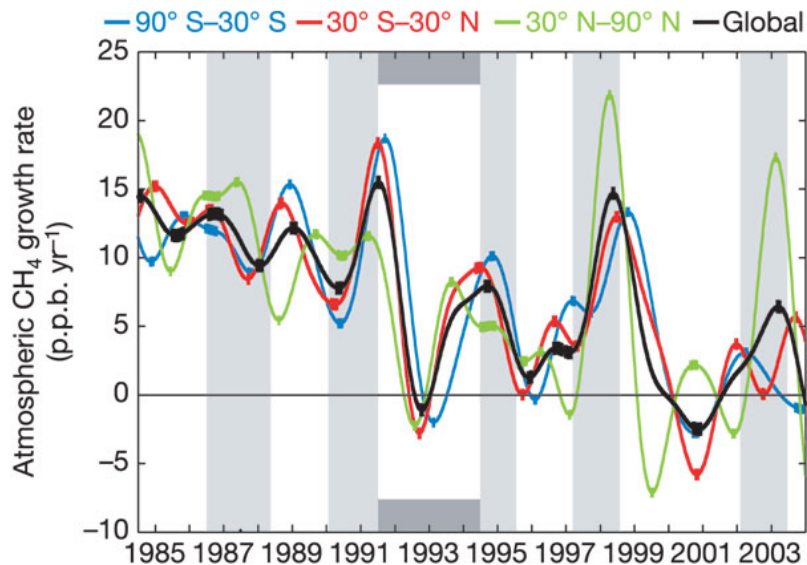


Figure 1.5: Growth rate of CH₄ over the last two decades as determined from the assimilation of air flask measurements from NOAA into an inversion model (figure taken from Bousquet et al. (2006)). Black indicates the global growth rate, whilst the southern hemisphere is shown in blue, the tropics in red and the northern hemisphere in green. El Niño events are indicated in light grey whereas dark grey highlights the period following the eruption of Mount Pinatubo in 1991.

1.4.2 Trends in Atmospheric CH₄ Concentrations

Ice core measurements imply that pre-industrial concentrations of atmospheric CH₄ have varied between approximately 300 parts per billion (ppb) during glacial periods and 700 ppb during inter-glacial periods [Karlsson and Simpson (2010)] over the last 650 kyrs (see Figure 1.1). However, with the onset of large-scale industrial activity in the early 1700s, emissions of GHGs began to rise exponentially. The 2005 global mean CH₄ volume mixing ratio (VMR) was calculated to be 1774.62 ± 1.22 ppb from surface flask measurements made at forty National Oceanic and Atmosphere Administration (NOAA) sites. Gas chromatography measurements taken from five Advanced Global Gases Experiment (AGAGE) sites result in a similar value of 1774.03 ± 1.68 ppb for the same year. Increased anthropogenic emissions have therefore resulted in an almost three-fold increase in levels of atmospheric CH₄ of over the last three hundred years [Forster et al. (2007)].

Although methane concentrations have risen continuously since the industrial revolution, up until the early 1990s the *rate* of this rise was also increasing year on year. However, since that time the atmospheric growth rate has been in a period

of decline leading to a leveling off of CH₄ levels [Dlugokencky et al. (2003); Rigby et al. (2008)]. Figure 1.5 shows a decreasing trend in the CH₄ growth rate, observed in measurements from a number of NOAA air sampling sites, during the period 1984–2004. The atmospheric loading of CH₄ is largely regulated by the balance between global CH₄ emissions and the rate at which CH₄ destruction by OH occurs in the troposphere. A decrease in growth rate is therefore the result of either a reduction in CH₄ emissions or an increase in levels of tropospheric OH. By modeling the observed decrease using a 3D chemical transport model (CTM) Dlugokencky et al. (2003) attribute the declining CH₄ growth rate to a reduction in fossil fuel emissions between 1990–1995. Bousquet et al. (2006) also conclude that reduced anthropogenic emissions are to blame and suggest in addition that wetland emissions dominate the observed variability over the period 1984–2004. The leveling off of CH₄ appears however to have been a temporary phase in the overall increase of CH₄ emissions, with measurements from the AGAGE network showing renewed growth in 2007 [Rigby et al. (2008)]. Similarly, globally averaged NOAA measurements indicate an increase in atmospheric CH₄ of 8.3 ± 0.6 ppb in 2007 and 4.4 ± 0.6 ppb in 2008 [Dlugokencky et al. (2009)].

1.4.3 Ground Based Remote Sensing

The Total Carbon Column Observing Network (TCCON) [Wunch et al. (2011)] consists of a series of ground based Fourier Transform Spectrometer (FTS) instruments which are used to retrieve trace gas total columns from solar spectra in the NIR/SWIR and is a typical example of ground based remote sensing. TCCON measurements cover a broad spectral range (645–2564 nm) and are therefore ideal for the validation of space based retrievals in the NIR/SWIR, particularly those from the Scanning Imaging Absorption Spectrometer for Atmospheric Chartography (SCIAMACHY) [see Barkley et al. (2007); Bösch et al. (2006)]. The TCCON initially came online in 2004 with sites at Bremen, Lauder, Park Falls and Ny Alesund* but has since grown to a network of 18 sites, shown in Figure 1.6, plus 2 additional sites in Japan and Reunion Island established during 2011 and a further site currently planned for Antarctica.

*An existing site incorporated into the TCCON; originally established in 2002.

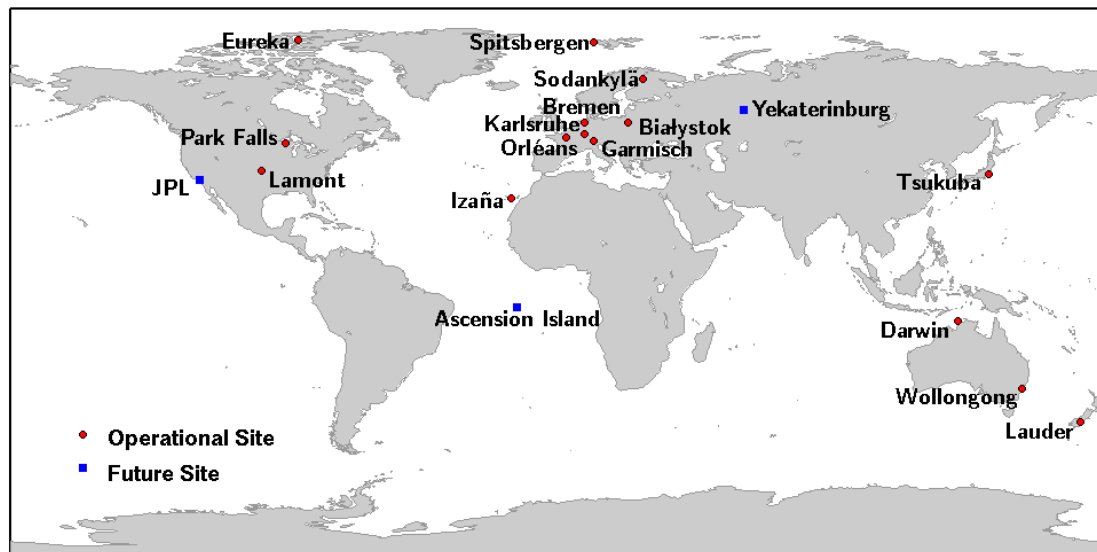


Figure 1.6: TCCON observation sites accurate as of 30/04/2010 (figure obtained from <https://tccon-wiki.caltech.edu/>).

1.4.4 Satellite Retrievals of Total Column CH₄

In-situ measurements, such as those from surface flasks at NOAA sites, provide highly accurate datasets of GHG concentrations over a long time period and are crucial to our understanding of GHG fluxes. However, such measurements are only representative of the localised area surrounding the measurement site and are therefore spatially limited. In addition, the distribution of in-situ measurement sites around the globe is often restricted by political or geographical limitations, resulting in extensive regions where no measurements are available. In contrast, satellite instruments can offer the scientific community unparalleled spatial and temporal coverage of the entire atmospheric system, monitoring trace gas concentrations for continuous time periods. Space-based measurements are a form of remote sensing—a term which refers to the fact that using this technique trace gases concentrations are not measured directly but instead are inferred from radiance measurements via the application of a retrieval algorithm. Table 1.3 compares all past and present space-based instruments from which retrievals of CH₄ have been made.

Instrument	Full Name	Operational Period	Measurement Type	Measurement Height	Observation Geometry	CH ₄ References
TES*†	Tropospheric Emission Spectrometer	2004–Present	TIR	Trop., Strat.	Limb, Solar Occ.	Payne et al. (2009)
IASI*†	Infrared Atmospheric Sounding Interferometer	2006–Present	TIR	Trop., Strat.	Nadir	Razavi et al. (2009) Crevoisier et al. (2009)
HALOE	Halogen Occultation Experiment	1991–2005	Discrete windows in SWIR-TIR	Strat.	Solar Occ.	Ruth et al. (1997)
ILAS I, II	Improved Limb Atmospheric Sounder	1996–1997	Discrete windows in Vis-TIR	Strat.	Solar Occ.	Ejiri et al. (2006)
MIPAS	Michelson Interferometer for Passive Atmospheric Sounding	2002–Present	TIR	Upper Trop., Strat., Meso.	Limb	Payan et al. (2007)
SCIAMACHY*	Scanning Imaging Absorption Spectrometer for Atmospheric Chartography	2002–Present	UV/Vis/NIR/SWIR	Trop., Strat., Meso.	Nadir, Limb, Solar Occ., Lunar Occ.	Frankenberg et al. (2008a) Schneising et al. (2009)
TANSO-FTS*	Thermal And Near infrared Sensor for carbon Observations- Fourier Transform Spectrometer	2009–Present	SWIR/TIR	Trop., Strat., Meso.	Nadir	Parker et al. (2011)

Table 1.3: Details of space-based instruments from which retrievals of atmospheric CH₄ have been performed.

*Instruments which are sensitive to the troposphere.

†IASI and TES retrievals are weighted towards the mid-troposphere however IASI has the potential to determine near-surface information also.

Defining Trace Gas Columns

Trace gas abundances are typically measured in terms of their vertical column density (VCD) which describes the column integrated number of molecules in a vertical atmospheric column, of cross-sectional area 1 cm², as seen from the top of the atmosphere (TOA). Since VCD is dependent on column mass, and is therefore sensitive to the Earth’s surface topography, a more useful quantity is the VMR; a concentration defined in terms of the ratio of trace gas molecules to the total number of molecules, usually given in units of parts per million (ppm) or parts per billion (ppb). XCO₂ and XCH₄ specifically refer to the dry air column-averaged mole fractions of CO₂ and CH₄ respectively and have been adopted throughout the thesis to describe the retrieved total column VMRs.

The Proxy Approach

The proxy approach converts a satellite retrieved VCD (molecules cm⁻²) to VMR (ppm; ppb) by taking the ratio of the retrieved VCD (VCD_R) to the VCD of a trace gas which is considerably less variable than the target trace gas and has an absorption band in close spectral proximity (VCD_P). This ratio is then multiplied by a mean model value of the proxy trace gas as follows:

$$\text{VMR}_R = \frac{\text{VCD}_R}{\text{VCD}_P} \text{VMR}_P. \quad (1.9)$$

Since scattering is wavelength dependent, the majority of spectral effects due to aerosols and clouds are expected to cancel out by using this method. A certain level of inherent error is introduced by use of the spectral ratio approach since VMR_P is only an approximation of the true VMR; any error in VMR_P with respect to the true atmospheric column will therefore propagate, making VMR_R incorrect by the same degree. However, it is assumed that the error associated with using VMR_P is small compared to the error due to scattering and is therefore justifiable. For retrievals of CH₄ within the 1.63–1.67 μm spectral region, CO₂ retrieved from 1.56–1.59 μm can be used as a spectral proxy [Frankenberg et al. (2006)], as described in Section 3.3.2.

Existing Retrievals of XCH₄

Satellite retrievals of XCH₄ from the Scanning Imaging Absorption Spectrometer for Atmospheric Chartography (SCIAMACHY) have previously been produced using independent differential optical absorption spectroscopy (DOAS) based retrieval

schemes by the following research groups:

- Netherlands Institute for Space Research (SRON) using the Iterative Maximum A Posteriori (IMAP)-DOAS retrieval method [Frankenberg et al. (2005b)].
- Institute of Environmental Physics (IUP) at the University of Bremen using the Weighting Function Modified (WFM)-DOAS retrieval method [Buchwitz et al. (2000)].

The objective of this section is to discuss the results of previous retrievals of XCH₄, hence background details of the IMAP-DOAS and WFM-DOAS retrieval schemes are not provided here. However, the theory behind DOAS type retrievals is explained in Section 2.4.2 and a description of WFM-DOAS in particular is given in Section 2.4.5 since this retrieval method paved the way for Full Spectral Initiation (FSI) WFM-DOAS which is the retrieval algorithm utilised in this work.

WFM-DOAS Retrievals of XCH₄

In an initial study which focused on the period September–October 2003, WFM-DOAS retrievals of XCH₄ were performed using data from SCIAMACHY channel 8 (2259–2386 nm) and revealed enhanced XCH₄ over India, Southeast Asia and central Africa. Comparison with the Tracer Model 5 (TM5) CTM showed that model and observed results agree to within 5% and indicate that the largest emissions originate from natural sources such as rice paddies and wetlands. The initial version of WFM-DOAS (v0.4) suffered from a time dependent bias of up to –15% as a result of the continually changing ice layer build-up on the channel 8 detector (discussed further in Section 3.1.3). This was rectified by applying a time-dependent correction factor which corresponds to the time since the last ice-layer decontamination phase (heating of the detector in order to remove the ice layer) producing WFM-DOAS v0.41 results.

Due to biases caused by ice contamination of SCIAMACHY channel 8, the more recent WFM-DOAS version 1.0 retrieval [Schneising et al. (2009)] utilises spectra from SCIAMACHY channel 6. The resulting yearly averaged XCH₄ for 2004 is shown in Figure 1.7. Comparison of XCH₄ from WFM-DOAS version 1.0 with the TM5 CTM revealed unexpectedly high CH₄ concentrations over the tropics, which were unlikely to be the result of using the proxy approach for column normalisation.

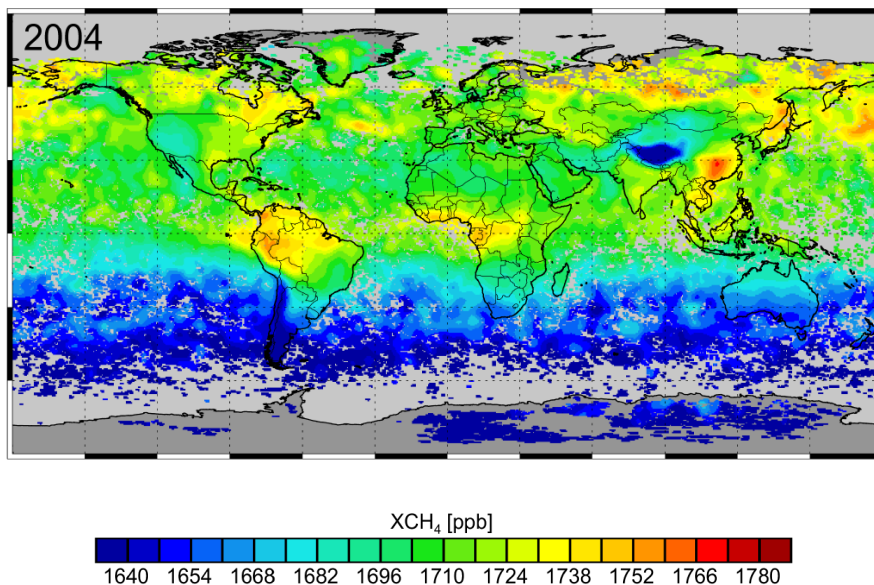


Figure 1.7: 2004 yearly average of methane total column XCH_4 retrieved using WFM-DOAS version 1.0 (figure taken from Schneising et al. (2009)).

IMAP-DOAS Retrievals of XCH_4

An initial study of the months August–November 2003 [Frankenberg et al. (2005a)], in which IMAP-DOAS retrievals of SCIAMACHY XCH_4 were compared with the TM3 CTM, revealed large emissions from the plains of India, Southeast Asia and China. Emissions from India were attributed to extensive rice cultivation, prevalent in the area during the autumn months considered in the study, and domestic ruminant cattle. In both China and the USA, the observed CH_4 was attributed to emissions from highly populated regions, where the burning of fossil fuel for large-scale industry, automotive purposes and waste treatment contributes greatly to methane concentrations. Comparison of the retrieved values with TM3 highlighted large discrepancies in CH_4 concentrations over India, northern South America and the tropics.

Following the initial short study, IMAP-DOAS was then applied to the retrieval of CH_4 for the two years 2003 and 2004 [Frankenberg et al. (2006)] and results were compared with an updated CTM (TM4). A two-year average of retrieved total column CH_4 VMR is shown in Figure 1.8 and displays a clear north-south gradient. This was expected due to the large magnitude of both natural and anthropogenic emissions in the populated northern hemisphere as opposed to the southern hemisphere. Variations in the retrieved VMR were at most 5% from the global mean,

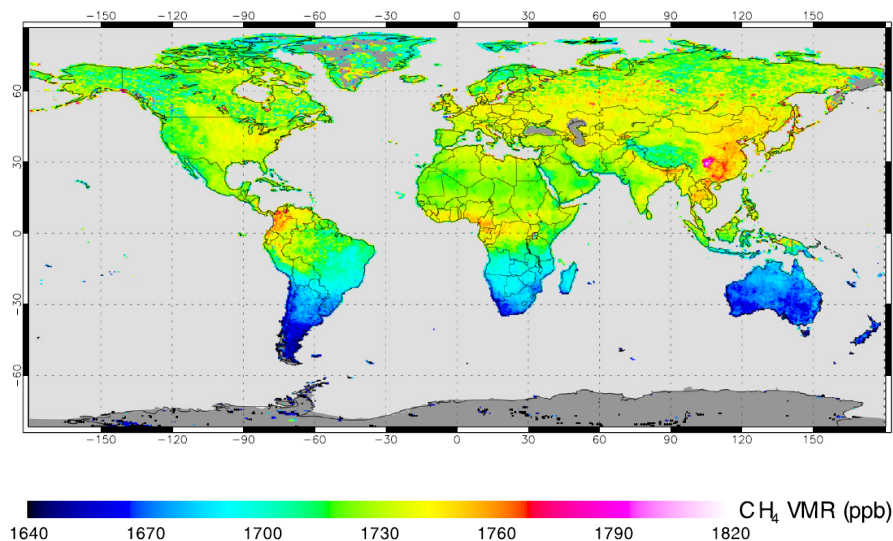


Figure 1.8: Two-year mean total column XCH₄ retrieved from SCIAMACHY data from 2003–2004 using IMAP-DOAS (figure taken from Frankenberg et al. (2006)). Data is shown on a $0.5^\circ \times 0.5^\circ$ grid.

with very little variation on local scales since, in general, CH₄ emissions quickly become well mixed due to the relative longevity of atmospheric methane. As in the initial study [Frankenberg et al. (2005a)], elevated CH₄ VMRs over tropical regions were once again observed, suggesting an underestimation of tropical emissions by the CTM.

The observation of unexpectedly high CH₄ concentrations over the tropics coincided with the report of in-situ emission of CH₄ from living plants under aerobic conditions [Keppler et al. (2006)]. Initially these two results were thought to be related, however subsequent studies into the emission of CH₄ from plants failed to reproduce the results published by Keppler et al. (2006). In particular, Vigano et al. (2008) reported the emission of CH₄ from detached plant material only when placed under UV irradiation, whereas Dueck et al. (2007) reported no observed CH₄ emission from plants placed in an artificially high carbon dioxide environment (isotope carbon-13 enriched) in order to emphasise the presence of any CH₄ emission. As a result, doubt has been cast on the credibility of emissions of CH₄ from plants under aerobic conditions. Furthermore, the use of updated H₂O spectroscopic parameters within the IMAP-DOAS retrieval led to a downward revision of CH₄ VMRs over tropical regions [Frankenberg et al. (2008a)], as shown in Figure 1.9.

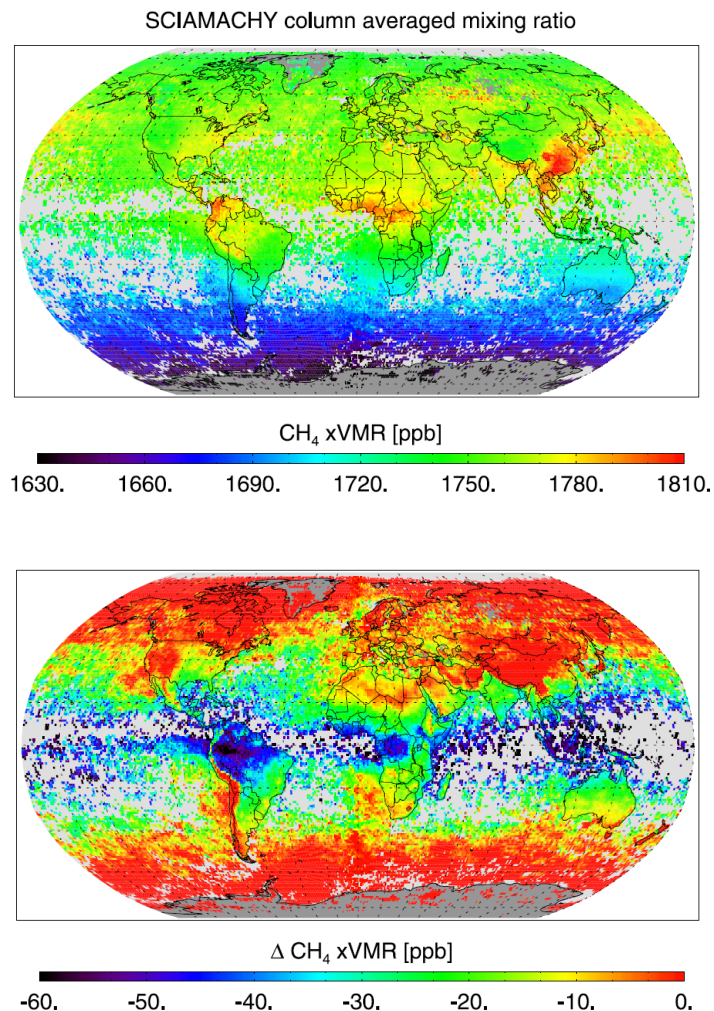


Figure 1.9: Yearly average of total column XCH₄ retrieved using IMAP-DOAS with (top) an updated H₂O spectroscopy and (bottom) the corresponding difference between retrievals performed both with and without the spectroscopic update applied (figures taken from Frankenberg et al. (2008a)).

1.5 Thesis Overview

Since CH₄ is such a potent GHG, a greater understanding of the partitioning of CH₄ emissions between individual sources and sinks and quantification of their spatial and temporal variability is required in order to regulate anthropogenic emissions and mitigate future climate change. In particular, the strength of emissions from wetlands, rice paddies and possible future emissions from permafrost regions resulting from the destabilisation of methane hydrate are not currently well known. To constrain estimates of CH₄ sources from model inversions, satellite measurements with a precision of < 1–2% are required [Meirink et al. (2006); Frankenberg et al.

(2006)]. However, scattering in the SWIR caused by the presence of aerosols and cirrus clouds in a satellite observed scene can cause significant retrieval errors if not properly accounted for. The objective of this thesis is therefore to provide a better understanding of the errors arising from spectra contaminated by scattering due to aerosols and ice clouds. This has been achieved in a series of stages which address the following aims:

1. To modify the FSI WFM-DOAS retrieval algorithm for the retrieval of atmospheric CH_4 .
2. To perform retrievals of XCH_4 over a test region and validate results against ground based data.
3. To conduct a series of sensitivity simulations in order to assess the impact of scattering by aerosols and thin ice clouds on retrieval errors.
4. To subsequently modify the FSI WFM-DOAS retrieval algorithm to account for scattering due to aerosols.

Following from the introduction to the role of atmospheric CH_4 in climate change given in this chapter, Chapter 2 introduces the concept of remote sensing and the challenges faced when performing space based-measurements in the SWIR spectral region. Chapter 3 introduces the SCIAMACHY instrument and discusses the calibration of SCIAMACHY L1B data. This chapter also details the updates made to the FSI WFM-DOAS retrieval algorithm for retrievals of CH_4 from SCIAMACHY data. Chapter 4 details three sensitivity studies performed to assess 1) the sensitivity of the FSI WFM-DOAS retrieval algorithm to inaccurate a priori data, 2) retrieval errors caused by the introduction of a simple scattering layer and 3) global biases introduced by the simulation of realistic aerosol and ice cloud profiles. Chapter 5 presents retrievals of total column XCH_4 over North America for the year 2004 and compares retrievals with ground based measurements from Park Falls. In this chapter, the performance of the original FSI WFM-DOAS algorithm is compared to retrievals obtained when updates to a priori albedo and aerosol were applied. Finally, Chapter 6 contains conclusions drawn from the results of Chapters 4 and 5.

Chapter 2

Remote Sensing of CH₄

2.1 Introduction

This chapter aims to introduce the concept of remote sensing, with an emphasis on the underlying physics involved in the SWIR spectral region, and begins with an introduction to satellite remote sensing in Section 2.2. Section 2.3 then provides an overview of the fundamentals of molecular spectroscopy relevant to the retrieval of XCO₂ and XCH₄ in the SWIR. An introduction to Differential Optical Absorption Spectroscopy (DOAS) and its application to the SWIR spectral region in the form of WFM-DOAS is given in Section 2.4. As such, this section provides the foundation for understanding FSI WFM-DOAS; the retrieval method used within this thesis. The chapter concludes with a discussion of the detrimental effect of atmospheric scattering on retrievals in the SWIR caused by aerosols and clouds in Sections 2.5 and 2.6 respectively.

2.2 Satellite Remote Sensing

TOA radiances measured by space based remote sensing instruments can be used to infer atmospheric greenhouse gas concentrations since the interaction between radiation and atmospheric trace gases results in measurable absorption features in observed spectra. Satellite remote sensing instruments therefore provide a way to observe the atmosphere from a unique perspective and have the advantage of being able to retrieve either partial or total atmospheric columns. Furthermore, space based instruments have the ability to achieve global coverage in a matter of days and thereby complement data from in-situ measurements.

Passive remote sensing of the atmosphere from space involves observing the light from an existing radiation source which has passed through the atmosphere on its path to the instrument. The two approximate blackbody sources available which can be utilised for this purpose are: the Sun at a temperature of ~ 5800 K, radiating strongly in the visible and NIR, and the Earth at ~ 288 K which absorbs incident solar radiation and subsequently re-radiates at wavelengths in the TIR. Since the Earth is at a significantly lower temperature than the Sun, the minimum wavelength of its blackbody emission is around $4 \mu\text{m}$ [Liou (1992)]. As a result, blackbody emission from the Earth does not overlap with solar emission in the SWIR and subsequently radiative transfer calculations involving solar SWIR radiation and the Earth's TIR radiation can be treated independently. CO_2 and CH_4 both exhibit absorption features in the TIR and SWIR, however these two spectral regions can be used to probe the atmosphere in different ways depending on whether a total or partial column retrieval product is required.

Thermal Infrared (TIR)

Solar radiation incident on the Earth's surface is either absorbed, resulting in warming, or simply reflected back into space depending on the value of the localised surface albedo. When considering the vertical sensitivity of space based TIR observations of the atmosphere it is useful to think of the atmosphere in terms of layers at different altitude. Since atmospheric pressure, and hence gas concentration, peaks at the Earth's surface, TIR radiation emitted from the surface (at temperature T_{surf}) has a high chance of being absorbed by the relatively dense atmospheric layers directly above it. Radiation in the TIR therefore has a shorter path length (the mean distance traversed by radiation before being absorbed) for stronger lines at low altitudes. In addition, low altitude atmospheric layers (where pressures are high enough to maintain local thermodynamic equilibrium) also emit blackbody radiation, albeit at a slightly reduced temperature to T_{surf} . Since these temperatures are sufficiently comparable, atmospheric blackbody emission tends to obscure any spectral features due to the absorption of radiation emitted by the surface and the atmospheric layers below.

With increasing altitude, atmospheric pressure decreases exponentially according to the hydrostatic equation whereas atmospheric temperature displays significant variation in its vertical profile shape, as shown in Figure 2.1. Although temperatures

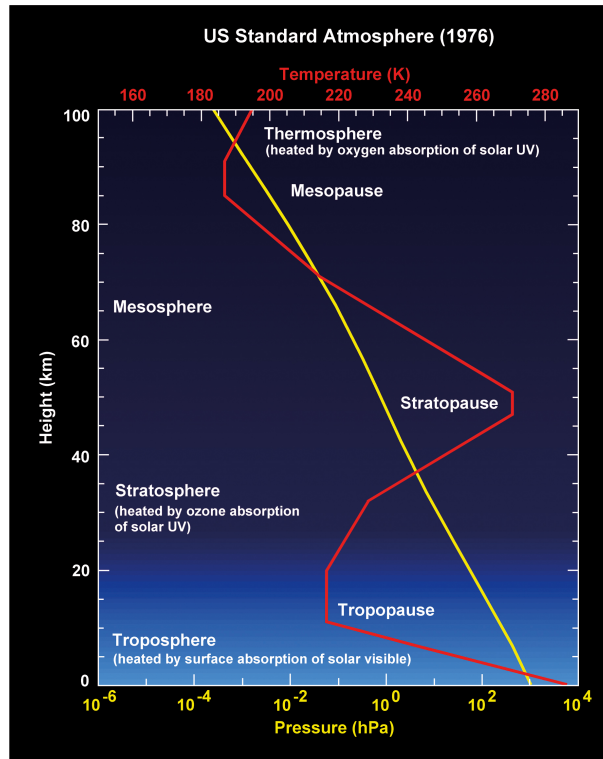


Figure 2.1: Typical atmospheric pressure and temperature profiles derived from the US standard atmosphere (figure taken from Gottwald et al. (2006)). Note the log scale on the x-axis, indicating that pressure decreases exponentially with altitude.

rise through the stratosphere and begin to approach T_{surf} , the contribution from TIR radiation in these higher altitude layers is smaller since the pressure is far less than at the surface; there is simply less gas present to radiate. Cooler atmospheric regions, such as the upper troposphere and lower stratosphere, emit very little in the TIR and are therefore able to produce strong absorption features. In general the TOA TIR spectrum consists of a continuum of blackbody radiation emitted from the surface and low altitude atmospheric layers coupled with absorption features from sparser, low temperature layers in the mid troposphere or above.

In summary, TIR observations rely on a significant temperature gradient between the atmosphere and surface for absorption to be observed hence TIR measurements are typically most sensitive in the mid to upper troposphere, where temperatures are sufficiently low with respect to T_{surf} . As a result, TIR observations are generally used to perform partial column retrievals which are useful for obtaining height resolved information but tend to have more limited sensitivity to the boundary layer; boundary layer concentrations are the most strongly influenced by major sources of

surface trace gas emission. A major advantage of TIR measurements however is the ability to observe during both day and night since TIR emission is not dependent on continuous solar illumination.

Shortwave Infrared (SWIR)

Although the atmosphere can be viewed with the Sun in the direct instrument line of sight (a viewing geometry known as solar occultation) the method discussed here involves observing sunlight that has been reflected from the Earth's surface and scattered by the atmosphere. In contrast to observations in the TIR, for measurements made in the SWIR thermal emission from the Earth can be largely ignored since there is minimal overlap between the blackbody emission of the Sun and Earth. As a result, measurements in the SWIR can probe the entire atmospheric column and hence provide information about the the boundary layer where trace gas emissions peak. Since measurements in the SWIR rely on reflected sunlight, measurements can only be made on the illuminated side of the Earth and over regions of sufficiently high albedo, such as non-water surfaces. The poor reflectivity of water means that, in general, measurements over the ocean are only possible using sunglint observations or by utilising low lying cloud as a pseudo surface. In the latter case, the atmospheric column beneath the cloud is effectively cut off resulting in a loss of information regarding the boundary layer.

2.3 Molecular Spectroscopy in the SWIR

Spectroscopy is the study of the interaction between electromagnetic radiation and matter from which information about the constituent atoms and molecules of a substance can be gained. Changes in molecular energy occur as the result of one of four different mechanisms; the excitation of an electron within the molecule, molecular vibration, molecular rotation or translation. The Born-Oppenheimer approximation [Banwell and McCash (1994)] allows the total energy of a molecule to be described as the sum of energies resulting from each of the these modes:

$$E_{Tot} = E_e + E_{vib} + E_{rot} + E_{tr}. \quad (2.1)$$

As a result, the different mechanisms of molecular energy exchange can be treated independently and adhere to a well defined hierarchy of energies. Electronic transitions are by far the most energetic, involving radiation at UV wavelengths to excite

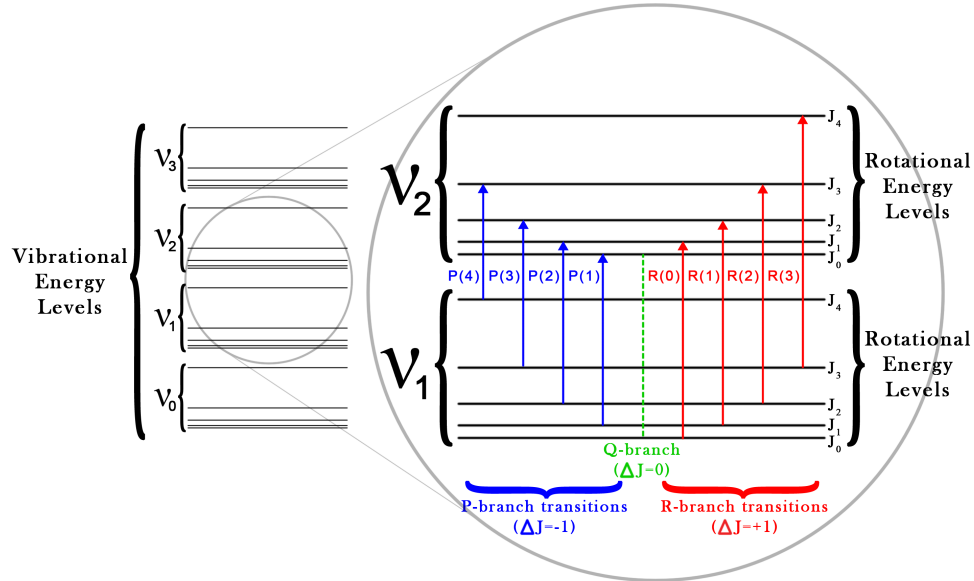


Figure 2.2: Energy level diagram for vibrational (ν) and rotational (J) transitions, showing the P, Q and R branches of coupled vibration-rotation transitions (figure produced by A. Durose and D. Knappett).

the constituent electrons of a molecule, followed by molecular vibrations, corresponding to energies in the IR, and molecular rotation, which relates to energies in the microwave region. Molecular translation is the least energetic of the available molecular transitions and its contribution can be considered negligible for the purposes of SWIR spectroscopy.

2.3.1 Vibration-Rotation Transitions

In the majority of cases when a vibrational transition occurs a rotational transition occurs simultaneously, giving rise to vibration-rotation transitions. These coupled transitions involve energies in the IR spectral region and form the basis of retrievals of atmospheric CO_2 and CH_4 . Selection rules imposed by quantum mechanics only allow specific, quantized energy transitions to occur. For rotational transitions the selection rule is $\Delta J = \pm 1$, where J is the rotational quantum number, i.e. rotational transitions can only span one energy level at a time. For anharmonic vibrational transitions the selection rule is $\Delta \nu = \pm 1, \pm 2, \pm 3, \dots$ where ν is the vibrational quantum number. Here the fundamental transition ($\Delta \nu = \pm 1$), tends to dominate whereas ‘overtone’ transitions ($\Delta \nu = \pm 2, \pm 3$) are generally far weaker and therefore less likely to occur.

Allowed vibration-rotation transitions can therefore be classified into two distinct groups, where an identical change in ν is accompanied by either a positive or negative change in rotational energy; R-branch transitions involve a positive ΔJ and P-branch transitions involve a negative ΔJ [Hollas (2002)]. The Q-branch describes allowed vibrational transitions where no change in rotational energy occurs (i.e. $\Delta J = 0$). Strong Q branches consist of overlapping lines and are therefore particularly prone to line mixing. For further details regarding molecular spectroscopy see Appendix A.

2.3.2 CO₂ and CH₄ Absorption Bands

As a linear molecule, CO₂ possesses characteristics similar to that of a diatomic molecule (the simplest model of molecular structure) and hence exhibits well defined P and R-branches, as can be seen in Figure 2.3. In this example, the band centre (characterised by a lack of absorption) is at 1575.5 nm and is flanked by a set of P-branch absorption lines at higher wavelengths (lower energy) to the right of the figure, and a set of R-branch lines at lower wavelengths (higher energy) to the left of the figure.

CH₄ is classed as a spherical top molecule since all its moments of inertia are identical. Spherical top molecules have a symmetrical structure and therefore do not possess an electric dipole moment or generate a purely rotational spectrum [Liou (1992)]. As CH₄ is a non-linear, polyatomic molecule its vibration-rotation spectrum is far more complex than in a simple diatomic or linear molecule case. Figure 2.3 shows the absorption spectrum associated with the $2\nu_3$ CH₄ band in the wavelength range 1625–1675 nm, as used by the FSI WFM-DOAS retrieval. The Q-branch can be clearly seen at 1666 nm, with well defined R-branch absorption lines at regular intervals to the left [Frankenberg et al. (2008b)].

2.4 Basic Radiative Transfer and DOAS Retrieval Theory

This section focuses on the macroscopic behavior of radiation, collectively described by its optical properties. Using a classical approach to radiation, the concept of DOAS is introduced, which lies at the heart of the FSI-WFM DOAS retrieval method.

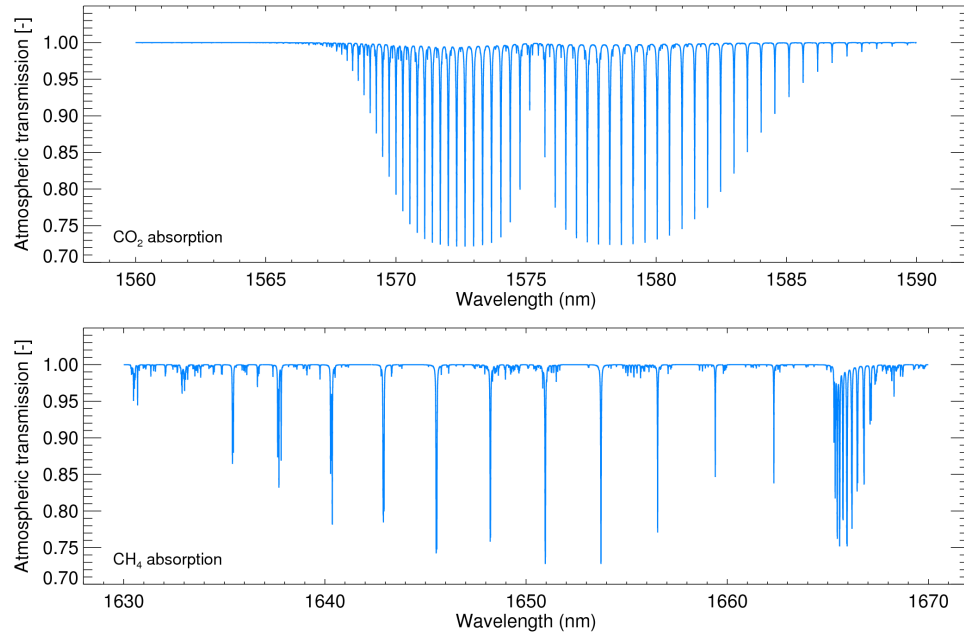


Figure 2.3: Absorption spectra for CO₂ (top) and CH₄ (bottom), focusing on the wavelength windows used for trace gas retrievals within this thesis. In each case, atmospheric transmission was obtained by running the SCIATRAN radiative transfer model both with and without the trace gas present and then calculating the difference.

2.4.1 Basic Radiative Transfer

The passage of light through an absorbing medium results in a decrease of the incident intensity, I_0 , which is proportional to the concentration of absorbing particles and molecules encountered along the light path. The fractional decrease in intensity due to absorption is described by Lambert's law which relates incident and transmitted intensity to properties of the absorbing material. By considering monochromatic light of wavelength λ , which changes in intensity by an amount dI over a small increment of the light path dl , Lambert's law can be expressed as:

$$dI(\lambda) = -\sigma(\lambda)nI(\lambda)dl, \quad (2.2)$$

where $\sigma(\lambda)$ is the molecular absorption coefficient, or molecule absorption cross-section, which describes the probability of absorption occurring in terms of a physical area, expressed in cm². The term n represents the number concentration of absorbing or scattering particles per unit volume (molecules cm⁻³). The total intensity, I , can be found simply by the integrating Equation 2.2 over the entire light path l :

$$I(\lambda) = I_0(\lambda) \exp\left(-\int \sigma(\lambda)n dl\right). \quad (2.3)$$

The exponential decay of intensity with absorption is described by Beer's law, hence Equation 2.3 is referred to as the Lambert-Beer law since it combines elements from both of the aforementioned physical laws. The Lambert-Beer law can be simplified by introducing a quantity known as optical depth, τ , which expresses the quantity of light removed from a beam by scattering or absorption during its passage through a medium. In its simplest form, the optical depth is expressed as the logarithm of the ratio of transmitted to incident light (I and I_0 respectively):

$$\tau(\lambda) = -\ln\left(\frac{I(\lambda)}{I_0(\lambda)}\right) = \int \sigma(\lambda)n dl, \quad (2.4)$$

hence, Equation 2.3 can be simplified to give:

$$I(\lambda) = I_0(\lambda) \exp(-\tau(\lambda)). \quad (2.5)$$

Thus far, only a single absorbing gas has been considered, whereas in reality spectral absorption is often the combined effect of absorption by several trace gases. Furthermore, optical depth as defined in Equation 2.4 only takes into account molecular absorption, however light intensity can also be diminished by photons being scattered out of the light path by collisions with particles of various sizes. In fact, particulate size governs the type of scattering mechanism which occurs; for particles smaller than the wavelength of the incident light (such as air molecules) photons undergo Rayleigh scattering whereas for particles with dimensions that exceed the wavelength of light (i.e. aerosols), photons undergo Mie scattering. The loss of intensity from the incident beam due to Rayleigh and Mie scattering can be quantified by extinction coefficients, κ_R and κ_M respectively. By considering the case of multiple absorbing trace gases and also taking both Rayleigh and Mie scattering into account, Equation 2.3 becomes:

$$I(\lambda) = I_0(\lambda) \exp\left(-\int \left(\sum_i (\sigma(\lambda)n dl) + \kappa_R + \kappa_M\right)\right). \quad (2.6)$$

This expanded version of the Lambert-Beer law now accounts for the most common atmospheric effects on spectral radiance, however scattering due to aerosols and clouds is not considered and the influence of air turbulence on the traversed light path has been neglected for simplicity.

2.4.2 Differential Optical Absorption Spectroscopy (DOAS)

As discussed in Section 2.4.1, the Lambert-Beer law relates the transmitted intensity of photons through an absorbing medium to the incident intensity and properties of the absorbing material, in particular the absorption cross-section and concentration of the absorbing particles. The aim of trace gas retrievals is to determine the concentration of a particular trace gas in the atmosphere from the absorption features present in an observed spectrum. However, as mentioned in Section 2.4.1, high frequency spectral features are often the combined result of absorption by more than one trace gas and therefore must first be separated out.

In order to discriminate between spectral features caused by a specific trace gas and those due to background absorption and scattering, DOAS utilises the fact that different absorption mechanisms display distinct spectral characteristics. A number of trace gases possess high frequency spectral absorption features which peak sharply at specific wavelengths; these gases are classed as line absorbers and include species such as CO_2 , CH_4 and N_2O . In contrast to line absorption, atmospheric scattering and continuum absorption by trace gases result in broadband spectral features. Broadband absorption features vary slowly with wavelength in comparison to sharp narrowband absorptions and therefore can be considered to constitute the background spectral continuum over localised spectral regions. Spectral features due to line absorption can be distinguished from the broadband spectral continuum by considering the molecular absorption cross-section, $\sigma_i(\lambda)$, in terms of its high and low frequency components, $\sigma_{ih}(\lambda)$ and $\sigma_{il}(\lambda)$ respectively:

$$\sigma_i(\lambda) = \sigma_{ih}(\lambda) + \sigma_{il}(\lambda). \quad (2.7)$$

Using this convention, Equation 2.6 is modified to become:

$$I(\lambda) = I_0(\lambda) \exp \left[- \int_0^L \left(\sum_i (\sigma_{il}(\lambda)n_i) + \kappa_R + \kappa_M \right) dl \right] \exp \left[- \int_0^L \left(\sum_i (\sigma_{ih}(\lambda)n_i) \right) dl \right]. \quad (2.8)$$

In reality the absorption cross-section varies with pressure and temperature, both of which fluctuate considerably in the atmosphere. However for weak absorbers these

variations are negligible and $\sigma_i(\lambda)$ can be assumed to remain constant along the light path. As a result, $\sigma_i(\lambda)$ can be taken outside of the integral in Equation 2.4, hence optical depth can be expressed as:

$$\tau(\lambda) = \sigma(\lambda) \int n dl = \sigma(\lambda)S, \quad (2.9)$$

where S is the integral of the trace gas concentration along light path l and is a key parameter in DOAS theory known as the slant column density. Furthermore, since the cross-section has been divided into its narrow and broadband components, the first exponential on the right hand side of Equation 2.8 can be combined with I_0 to represent the localised spectral background and replaced by a single term, I'_0 :

$$\begin{aligned} I(\lambda) &= I_0(\lambda) \exp \left[- \left(\sum_i (\sigma_{il}(\lambda)S_i) + \kappa_R + \kappa_M \right) \right] \exp \left[- \sum_i (\sigma_{ih}(\lambda)S_i) \right] \\ &= I'_0 \exp \left[- \sum_i (\sigma_{ih}(\lambda)S_i) \right]. \end{aligned} \quad (2.10)$$

2.4.3 Spectral Fitting

The implementation of DOAS in the context of atmospheric absorption involves the comparison of an observed spectrum (for example a SCIAMACHY measurement) with theoretical or laboratory measured properties of the trace gas of interest. In order to fit observed quantities to a priori parameters the DOAS technique employs a linear least squares fitting approach that requires a more detailed expression for the optical depth. Starting with a rearrangement of Equation 2.10:

$$\frac{I(\lambda)}{I_0(\lambda)} = \exp \left[- \left(\sum_i (\sigma_{ih}(\lambda)S_i) + \sum_i (\sigma_{il}(\lambda)S_i) + \kappa_R + \kappa_M \right) \right], \quad (2.11)$$

a new expression for optical depth is obtained:

$$\tau(\lambda) = -\ln \left(\frac{I(\lambda)}{I_0(\lambda)} \right) = \sum_i (\sigma_{ih}(\lambda)S_i) + \sum_i (\sigma_{il}(\lambda)S_i) + \kappa_R + \kappa_M. \quad (2.12)$$

The local background spectral continuum can be represented by a polynomial which varies smoothly with wavelength to account for the low frequency spectral features attributed to absorption and scattering:

$$\sum_m k_m \lambda^m = \sum_i (\sigma_{il}(\lambda) S_i) + \kappa_R + \kappa_M. \quad (2.13)$$

By substituting the polynomial approximation of the background spectral continuum into Equation 2.12, the optical depth can be expressed as:

$$\tau(\lambda) = \sum_i (\sigma_{ih}(\lambda) S_i) + \sum_m k_m \lambda^m. \quad (2.14)$$

The effect of subtracting the broadband spectral component (background intensity plus low frequency scattering /absorption structures) from the observed spectrum is to single out the narrowband absorption features corresponding only to trace gas absorption. In the context of the DOAS fitting procedure, optical depth is an observed quantity whereas the high frequency cross-sections, $\sigma_{ih}(\lambda)$, are measured in a laboratory and can be obtained from publicly available spectral databases such as the high-resolution transmission (HITRAN) molecular absorption database [Rothman et al. (2005)]. The DOAS linear least squares minimisation takes the form:

$$\chi^2 = [\tau_{obs} - \tau]^2 = \left[\tau_{obs} - \sum_i (\sigma_{ih}(\lambda) S_i) - \sum_m k_m \lambda^m \right]^2 \rightarrow \min, \quad (2.15)$$

where the fit parameters are comprised of the slant column density, S_i , and the polynomial coefficients, k_m .

It should be noted that the equations described thus far refer to an idealised measurement whereas in reality the signal recorded by a detector is limited by instrumental resolution and detector size. In an ideal scenario a detector would record the intensity of monochromatic light of wavelength λ_c as a delta function, without any contribution to the signal from any other spectral region. In practice, however, the light incident on a detector has been dispersed to some degree by passing through an instrumental aperture, or entrance slit, and therefore the detector records a signal not only at wavelength λ_c but over a small range of wavelengths centred on λ_c . Furthermore, detectors are comprised of a number of individual pixels, each of which integrates the incident light over a small, finite wavelength interval. The resulting spectrum is therefore a summation of the signal detected by discrete pixels. Combination of these effects gives rise to the spectral response function of the instrument which is characterised by an instrument line shape (ILS), or ‘slit width’. A measured spectrum is therefore a convolution of the true spectrum with an appropriate ILS

(typically a Gaussian) designated here by H :

$$\begin{aligned}
 I^*(\lambda) &= I(\lambda) * H = - \int_{-\infty}^{+\infty} I(\lambda - \lambda') H(\lambda') d\lambda' \\
 &\approx - \int_{-\Delta x}^{+\Delta x} I(\lambda - \lambda') H(\lambda') d\lambda'.
 \end{aligned}
 \tag{2.16}$$

2.4.4 Implementing DOAS in the SWIR

Photon absorption in the UV/VIS spectral region results in high energy transitions, involving the excitation of electrons, which are unaffected by external atmospheric conditions. Energies associated with photons in the SWIR, however, are insufficient to cause electron excitation and instead result in molecular transitions, typically between vibrational and rotational energy levels (see Sections 2.3). The Lambert-Beer law (as written in Equation 2.10) assumes that $\sigma_{ih}(\lambda)$ is constant along the light path, l , but at low energies, such as those in the SWIR, the influence of varying atmospheric conditions, particularly pressure and temperature, cause $\sigma_{ih}(\lambda)$ to change significantly with altitude. As a result, the integral in Equation 2.8 can no longer be simplified to provide a single optical depth applicable to the entire column and the approximation made in Equation 2.9 no longer holds. Furthermore, instruments of moderate spectral resolution such as SCIAMACHY are unable to resolve individual absorption lines [Gottwald et al. (2006)] and consequently the measured optical depth is a sum of τ over a range of wavelengths (dependent on instrument resolution) rather than corresponding to a specific wavelength as called for by Equation 2.8. For line absorbers such as CO_2 and CH_4 , where sharp changes in optical depth over relatively small spectral regions occur, the relationship between observed optical density and trace gas slant column density, S_i , no longer holds.

2.4.5 Weighting Function Modified Differential Optical Absorption Spectroscopy (WFM-DOAS)

By redefining Equation 2.14 in terms of satellite observed intensity, I , the following expression is obtained:

$$\ln I(\lambda) = \ln I_0(\lambda) - \sum_i (\sigma_{ih}(\lambda) S_i) - \sum_m k_m \lambda^m.
 \tag{2.17}$$

Since $\sigma_{ih}(\lambda)$ is highly temperature and pressure dependent in the SWIR, as discussed in Section 2.4.4, it follows that DOAS in its original form is insufficient to perform retrievals of CO₂ and CH₄ in the SWIR spectral region. Taylor's theorem describes a function $f(x)$ by an expansion about a point a as follows:

$$f(x) = f(a) + \frac{df}{da}(x-a) + \frac{d^2f}{da^2} \frac{(x-a)^2}{2!} + \dots \quad (2.18)$$

Weighting Function Modified Differential Optical Absorption Spectroscopy (WFM-DOAS) makes allowances for the intricacies of the SWIR region by expressing the TOA satellite observed intensity at i spectral points as a first order Taylor expansion using RTM modelled intensities and replacing the absorption cross-sections with column weighting functions:

$$\begin{aligned} \ln I_i^{meas}(V^t, b^t) \approx & \ln I_i^{mod}(\bar{V}, \bar{b}) + \left[\frac{\partial \ln I_i^{mod}}{\partial \bar{V}} \Big|_{\bar{V}} \times (\hat{V} - \bar{V}) \right] \\ & + \left[\frac{\partial \ln I_i^{mod}}{\partial \bar{b}_j} \Big|_{\bar{b}_j} \times (\hat{b}_j - \bar{b}_j) \right] + P(k_m). \end{aligned} \quad (2.19)$$

Here V^t , \bar{V} and \hat{V} are the true, modelled and retrieved VMRs respectively. Derivatives of intensity with respect to the VCD are the column weighting functions which describe the sensitivity of a retrieval by quantifying the change in the observed spectrum given a perturbation in the true VCD [Buchwitz et al. (2000)]. The weighting functions are modelled by a RTM and therefore explicitly take into account the temperature and pressure dependence of absorption throughout the atmospheric column, replacing the need for absorption cross-sections in the standard DOAS approach (i.e. Equation 2.17). The term b_j represents a collection of parameters describing the atmospheric state, such as temperature and pressure which are not well known a priori. $P(k_m)$ is a low-order polynomial, included to account for the broadband spectral continuum [Buchwitz et al. (2000)].

The WFM-DOAS retrieval algorithm is based on a linear least squares fitting procedure which scales the a priori model spectrum, hereafter referred to as the reference spectrum, and its constituent a priori atmospheric parameters (i.e temperature, pressure, trace gas VCD etc), by adjusting all spectral points in the retrieval window simultaneously in order to match the observed spectrum. The VCD weighting function is multiplied by the difference between \hat{V} and \bar{V} (ΔV) which is the amount of molecules that the a priori VCD must be adjusted by for the modelled intensity

to fit the observed intensity. ΔV is optimised during a linear least squares fit and results in a scaling factor for converting the a priori VCD into a retrieved VCD. In vector form, Equation 2.19 becomes:

$$\|\mathbf{y} - \mathbf{A}\mathbf{x}\|^2 = \|\text{RES}_i\|^2 \longrightarrow \min \text{ w.r.t } \mathbf{x}, \quad (2.20)$$

where \mathbf{y} represents the difference between measured and modelled intensities, \mathbf{A} is a matrix of the column weighting functions and \mathbf{x} represents the difference between the modelled and true fit parameters [Buchwitz et al. (2000), Barkley (2007)]. Elements of \mathbf{y} , \mathbf{A} and \mathbf{x} take the following form:

$$y_i = \frac{\ln I_i^{\text{meas}} - \ln I_i^{\text{mod}}}{\sigma_i}, \quad (2.21)$$

$$x_1 = \frac{(\hat{V} - \bar{V})}{\bar{V}}; x_2 = \frac{(\hat{b}_j - \bar{b}_j)}{\bar{b}_j}, \quad (2.22)$$

$$A_i = \frac{\partial \ln I_i^{\text{mod}}}{\partial \bar{V}} \Big|_{\bar{V}} \frac{\hat{V}}{\sigma_i}. \quad (2.23)$$

Note that in Equations 2.21–2.23 σ_i represents the measurement noise (not the absorption cross-section) defined as the standard deviation of the intensity over the mean intensity. Given its position on the denominator, σ_i is only significant if the noise varies significantly with wavelength, in which case a higher weighting is given to the less noisy spectral points in the WFM-DOAS fit. The solution to the WFM-DOAS linear fit is given by $\hat{x} = C_x A^T y$, where C_x is the covariance matrix of the fit (see Buchwitz et al. (2000) for a full mathematical description). The error on retrieved parameters is given by:

$$\sigma_{\hat{V}_j} = \sqrt{\frac{(C_x)_{jj} \sum_i \text{RES}_i^2}{(m - n)}}, \quad (2.24)$$

where the subscript j indicates the index of the diagonal element in the covariance matrix, m is the number of points in the spectral fit and n is the number of fit parameters [Barkley (2007)].

For WFM-DOAS, a priori data required to linearise the least squares fit is obtained from a look-up table (LUT) consisting of model spectra and weighting functions pre-calculated by the SCIATRAN [Rozanov et al. (2005)] radiative transfer model

(RTM). Employing a LUT approach allows the algorithm to be run extremely quickly (an important quality for retrieval methods which aim to produce global data products) since on-line radiative transfer calculation are not required. However, using pre-calculated spectra introduces the risk of using a priori data which is substantially different to the true atmospheric state. Since the WFM-DOAS least squares fit only consists of a single iteration it is important that the a priori data is as accurate as possible otherwise an erroneous VCD result will be obtained. For cases in which the a priori data differs greatly from the true state an iterative approach such as IMAP-DOAS [Frankenberg et al. (2005b)] is required.

2.4.6 Full Spectral Initiation (FSI) WFM-DOAS

The Full Spectral Initiation (FSI) WFM-DOAS algorithm [Barkley et al. (2006)] is a modification to the aforementioned WFM-DOAS algorithm for which a priori data tailored to each satellite observed scene is used to create the reference spectrum. By modelling each atmospheric scene individually FSI WFM-DOAS is expected to obtain a more accurate linearisation point for the linear least squares fit than the LUT approach of WFM-DOAS, and thus produce more accurate retrievals. This is a significant advantage of FSI over other WFM-DOAS based methods which do not, in general, use an iterative approach to achieve an optimised result.

Reference spectra for the FSI WFM-DOAS retrieval are created by running the SCI-ATRAN RTM [Rozanov et al. (2005)] initialised with a series of a priori atmospheric parameter profiles which have been interpolated to the exact date and time of each SCIAMACHY observation. By introducing the on-line computation of model reference spectra, total retrieval time is significantly increased; FSI WFM-DOAS takes approximately 2.5 minutes to retrieve a total trace gas column as opposed to a matter of seconds for the original WFM-DOAS method.

2.5 Scattering by Aerosols in the SWIR

2.5.1 Defining Atmospheric Aerosol

The term ‘aerosol’ refers to tiny particulate matter ($\sim \mu\text{m}$), which exists in either a solid or liquid state, that is suspended in a gas. In a sense, clouds are a special category of aerosol, specifically consisting of water particles either in solid or liquid

form which are suspended in the atmosphere. Aerosols affect the climate both by direct interaction and via secondary effects. The direct effect of aerosols on climate refers to the scattering and absorption of radiation by aerosol particles, leading to atmospheric cooling and warming respectively. Despite the opposing effects of these two direct processes, the overall effect on the climate is that of net cooling [Forster et al. (2007)].

The secondary effect of aerosols on the climate derives from the ability of aerosols to alter cloud microphysics. Particles with radii $> 0.1 \mu\text{m}$ are effective cloud condensation nuclei and therefore promote cloud formation. As well as seeding clouds, aerosol particles can also act as a catalyst for chemical reactions by providing a surface for reactions to take place upon.

A number of studies have been performed which focus on the impact of aerosols on total column retrievals of CO_2 from SCIAMACHY [Mao and Kawa (2004), Houweling et al. (2005)]. However, significantly fewer studies have quantified the effect of aerosols on retrievals of CH_4 , providing the need for the work presented in this thesis. This section introduces the basic radiative properties of aerosols (see Section 2.6 for cirrus clouds) as background to the aerosol sensitivity tests performed in Chapter 4 and the subsequent retrieval modifications made to account for aerosol effects on retrievals of CH_4 in Chapter 5.

2.5.2 Sources

Atmospheric aerosols originate from both natural and anthropogenic processes and their sources can be categorised as either primary or secondary in nature. Primary sources largely produce natural aerosols, for example, oceans give rise to sea-salt, weathering produces mineral and dust deposits and organic material produces airborne pollen and spores. In contrast, secondary sources are the product of chemical reactions of precursor gases in the atmosphere which nucleate or condense, forming aerosols such as sulphates or nitrates. Table 2.1 gives an overview of various aerosol types along with their properties and typical sources as defined by the Global and regional Earth-system (Atmosphere) Monitoring using Satellite and in-situ data (GEMS)* project.

Primary aerosol sources (particularly sea-salt and desert dust) dominate global

*A full description of the GEMS project can be found at <http://gems.ecmwf.int/>

aerosol production, however, anthropogenic emissions are still significantly large. The majority of aerosols are found within the atmospheric boundary layer since aerosols are generally emitted from the Earth's surface and the atmospheric sink is particularly effective at removing aerosol.

2.5.3 Sinks

In comparison to long-lived trace gases, which can remain in the atmosphere for tens or hundreds of years, the lifetime of atmospheric aerosols is extremely short. Aerosols are typically airborne for anything up to a few weeks, depending on particle mass and meteorological factors. Aerosols are predominantly cleansed from the atmosphere by either dry or wet deposition. Dry deposition describes the tendency of particles to be deposited on the Earth's surface due to atmospheric turbulence or inherent gravitational forces acting on the aerosol particles. Wet deposition refers to the removal of atmospheric aerosol by precipitation; aerosol particles can either seed clouds and then fall if subsequent precipitation occurs or become incorporated in water droplets during an existing precipitation event.

2.5.4 Scattering Properties of Aerosols

Aerosol Radii Distributions

Aerosol particle radii range from around 0.005–100 μm and can vary considerably even within a particular aerosol species. Therefore the number density $n(r)$ (where r is the particle radius) of particles that make up a specific aerosol type is usually represented by a log-normal distribution (normal distribution of the *logarithm* of r) [Tobias (1993)] of the following form:

$$n(r) = \text{const } r^{-1} \exp \left[-\frac{(\ln r - \ln r_g)^2}{2 \ln^2 \sigma_g} \right] \quad (2.25)$$

Here, r_g and σ_g are the mode and standard deviation of the log-normal distribution respectively. In most cases a single log-normal distribution is sufficient, however occasionally the summation of multiple log-normal distributions is necessary [Davies (1974)] in order to correctly characterize the spread of particle radii. Table 2.1 lists the parameters necessary to characterize the log-normal distributions of the 9 GEMS aerosol types.

Aerosol type	Label(s)	r_{\min}	r_{\max}	r_g	σ_g	Source of RI data	Source
Sea Salt (Bin 1)	SS1	0.03	0.5	0.1992 1.992	1.9, 2.0	Mie calc.	Oceans
Sea Salt (Bin 2)	SS2	0.5	5.0	0.1992 1.992	1.9, 2.0	"	"
Sea Salt (Bin 3)	SS3	5.0	20.0	0.1992 1.992	1.9, 2.0	"	"
Desert Dust (Bin 1)	DD1	0.03	0.55	0.29	2.0	Shettle and Fenn (1979)	Desert and arid regions
Desert Dust (Bin 2)	DD2	0.55	0.9	0.29	2.0	"	"
Desert Dust (Bin 3)	DD3	0.9	20.0	0.29	2.0	"	"
Organic Matter	OM1 (hydrophillic) OM2 (hydrophobic)	0.002	20.0	0.0355	2.0	Schmid (2008)	Chemical reactions of volatile organic compounds (VOCs)
Black Carbon	BC1 (hydrophillic) BC2 (hydrophobic)	0.005	0.5	0.118	2.0	Shettle and Fenn (1979)	Forest fires; anthropogenic emissions
Sulphate	Su	0.002	20.0	0.0355	2.0	Mie calc.	Chemical reactions of gaseous precursors (originating from volcanic and anthropogenic activity)

Table 2.1: Parameters characterizing 9 GEMS aerosol types, including minimum and maximum radii (r_{\min} and r_{\max}), mode r_g and standard deviation σ_g of the log-normal distribution of radii. The source of each aerosol type and suitable refractive index (RI) profiles (for use in Mie calculations) are also provided for each case. Parameter values were obtained via personal correspondence with J.-J. Morcrette from the GEMS project.

Chemical Composition and Refractive Index

The chemical composition and structure of an aerosol particle determines its optical properties, in particular the complex refractive index m given by:

$$m(\lambda) = n(\lambda) - ik(\lambda). \quad (2.26)$$

The real part n (not to be confused with number density) of the refractive index is a measure of the extent to which light is bent or ‘refracted’ as it passes through a given material and determines the degree of scattering that occurs. The imaginary part k characterises the absorption of the material.

Extinction and Single Scattering Albedo

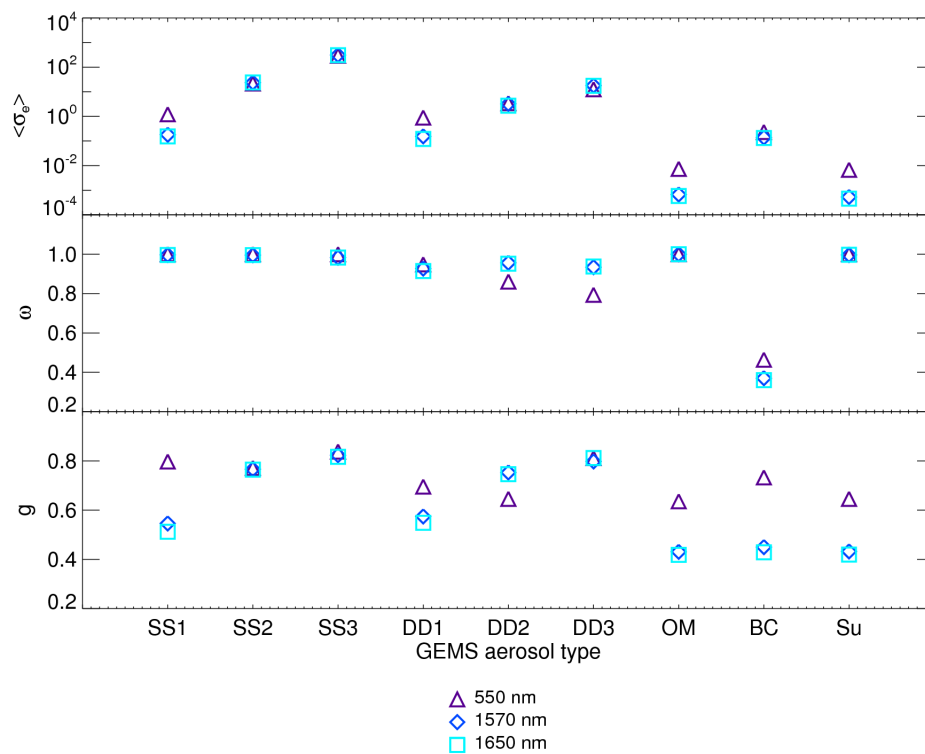


Figure 2.4: Ensemble averaged extinction cross-section per particle $\langle\sigma_e\rangle$, single scattering albedo ω and asymmetry parameter g derived from Mie theory for the 9 GEMS aerosol types. Parameters are given for wavelengths corresponding to the centre of the CO₂ and CH₄ retrieval windows (1570 nm and 1650 nm respectively) as well as for a reference wavelength of 550 nm.

Extinction is a measure of how much radiation a material or substance removes from its original light path either by scattering or absorption. The extinction cross-

section σ_e (as described in Section 2.4.1) can be expressed in terms of the extinction efficiency Q_{ext} , which quantifies the ability of a particle of a given cross-sectional area to interact with radiation, as follows:

$$\sigma_e = Q_{\text{ext}}\pi r^2, \quad (2.27)$$

where r is the radius of the particle. Cross-sections of scattering (σ_s) and absorption (σ_a) can also be calculated by replacing Q_{ext} by Q_{sca} and Q_{abs} respectively. Following from Equation 2.27 the volume extinction coefficient κ_e (extinction per unit volume of a material) is then simply σ_e multiplied by the particle size distribution $n(r)$ and integrated over all (or a given range of) radii:

$$\kappa_e = \int_0^{\infty} Q_{\text{ext}}\pi r^2 n(r) dr = \int_0^{\infty} \sigma_e n(r) dr. \quad (2.28)$$

The extinction term κ_e contains a contribution from both absorption and scattering processes, i.e. $\kappa_e = \kappa_s + \kappa_a$, where κ_s and κ_a are obtained from Equation 2.28 by replacing σ_e with σ_s and σ_a respectively. A useful quantity to define is the single scattering albedo ω which is simply the ratio of the scattering and extinction coefficients:

$$\omega = \frac{\kappa_s}{\kappa_e}. \quad (2.29)$$

Using Equation 2.29, the absorption coefficient can easily be obtained if both the extinction and single scattering albedo are known, as follows:

$$\kappa_a = \kappa_e(1 - \omega). \quad (2.30)$$

Figure 2.4 shows typical values for the ensemble averaged cross-section per particle $\langle\sigma_e\rangle$, ω and the asymmetry parameter g (the cosine-weighted average of the phase function) for 9 GEMS aerosol definitions. Note that the value of ω for black carbon in Figure 2.4 is significantly lower than all other GEMS aerosol types since black carbon is far more absorbing than other aerosols.

Scattering Phase Function

A phase function represents the intensity of scattered light as a function of scattering angle and can be modelled by a Legendre polynomial. Phase function moments (PFM) are simply the coefficients of the Legendre series expansion and are often

required by radiative transfer models to characterise a phase function.

2.6 Scattering by Clouds in the SWIR

Whilst water clouds are generally very bright and therefore easy to identify in a satellite scene, thin ice clouds known as cirrus clouds are notoriously difficult to detect and can cause significant atmospheric scattering which at present is rarely taken into consideration within atmospheric retrievals. Cirrus clouds are typically found between altitudes of 6–18 km at mid-latitudes and cover approximately 22% of the globe, however coverage over the tropics can be as much as 70% [Liou (2005)].

2.6.1 Scattering Properties of Clouds

Cloud Ice Water Content

The concentration of water droplets within a cloud is characterized by the cloud ice water content (IWC, omitting the leading ‘C’ here for brevity), usually expressed in units of g m^{-3} . Note, cloud liquid water content (LWC) is defined in the same manner therefore the following discussion is also applicable to liquid water clouds. To define IWC in terms of microscopic cloud parameters, it is necessary to first define distributions of cloud droplet cross-sectional area A_d and volume V_d respectively as follows [Stephens (1994)]:

$$A_d = \int_0^{\infty} \pi r^2 n(r) dr, \quad (2.31)$$

$$V_d = \frac{4}{3} \int_0^{\infty} \pi r^3 n(r) dr, \quad (2.32)$$

where $n(r)dr$ is an arbitrary number density distribution which describes the concentration of cloud droplets with a range of radii r to $r + dr$. Using Equation 2.32, IWC can be simply expressed as:

$$\text{IWC} = \rho_I V_d, \quad (2.33)$$

where $\rho_I = 0.92 \text{ g cm}^{-3}$ is the density of ice and V_d is unitless.

Cloud Droplet Effective Radius

It is also useful to introduce the effective radius, r_e , which characterises the distribution of cloud droplet radii [Liou (1992)]:

$$r_e = \frac{\int_0^{\infty} \pi r^3 n(r) dr}{\int_0^{\infty} \pi r^2 n(r) dr}. \quad (2.34)$$

For ice particles r_e can be calculated by following the simplified parameterisation for ice particle effective size D_e from Sun and Rikus (1999), in conjunction with the low temperature correction of Sun (2000). The Sun and Rikus method is a linear approximation of the MH97 parameterisation [McFarquhar and Heymsfield (1997)] of hexagonal ice particle effective size in which D_e is characterised by the following empirical equation:

$$D_e = a(\text{IWC}) + b(\text{IWC})(T + 190.0) + f. \quad (2.35)$$

Here, T is the temperature in Celsius, $a(\text{IWC})$ and $b(\text{IWC})$ are coefficients of the linear fit to results of the MH97 parameterisation, given by:

$$a(\text{IWC}) = 45.8966 \cdot \text{IWC}^{0.2214}, \quad (2.36)$$

$$b(\text{IWC}) = 0.7957 \cdot \text{IWC}^{0.2535}, \quad (2.37)$$

where IWC is expressed in units of g m^{-3} and f is a correction required for low temperatures, expressed as:

$$f = 1.23561 + 0.0105T. \quad (2.38)$$

The effective radius is then related to D_e as follows:

$$r_e = \frac{3\sqrt{3}}{8} D_e. \quad (2.39)$$

Optical Properties

IWC can be related to the volume extinction coefficient κ_e by employing the large particle limit which, assuming a spherical particle, states that for wavelengths that satisfy the condition $2\pi r/\lambda \gg 1$ the extinction efficiency tends towards an asymptotic limit of $Q_{ext} = 2$ [Stephens (1994)]. By applying the asymptotic limit in

Equation 2.27, then substituting for σ_e in Equation 2.28, κ_e can be expressed as follows:

$$\kappa_e = 2 \int_0^{\infty} \pi r^2 n(r) dr. \quad (2.40)$$

By substituting Equations 2.33 and 2.34 for IWC and r_e respectively into Equation 2.40 the following expression relating κ_e and IWC is obtained [Slingo and Schrecker (1982)]:

$$\kappa_e = \frac{3 \text{IWC}}{2 \rho_I r_e}. \quad (2.41)$$

Given IWC in g m^{-3} , ρ_I in g cm^{-3} and r_e μm , Equation 2.41 provides κ_e in units of m^{-1} . Since optical depth τ is simply κ_e integrated over a path length dl , and similarly ice water path (IWP) is IWC integrated over dl , a parallel expression relating τ and IWP can be defined as follows:

$$\tau(\lambda) = \int_0^L \kappa_e dl = \frac{3 \text{IWP}}{2 \rho_I r_e}. \quad (2.42)$$

Chapter 3

FSI for the Retrieval of CH₄ from SCIAMACHY

3.1 The SCIAMACHY Instrument

3.1.1 Introducing SCIAMACHY

The Scanning Imaging Absorption Spectrometer for Atmospheric Chartography (SCIAMACHY) instrument [Burrows et al. (1995), Bovensmann et al. (1999)] is a passive nadir/limb viewing spectrometer of moderate resolution with 8 channels covering the wavelength range 214–2386 nm which span the UV, Vis, NIR and SWIR spectral regions. SCIAMACHY detects sunlight reflected from the Earth’s surface that has been modified by atmospheric scattering (i.e. ‘Earthshine’ spectra) and can be used in conjunction with reference solar spectra in DOAS based retrievals to determine the concentration of various atmospheric trace gases. SCIAMACHY is the successor of the Global Ozone Monitoring Experiment (GOME) and began operations in 2002 onboard ESA’s Environmental satellite ‘ENVISAT’ which circles the Earth at an altitude of 799.8 km in a polar, sun-synchronous orbit. ENVISAT was originally intended to operate for around five years [Lichtenberg (2006)] but has exceeded expectation and continues to operate to this day, albeit in a lower orbital configuration to conserve remaining fuel reserves. Whereas GOME focused primarily on the observation of stratospheric ozone and related gases, the scope of SCIAMACHY was intended to be far broader, encompassing retrievals of trace gases, aerosols and clouds in the form of total column, tropospheric and stratospheric profiles (see Figure 3.1 for a list of retrieved atmospheric constituents and their corresponding spectral windows). By detecting trace gas absorption in the

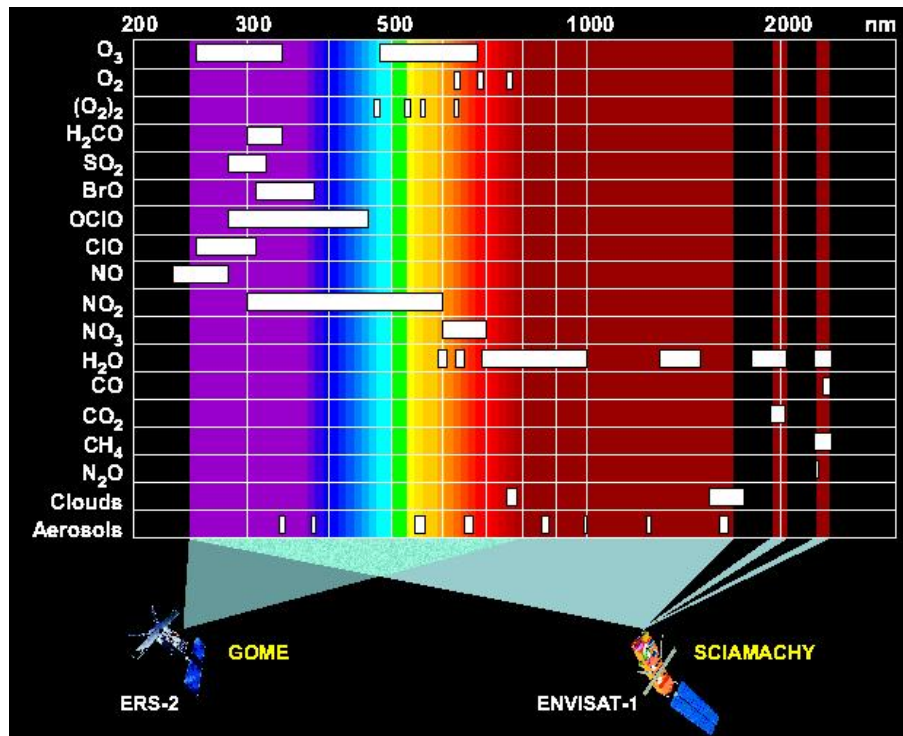


Figure 3.1: Spectral regions observed by both GOME and SCIAMACHY (figure taken from BREMEN). Note that CO_2 and CH_4 were originally intended to be retrieved from the SWIR ($\sim 2 \mu\text{m}$) however due to problems with the detectors covering this spectral range, these retrievals are instead performed using spectral windows around $1.57 \mu\text{m}$ and $1.65 \mu\text{m}$ respectively.

SWIR, SCIAMACHY has high sensitivity to the lowest atmospheric layers where anthropogenic trace gas emissions peak, as opposed to TIR instruments which are most sensitive to the upper troposphere (refer to Section 2.2 for further discussion).

3.1.2 Orbit and Viewing Geometry

Prior to orbital reconfigurations in October 2010* ENVISAT performed just over 14 orbits per day (100.6 minutes per orbit) with global coverage in 3 days (in nadir mode) and a repeat cycle of 35 days. In this orbital configuration, ENVISAT crossed the equator at 10:00 am local time [Gottwald et al. (2006)] on the descending orbital node.

SCIAMACHY can observe the Earth's atmosphere in 3 different viewing geometries as shown in Figure 3.2; nadir (directly downwards), limb (horizontally through

*For further details see <http://atmos.caf.dlr.de/projects/scops/>

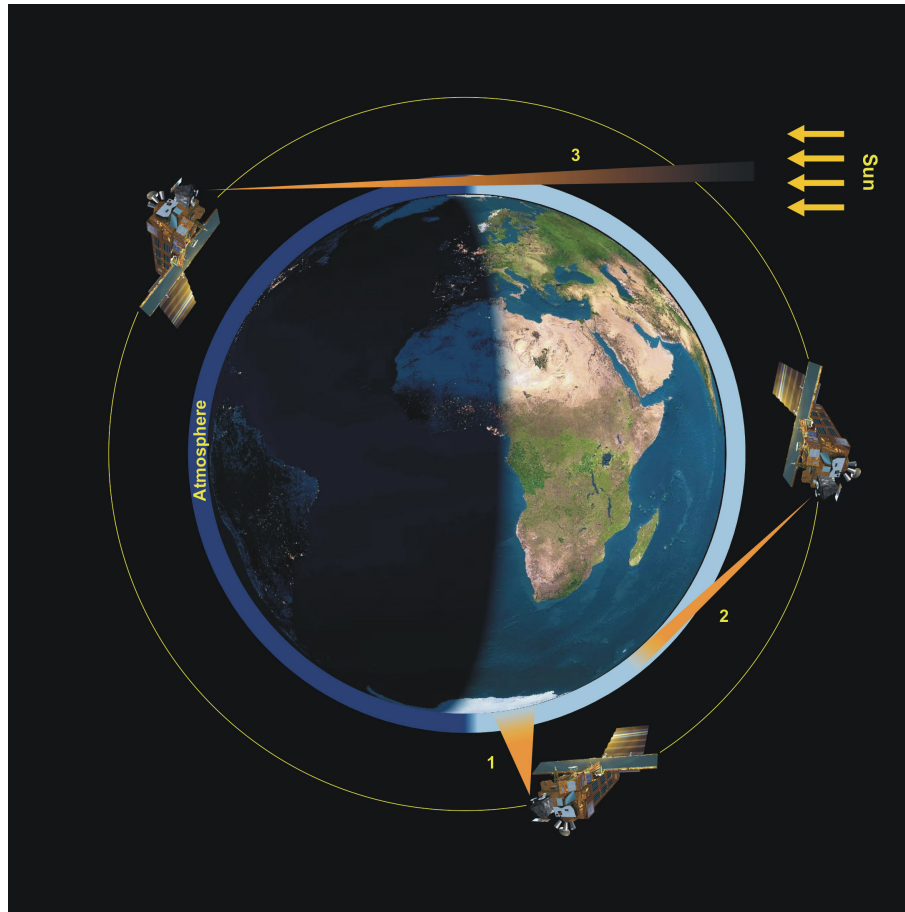


Figure 3.2: The three observational modes of SCIAMACHY; nadir(1), limb (2) and solar(/moon) occultation (3) (figure taken from Gottwald et al. (2006)).

the atmosphere) or in solar/moon occultation (limb but pointing directly at the Sun or moon). During nominal operations, SCIAMACHY executes a sequence of measurement ‘states’- each a series of predetermined commands corresponding to a dedicated task. There are 70 measurement states in total, of which 34 are for scientific purposes, 26 for onboard calibration, 4 for onboard monitoring and 6 for calibration analysis [Gottwald et al. (2006)]. Despite the high number of possible measurement states, the majority of SCIAMACHY’s operational time (on the illuminated side of the Earth) is spent alternating between nadir and limb measurement states.

SCIAMACHY’s field of view has a swath width of 960 km (i.e. ± 480 km with respect to the ground track) and measurements are performed as the instrument scans across the swath from left to right. The number of measurements made in one sweep across the swath is variable and depends on the integration time of the

Channel	Spectral range (nm)	Resolution (nm)
1	214-334	0.24
2	300-412	0.26
3	383-628	0.44
4	595-812	0.48
5	773-1063	0.54
6	971-1773	1.48
7	1934-2044	0.22
8	2259-2386	0.26

Table 3.1: Spectral coverage and resolution of SCIAMACHY’s eight channels.

measurement state being executed, thus allowing for a trade off between temporal and spatial resolution in different channels [Gottwald et al. (2006)]. For channel 6 the integration time is 0.125 s which corresponds to a footprint size of 30×60 km.

3.1.3 Spectral Coverage

The spectral coverage and resolution for each of SCIAMACHY’s eight spectral channels is given in Table 3.1. Retrievals of CO_2 and CH_4 can be performed in the IR channels 6–8. Although both CH_4 and CO_2 absorb strongly in the wavelength region covered by channels 7 and 8, both of these channels suffer from a severe lack of transmission (and consequently decreased signal to noise) caused by the build up of a thin layer of ice on the detectors after launch [Gloude-mans et al. (2005), Lichtenberg (2006)]. The ice contamination is thought to have been caused by the leakage of water vapour from ENVISAT’s carbon fibre frame once in orbit, some of which infiltrated SCIAMACHY and subsequently condensed out onto the detectors and froze. Fortunately, contamination is isolated to channels 7 and 8 only since these channels cover the highest wavelength regions and therefore require the most cooling to reduce thermal noise. Periodic decontaminations are performed, during which all detectors are heated, to remove the build up of ice from the two affected channels. However, once nominal temperatures are resumed the ice layer reforms making retrievals of CH_4 using data from these channels prone to a significant time-dependent bias [Buchwitz et al. (2005a); Buchwitz et al. (2005b)]. Since the bias introduced is not well characterized, CH_4 retrievals are generally performed using spectra from channel 6 which contains weaker absorption features than channels 7 and 8 but is unaffected by ice. As a result, SCIAMACHY spectra from channel 6 are used in this thesis.

3.2 Calibration of SCIAMACHY L1B Data

The raw electronic signal measured by SCIAMACHY (in binary units, BU) is designated as level 1b (L1b) data which requires calibration to convert into spectral radiance in units of $\text{W m}^{-2} \text{nm}^{-1}$ (a typical level 1c (L1c) calibration product). Using the official ESA tool for the calibration of SCIAMACHY L1b data (SciaL1c) specific measurement data sets (MDS) can be extracted from an L1b file and up to 10 different calibration options, detailed in Table 3.2, can be applied depending on user requirements.

Barkley et al. (2006) utilised version 5.01 of SCIAMACHY data for retrievals of CO_2 and produced full radiometrically calibrated spectra in order to obtain the mean intensity (and thus estimate albedo) for each SCIAMACHY scene. However, at that time the radiometric, stray-light, polarization and dark current calibrations applied by the SciaL1c tool were not of a high enough standard to produce suitable spectra for the FSI WFM-DOAS fit. Since DOAS only relies on the differential of spectral intensity radiometric calibration is not strictly necessary and can be neglected, however corrections for stray-light and dark current are still required. As a result, Barkley et al. (2006) applied a wavelength correction using SciaL1c and then manually applied the remaining necessary calibrations using L1b auxiliary data to obtain a calibrated signal in units of BU for the FSI WFM-DOAS fit. Retrievals performed in this thesis are based on a more recent SCIAMACHY data release (version 7.03) however the updates which constitute this new release do not affect the SWIR channels. As a result, the use of a manually calibrated signal for FSI WFM-DOAS retrievals is maintained.

The calibration procedure for channels 1–5 differs from that of the SWIR channels 6–8, therefore only calibrations relevant to the SWIR channels and of particular importance for the CH_4 FSI retrieval have been described here in further detail.

3.2.1 Non-Linearity in the SWIR Channels

In addition to optional calibrations, a correction for the non-linear response of pixels in channels 6–8 must be applied ahead of any other calibrations. The SciaL1c tool only applies a non-linearity calibration if the option to apply ‘all calibrations’ is selected otherwise the correction must be applied manually. The effect of non-linearity is different for each of the SWIR channels (6, 6+, 7 and 8), resulting in the

Calibration option	Relevant spectral channels	Description	Maximum effect (BU)
Memory effect	1–5	A non-linearity effect governed by the previous detector read-out (including dark signal and offsets).	250
Leakage current	1–8	A component of the total dark current that results from stray thermal electrons.	0.04–0.5 BU s ⁻¹ [Kleipool (2002)]
PPG	6–8	The non-uniform response to a signal by neighbouring pixels.	-
Etalon	1–5	Interference of light caused by a protective layer of SiO ₂ covering the S _i detectors, resulting in a periodic, wave-like oscillation (dampened with increasing wavelength) in the measured intensity.	-
Stray light	1–8	Radiation incident on the detector which is not from the intended source and can be caused by two distinct mechanisms: - Spatial stray light is the result of light scattered into the detector from outside of the instrument field of view. - Spectral stray light results from radiation being scattered within the instrument set-up onto a detector which is intended to measure light of a different wavelength.	Spatial: only affects nadir measurements over the North Pole. Spectral: 0.14% of signal for uniform stray light and 0.1% for ghost stray light.
Spectral calibration	1–8	Attribution of wavelength values to pixels.	-
Polarization	1–8	Corrects for the response of a detector to the polarisation of incident light.	Polarization in the IR channels is moderately weak.
Radiance	1–8	Radiometric calibration, converting from a raw signal (BU) to radiance (W m ⁻² nm ⁻¹).	5% error for reflectance spectra.
PMD sun normalisation		Sun normalisation using Polarisation Measurement Device (PMD) data.	-
Monitoring factors (m-factors)		Dedicated in-orbit observation modes provide monitoring factors which quantify the degradation of SCIAMACHY with time. Application of the m-factors restores measured signals to their equivalent magnitude before degradation thus allowing ground based calibrations to be applied.	-
Non-linearity	6–8	Non linearity of the IR channels 6–8.	250

Table 3.2: Calibration options available in the SciaL1c tool for the calibration of SCIAMACHY L1b data along with a description of each correction. If available, maximum errors have been given in binary units (BU) [Lichtenberg (2006); Scherbakov (2009); Kleipool (2002)].

definition of fourteen separate correction curves (see Kleipool (2003)).

3.2.2 Dark Signal and Leakage

The false signal recorded when a detector is not illuminated by incident radiation is known as a dark signal (DS). For channels 1–5 the dark signal is made up of two components; a constant additive known as the analog offset (AO), or fixed pattern noise, added to ensure a positive signal is measured and a leakage current (LC), also known as dark current, which is caused by stray electrons in the detector and is linearly dependent on time [Slijkhuis (1999)]. For IR channels 6–8, the dark signal is dominated by a thermal background, $B_{\text{th}}(\phi)$, generated by the instrument itself. The thermal dark signal is dependent on orbital phase ϕ since changes in orbital position (and hence solar illumination) affect the temperature of the instrument [Lichtenberg (2006)]. The total dark signal for a generic SCIAMACHY channel can be expressed in standard form as:

$$DS = f_{\text{coadd}} (\text{AO} + \text{LC} \cdot t_{\text{PET}} + B_{\text{th}}(\phi) \cdot \text{QE}(T_{\text{det}}, \lambda) \cdot \Gamma_{\text{ice}} \cdot t_{\text{PET}}), \quad (3.1)$$

where $\text{QE}(T_{\text{det}}, \lambda)$ is the quantum efficiency of the channel, dependent on both the temperature of the detector, T_{det} , and the wavelength of radiation detected, λ . Γ_{ice} is the transmission coefficient associated with an ice layer build up on detector channels 7 and 8 (note, channel 6 is unaffected) [Gottwald et al. (2006)]. It is important to note that the third term in the brackets on the right hand side of Equation 3.1 describes the dark signal associated with background thermal noise and is therefore only applicable to channels 6–8; for all other channels this term is neglected. Since both $B_{\text{th}}(\phi)$ and LC are time dependent parameters, and can therefore vary between orbits, the dark signal is measured during five ‘dark states’ per orbit (states 8, 26, 46, 63 and 67), each corresponding to a different t_{PET} , as shown in Table 3.3.

Measurement State	Pixel Exposure Time [PET] (s)
8	5.00000
26	0.03125
46	0.25000
63	0.50000
67	0.12500

Table 3.3: Details of measurement states during which dark signal measurements are performed, along with their corresponding PET values.

The spectral retrieval windows for CH₄ and CO₂ both reside within SCIAMACHY detector cluster 43, which covers the wavelength range 971–1773 nm and is associated with a t_{PET} of 0.125 s. For each dark state, measurements of the AO, variable leakage current and the average dark spectrum (average of the dark measurements per state) are made.

3.2.3 Pixel To Pixel Gain

Pixel to pixel gain (PPG) refers to the non-uniform response of neighbouring pixels to incident light and is only relevant to channels 6–8. The PPG effect is calculated by measuring the spectrum of a white light source (WLS) whilst in orbit, then subtracting a smooth, idealised WLS spectral curve to discern the remaining PPG related spectral features.

3.2.4 Dead and Bad Pixels

Spectral points in measured SCIAMACHY spectra are discarded if they are flagged as dead pixels in the L1b data product or are outside of the limits of the manual bad pixel mask, defined in Table 3.4.

Data filters
$0 < \text{signal} < 65000 \text{ BU}$
$0 < \text{DC} < 20000 \text{ BU}$
$\sigma_{\text{DC}} < 15 \text{ BU}$
shot noise $< 15 \text{ BU}$

Table 3.4: The range of acceptable values of the SCIAMACHY signal, dark current (DC), standard deviation of the dark current σ_{DC} and shot noise, that constitute the manual bad pixel mask. For a given spectral point, if any of the stated thresholds are exceeded the point is classified as a bad pixel and subsequently ignored in the retrieval.

3.3 FSI WFM-DOAS for the Retrieval of CH₄

The original FSI WFM-DOAS retrieval scheme was initially developed for retrievals of XCO₂ and is described in detail by Barkley et al. (2006). The aim of this section therefore is to give an overview of the FSI WFM-DOAS retrieval algorithm and highlight the fundamental changes implemented to enable retrievals of XCH₄.

3.3.1 An Overview of FSI WFM-DOAS V2

The FSI WFM-DOAS retrieval begins by reading in both the manually calibrated signal and the full radiometrically calibrated SCIAMACHY spectrum corresponding to a cloud free scene; a priori albedo is then estimated from a look up table, given the SZA and mean intensity of the fully calibrated SCIAMACHY observation. Profiles of a priori pressure, temperature and VMR of the trace gas to be retrieved, which have each been interpolated to the time and location of the SCIAMACHY measurement, are used to initialise the SCIATRAN radiative transfer model for the creation of a reference spectrum- effectively a ‘best guess’ of the measured SCIAMACHY spectrum. The FSI WFM-DOAS linear least squares fit (see Figure 3.3) then scales the reference spectrum to match the manually calibrated SCIAMACHY spectrum, using the resulting scaling factor to retrieve the trace gas VCD given its a priori value.

For the retrieval of CH₄ the proxy approach for VCD normalisation (see Section 1.4.4) was implemented to reduce errors in the resulting VMR caused by atmospheric scattering. Employing the proxy approach required that both CO₂ and CH₄ were retrieved in series for each SCIAMACHY scene, resulting in a doubling of the computational time required for retrievals by Barkley et al. (2006). The original RTM (SCIATRAN 2.0) was replaced by the newly released SCIATRAN 2.2, enabling greater control over the definition of atmospheric conditions, particularly aerosols and clouds. A reduction in resolution of the reference spectrum by a factor of 2 was found to have a negligible effect on the WFM-DOAS fit, but resulted in greatly improved retrieval efficiency and thus largely offset the effect of implementing the proxy approach for VCD normalisation. Figure 3.4 depicts the main structure of the modified FSI WFM-DOAS retrieval, hereafter referred to as FSI WFM-DOAS V2, and Table 3.5 provides a summary of the a priori data used.

3.3.2 The Proxy Approach for CH₄ Column Normalisation

In order to convert a retrieved total column CO₂ VCD to VMR Barkley et al. (2006) utilized a priori surface pressure as a proxy for the total atmospheric column mass. This method assumes, however, that the observed radiation has traversed the entire atmospheric column and neglects the presence of clouds or aerosols which can dramatically alter the light path of observed radiation via scattering. An alternative method of total column normalisation is to employ the proxy approach, described

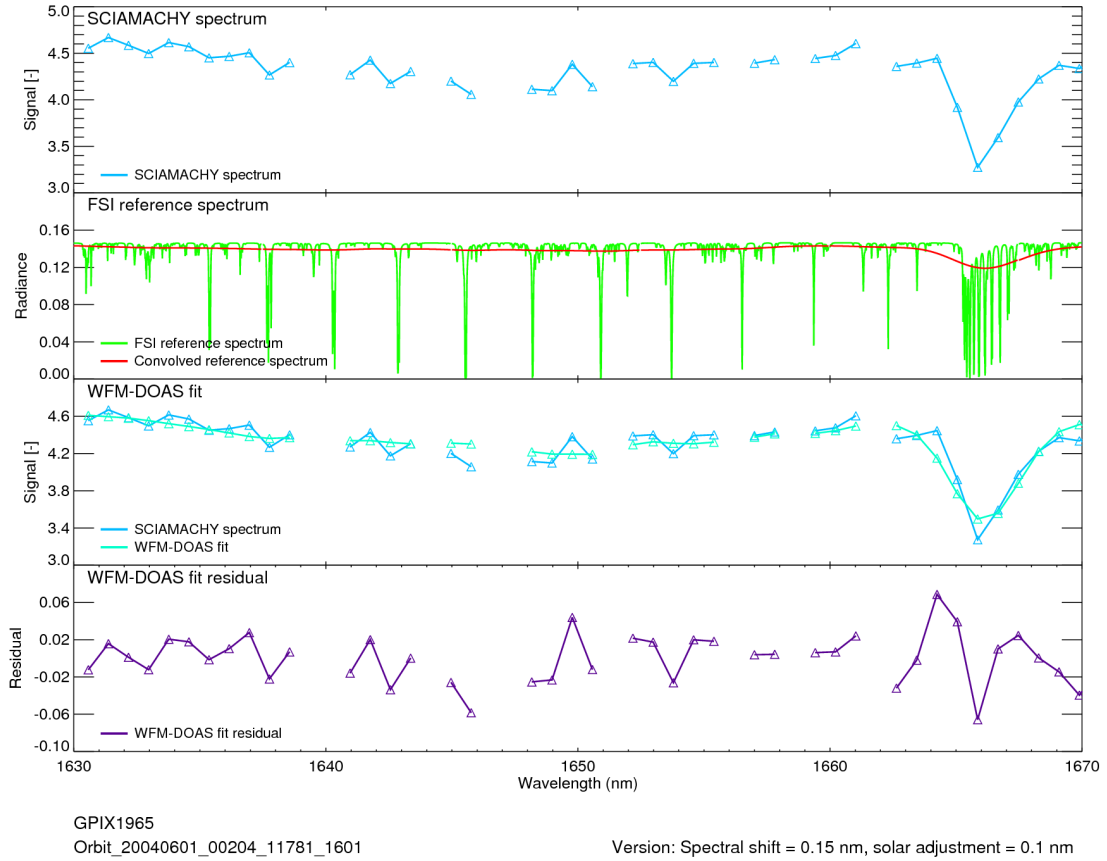


Figure 3.3: Spectra from various stages of a typical FSI WFM-DOAS V2 spectral fit. Spectral panels in order from the top: SCIAMACHY manually calibrated signal; High resolution FSI reference spectrum simulated by SCIATRAN overlaid with the same spectrum convolved with the SCIAMACHY instrument slit function; WFM-DOAS fit (with the original SCIAMACHY spectrum for comparison); WFM-DOAS fit residual. Gaps in the spectra indicate where spectral points have been omitted due to either being flagged as dead pixels in the SCIAMACHY L1b product, or removed by the manual bad pixel mask (see Section 3.2.4).

in Section 1.4.4. Adopting this method of normalisation within FSI WFM-DOAS V2 (using a retrieved CO₂ VCD as the spectral proxy to determine XCH₄) results in a doubling of the retrieval time since the VCDs of CO₂ and CH₄ must be retrieved in series. Consequently, the time typically required to determine XCH₄ using the proxy method is around 5 minutes, since total columns of both CO₂ and CH₄ must be retrieved.

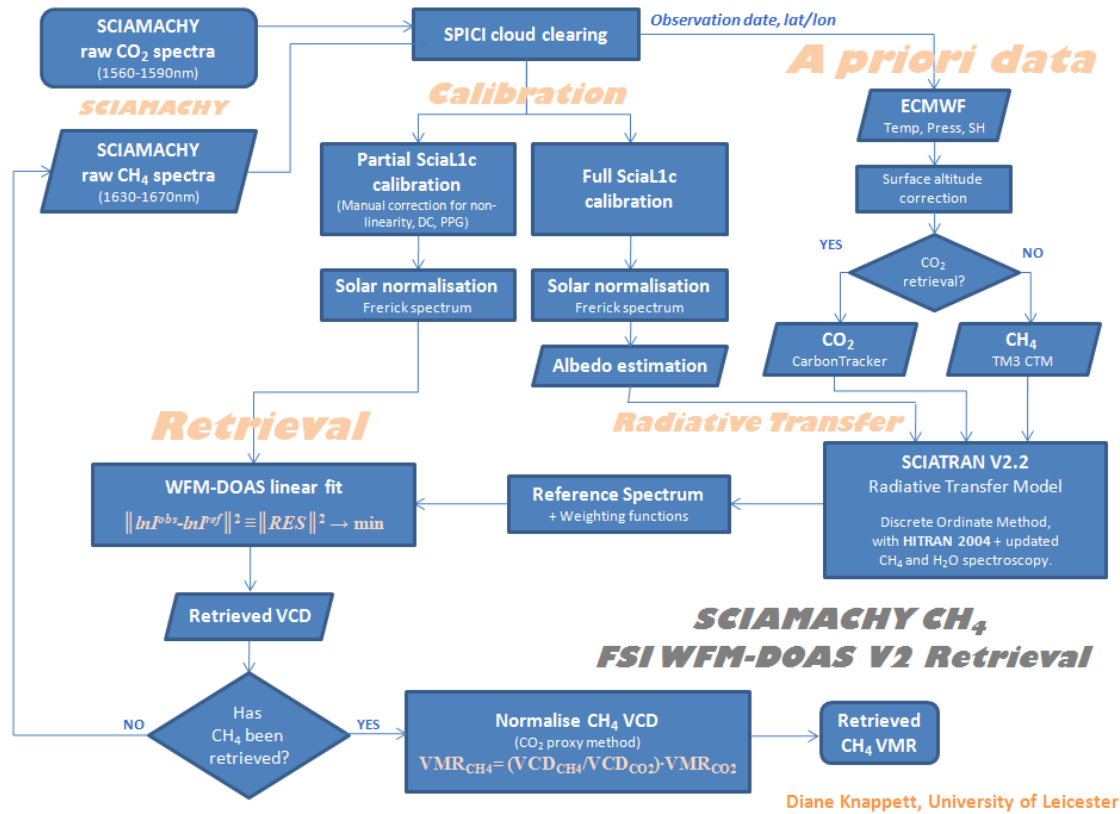


Figure 3.4: Flowchart portraying the progression of the FSI WFM-DOAS V2 retrieval algorithm. Fully calibrated spectra are required to obtain mean spectral intensity which is used in conjunction with SZA to determine the albedo of a scene; the manually calibrated SCIAMACHY signal is used for retrievals since a better dark correction is achieved.

3.3.3 Trace Gas Climatologies

CO₂ mole fractions (in ppm) were obtained from the National Oceanic and Atmospheric Administration (NOAA) CO₂ data assimilation system CarbonTracker* [Peters et al. (2007)]. CarbonTracker combines both atmospheric transport and surface flux exchange models to estimate CO₂ mole fraction profiles for 25 model levels which are then scaled to fit surface flask sample measurements (made to an accuracy of 0.1 ppm) from sites around the globe. Additional data from light aircraft campaigns and a tall tower network complement surface measurements over North America. Globally, CarbonTracker data is gridded on a 3°×2° grid, however data for North America is also available on a higher resolution grid of 1°×1°.

*CarbonTracker mole fractions can be freely downloaded from <ftp://ftp.cmdl.noaa.gov/ccg/co2/carbontracker/molefractions/>

Parameter(s)	Grid boundaries (lon/lat)	Spatial Resolution [Number of lon/lat]	Temporal Resolution	Levels	Model
T H ₂ O q	-180° to 178.5°/ 90° to -90°	1.125°×1.125° [320, 161]	6 hours	60	
LNSP	-180° to 178.5°/ 90° to -90°	1.125°×1.125° [320, 161]	6 hours	1	
CO ₂	-178.5° to 178.5°/ -89° to 89°	3°×2° [120, 90]	3 hours	25	CarbonTracker
CH ₄	-180° to 175°/ -90° to 90°	5°×(180/47)° [72, 48]	Monthly	19	TM3

Table 3.5: Summary of meteorological and trace gas climatologies used by the FSI WFM-DOAS V2 retrieval.

A CH₄ mole fraction climatology produced by the TM3 chemical transport model was acquired via email correspondence with Sander Houweling for use in the FSI WFM-DOAS V2 retrieval.

3.3.4 Albedo

The albedo of a surface describes its fractional reflectance. In satellite retrievals, the albedo of the Earth determines the amount of sunlight reflected from the Earth’s surface back towards an orbiting satellite; the greater the albedo, the more light is reflected towards the detector. Since the topography of the Earth is not uniform its albedo is typically represented by a Bidirectional Reflection Distribution Function (BRDF) which takes into account the properties of the surface and the viewing geometry. Employing a BRDF greatly increases the complexity of radiative transfer calculations therefore a Lambertian surface (which assumes light is scattered equally in all directions) has been utilised in the creation of reference spectra for FSI WFM-DOAS in order to minimise computational time.

Since the SCIAMACHY nadir ground pixel footprint is 30×60 km in channel 6, the albedo is generally significantly inhomogeneous over the ground pixel area. Using SCIATRAN to calculate albedo values for an ensemble of intensity and SZA scenarios, Barkley et al. (2006) compiled a look up table which could be used to represent the mean albedo of the observed scene from the mean SCIAMACHY radiance. The same method is also employed here for the estimation of albedo for

both CO₂ and CH₄ retrievals.

3.3.5 Spectroscopy

The following spectroscopic parameters were required for each of the trace gas molecules to be modelled by SCIATRAN: isotopologue number, wavenumber (cm⁻¹), intensity (cm⁻¹/(molecule cm⁻²)), air-broadened half-width (HWHM) (cm⁻¹ atm⁻¹), lower state energy (cm⁻¹) and the coefficient of the temperature dependence of the air-broadened half-width. These parameters were obtained for CO₂, CH₄ and H₂O for a standard temperature of 296 K from the HITRAN 2004 Rothman et al. (2005) database and were modified to include updates to the spectroscopy of CH₄ [Frankenberg et al. (2008b)] and H₂O [Frankenberg et al. (2008a)].

3.3.6 ECMWF Meteorology

Global profiles of atmospheric temperature T , specific humidity q and water vapour (H₂O) for 60 model levels, along with logarithmic surface pressure (lnsp) for the surface level only, were obtained from the European Centre for Medium-Range Weather Forecasts (ECMWF) Operational Analysis dataset[†] at a 1.125°×1.125° resolution.

Model Levels

ECMWF model levels correspond to the centre of an atmospheric layer. Atmospheric layers are defined by the pressures at their boundaries, known as ‘half-level’ pressures, given by the following equation:

$$p_{k+\frac{1}{2}} = A_{k+\frac{1}{2}} + B_{k+\frac{1}{2}}p_{\text{surf}}, \quad (3.2)$$

where p_{surf} is the pressure at the Earth’s surface and $A_{k+\frac{1}{2}}$ and $B_{k+\frac{1}{2}}$ are constants defined for each atmospheric layer[‡]. The subscript k can have values in the range $0 \leq k \leq n_{\text{levs}}$, where n_{levs} is the total number of model levels in the atmospheric profile. The ECMWF model levels therefore correspond to ‘full-level’ pressures p_k :

$$p_k = \frac{1}{2} \left(p_{k-\frac{1}{2}} + p_{k+\frac{1}{2}}p_{\text{surf}} \right). \quad (3.3)$$

[†]Further details can be found at:

http://badc.nerc.ac.uk/view/badc.nerc.ac.uk__ATOM__dataent_ECMWF-OP

[‡]Tabulated values of the constants A and B can be found at:

http://www.ecmwf.int/products/data/technical/model_levels/model_def_60.html

Spatial and Temporal Interpolation

ECMWF data is provided for four time steps per day; 00:00, 06:00, 12:00 and 18:00 Coordinated Universal Time (abbreviated ‘UTC’) and therefore requires interpolation to the time of the SCIAMACHY observation (SCIAMACHY measurements are labeled with a pixel start time which can be easily converted to UTC) before spatial interpolation is performed. For each day, ECMWF data for five time steps was read in (four from the day in question plus 00:00 from the following day) thus ensuring full coverage of the 24 hour time period. Interpolation in time of global arrays corresponding to each profile level in turn was then carried out, resulting in a global array of ECMWF profiles corresponding to the UTC time of the SCIAMACHY measurement.

ECMWF model sigma levels can be converted to pressure levels using $\ln sp$, and subsequently to altitude using the hydrostatic equation. Since the hydrostatic equation only calculates the *relative* change in height corresponding to a change in pressure, the lowest level of all altitude profiles was set to 0 m by default (represented by the black profiles in Figure 3.5). As a result, altitude profiles can only be compared in relative terms since there is no common frame of reference; the lowest level of a given altitude profile can therefore just as easily correspond to the bottom of a ravine as to the top of a mountain. Consequently, bilinear interpolation of the four ECMWF grid profiles surrounding a SCIAMACHY scene is non-trivial and requires the implementation of a standardised altitude grid against which all profiles can be measured. Although profiles of pressure are comparable, the SCIATRAN RTM requires atmospheric profiles corresponding to altitude. Furthermore, since only the elevation (and not surface pressure) of each SCIAMACHY observed location is known, the interpolation of the ECMWF profiles had to be performed in altitude.

To achieve this end, firstly a global grid of surface geopotentials [$\text{m}^2 \text{s}^{-2}$] was obtained from the ECMWF orography dataset on a matching $1.125^\circ \times 1.125^\circ$ grid and the four values corresponding to grid points enclosing the SCIAMACHY observed scene were extracted. Geopotentials at these four locations were converted to geometric height (in m) and then added to the corresponding original altitude grid profiles (in which the lowest level was defined as 0 m) thus making all altitude profiles comparable by using sea level as a common point of reference (resulting in the red profiles in Figure 3.5). The GTOPO30[§] digital elevation map was used to deter-

[§]For further details see:

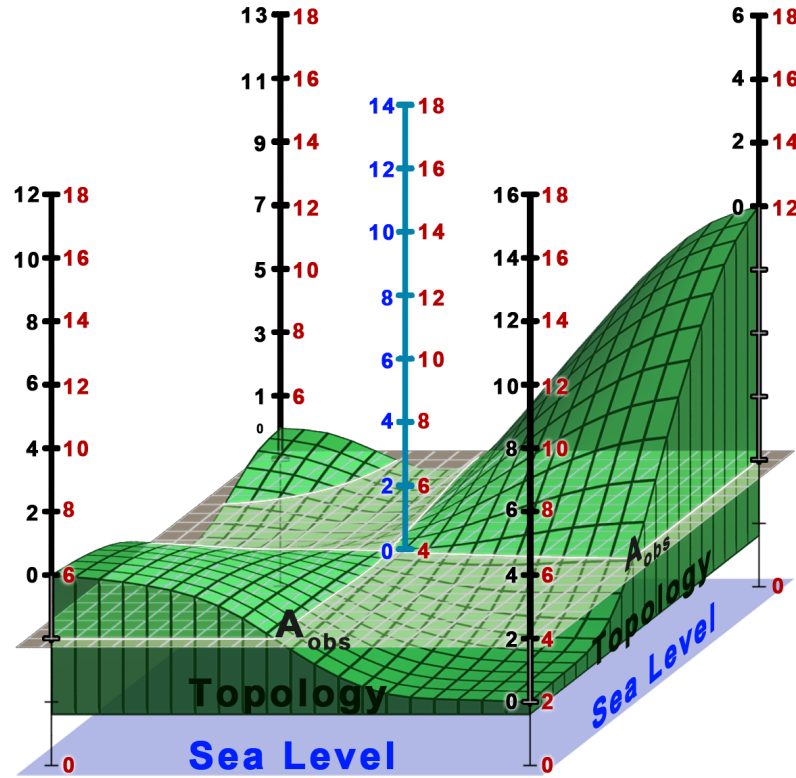


Figure 3.5: Diagram to illustrate the improved interpolation of ECMWF profiles to an observed location. Geometric heights were added to original ECMWF altitude profiles corresponding to a regular grid (indicated in black) in order to create profiles of altitude that were relative to sea level (shown in red). A new altitude profile was then created for the observed location (with surface geometric height A_{obs}) onto which the corner profiles could then be correctly interpolated (figure produced by A. Durose and D. Knappett).

mine the elevation of the centre of the SCIAMACHY observed scene; this altitude then was inserted into each of the four altitude corner profiles, creating an *additional* profile level. For each corner profile, P was calculated using the hydrostatic equation, for the case where temperature T varies with height z , given by:

$$P = P_0 \exp \left(-\frac{g}{R} \int_0^{z_1} -\Gamma(z)^{-1} \right), \quad (3.4)$$

where $R = 8.315$ is the ideal gas constant [$\text{J K}^{-1} \text{mol}^{-1}$] and g is the acceleration due to gravity. $\Gamma(z)$ is the lapse rate of T and thus describes the decreasing gradient of T with altitude:

$$\Gamma(z) = -\frac{dT}{dz}. \quad (3.5)$$

Different methods of determining $\Gamma(z)$ were used depending on whether the surface geometric height of the SCIAMACHY observation, A_{obs} , was above or below the lowest altitude of the corresponding ECMWF altitude profile, A_{E} . For the case where $A_{\text{obs}} > A_{\text{E}}$, a simple mean of T from the nearest two model levels was used. For the case where $A_{\text{obs}} < A_{\text{E}}$, extrapolation of the gradient between the lowest two layers was likely to lead to severe overestimation of T at the height A_{obs} since there is usually a sharp increase in the gradient of T on approach to the Earth's surface (as shown in Figure 2.1). As a result, the mean lapse rate calculated from the 6 lowest ECMWF model levels (5 layers) was employed to ensure a more reasonable estimate of T was established. The same approach was also used to determine values of q and H₂O given the relative position of A_{obs} to A_{E} .

A standard 30 level altitude profile (optimised to be used within SCIATRAN) was added to A_{obs} to create a profile for the observed location that was also referenced to sea level (the central blue profile in Figure 2.1). The corner profiles were each interpolated vertically to match the altitudes of the new profile at the observed location, and then (since all four corners now shared a common altitude profile) each level was bilinearly interpolated in the horizontal plane to create new profiles of P , T , q and H₂O tailored to the observed location.

This method of profile standardisation is important for ECMWF meteorological data because profiles of P and T in particular tend to change rapidly with altitude therefore a failure to take surface topography into account could lead to a mismatch of profiles during interpolation and hence significant error. In contrast, trace gas profiles of CO₂ and CH₄ tend to vary slowly with altitude, and are of lower spatial (and temporal in the case of CH₄) resolution, therefore a similar standardisation is unnecessary.

3.3.7 Radiative Transfer using SCIATRAN 2.2

Radiative transfer (RT) calculations for the creation of reference spectra were performed using SCIATRAN version 2.2 [Rozanov (2007); Rozanov et al. (2005)]. A plane parallel approximation was considered suitable for atmospheric simulations since the approximation holds well for near-nadir observations with SZA < 75°

[Rozanov (2007)], which encompasses the majority of SCIAMACHY observations used in this thesis. Furthermore, the use of a plane parallel approximation is preferred over a more computationally expensive spherical or pseudo-spherical approach for the reduction of overall retrieval run-time. RT was performed using the Discrete Ordinate Method (DOM). For further details regarding the set up of SCIATRAN 2.2 see Appendix B.

3.4 Sources of Retrieval Error

Atmospheric trace gas retrievals are subject to both random and systematic errors. Random errors vary unpredictably and therefore cannot easily be accounted for. An example of random error is photon shot noise which results from random fluctuations in the number of photons arriving at a detector. Systematic error refers to a constant offset in a set of measurements caused by instrument bias or subsequent analysis of the measurement and, if known, can usually simply be subtracted from the measurement. For FSI WFM-DOAS V2 retrievals of XCH₄ from SCIAMACHY, errors can be broadly classified into the following categories:

- Instrument: Random errors induced by the detector electronics (i.e. dark current, shot noise).
- Lightpath: Systematic errors due to alteration of the photon light path by albedo, SZA or optical depth.
- Retrieval: Systematic errors caused by the numerical method, approximations or a priori data used in the retrieval method.

Random errors affect the *precision* of a measurement, that is, the spread of values obtained when a measurement is repeated several times under the same experimental conditions. The *accuracy* of a measurement refers to the proximity of the measurement to the true value and encompasses both random and systematic errors [Rodgers (2000)].

3.4.1 Instrument Noise

SCIAMACHY channels 6–8 utilise purpose built indium gallium arsenide (InGaAs) [Hoovgeveen et al. (2001)] semi-conductor detectors, in contrast to the standard silicon detectors employed by channels 1–5. The InGaAs material provides sufficient

sensitivity in the SWIR region whilst avoiding the need for excessive cooling to achieve a suitable SNR; operating temperatures of below 100 K are usually required in the 1–2.4 μm range covered by channels 6–8, however InGaAs detectors provide acceptable performance at a temperature of just 150 K [Hoovgeveen et al. (2001)]. The SWIR channels are primarily affected by dark current, Johnson noise (voltage fluctuations caused by the thermal motion of electrons in a conductor) and shot noise [Hoovgeveen et al. (2001)]. Dark current can be effectively corrected for using manual calibrations (see Section 3.2.2), since measurements of DC in channel 6 (for the same integration time as the radiance measurements) are made every orbit, however shot noise and Johnson noise cause unavoidable random error.

Using WFM-DOAS version 1.0, Schneising et al. (2009) report theoretical random errors due to noise of 0.7% on the retrieved CO_2 VCD and 1.5% on the retrieved CH_4 VCD, valid for an albedo of 0.2 and SZA of 50° . This corresponds to a combined error of around 1.7% on the retrieved XCH_4 for a single ground pixel. Correspondingly, for the optimal estimation based IMA-DOAS retrieval Frankenberg et al. (2006) report errors due to instrumental noise of 1.5% for the retrieved CO_2 VCD and 1% for the retrieved CH_4 VCD, resulting in a combined error of 1.8% on XCH_4 . The error due to instrument noise can be significantly reduced by calculating the monthly mean of n retrievals, since random errors reduce with \sqrt{n} .

3.4.2 Spectroscopy

Frankenberg et al. (2008a) found that utilising water vapour spectroscopy from the HITRAN 2004 database results in errors of up to 3% in CH_4 retrievals over the tropics. However, by implementing the improved water vapour spectroscopy from Jenouvrier et al. (2007) this bias is removed. In addition, Frankenberg et al. (2008b) showed that the use of incorrect pressure broadening parameters in the $2\nu_3$ CH_4 band can cause errors of 1% in CH_4 retrievals.

3.4.3 Albedo

Albedo is fundamental in determining the SNR. For a fixed trace gas column an increase in albedo leads to a greater fraction of light being reflected, resulting in not only an increase in intensity but also the lengthening of spectral lines since a greater amount of absorption is incurred. XCH_4 retrieval errors related to albedo in WFM-DOAS version 1.0 were found to be around 0.1% by Schneising et al. (2009).

3.4.4 SZA

SZA is the angle of the Sun with respect to the zenith; for an observer at an arbitrary location on the Earth a SZA of 0° indicates that the Sun is directly overhead, whereas a SZA of 90° means that the Sun is approximately at the horizon. With increasing SZA, light must travel through a greater amount of atmosphere, resulting in an extended lightpath but reduced intensity, thus affecting the SNR.

3.4.5 Aerosols and Cirrus Clouds

During this thesis study, a complementary but more limited study into the effects of aerosol and cirrus cloud contamination on retrievals of XCH_4 from space-based solar backscatter measurements was conducted by Butz et al. (2010). In this study the impact of scattering due to an ensemble of aerosol and cirrus cloud scenarios on optimal estimation based retrievals of XCH_4 from simulated SCIAMACHY and GOSAT measurements was assessed when using a proxy method approach (see Section 1.4.4) for VCD normalisation. The sensitivity of a ‘full-physics’ retrieval was also investigated but for GOSAT simulated measurements only.

Aerosol optical depth (AOD) was modelled by the global aerosol model ECHAM5-HAM and scaled to match the monthly median optical depth from MODIS. Similarly, cloud optical depths (COD) were simulated using a ray-tracing model and then scaled to match the monthly median cirrus optical thickness from the Cloud Aerosol Lidar with Orthogonal Polarization (CALIOP). Consequently, optical depth limits of 0.2 and 0.4 (at $0.55 \mu\text{m}$) were imposed on AOD and COD respectively. The resulting total particle optical depth of each scene was therefore typically below 0.5 at $1.65 \mu\text{m}$. Although simulations were performed using realistic aerosol and cirrus cloud profiles, a limitation of this study is that aerosol and cloud layers were not systematically varied with altitude.

Butz et al. (2010) report errors of typically less than 0.6% were encountered for proxy method retrievals of XCH_4 and less than 0.8% when using the full physics approach. Overall, errors were less than 2% for the vast majority of scenes in both retrievals. Although the proxy approach was employed in this study, the underlying retrieval scheme is based on optimal estimation and therefore differs from FSI WFM-DOAS used in this thesis.

3.4.6 Quantifying Error Sensitivity

Table 3.6 defines a number of simulated atmospheric scenarios of different AOD, surface albedo and SZA. For each scenario, a SCIAMACHY spectrum was simulated using SCIATRAN, assuming a constant XCH₄ of 1774 ppb. In each case the percentage difference between the FSI WFM-DOAS V2 retrieved XCH₄ and the original XCH₄ is given in the final column. These results show that large AOD causes a substantial retrieval error whereas SZA and albedo have a smaller effect.

Scenario ID	AOD	a	SZA	UP XCH ₄ [%]
1a	0.0	0.34	20°	-0.01
1b	0.0	0.34	70°	-0.24
1c	0.0	0.15	20°	-0.10
1d	0.0	0.15	70°	-1.60
2a	1.0	0.34	20°	7.59
2b	1.0	0.34	70°	10.88
2c	1.0	0.15	20°	7.16
2d	1.0	0.15	70°	10.47

Table 3.6: Percentage difference between the unperturbed retrieved XCH₄ and true XCH₄ (1774 ppb) for eight different scenarios.

To quantify the errors associated with a priori pressure and temperature, simulations were run in which the respective a priori columns were perturbed by various amounts ($\pm 0.5\%$, 2% and 5% for pressure and $\pm 1\%$, 2% and 5% for temperature). Tables 3.7 and 3.8 show the *additional* percentage error, caused by perturbations to pressure and temperature profile respectively, incurred on top of the percentage error given in the final column of Table 3.6. From these results it can be seen that discrepancies in the a priori pressure profile can cause significant error, however the errors associated with changes in the temperature profile are far less significant.

In just the few simulations presented here AOD appears to cause significant error compared to other retrieval parameters such as SZA and albedo. Since thin cirrus clouds are difficult to detect using standard cloud filtering methods and cause similar scattering to that of aerosols their presence in a satellite observed scene is also expected to cause large retrieval errors. As a result, aerosols and thin cirrus clouds are a top priority for further study in the effort to minimise retrieval biases.

Scenario	+0.5%	-0.5%	+2%	-2%	+5%	-5%
1a	0.11	-0.12	0.46	-0.46	1.12	-1.18
1b	0.12	-0.12	0.47	-0.48	1.15	-1.22
1c	0.11	-0.11	0.45	-0.46	1.11	-1.17
1d	0.11	-0.11	0.45	-0.46	1.11	-1.18
2a	0.14	-0.14	0.55	-0.56	1.35	-1.41
2b	0.15	-0.15	0.60	-0.61	1.47	-1.54
2c	0.14	-0.14	0.54	-0.55	1.32	-1.38
2d	0.15	-0.15	0.58	-0.59	1.42	-1.50

Table 3.7: Pressure profile error budget. Difference in XCH_4 [%] between retrievals where the a priori pressure profile was scaled by the amount shown at the top of each column and an unperturbed case.

Scenario	+1%	-1%	+2%	-2%	+5%	-5%
1a	-0.002	0.002	-0.005	0.003	-0.004	-0.002
1b	-0.001	0.002	0.000	0.004	0.028	0.000
1c	-0.002	0.002	-0.005	0.003	-0.003	-0.002
1d	-0.004	0.005	-0.007	0.010	0.008	0.014
2a	0.009	-0.008	0.018	-0.016	0.061	-0.044
2b	0.124	-0.120	0.253	-0.238	0.683	-0.592
2c	0.031	-0.030	0.063	-0.060	0.176	-0.156
2d	0.152	-0.148	0.309	-0.294	0.825	-0.733

Table 3.8: Temperature profile error budget. Difference in XCH_4 [%] between retrievals where the a priori temperature profile was scaled by the amount shown at the top of each column and an unperturbed case.

Chapter 4

The Effect of Aerosols and Cirrus Clouds on Atmospheric Retrievals of CH₄

4.1 Introduction

The basis of atmospheric trace gas retrievals is that the concentration of a trace gas can be inferred by the analysis of its absorption features in measured spectra. However, the presence of aerosols and clouds in a satellite observed scene can significantly alter the original light path and thus bias, sometimes severely, the retrieved total column [Reuter et al. (2010); Butz et al. (2010)]. Retrieval errors incurred as a result can be reduced by taking clouds and aerosols into consideration within the retrieval algorithm or by compensating for their effect in a post-retrieval VCD normalisation procedure. For example, employing the CO₂ proxy approach (described in Section 1.4.4) to normalise retrieved CH₄ total columns is generally assumed to account for atmospheric scattering by aerosols and clouds in SWIR retrievals of XCH₄. However, since scattering, absorption and surface albedo are wavelength dependent, and CO₂ and CH₄ are retrieved from different spectral windows within FSI WFM-DOAS V2, some discrepancies remain when utilising the proxy approach. This chapter aims to quantify the magnitude of such errors.

The following sections detail three sensitivity simulations created to assess the performance of FSI WFM-DOAS V2 to different atmospheric scattering scenarios. Section 4.2 investigates errors incurred by the use of inaccurate a priori aerosol data using SCIATRAN 2.0. In Section 4.3 implementation of SCIATRAN 2.2 is de-

scribed, allowing a simple box-like scattering layer for both aerosol and thin cloud scenarios to be simulated and the effect of systematically varying optical depth and altitude to be investigated. Section 4.4 introduces a global sensitivity test performed to identify regions where the presence of aerosols and cirrus clouds are likely to cause significant retrieval biases. Results show that in the most extreme cases an overestimation of up to 35% is encountered in the retrieved XCH₄.

4.2 Simulation 1: Quantifying the Effects of Inaccurate A Priori Data

This section details a series of tests carried out to assess the sensitivity of FSI WFM-DOAS V2 retrievals of XCH₄ to the use of incorrect a priori aerosol data, the exclusion of a priori aerosol data and different methods of VCD normalisation. FSI WFM-DOAS V2 retrievals were carried out for SCIATRAN 2.0 simulated SCIAMACHY spectra corresponding to a set of systematically varied aerosol scenarios and fixed atmospheric trace gas profiles.

To avoid confusion in the following discussion, values of optical depth used to simulate spectra for input to the FSI retrieval will be denoted as τ_{sim} , whereas optical depths corresponding to FSI retrieval aerosol scenarios will be referred to as τ_{ret} .

4.2.1 Simulated SCIAMACHY Spectra

The radiative properties of atmospheric aerosol can be broadly defined by three main parameters; aerosol type, profile shape and optical depth. In total, SCIAMACHY spectra corresponding to 64 different aerosol scenarios resulting from the permutation of parameters defined in Table 4.1 were simulated. Two predetermined aerosol mixtures from LOWTRAN (low-resolution propagation model of atmospheric transmittance) were used for this sensitivity test:

- Rural aerosol: 70% water soluble substance, 30% dust-like aerosol
- Urban aerosol: 20% soot, 80% ‘rural’ aerosol mixture

For a rural aerosol type, land cover was set to either grassland or desert, boundary layer (BL) visibility was varied between 23 and 50 km, humidity between 80 and 90% and the tropospheric (TR) visibility was fixed at 50 km, resulting in a range of

Parameter		Tropical Lat (-5.0 N, -65.0 E)	Northern Lat (60.0 N, 75.0 E]
XCH ₄		1845 ppb	1766 ppb
SZA		20,40,60,70	20,40,60,70
Surface albedo		grassland, desert	forest, wetland
Aerosol	Type	rural	urban
	BL visibility [km]	23,50	2,10
	TR visibility [km]	50	23
	Humidity (BL/TR) [%]	80,99	0,70

Table 4.1: Parameters used to define 64 atmospheric scenarios for the simulation of SCIAMACHY spectra; a priori XCH₄, SZA, surface albedo and aerosol properties (boundary layer (BL) visibility, tropospheric (TR) visibility and humidity).

τ_{sim} between 0.039 and 0.106. For urban aerosol scenarios, land cover was defined as either forest or wetland, BL visibility was varied between 2 and 10 km, humidity between 0 and 70% and TR visibility was fixed at 23 km, resulting a range of τ_{sim} between 0.235 and 1.109. For both rural and urban scenarios the SZA was varied between 20°, 40°, 60° and 70°. Surface albedo values representative of each land type within the CO₂ and CH₄ retrieval wavelength regions were obtained by interpolating albedo profiles available from the Airborne Visible/Infrared Imaging Spectrometer (AVIRIS) database to the central wavelength of each retrieval window (see Figure 4.1). In keeping with the four land types used, a tropical location (5.00 S, 65.00 W) was chosen as the setting for rural scenarios whereas a mid to northern latitude location (60.00 N, 75.00 E) was chosen as a typical urban setting. The selection of location was important to ensure a suitable pairing of simulated aerosol scenarios with realistic trace gas and meteorological profiles.

Figure 4.2 shows how a typical SCIATRAN extinction profile (BL visibility = 23 km and TR visibility = 50 km) at 1650 nm changes with increasing humidity for both rural and urban BL aerosol scenarios in the BL and TR. Above 10 km the model profile is independent of humidity and has therefore been omitted for clarity. For rural aerosols an increase in humidity always results in an increase of the extinction profile. For an urban BL aerosol mixture the extinction at 0% humidity exceeds the extinction in both the 70% and 80% humidity cases, however the extinction at 99% humidity remains larger than at 0%.

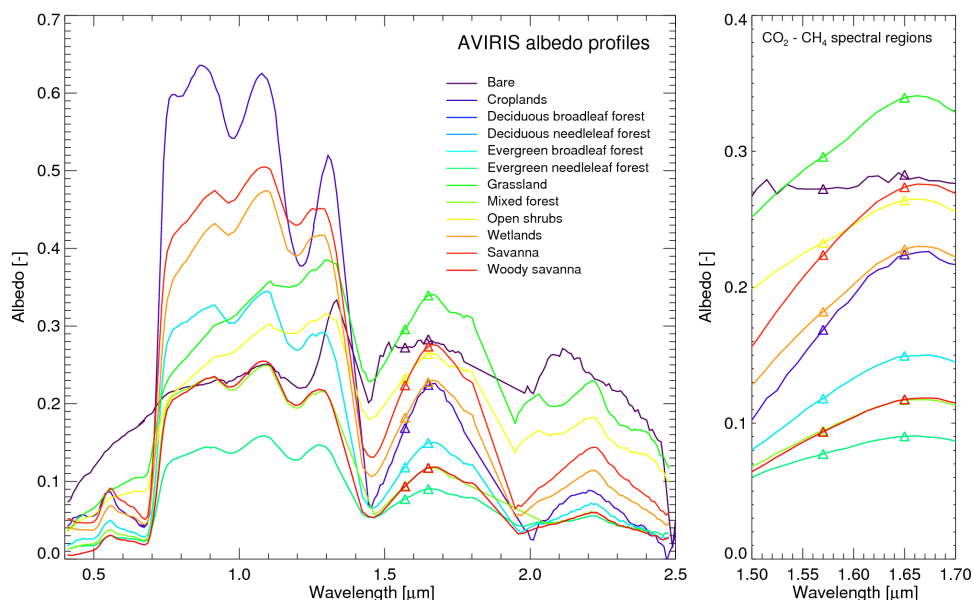


Figure 4.1: AVIRIS surface albedo profiles for the wavelength range 0.4–2.5 μm . Right hand side panel shows the wavelength region encompassing both the CO₂ and CH₄ retrieval windows.

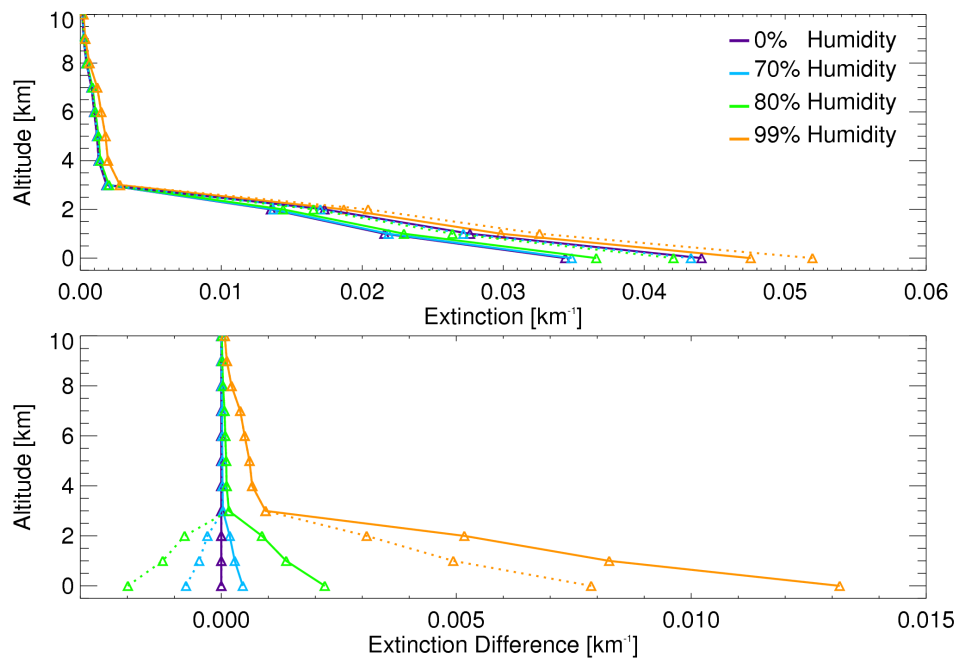


Figure 4.2: SCIATRAN extinction profiles for a BL visibility of 23 km and a TR visibility of 50 km, spanning the BL (0–2 km) and TR (3–10 km) for both rural (solid line) and urban (dotted line) BL aerosol types. The top panel shows extinction profiles for the four different humidity values (0%, 70%, 80% and 99%) whereas the lower panel shows the *difference* between the extinction in each case minus the extinction at 0% humidity.

4.2.2 FSI Retrieval Aerosol Scenarios

For each of the 64 simulated observations 81 retrievals were performed, 80 of which result from different combinations of the a priori aerosol parameters defined in Table 4.2 and one control case for which scattering in SCIATRAN 2.0 was turned off (this will be referred to as the ‘non-scattering’ retrieval). Aerosol scenarios used for retrievals differed to the simulated aerosol scenarios by various amounts so that the effects of using inaccurate a priori data could be systematically assessed. To ensure that retrieval errors resulted primarily from the varying of aerosol parameters, a priori surface albedo was fixed to the AVIRIS interpolated value used to create simulated spectra.

Parameter		Value
Aerosol	Type	rural, urban
	BL visibility [km]	2,5,10,23,50
	TP visibility [km]	23,50
	Humidity (BL/TP) [%]	0,70,80,99

Table 4.2: Parameters used to define aerosol scenarios for the 80 FSI WFM-DOAS V2 retrievals performed for each of the 64 simulated SCIAMACHY spectra defined in Table 4.1.

4.2.3 Results

Errors incurred due to the use of the adjusted aerosol a priori parameters are quantified here by ΔXCH_4 which is simply the retrieved column $XCH_{4(\text{ret})}$ minus the simulated column $XCH_{4(\text{sim})}$ in ppb:

$$\Delta XCH_4 = XCH_{4(\text{ret})} - XCH_{4(\text{sim})}. \quad (4.1)$$

The systematic initialisation of the retrieval with adjusted a priori aerosol parameters resulted in values of ΔXCH_4 which were highly dependent on surface albedo and SZA. Subsequently, the discussion of results has been divided into cases of low, moderate and high optical depth, with cases for each SZA discussed individually. It should be noted that in each simulation, one retrieval case was initialised with the ‘correct’ a priori aerosol, however even in these cases the retrieved column is typically different to the simulated column by around 1 ppb ($\sim 6 \times 10^{-4}\%$) due to numerical rounding within the retrieval algorithm.

Low Aerosol Loading (Rural Aerosol of $\tau_{\text{sim}} = 0.04$)

For SCIAMACHY scenes of very low optical depth ($\tau_{\text{sim}} = 0.04$), shown in Figure 4.3, initialisation of the retrieval with the wrong a priori aerosol resulted in the following errors:

- For SZA=20°, ΔXCH_4 was below 1% even for $\tau_{\text{ret}} > 1.0$.
- For SZA=60°, ΔXCH_4 was generally below 1%, but resulted in an underestimate of the column by $\sim 1.5\%$ for $\tau_{\text{ret}} > 1.0$ in cases of wrongly estimated aerosol type or humidity.
- For SZA=70°, ΔXCH_4 was below 1% for $\tau_{\text{ret}} < 0.5$, however for $\tau_{\text{ret}} > 0.5$ the use of incorrect aerosol or humidity can lead to a column underestimation of up to 50 ppb ($\sim 3\%$).

In all cases, the non-scattering retrieval is a good approximation of the true atmospheric state, resulting in minimal error ($\Delta\text{XCH}_4 \sim \pm 2$ ppb) for all values of SZA and surface albedo.

Moderate Aerosol Loading (Urban Aerosol of $\tau_{\text{sim}} = 0.24$)

For SCIAMACHY scenes of moderate optical depth shown in Figure 4.4, the following retrieval errors were incurred:

- For SZA=20°, ΔXCH_4 was below 1%, as in the low AOD case.
- For SZA=60°, ΔXCH_4 was generally below 1%, but resulted in an underestimate of the column by $\sim 1.5\text{--}2\%$ for $\tau_{\text{ret}} > 1.0$ in cases of wrongly estimated aerosol type or humidity.
- For SZA=70° in the case of $\tau_{\text{ret}} < \tau_{\text{sim}}$, the column was underestimated by around 0.5% in the non-scattering case and slightly less for all other aerosol scenes. For $\tau_{\text{ret}} > \tau_{\text{sim}}$, ΔXCH_4 rapidly becomes increasingly negative, with a maximum underestimation of 50 ppb in cases of severely incorrect aerosol type and humidity.

In general, the non-scattering retrieval performs well at low SZA, but for SZAs $> 60^\circ$ the majority of aerosol scenarios produce a smaller ΔXCH_4 .

High Aerosol Loading (Urban Aerosol of $\tau_{\text{sim}} = 1.11$)

For the highest optical depth scenes considered, shown in Figure 4.5, the following errors were incurred:

- For SZA=20°, ΔX_{CH_4} was below 1% for scenes of relatively high surface albedo, whereas for a low surface albedo (wetland) case ΔX_{CH_4} increased to $\sim 1\%$.
- For SZA=60°, ΔX_{CH_4} was just over 2% in the majority of high surface albedo cases, whereas for a low surface albedo case ΔX_{CH_4} was $\sim 3\%$. For this scenario, relatively small inaccuracies in the a priori aerosol result in significant error.
- For SZA=70° ΔX_{CH_4} was between 2–4% in the majority of cases, with comparable errors incurred in both high and low surface albedo scenarios.

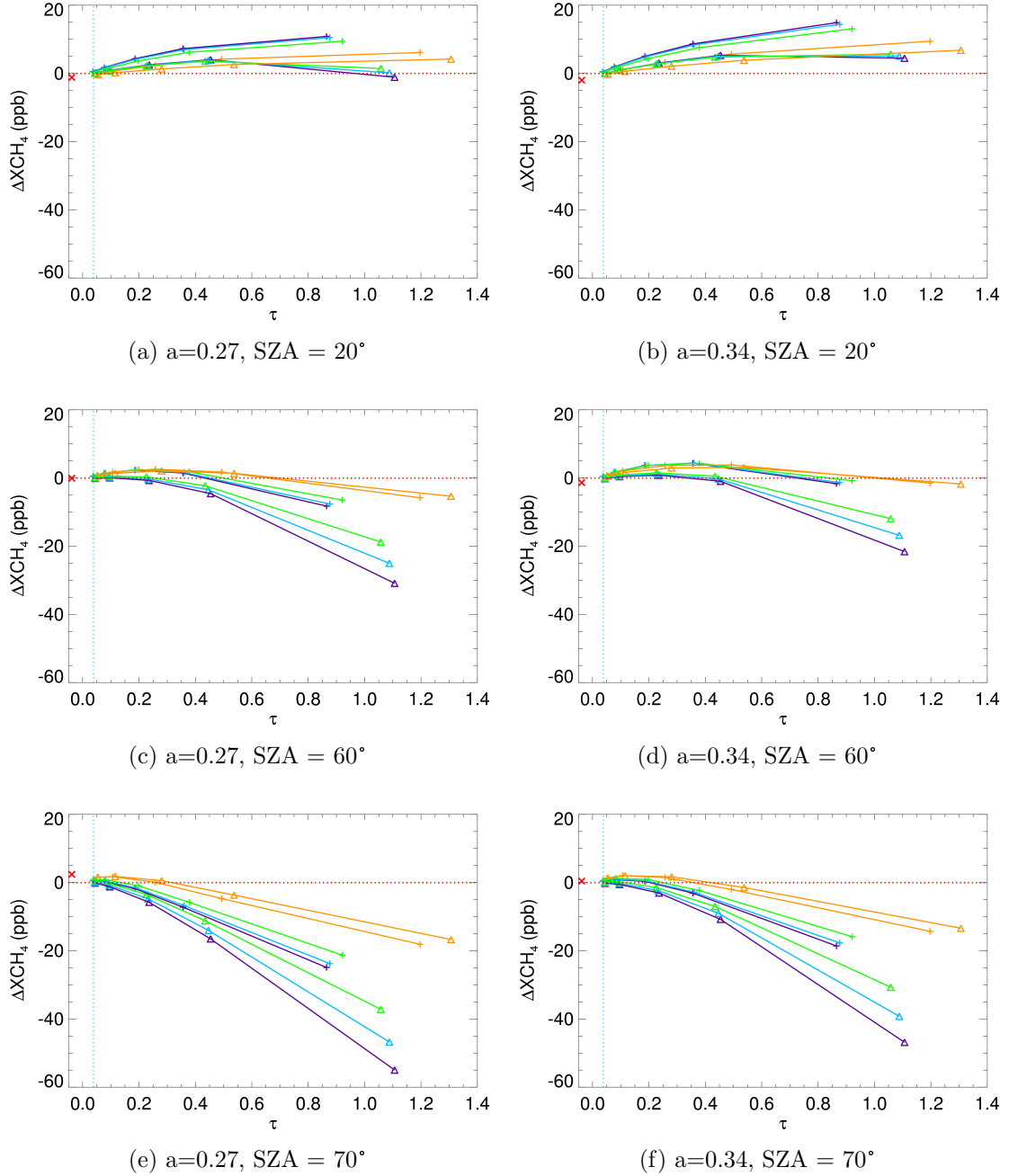


Figure 4.3: Sensitivity tests for a low aerosol loading scenario (rural aerosol, $\tau_{sim} = 0.0385$) as a function of τ_{ret} (optical depth for FSI reference spectrum), for SZAs of 20° , 60° and 70° .

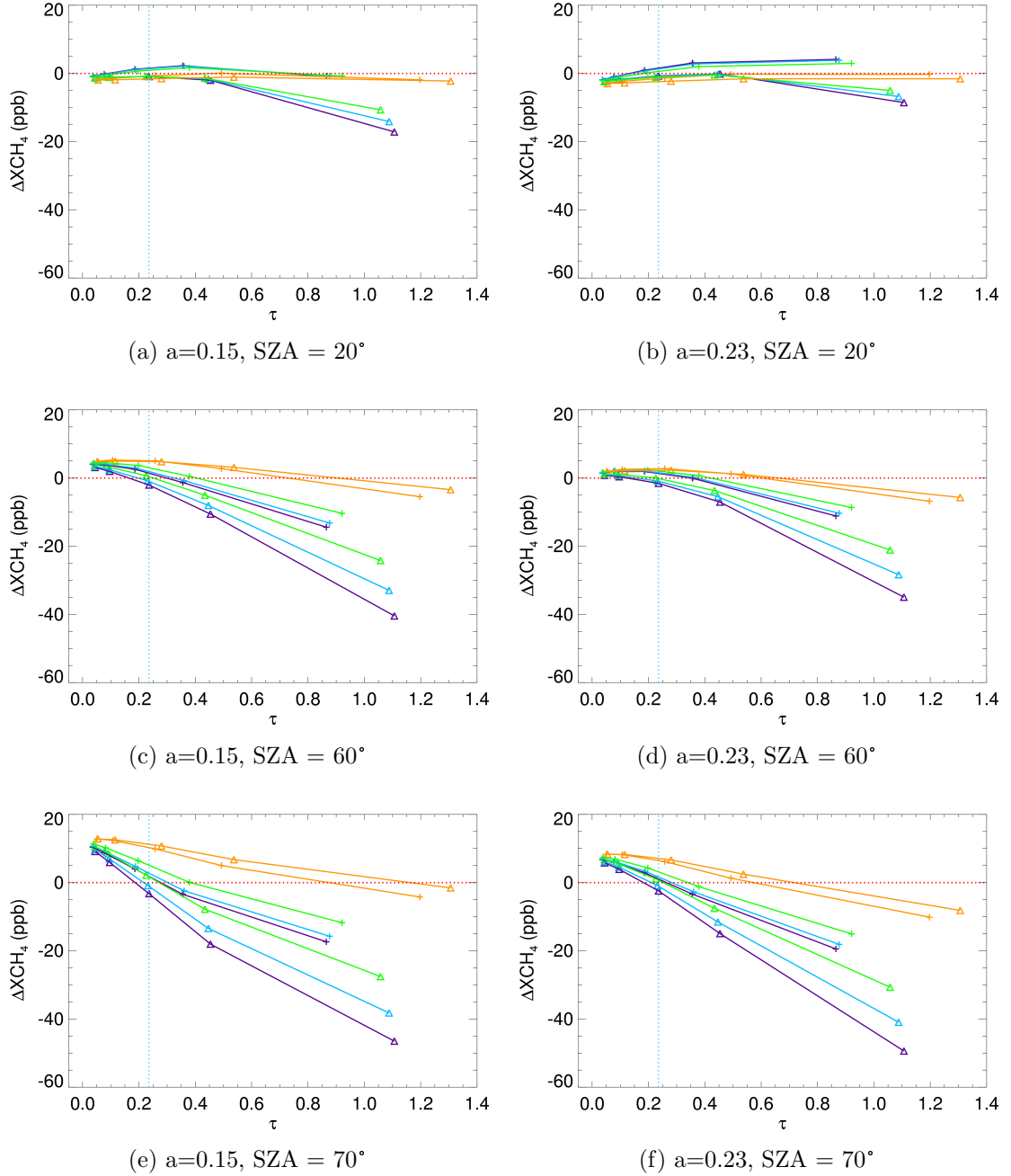


Figure 4.4: Sensitivity tests for a moderate aerosol loading scenario (urban aerosol, $\tau_{sim} = 0.235$) as a function of τ_{ret} (optical depth for FSI reference spectrum), for SZAs of 20° , 60° and 70° .

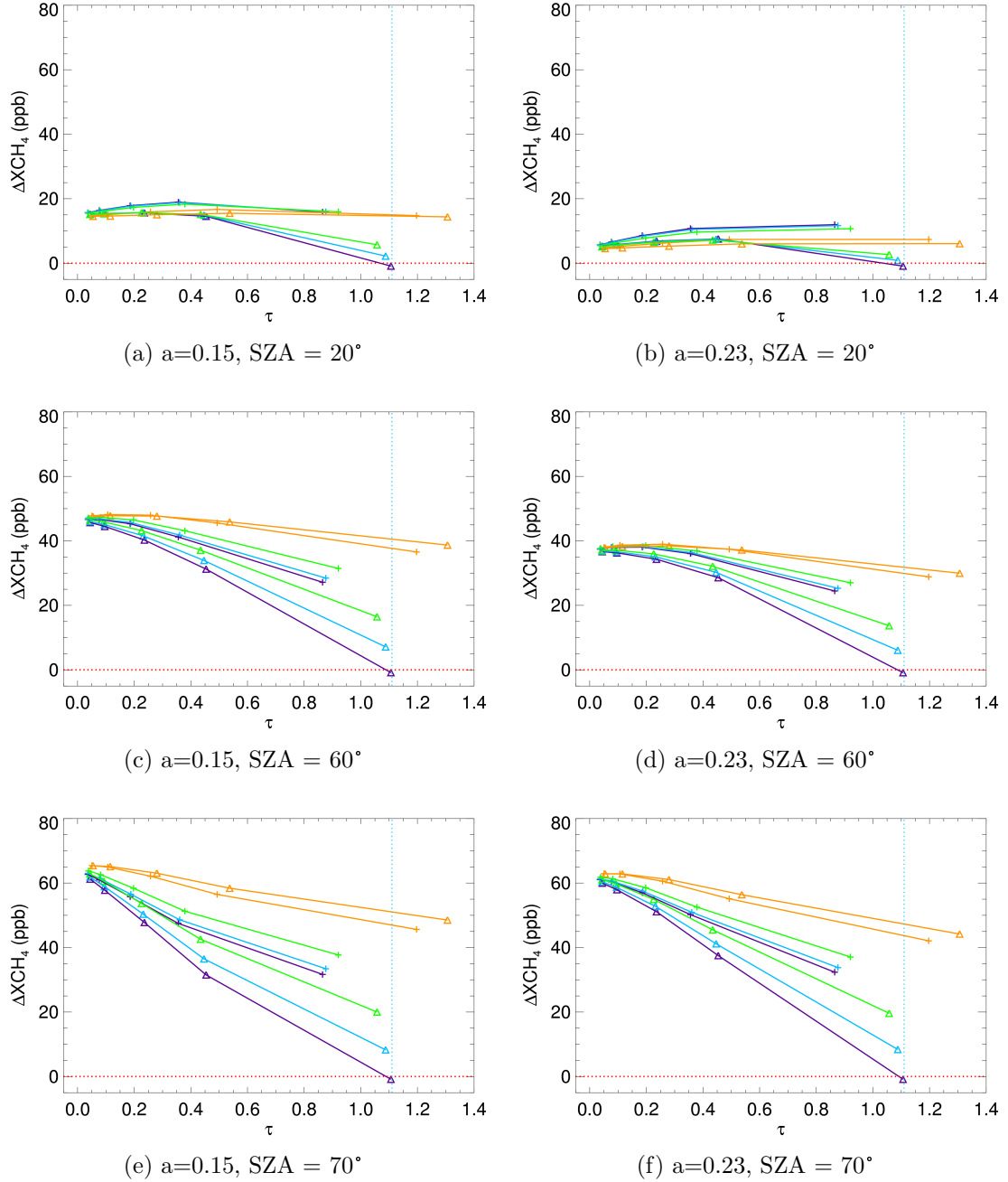


Figure 4.5: Sensitivity tests for a high aerosol loading scenario (urban aerosol, $\tau_{sim} = 1.11$) as a function of τ_{ret} (optical depth for FSI reference spectrum), for SZAs of 20°, 60° and 70°.

4.2.4 Summary of Simulation 1

The systematic initialisation of FSI WFM-DOAS V2 retrievals with incorrect aerosol a priori data revealed that for simulated SCIAMACHY scenes of low optical depth, the use of high a priori aerosol can lead to significant error (large ΔXCH_4) but generally only when combined with high SZA or low surface albedo. For simulated SCIAMACHY scenes of moderate optical depth, the use of a non-scattering retrieval causes noticeable error for SZAs greater than 60° . However, in this case the overestimation of a priori AOD results in greater ΔXCH_4 than the non-scattering case. For simulated SCIAMACHY scenes of high optical depth, the non-scattering retrieval produces very high ΔXCH_4 , particularly in cases where $SZA > 60^\circ$, however even slight inaccuracy in the a priori aerosol (for example the wrong aerosol type or humidity) results in large errors in these cases.

In conclusion, for simulated SCIAMACHY scenes of low optical depth FSI WFM-DOAS V2 performs well, however as AOD increases, the requirement of accurate a priori aerosol data becomes increasingly important. This is particularly true at high SZAs between 60° – 70° (and larger angles). Hence, without suitable aerosol correction, FSI WFM-DOAS retrievals give good performance relative to the 2% level for SZAs less than 60° , and for low to moderate aerosol loadings when the aerosol layer is located in the lowermost layers of the troposphere.

4.3 Simulation 2: Effect of a Basic Aerosol/Cloud Layer

A series of simulations were performed in which a simple, box-like aerosol/cloud layer was generated using SCIATRAN 2.2 in order to quantify the fundamental effects of aerosols and clouds on retrieval errors. SCIATRAN 2.2 affords its users far greater control of aerosol and cloud parameters than SCIATRAN 2.0, enabling the user to explicitly define profiles of extinction and corresponding phase function moments rather than being restricted to predefined aerosol types and secondary parameters such as boundary layer visibility. As a result, parameters governing the physical and optical properties of the scattering layer, outlined in Table 4.3, were systematically varied to cover a range of realistic scattering scenarios up to a limit of $\tau = 1.0$. In the FSI WFM-DOAS V2 retrieval a basic, low optical depth aerosol is assumed, based on the season and whether the satellite scene is classed as a rural or urban location.

For FSI WFM-DOAS V2 retrievals of XCH₄ from SCIAMACHY a strict cloud filter based on the ratio of polarisation measurements is employed to remove cloudy scenes, hence a scene of $\tau = 1.0$ would not normally be processed. However, using the proxy approach retrievals over cloudy scenes can be conducted since, in theory, the effects of cloud contamination should ratio out. The imposed constraint of $\tau = 1.0$ is therefore beyond the strict limits of the existing cloud filter but allows for scenes which may still be processed when utilising the proxy method normalisation. Results from these simulations are intended to be used for the interpretation of results from global sensitivity tests, detailed in Section 4.4, in which realistic aerosol and cloud scenarios of greater complexity were simulated.

4.3.1 Defining a Simple Scattering Layer

Extinction profiles (in units of km⁻¹) were calculated by dividing the optical depth by the scattering layer thickness in km. By default, SCIATRAN 2.2 interpolates extinction profiles between the corresponding user-supplied altitude levels; to ensure the modelled scattering layer possessed clear boundaries, therefore, two additional altitude levels corresponding to zero extinction were defined at a distance of 1×10^{-4} m both below and above the scattering layer.

	Layer top (km)	Simulated optical depth	Surface albedo	SZA (°)	Layer thickness (km)
Aerosol	1, 3, 6, 9	0.01, 0.05, 0.1 0.25, 0.5, 1.0	Grassland, Bare, Wetlands, Evergreen needleleaf forest	20, 60, 70	1.0
Ice cloud	6, 9, 12				

Table 4.3: Physical and optical properties of a simple aerosol/cloud layer for the simulation of spectra using SCIATRAN 2.2. The layer was simulated as 1 km thick in all cases, therefore for the scenario where the aerosol layer top altitude is 1 km, the scattering layer occupies the entire atmospheric region from 1 km down to the Earth’s surface.

Introducing an optically thick scattering layer to the RTM effectively cuts off part of the atmospheric column; the resulting spectrum is therefore only representative of the atmosphere above the scattering layer. Implementing the proxy approach (see Section 1.4.4) to normalise retrieved VCDs involves multiplying by a mean model *total column* CO₂ VMR and thereby assumes that the observed radiation has traversed the entirety of the atmospheric column. As a result, a priori trace gas profiles were set to a constant value of 379 ppm for CO₂ and 1774 ppb for CH₄ to simplify the interpretation of retrieval errors.

4.3.2 Determining the Angstrom Exponent

The Angstrom exponent α describes the wavelength dependence of optical depth and is defined as follows:

$$\alpha = -\frac{\log \frac{\tau_1}{\tau_0}}{\log \frac{\lambda_1}{\lambda_0}} \quad (4.2)$$

As a result, α can be used to calculate the optical depth at a wavelength λ_1 , given the optical depth at a reference wavelength λ_0 :

$$\tau_{\lambda_1} = \tau_{\lambda_0} \left(\frac{\lambda_1}{\lambda_0} \right)^{-\alpha} \quad (4.3)$$

The Angstrom exponent is inversely related to the size of the scattering particle; the larger the exponent, the smaller the particle it describes. The values of τ in Table 4.3 are defined for the CH₄ retrieval window at 1650 nm and therefore must

be scaled by α to obtain the corresponding values of τ for the CO₂ retrieval window centred on 1570 nm. For each of the 9 GEMS aerosol types a global grid of total column optical depth corresponding to wavelengths of 1570 nm and 1650 nm (λ_1 and λ_0 respectively in Equation 4.3) for an arbitrary day in 2004 was used to calculate a corresponding grid of α values. The global mean of α for each aerosol type (see Figure C1) was then used to determine the aerosol optical depth at 1570 nm for the simulation of an aerosol scattering layer in the CO₂ spectral retrieval window.

4.3.3 Results

Figures 4.6a and 4.6b show that for the simulated aerosol scattering layer ΔXCH_4 was always found to be positive (i.e. retrieved XCH₄ was always overestimated with respect to the simulation). Focusing on the high surface albedo case shown in Figure 4.6a the following errors were observed for an aerosol layer simulated at increasing altitudes:

- At 1 km, ΔXCH_4 is very small regardless of optical depth since the light path is only slightly altered from its original trajectory. For this case SZA has very little effect.
- At 3 km, ΔXCH_4 of up to 10% is observed, with a SZA of 60° resulting in marginally higher errors (~ 1–2%) than at a SZA of 20°.
- At 6 km, ΔXCH_4 of up to 20% occurs for a SZA of 20°, with an additional error of ~ 10% for SZAs of 60°.
- At 9 km, ΔXCH_4 of up to ~ 50% is incurred at a SZA of 20° and is doubled for a SZA of 60°, just exceeding 100% at an optical depth of 1.0.

Figure 4.6b shows retrieval errors corresponding to the same set of altitudes and SZAs as shown in Figure 4.6a, but for cases of a lower simulated surface albedo. The same fundamental behaviour as described above is observed in the ΔXCH_4 calculated for the low albedo cases however their magnitude is substantially increased.

The inclusion of a simulated cirrus cloud layer results in a very similar increase of ΔXCH_4 with altitude to the aerosol case since the underlying scattering and subsequent path lengthening/shortening effects are similar for aerosols and cloud. However, Figures 4.7a and 4.7b show that for comparable altitudes, spectra pertaining to cirrus cloud contaminated scenes result in a lower ΔXCH_4 than the corresponding

aerosol cases. This is most likely due to differences between the modelled PFM's for aerosols and clouds.

Figure 4.8 shows the FSI retrieval fit error σ_{XCH_4} (described in Section 2.4.5) plotted against optical depth. Since these simulated spectra do not contain measurement noise, if the retrieval a priori data was perfectly accurate then the retrieval fit would also be perfect and the resulting residual would be zero at every spectral point (hence σ_{XCH_4} would be zero). In the absence of spectral noise therefore, a perfect fit should still be achieved even if significant scaling is required to fit the observed spectrum; the fact that σ_{XCH_4} is non-zero and increases with optical depth suggests that the simulated SCIAMACHY spectrum in either the CO₂ or CH₄ spectral region (or both) becomes increasingly difficult to fit in the FSI retrieval.

Figure 4.10 shows various stages of the FSI WFM-DOAS V2 spectral fit for scenarios where an aerosol layer has been placed at altitudes of 1, 3, 6 and 9 km. To isolate errors caused by increasing the aerosol layer altitude, the scenarios shown all correspond to an optical depth of 1.0, SZA of 20° and the highest surface albedo case (grassland; a=0.34). From comparison of high resolution simulated SCIAMACHY spectra and FSI reference spectra (top panel in each plot) it can be seen that as the altitude of the aerosol layer is increased, the depth of simulated absorption lines decreases with respect to absorption lines in the FSI reference spectrum.

4.3.4 Discussion

The results of Figures 4.6 and 4.10 can be summarised by the following three observations:

1. Trace gas absorption decreases as the altitude of a scattering layer increases.
2. The FSI WFM-DOAS retrieved VCD *underestimates* the true VCD for both CO₂ and CH₄.
3. The FSI WFM-DOAS proxy normalised XCH₄ *overestimates* the true XCH₄.

In the following discussion each of the above observations will be addressed in turn, however first it should be noted that in general the satellite observed intensity is determined by three primary factors; sunlight reflected from the Earth's surface (regulated by surface albedo), sunlight scattered by aerosol/cloud (regulated by

aerosol/cloud optical depth) and the combination of the two. The relative contribution of light reflected by the surface and scattered by the atmosphere is determined by the aerosol/cloud optical depth; the larger the optical depth, the greater the proportion of light scattered at high altitude. Although the following discussion focuses on the aerosol simulation, due to similarities in the scattering behaviour of aerosols and cirrus clouds, the concepts highlighted are equally applicable to the cirrus cloud case.

Decrease of Trace Gas Absorption with Increasing Scattering Layer Altitude

The optical depth of spectral trace gas absorption features is dependent on the photon path length l , the number of absorbing particles n and the absorption cross-section σ , as described by Equation 2.4 (see Section 2.4.1). The changing, mostly decreased intensity, of trace gas absorption lines in simulated spectra as the altitude of the scattering layer is increased can therefore be attributed to a combination of the following effects:

- Change in total atmospheric path length (l)
- Reduced density of absorbing molecules (i.e. reduced n)
- Temperature and pressure dependence of the absorption cross-section (σ)

The primary effect of aerosol scattering is the alteration of photon path length. Path shortening is the result of reflection from the top of a scattering layer. In this instance the aerosol acts as a pseudo surface hence the column traversed by the observed light is cut short; the higher the scattering layer altitude, the greater the reduction of the original photon path length. Path lengthening occurs due to multiple scattering within the aerosol layer and/or between the aerosol layer and the Earth's surface. For an aerosol layer situated between 0–1 km, the spectral comparison shown in Figure 4.10 (second panel from the top) indicates that the simulated spectrum has longer absorption features than the FSI reference spectrum. In this particular case, path lengthening as a result of multiple scattering dominates over the path shortening. For an aerosol layer top height of 3 km, a balance between path shortening and lengthening is achieved whereby the increase in path length due to multiple scattering is largely offset by the overall path length shortening. At 6 km and above, path shortening dominates. The overall path length change is therefore the result of a trade-off between the effects of multiple scattering and direct reflection, with the height at which one effect dominates over the other depending on the

AOD.

The amount of absorption that occurs over a given path is dependent on the density of absorbing trace gas molecules. Although the *concentration* of trace gas molecules is constant throughout the column in these simulations, pressure (and therefore density) decreases exponentially with height. Since there are fewer molecules along a given path length at high altitude than at low altitude, the observed absorption will be reduced.

Finally, as contributing altitudes to the satellite observed absorption change due to path lengthening/shortening, the corresponding pressures and temperatures also vary. Consequently, the absorption cross-section changes with altitude.

Underestimation of the FSI WFM-DOAS V2 Retrieved VCD

Since the light path of photons is generally shortened by the presence of aerosol, in most cases the trace gas absorption features of the simulated spectra will be shallower than in the corresponding FSI reference spectra, and thus relate to a smaller VCD. In order to fit the reduced absorption lines of the simulation, FSI must therefore downscale from the a priori VCD, which corresponds to the entire column, in order to fit the observed spectrum corresponding to the partial column above the scattering layer.

In addition, FSI WFM-DOAS V2 utilises weighting functions calculated by SCIA-TRAN 2.2 which describe the variation of a number of parameters, such as temperature and pressure, at various altitudes and therefore encapsulate the temperature dependence of the absorption cross-sections. As such, the weighting functions characterise the entire atmospheric column, however when aerosol scattering is introduced at high altitude a large proportion of the observed absorption results from molecules above this height. During the FSI WFM-DOAS V2 linear fit the weighting functions are fixed, hence the retrieval can only account for changes in absorption by scaling the VCD. Where the weighting functions correspond to low altitude (high temperature), the VCD will therefore be wrongly scaled to fit the observed absorption (for a high σ_a a smaller VCD is required to account for the same amount of absorption incurred at low σ_a) since in reality the absorption occurs at a high altitude and thus at a lower temperature.

Overestimation of the Proxy Normalised XCH_4

For aerosol of high τ and altitude, the overall photon path length is significantly reduced since the column beneath the scattering layer has been effectively cut off. Given that τ is wavelength dependent, and that CO_2 and CH_4 are retrieved from different spectral windows, the change in path length induced by scattering is slightly different for each trace gas. Although this disparity is the same at any altitude, over a short path length the difference constitutes a greater fraction of the overall path and is therefore more pronounced. FSI WFM-DOAS V2 underestimates the CO_2 VCD by a greater fraction than the CH_4 VCD, hence by employing the proxy approach the *relative* difference between the path length changes incurred at 1570 nm (CO_2) and 1650 nm (CH_4) manifests as an increase in XCH_4 .

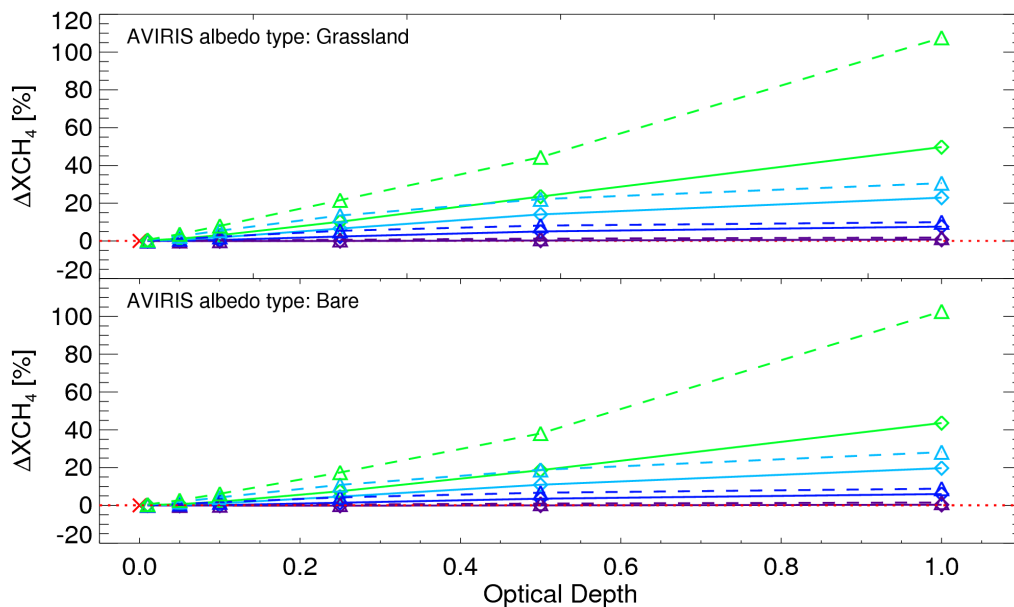
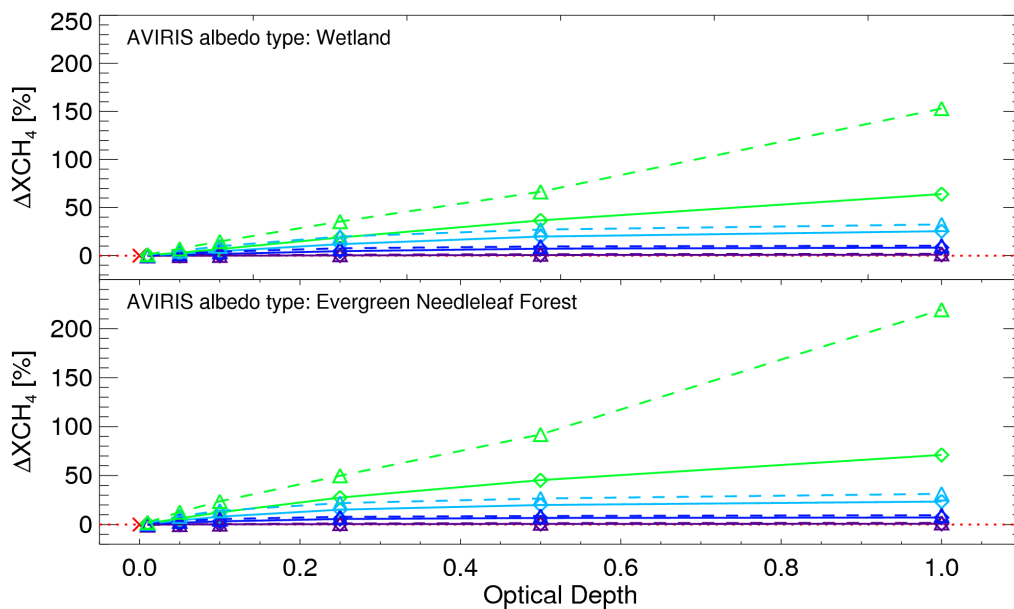
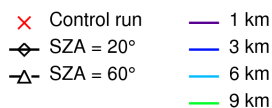
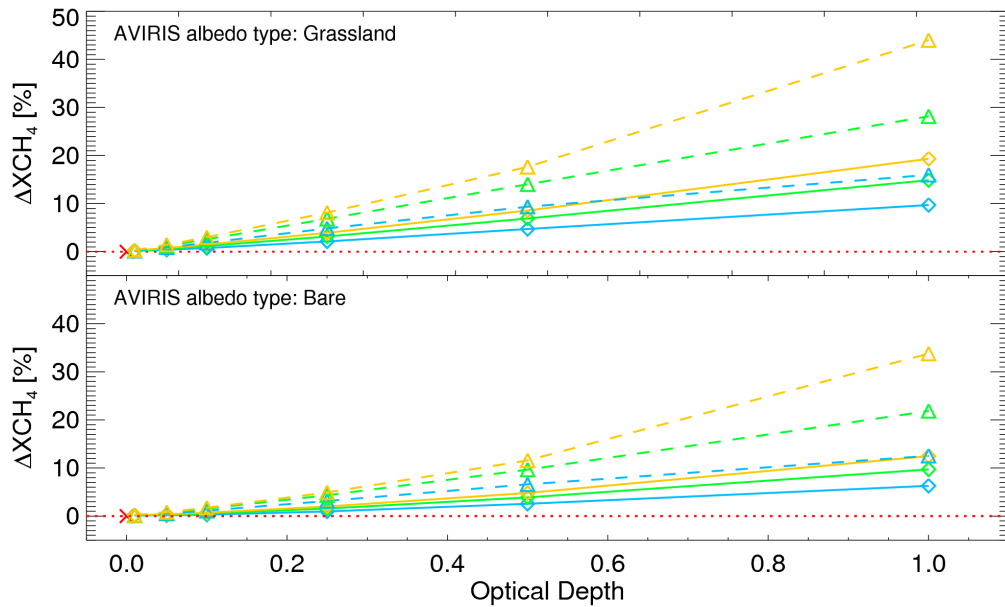
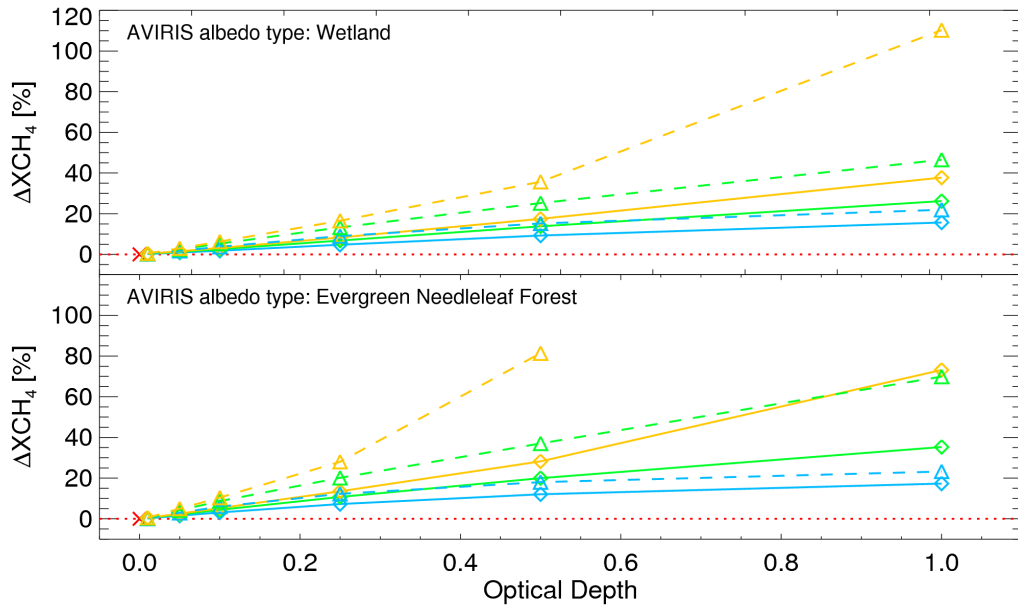
(a) ΔXCH_4 for aerosol scenarios of high albedo.(b) ΔXCH_4 for aerosol scenarios of low albedo.

Figure 4.6: Aerosol basic layer XCH_4 plotted against optical depth for (a) grassland/bare and (b) wetland/evergreen needleleaf forest albedo scenarios. The control run in each case is denoted by a red cross. For reference, a red dotted line indicates where $\Delta XCH_4 = 0\%$.



(a) ΔXCH_4 for cirrus cloud scenarios of high albedo.



(b) ΔXCH_4 for cirrus cloud scenarios of low albedo.

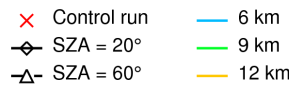


Figure 4.7: Cirrus cloud basic layer XCH_4 plotted against optical depth for (a) grassland/bare and (b) wetland/evergreen needleleaf forest albedo scenarios. The control run in each case is denoted by a red cross. For reference, a red dotted line indicates where $\Delta XCH_4 = 0\%$.

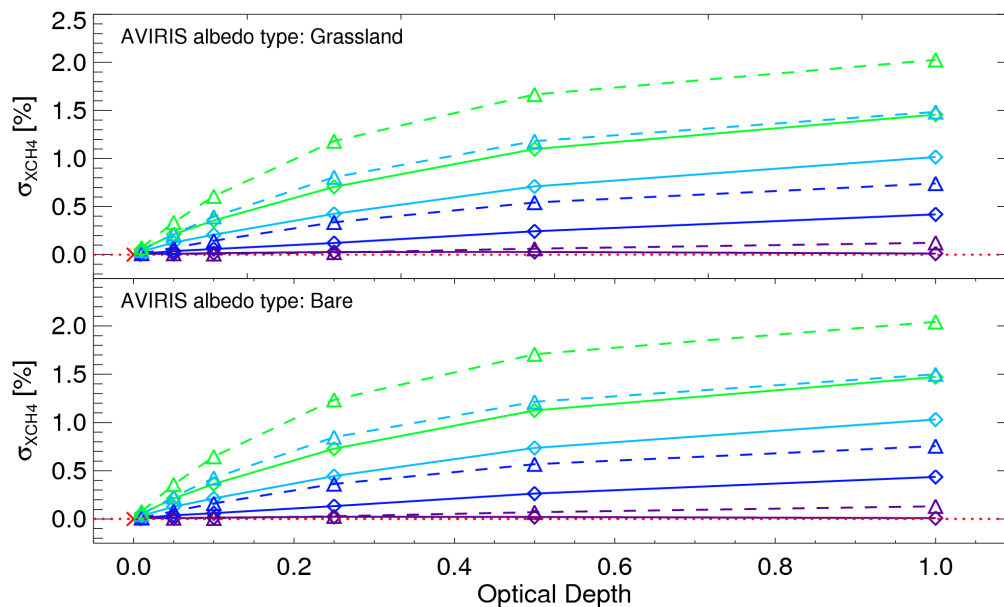
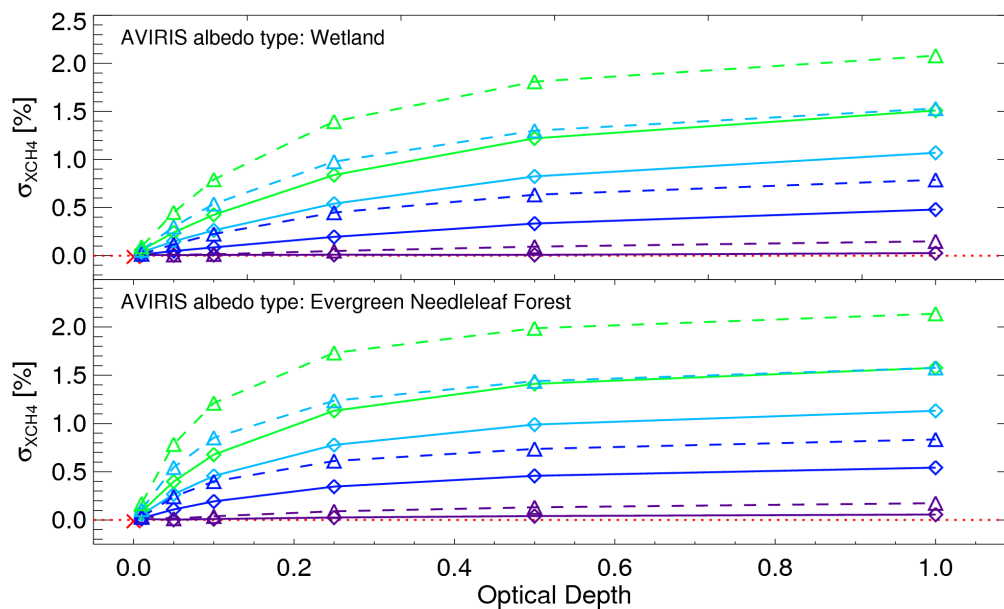
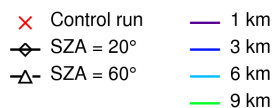
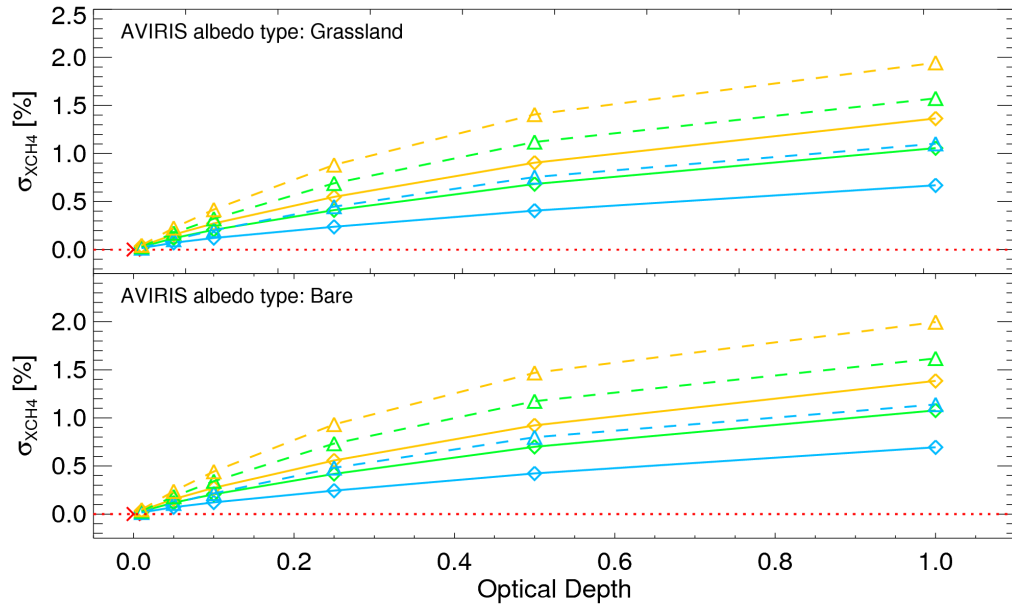
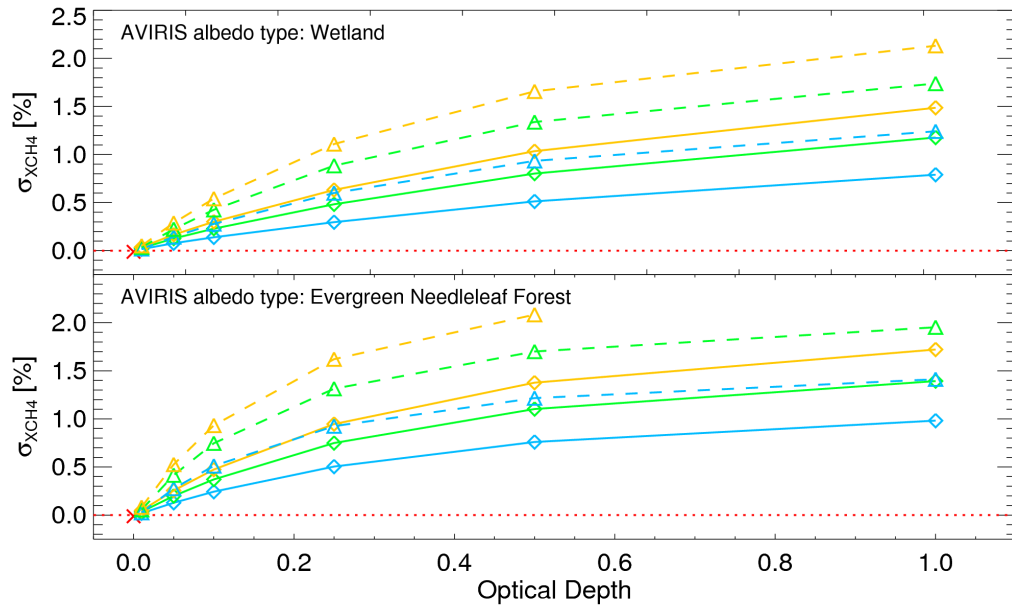
(a) σ_{XCH_4} for aerosol scenarios of high albedo.(b) σ_{XCH_4} for aerosol scenarios of low albedo.

Figure 4.8: Aerosol basic layer σ_{XCH_4} plotted against optical depth for (a) grassland/bare and (b) wetland/evergreen needleleaf forest albedo scenarios. The control run in each case is denoted by a red cross. For reference, a red dotted line indicates where $\sigma_{XCH_4} = 0\%$.



(a) σ_{XCH_4} for cirrus cloud scenarios of high albedo.



(b) σ_{XCH_4} for cirrus cloud scenarios of low albedo.

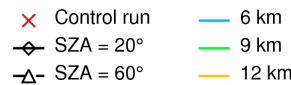


Figure 4.9: Cirrus cloud basic layer σ_{XCH_4} plotted against optical depth for (a) grassland/bare and (b) wetland/evergreen needleleaf forest albedo scenarios. The control run in each case is denoted by a red cross. For reference, a red dotted line indicates where $\sigma_{XCH_4} = 0\%$.

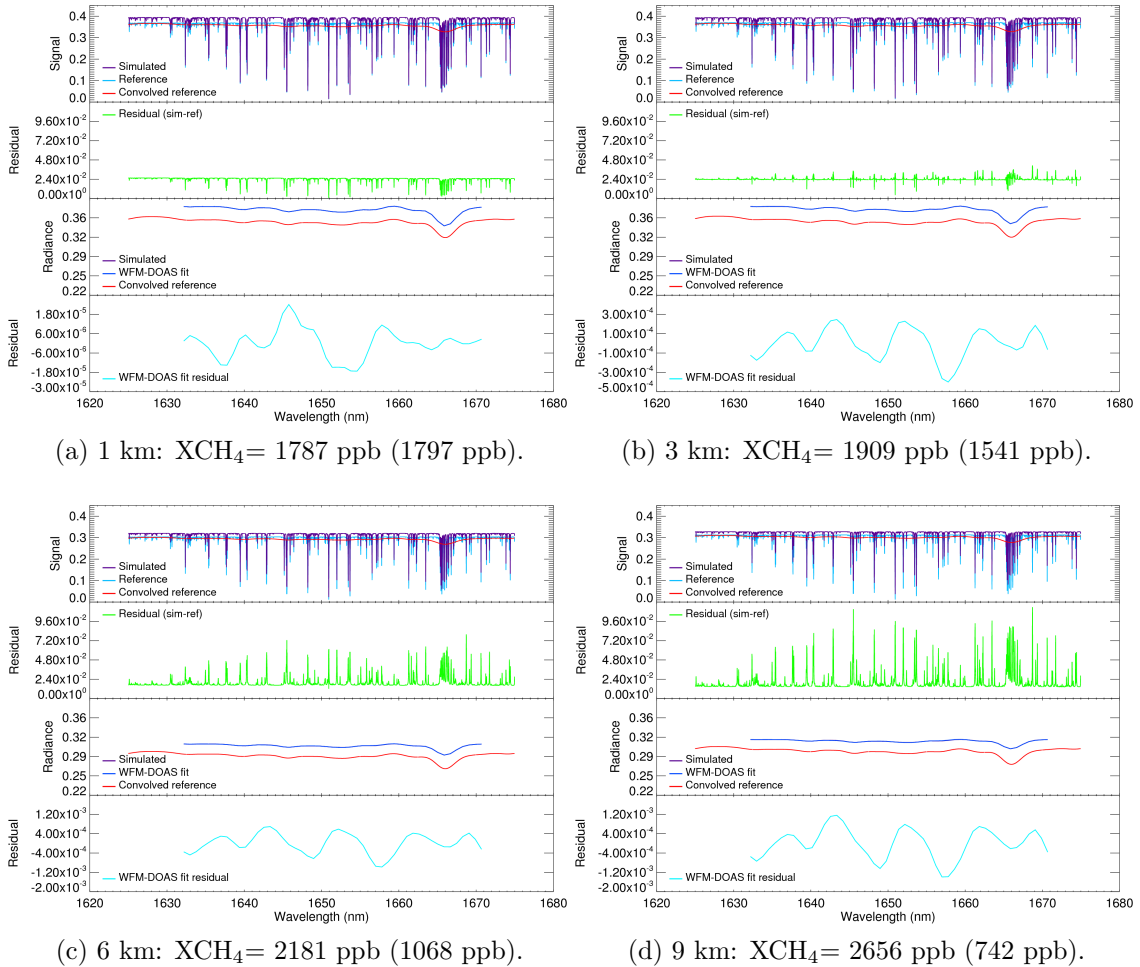


Figure 4.10: Spectral comparison for an aerosol layer simulated at altitudes of (a) 1 km, (b) 3 km, (c) 6 km and (d) 9 km. In all cases $\tau = 1$, $SZA = 20^\circ$ and surface albedo = 0.34 (AVIRIS grassland). In each plot, the top panel shows the high resolution simulated SCIAMACHY spectrum, the high resolution FSI reference spectrum and the convolution of the reference spectrum with the SCIAMACHY instrument line shape. The second panel shows the difference between the high resolution simulated and reference spectra. The third panel shows the convolved simulated and reference spectra along with the WFM-DOAS fit (the simulated spectrum is overlaid by the WFM-DOAS fit). The fourth panel shows the RMSE residual of the WFM-DOAS fit. In each case the proxy method normalised XCH_4 is given, along with the surface pressure normalised XCH_4 in brackets.

4.3.5 Summary of Simulation 2

FSI WFM-DOAS V2 retrievals of simulated SCIAMACHY scenes of systematically varied altitude, SZA and surface albedo reveal that the altitude at which scattering occurs has a significant impact on the magnitude of ΔXCH_4 . In particular, the presence of aerosols above 3 km results in an overestimation of the retrieved column by upwards of 10%. Moreover, at increasing altitudes the importance of SZA is greatly increased; scenes with a SZA of 60° generally result in a doubling of the ΔXCH_4 incurred for simulations at 20° . Low surface albedo values also adversely affect the magnitude of retrieval errors. Retrievals for scenes in which a cirrus cloud layer has been simulated display similar behaviour to the aerosol case, but result in lower errors for comparable scattering layer altitudes. For both cases, the retrieval errors also increase rapidly with low to moderate aerosol optical depths, indicating that higher retrieval errors are related to the presence of aerosols and clouds in the observed scene.

The addition of a scattering layer (whether aerosol or ice cloud) alters the light path of the observed radiation, thus changing the magnitude of the observed absorption features. In order to fit a SCIAMACHY spectrum which has been modified by scattering, the FSI retrieval has to down-scale the reference spectrum (i.e. the retrieved scaling factor is less than 1 for both CO_2 and CH_4), resulting in a reduction of the retrieved VCD with respect to its a priori value. Employing the proxy approach to normalise the retrieved VCD, however, results in an *overestimation* of XCH_4 which can be substantial. Overestimation occurs because the *relative* decrease in the retrieved CH_4 VCD is smaller than in the retrieved CO_2 VCD; by taking the ratio in Equation 1.9 this relative difference manifests itself as an apparent increase in the resulting XCH_4 .

4.4 Simulation 3: Global Aerosol and Cloud Sensitivity Tests

Global SCIAMACHY simulations were performed for realistic aerosol and ice cloud scenarios in order to ascertain which regions of the world are most affected by retrieval errors due to scattering of this nature. To ensure that the spectra simulated in this study adequately represented the diversity of atmospheric conditions encountered around the globe, a number of parameters had to be realistically simulated, such as topography, surface albedo and SZA, as well as having to take the typical equatorial overpass time of SCIAMACHY (10:00 am local time) into consideration. To correctly model the global aerosol and cirrus cloud distributions with SCIA-TRAN 2.2, profiles of atmospheric extinction were created using aerosol and cloud ice water content mass mixing ratios (MMR), in units of $\text{kg kg}_{\text{air}}^{-1}$, defined on 60 model (sigma) levels from GEMS. SCIAMACHY spectra were simulated on a $1.125^\circ \times 1.125^\circ$ grid in order to be consistent with the resolution of both ECMWF and GEMS data, thereby avoiding any unnecessary interpolation. Any grid locations over the ocean were automatically discarded from the analysis, since poor reflectivity from the sea surface renders the majority of ocean observations unsuitable for retrieval purposes (unless low, thick cloud is present, providing a reflective pseudo ‘surface’, or sun-glint causes sufficient light to be reflected). Solar zenith angles were accurately calculated according to each simulation location and date, and surface albedo was simulated by associating AVIRIS albedo data with the land-cover type from the Medium Resolution Imaging Spectrometer (MERIS) for each grid location.

Simulations were carried out for the first day of January, April, July and October of 2004 in order to encompass a range of atmospheric scenarios across the four seasons. In order to distinguish retrieval errors due to aerosols and ice clouds from those due to other parameters the following separate simulations were performed for each of the four days:

- Background: No aerosol or clouds simulated (control run).
- Aerosol: Aerosol only simulated- no clouds.
- Ice cloud: Ice cloud only simulated- no aerosol.
- Aerosol and ice clouds: Both aerosol and ice clouds simulated.

4.4.1 Simulation of Atmospheric Aerosol

GEMS aerosol MMR profiles were available for five main aerosol species; sea salt (SS), desert dust (DD), organic matter (OM), black carbon (BC) and sulphate (Su). Mass mixing ratios for both sea salt and desert dust were defined for three distinct particle size bins, whereas those for organic matter and black carbon were available in both hydrophilic (water soluble) and hydrophobic (water repellent) variations, bringing the total number of available GEMS aerosol types to 11. This section describes how GEMS profiles of MMR were converted into extinction and absorption for the simulation of SCIAMACHY spectra using SCIATRAN 2.2 and also describes the calculation of aerosol phase function moments which characterise the angular scattering distribution.

Relative Humidity

Specific humidity (SH) is defined as the ratio of water vapour to air (which includes both water vapour and dry air) within a given air mass and is among the meteorological parameters available from GEMS. SH is independent of other meteorological factors such as pressure and temperature however relative humidity (RH) takes these additional factors into account.

Mass Mixing Ratio to Extinction

The conversion of GEMS aerosol MMR [$\text{kg kg}_{\text{air}}^{-1}$] to optical depth, τ , requires the use of a mass extinction coefficient, k_{λ} [$\text{m}^2 \text{g}^{-1}$], which is dependent on wavelength (λ) and in some cases RH, which is itself dependent on pressure, p . Values of k_{λ} for each of the 11 GEMS aerosol types were obtained via email correspondence with Jean-Jaques Morcrette from the GEMS project and are given for 19 different wavelengths from 340-2130 nm. For aerosols affected by atmospheric humidity (sea salt, organic matter and sulphate), k_{λ} is defined for 12 different relative humidity values at each of the 19 wavelengths. For each atmospheric layer, a profile of k_{λ} corresponding to the specific retrieval λ was interpolated to the RH corresponding to the layer, creating a profile of k_{λ} for each GEMS aerosol type at each grid point. Plots showing profiles of k_{λ} for each of the 5 GEMS aerosol species (SS, DD, OM, BC, Su), indicating values interpolated to retrieval wavelengths, can be found in Appendix C.

By dividing the atmosphere into layers, and denoting the pressure across each layer as dp , the total column τ for each aerosol species i is obtained using the following

formula:

$$\tau_{\lambda i} = \int_{p_{\text{surf}}}^0 k_{\lambda i}(\text{RH}(p)) M_i(p) \left(\frac{dp}{g} \right). \quad (4.4)$$

The AOD for the four days simulated in this study is shown in Figure 4.11. Optical depth is simply the integral of extinction κ_e over the atmospheric column, from the surface at a pressure of p_{surf} up to the TOA where pressure tends to $p = 0$. Omitting the integral over pressure in Equation 4.4 therefore gives $\kappa_e(\lambda)$ for each aerosol type in units of reciprocal pressure Pa^{-1} :

$$\kappa_e(\lambda) = \frac{\tau_\lambda}{p_{\text{surf}}} = k_\lambda(\text{RH}(p)) \frac{M(p)}{g}. \quad (4.5)$$

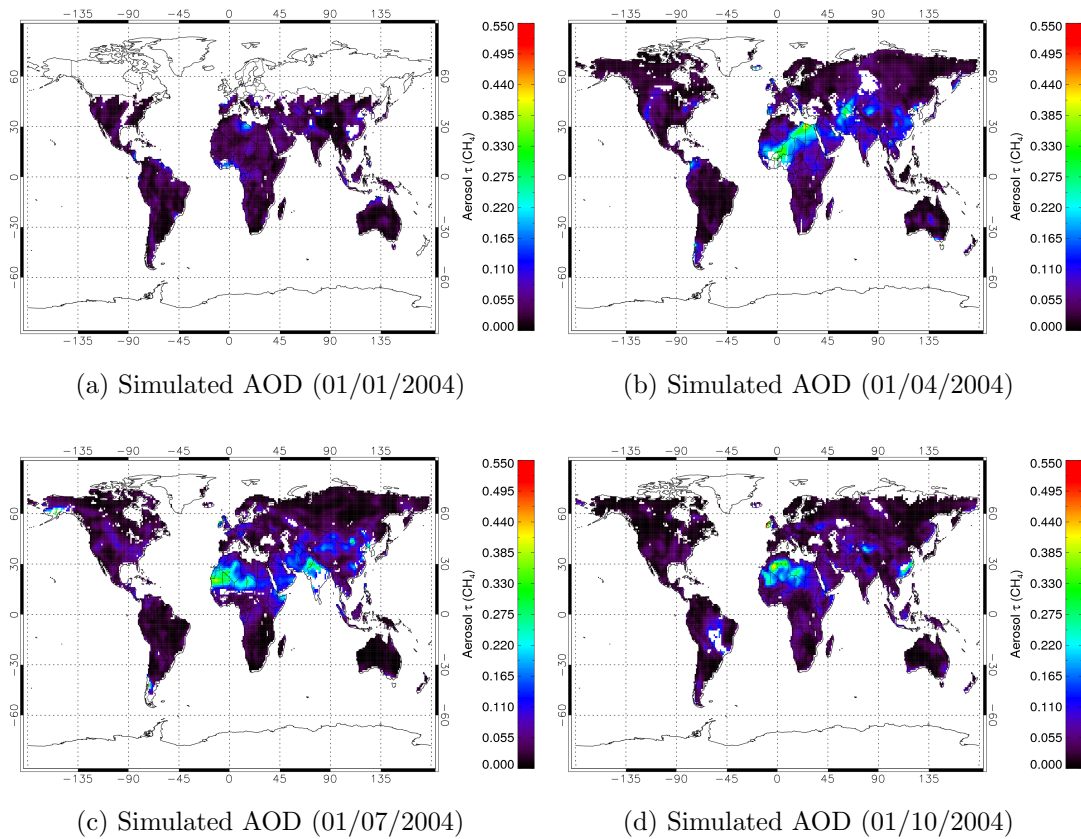


Figure 4.11: AOD simulated at 1650 nm, calculated from GEMS aerosol MMR for the first day of months January, April, July and October 2004. Data is given on a $1.125^\circ \times 1.125^\circ$ grid.

For κ_e in units of km^{-1} , τ must be divided by the length of the column l in km:

$$\kappa_e(\lambda) = \frac{\tau_\lambda}{l}. \quad (4.6)$$

Phase Function Moments

As described in Section 2.4.1 particles scatter light differently depending on their size. For aerosols, particle radius is either greater than or around the same scale as the wavelength of light in the SWIR therefore Mie scattering occurs (see Section 2.4.1 for a more detailed description). For simplicity, in this simulation it has been assumed that the particles of each aerosol type are spherical, therefore Mie theory [Mishchenko et al. (2002)] (which describes scattering by small spheres) was used to characterise aerosol phase functions (see Section 2.5.4). To calculate the Mie scattering properties of each aerosol type, parameters describing the particle size distribution and the refractive indices for the wavelength range of interest were required. Parameters defining the log-normal particle size distributions corresponding to the 11 GEMS aerosol types are shown in Table 2.1 in Section 2.

Both the real (n) and imaginary (k) components of the refractive index (which describe scattering and absorption respectively) for the wavelength region of interest were required for Mie scattering calculations. For sea salt and sulphate, n was calculated for 8 RH values (0%, 50%, 70%, 80%, 90%, 95%, 98% and 98%). For non-RH dependent aerosol types, n was taken from Shettle and Fenn (1979) for desert dust and soot (the latter used in place of black carbon) and was set to a constant value of $n = 1.46$ for organic matter, following the example of Schmid (2008).

Only one aerosol extinction profile was required per scene, created by summing the κ_e contributions from the 11 different GEMS aerosol types. Similarly, phase function moments for each of the aerosol types were combined. However, since different aerosol types are not present in equal quantities, and phase function moments themselves contain no information concerning their relative concentrations, the contribution of each aerosol type to the resulting mean phase function moment was weighted by the scattering component of the aerosol extinction, κ_s .

4.4.2 Simulation of Ice Clouds

Ice clouds were defined by their optical depth, altitude and base/top height, all of which were determined from GEMS profiles of cloud IWC, in addition to phase

function moments extracted from a precalculated database. For this study, any scenes possessing a combined total column aerosol and cloud optical depth of greater than 1 (i.e. $\tau_{\text{tot}} = \text{AOD} + \text{COD} > 1$) were discarded, since in reality cases of such high τ would be cloud-flagged and subsequently ignored in the retrieval [see Barkley (2007) for further details of the cloud filtering procedure employed by FSI WFM-DOAS]. GEMS profiles of IWC cover a range of altitudes from 0–20 km and therefore describe cases of low lying ice clouds and fog as well as high altitude cirrus clouds.

Calculating Inner-Cloud IWC

GEMS cloud IWC is provided on a set grid and parameters can generally be assumed to be homogeneously distributed across each grid box. In reality, cloud extent and structure is inherently inhomogeneous, especially on the scale of a typical GEMS grid box ($1.125^\circ \times 1.125^\circ$). The cloud cover fraction F_C is a measure of the extent to which the cross-sectional area of an atmospheric layer is obscured by cloud. The GEMS cloud IWC, denoted here as C_{GEMS} , represents the inner-cloud or cloud concentrated IWC, C_{conc} , weighted by the cloud cover fraction and is therefore representative of the cloud content over a whole grid box:

$$C_{\text{GEMS}} = C_{\text{conc}} F_C. \quad (4.7)$$

In effect, each cloud has been effectively ‘smeared out’ across the atmospheric layer to take into account the fact that cloud does not cover the entire grid box. To recover the original cloud concentrated value C_{conc} , C_{GEMS} must simply be divided by F_C .

Within this sensitivity test, simulated spectra are based on several input parameters, such as SZA and surface albedo, which correspond to a specific geographical location. Although parameters from GEMS correspond to an entire grid box, in the majority of cases these values are also valid for a singular location. For clouds however this poses a problem; C_{conc} is not representative of a grid box and would result in a hugely overestimated global cloud cover if used for this purpose. As a result, C_{GEMS} is employed in Equation 2.41 for the calculation of extinction whereas C_{conc} is used for the determination of cloud parameters which are dependent on IWC (in particular r_e) to ensure that physically realistic values are obtained.

GEMS cloud IWC has units of $\text{kg kg}_{\text{air}}^{-1}$ therefore a conversion to the standard units

of g m^{-3} was required to ensure that IWC was in the correct format for calculations of extinction. To achieve this, firstly the number of molecules in a volume 1 m^3 of air N_{air} for each layer was found:

$$N_{\text{air}} = \frac{P}{kT}, \quad (4.8)$$

where P and T denote layer pressure and temperature respectively and k is Boltzmann's constant. The mass of air in a volume 1 m^3 , M_a , is then given by:

$$M_a = \frac{N_{\text{air}} m_{\text{air}}}{1 \times 10^3 N_a}, \quad (4.9)$$

where $m_{\text{air}} = 28.96443 \text{ g mol}^{-1}$ is the molecular weight of air and N_a is Avagadro's constant. IWC in units of g m^{-3} is therefore related to IWC in units of $\text{kg kg}_{\text{air}}^{-1}$ as follows:

$$C[\text{g m}^{-3}] = 1 \times 10^3 C[\text{kg kg}_{\text{air}}^{-1}] M_a, \quad (4.10)$$

where C denotes cloud IWC and the factor of 1×10^3 converts the numerator from units of kg to g.

Cloud Grouping

A single GEMS profile may contain several layers containing cloud ice separated by regions where $\text{IWC} = 0.0$. Clouds are therefore defined here by grouping layers of similar cloud coverage together, e.g. layer i is assigned to a cloud group if the cloud cover fraction of that layer is within 0.2 of the cloud cover fraction in the layer $i - 1$ beneath:

$$f_{c(i)} \leq f_{c(i-1)} \pm 0.2. \quad (4.11)$$

Any abrupt change in cloud cover between adjacent layers is therefore taken to indicate the start of a new cloud, providing that $f_{c(i)} \neq 0$.

Internal Cloud Structure

For each individual cloud SCIATRAN 2.2 requires the profile of a dimensionless height variable z which describes the relative position of each cloud sub-layer, at height h , in relation to the cloud base:

$$z = \frac{(h_{\text{top}} - h)}{(h_{\text{top}} - h_{\text{base}})}. \quad (4.12)$$

Each cloud was defined by at least three values of z ; a base, centre and top. However, if a cloud consisted of a single layer the required parameters were only available for one value of z , corresponding to the centre of the atmospheric layer. In order to create the accompanying cloud top and base levels, the two bordering GEMS half-level pressures (see Section 3.3.6 for a description) were converted into altitude and appended to either side of the available level.

Optical Depth

Ice cloud total column optical depth (shown in Figure 4.12) was determined by calculating the ice cloud extinction from GEMS IWC (using Equation 2.41 in Section 2.6.1) and then summing over atmospheric layers as defined by GEMS model levels and their half-level boundaries. The result of filtering out all scenes where ice cloud optical depth exceeded 1.0 is shown in Figure 4.13. During the creation of SCIAMTRAN cloud profiles, layers of very low optical depth were discarded, changing the resulting total column optical depth. To ensure that the sum of optical depths of individually defined SCIAMTRAN clouds equalled the original GEMS calculated value, each SCIAMTRAN cloud in a given atmospheric column was attributed a fraction of the total column optical depth weighted by its vertical height (i.e. cloud top minus cloud base).

Cloud Phase Function Moments

Cirrus clouds generally consist of highly non-spherical, columnar ice crystals [Liou (1986)] therefore Mie theory cannot be used to determine the scattering properties of particles in this case. Instead, pre-computed cirrus cloud scattering phase functions [Baum (2010)] available for 18 values of D_e were used. For each cloud, the mean D_e of the constituent particles was calculated and then the scattering phase function corresponding to the nearest matching value of D_e was associated with it. Scattering phase functions for each of the 18 values of D_e were defined for 498 scattering angles, from 0 to 180°, and were converted to Legendre phase function moments* for input to SCIAMTRAN 2.2. Legendre moments, L_{PFM} , of an arbitrary function are defined in

*Performed using procedure ‘pmom.pro’ available from:
<http://www.astro.washington.edu/docs/idl/htmlhelp/slibrary28.html>

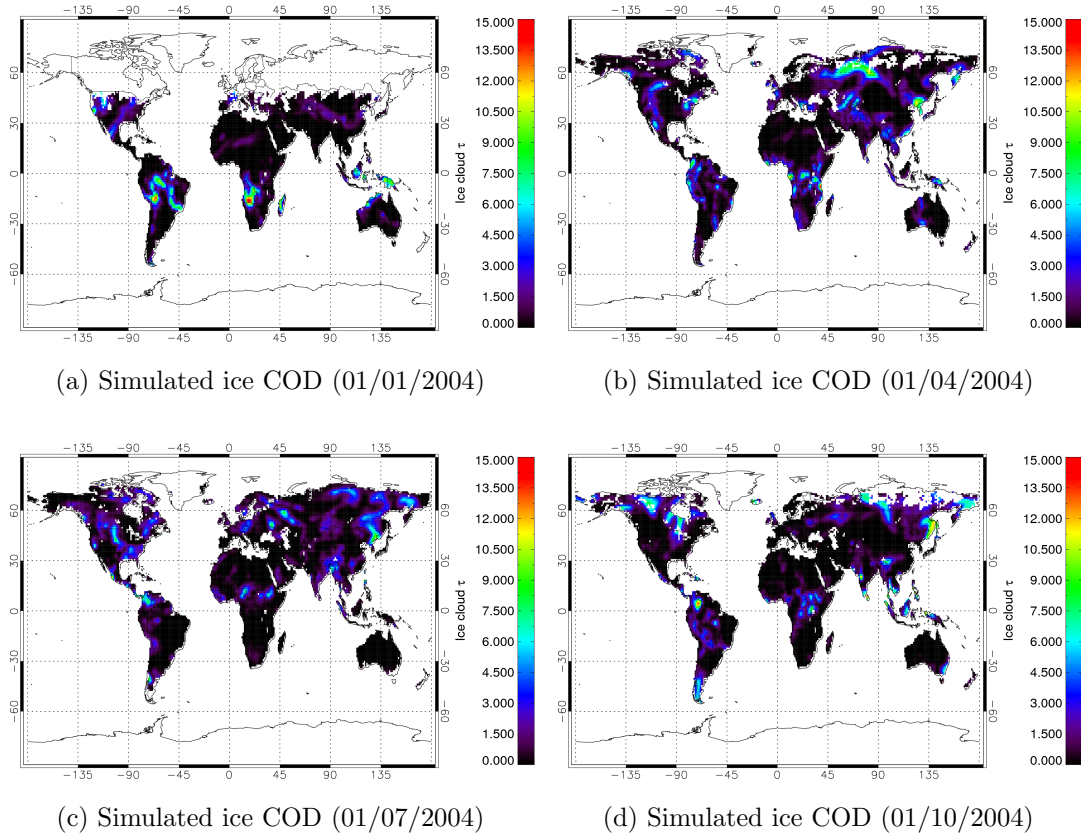


Figure 4.12: Simulated ice COD calculated from GEMS cloud ice MMR. Data is gridded on a $1.125^\circ \times 1.125^\circ$ scale.

the range -1 to 1, as follows:

$$L_{\text{PFM}}(i) = \frac{\int_{-1}^{-1} f(\phi)P(i, \phi)d\phi}{\int_{-1}^1 f(\phi)d\phi}, \quad (4.13)$$

where $P(i, \phi)$ is the Legendre polynomial, f is the scattering phase function and ϕ is the cosine of the scattering angle (in the range -1 to 1). It should be noted that the accuracy of the integration is dependent on the number of scattering angles for which the phase function is defined.

4.4.3 Trace Gas Profiles

Global maps of XCO_2 and XCH_4 corresponding to profiles used for simulation of SCIAMACHY spectra for each of the four seasons are shown in Figures 4.14 and 4.15 respectively.

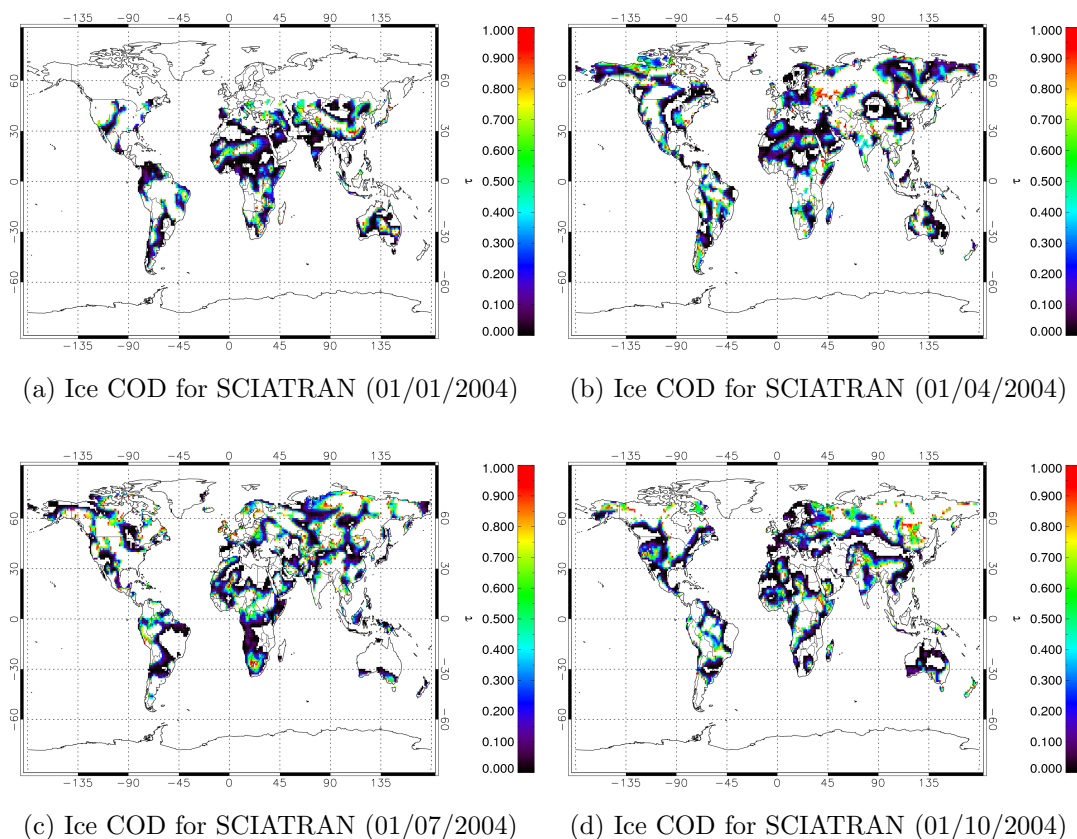


Figure 4.13: Ice COD corresponding to user defined SCIATRAN 2.2 cloud profiles. Data is gridded on a $1.125^\circ \times 1.125^\circ$ scale.

4.4.4 Surface Albedo

Surface albedo data from AVIRIS spanning the wavelength range $0.4\text{--}2.5 \mu\text{m}$ was available for the following surface types; Bare, Closed shrubs, Croplands, Deciduous broadleaf forest, Deciduous needleleaf forest, Evergreen broadleaf forest, Evergreen needleleaf forest, Grassland, Mixed forest, Open shrubs, Savanna, Wetlands and Woody savanna. MERIS land cover data (reclassified to match AVIRIS albedo types and regridded to $1.125^\circ \times 1.125^\circ$) was then used to correctly match the surface albedo files to different global regions. Separate albedo values were obtained for the CO_2 and CH_4 retrievals by interpolating the albedo data to the central wavelength of the respective spectral fitting windows. Scenes allocated with a MERIS land cover type of ocean, inland water, ice or snow were ignored.

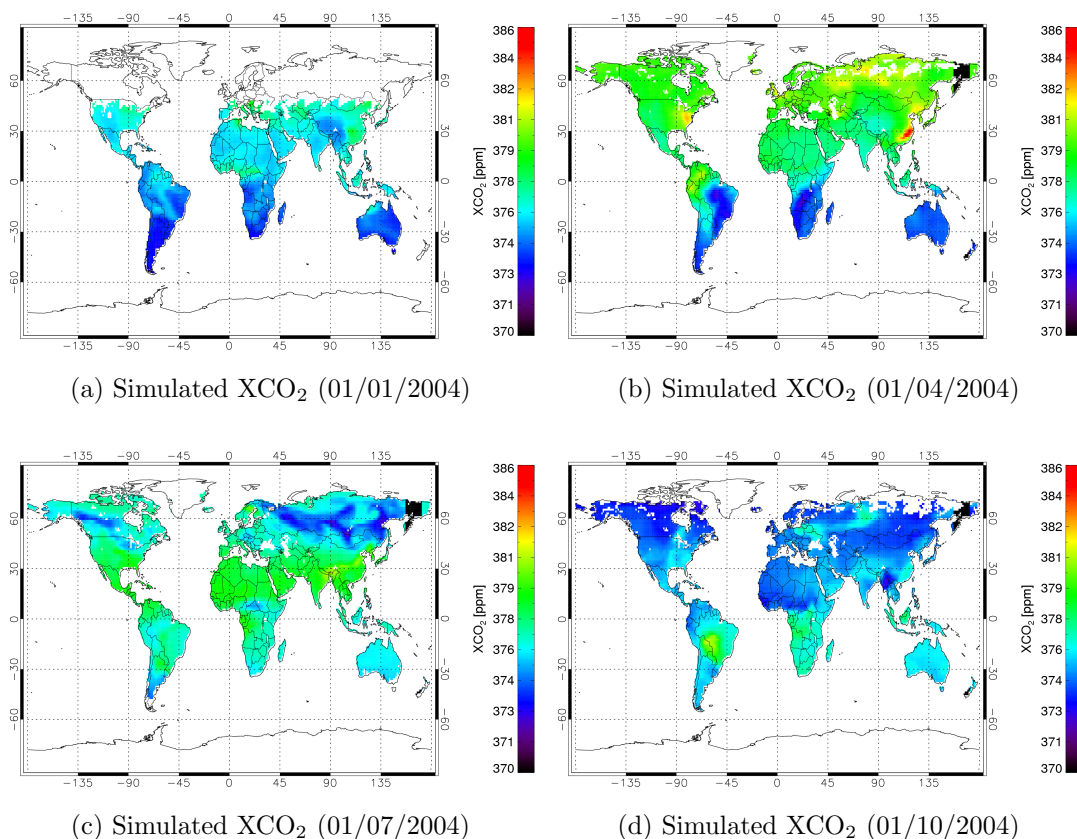


Figure 4.14: Global XCO₂ calculated from CarbonTracker profiles used for the simulation of SCIAMACHY spectra for January, April, July and October 2004. Data is gridded on a $1.125^\circ \times 1.125^\circ$ scale.

4.4.5 UTC Time Zones

To standardise time keeping around the world the globe is split into 24 major time zones which each differ by one hour and approximately correspond to a 15° increment in longitude. UTC is referenced from the time zone centred at 0° longitude and all other major UTC time zones are defined by an integer hour offset from this point.

When using global model data, for example from ECMWF or GEMS, the data is often defined for a specific time which corresponds to the UTC reference time at 0° longitude. A dataset corresponding to 12:00 midday therefore actually contains data that spans local times from 00:00 the same day at a longitude of -180° , to 00:00 of the following day approaching a longitude of 180° . As a result, data in each time zone was interpolated to a local time of 10:00 in order to correspond to the time of a typical SCIAMACHY overpass (see Section 3.1.2).

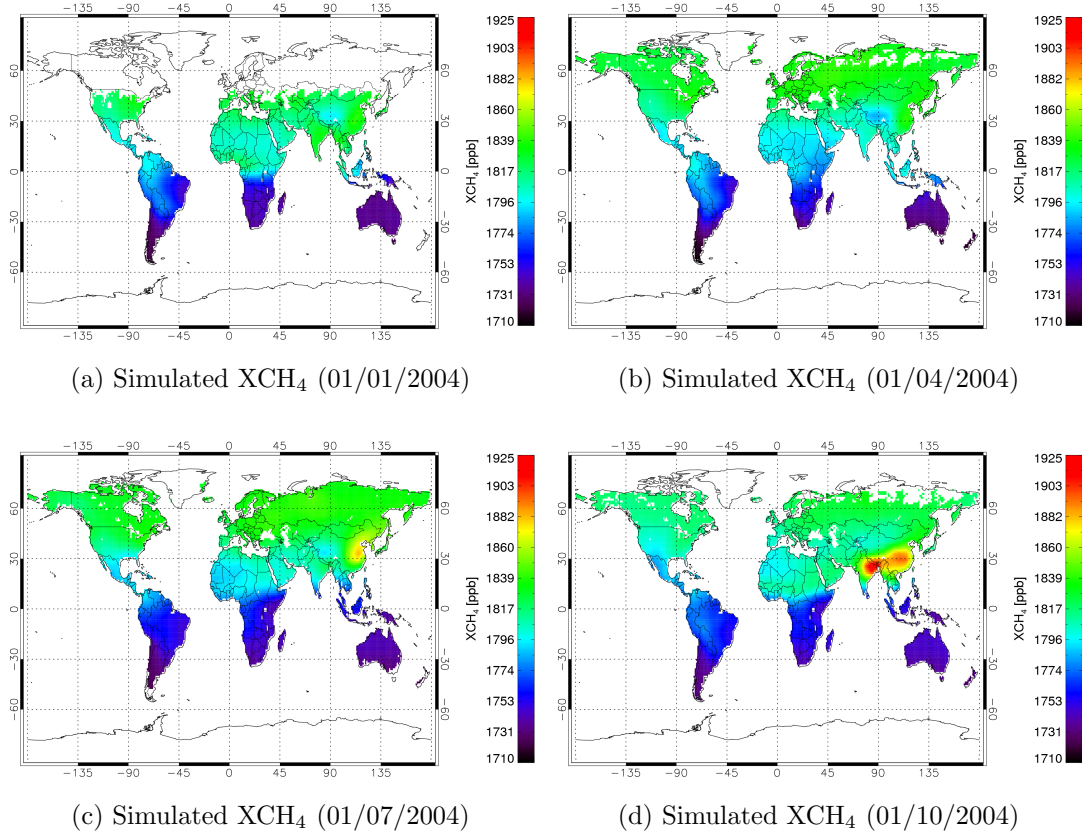


Figure 4.15: Global XCH₄ calculated from TM3 profiles used for the simulation of SCIAMACHY spectra for January, April, July and October 2004. Data is gridded on a $1.125^\circ \times 1.125^\circ$ scale.

4.4.6 Results

Figures 4.16 to 4.19 show the retrieved XCH₄ on the left and the corresponding Δ XCH₄ on the right for each of the separate simulation types (background, aerosol, ice cloud and combined aerosol and ice cloud). The colour bar for plots of Δ XCH₄ was specifically designed to emphasise regions where Δ XCH₄ is within 1% of the global mean XCH₄ for 2005 (i.e. ~ 17.74 ppb) by highlighting such regions in white. Column overestimation is depicted in red and yellow whereas column underestimation is shown in green and blue. Black areas over land represent regions where the total simulated optical depth exceeded 1 and was therefore discarded from the simulation.

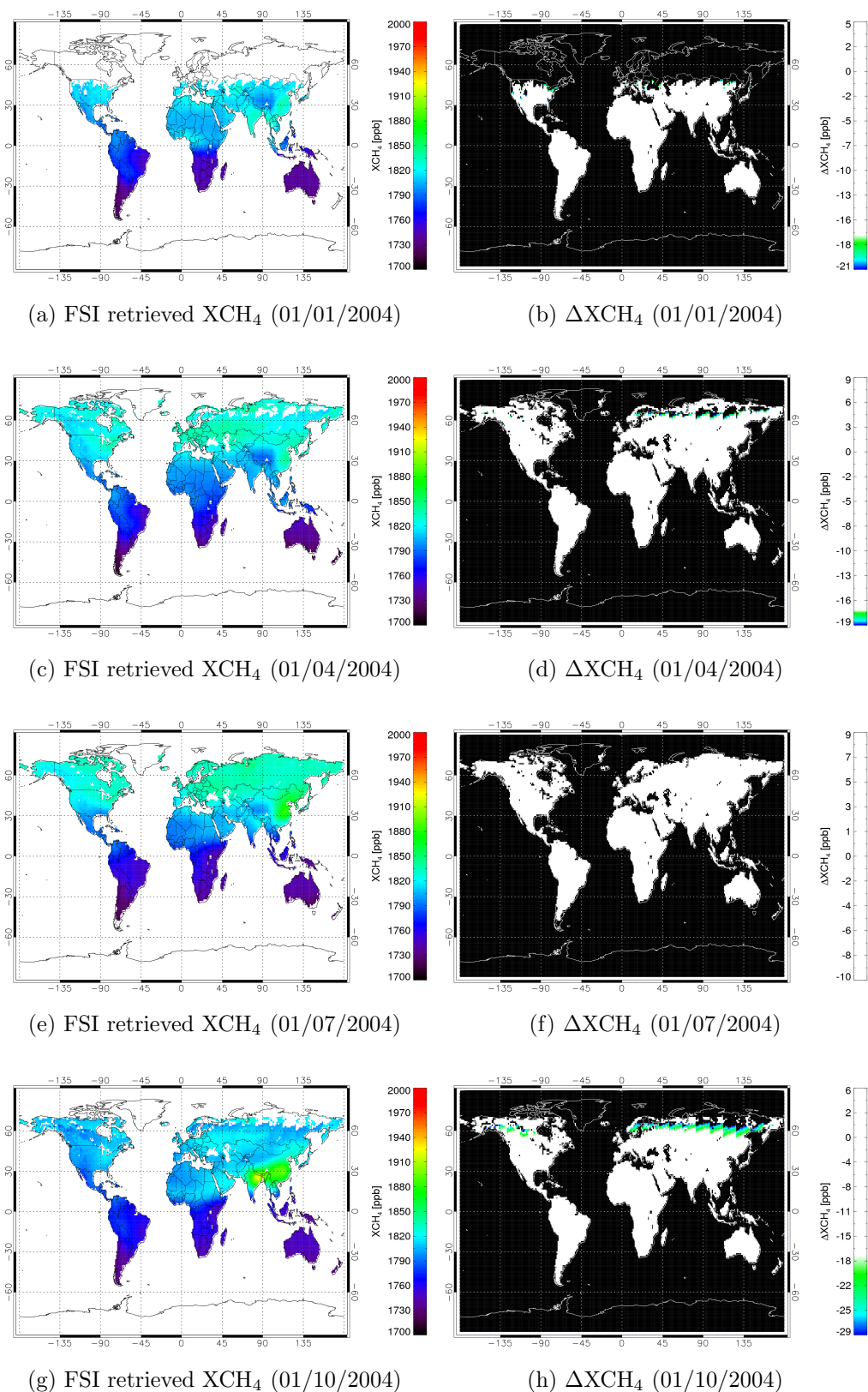


Figure 4.16: Retrieved XCH₄ (left) and ΔXCH₄ (right) for a background scenario, simulated for the first day of months January, April, July and October 2004 (top to bottom). Data is gridded on a 1.125° × 1.125° scale.

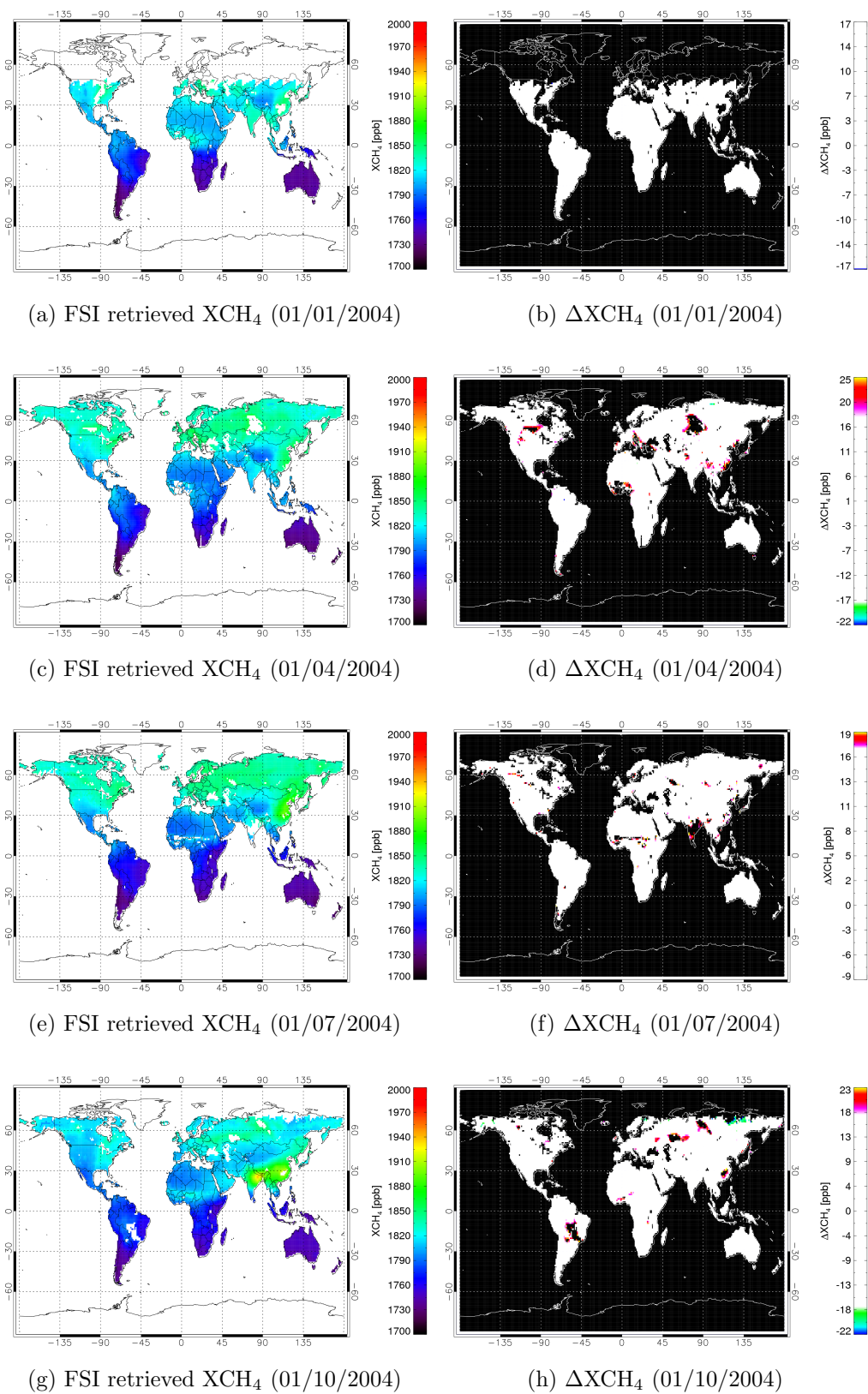


Figure 4.17: Retrieved XCH_4 (left) and ΔXCH_4 (right) for the aerosol scenario, simulated for the first day of months January, April, July and October 2004 (top to bottom). Data is gridded on a $1.125^\circ \times 1.125^\circ$ scale.

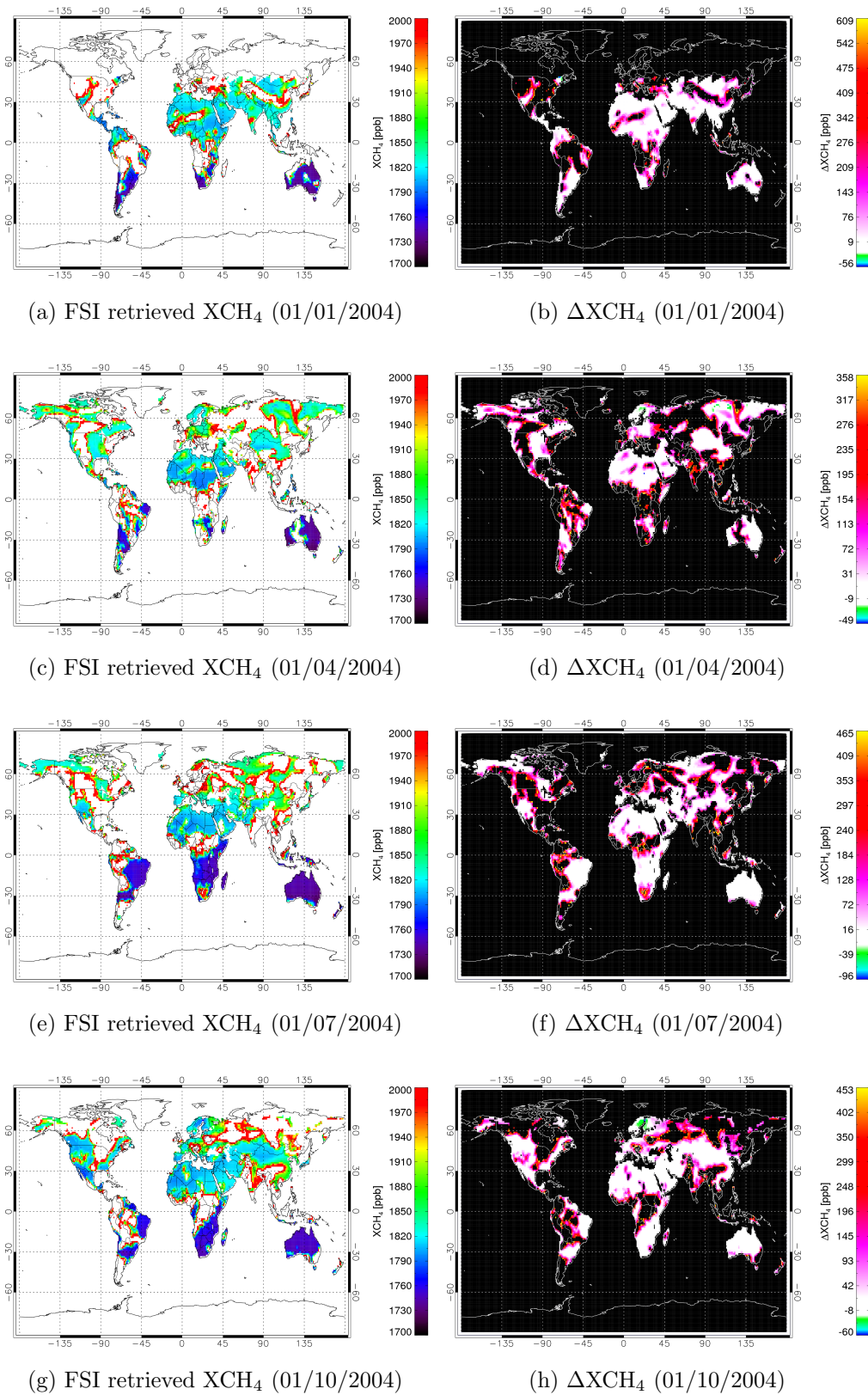


Figure 4.18: Retrieved XCH_4 (left) and ΔXCH_4 (right) for a cirrus cloud scenario, simulated for the first day of months January, April, July and October 2004 (top to bottom). Data is gridded on a $1.125^\circ \times 1.125^\circ$ scale.

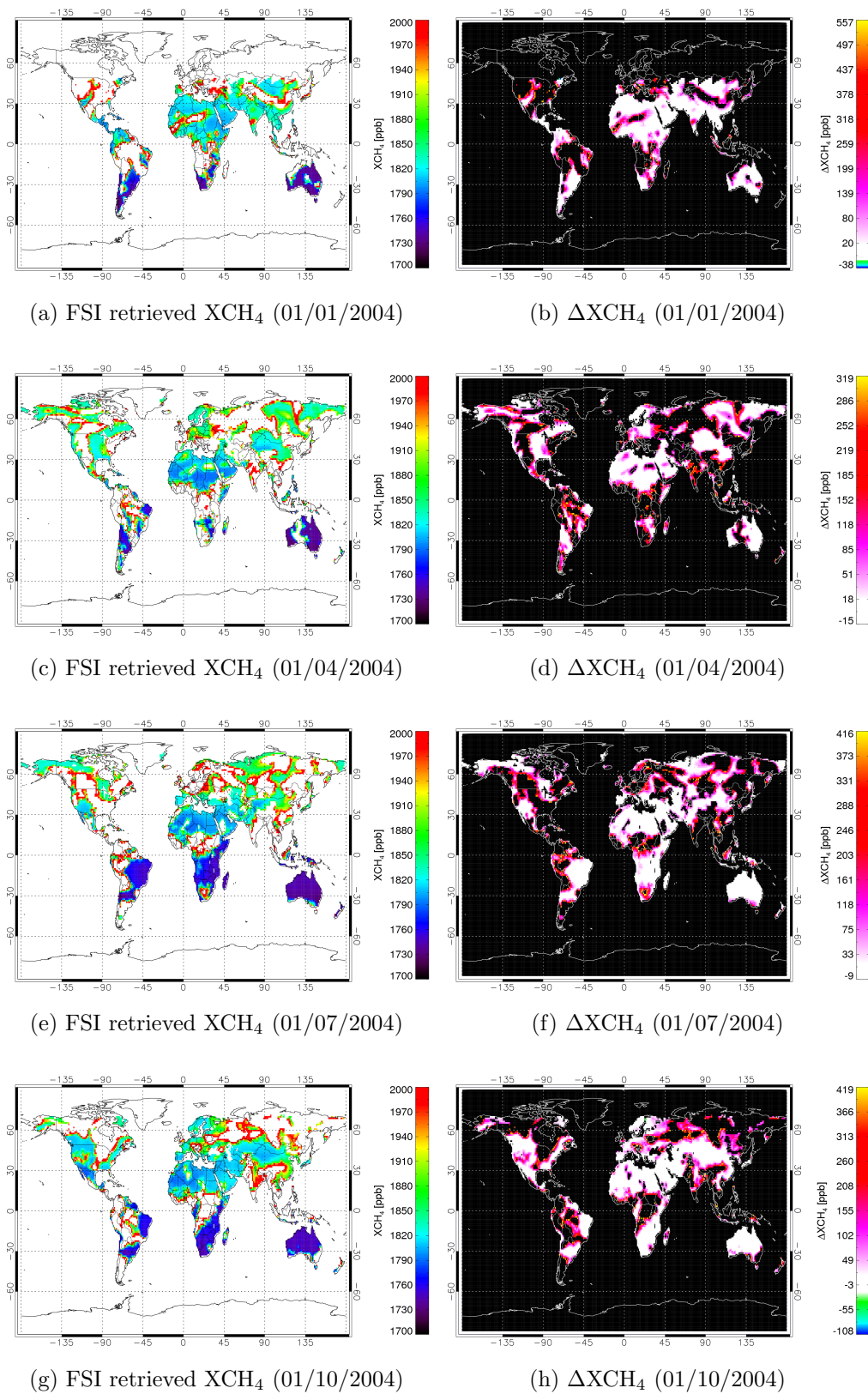


Figure 4.19: Retrieved XCH₄ (left) and ΔXCH₄ (right) for a combined aerosol and cirrus cloud scenario, simulated for the first day of months January, April, July and October 2004 (top to bottom). Data is gridded on a 1.125° × 1.125° scale.

Background

Figure 4.16 shows that some minor underestimation of XCH_4 is encountered at northern latitudes. Scatter plots of the ΔXCH_4 against SZA and surface albedo (Figures 4.21 and 4.22 respectively for October; for January, April and July see Figures C6 and C7 in Appendix C) reveal that these errors are primarily caused by high SZA coupled with very low surface albedo values, particularly at high latitudes in northern Asia and North America. A smaller degree of column underestimation is incurred at southern latitudes since the detrimental effects of large SZAs are partly offset by the higher surface albedos encountered in these regions. The underlying cause of the underestimation is likely to be that simulated SCIAMACHY spectra were created without any aerosol or cloud scattering considerations whereas by default FSI WFM-DOAS V2 always includes some level of background aerosol in the creation of reference spectra.

Aerosol

The addition of aerosol induced scattering to simulated spectra leads to overestimation of the retrieved total column by up to 25 ppb in a significant number of cases. This is because the basic estimate of aerosol induced scattering made by FSI generally underestimates the extent of scattering present (a reversal of the cause of errors in the background case). Underestimation of the total column at northern latitudes is greatly reduced with respect to the background simulation, since the inclusion of aerosol to the simulated cases more effectively matches the small, default aerosol component modelled by FSI WFM-DOAS V2 than in the background case. Minor underestimation of between 5–10 ppb occurs over northern Africa however the cause of this is as yet unknown. Figure 4.21 indicates that ΔXCH_4 is less correlated with SZA than in the background case, however significant correlation with surface albedo still exists.

Ice Clouds

With the inclusion of ice clouds the yield of viable scenes was greatly reduced since the simulated optical depth routinely exceeded 1; discarded scenes appear as black areas over land. Significant overestimation of XCH_4 is observed at the boundary of many such regions where optical depths approach the threshold value of 1. ΔXCH_4 reaches a maximum of 609 ppb for the January run but remains between 350–465 ppb for the other months. Column underestimation is relatively rare and generally

minor, but in a few cases can be as much as 96 ppb. These results show that a tight threshold on ice COD is still required even when employing the proxy method for total column normalisation.

Combined Aerosol and Ice Clouds

The bulk of the total optical depth for combined aerosol and cloud scenarios is due to the ice cloud component, therefore retrieval errors are predominantly driven by the presence of cirrus clouds and are similar to those incurred for the individual ice cloud simulation. Since a limit of $\tau = 1.0$ is imposed on *total* optical depth, the combined simulation contains fewer ice clouds with optical depths approaching 1 since the aerosol component pushes such cases over the imposed τ threshold.

Correlation of ΔXCH_4 with Optical Depth

Figure 4.23 reveals that the relationship between ΔXCH_4 and optical depth is heavily dependent on surface albedo in both aerosol (left) and ice cloud (right) cases.

For aerosol simulations with high surface albedo ($a > 0.27$), increasing AOD results in only a slight underestimation of the total column ($\Delta XCH_4 \sim -5$ ppb), whereas for albedo cases below ~ 0.25 , ΔXCH_4 increases sharply with increasing AOD, reaching ~ 20 ppb at an AOD of 0.02–0.03. Cases of very low surface albedo ($a \sim 0.01$) result in a significant underestimation of the total column (up to 22 ppb), even for negligible AOD; this is most likely due to the inability of FSI WFM-DOAS V2 to correctly estimate such low values of albedo (see Figure 4.22) using the pre-computed LUT [Barkley (2007)], given SZA and mean SCIAMACHY intensity.

ΔXCH_4 displays a pseudo linear relationship with ice COD, which is strongly dependent on surface albedo. As in the aerosol simulation, cases of high surface albedo result in the lowest ΔXCH_4 for increasing optical depth.

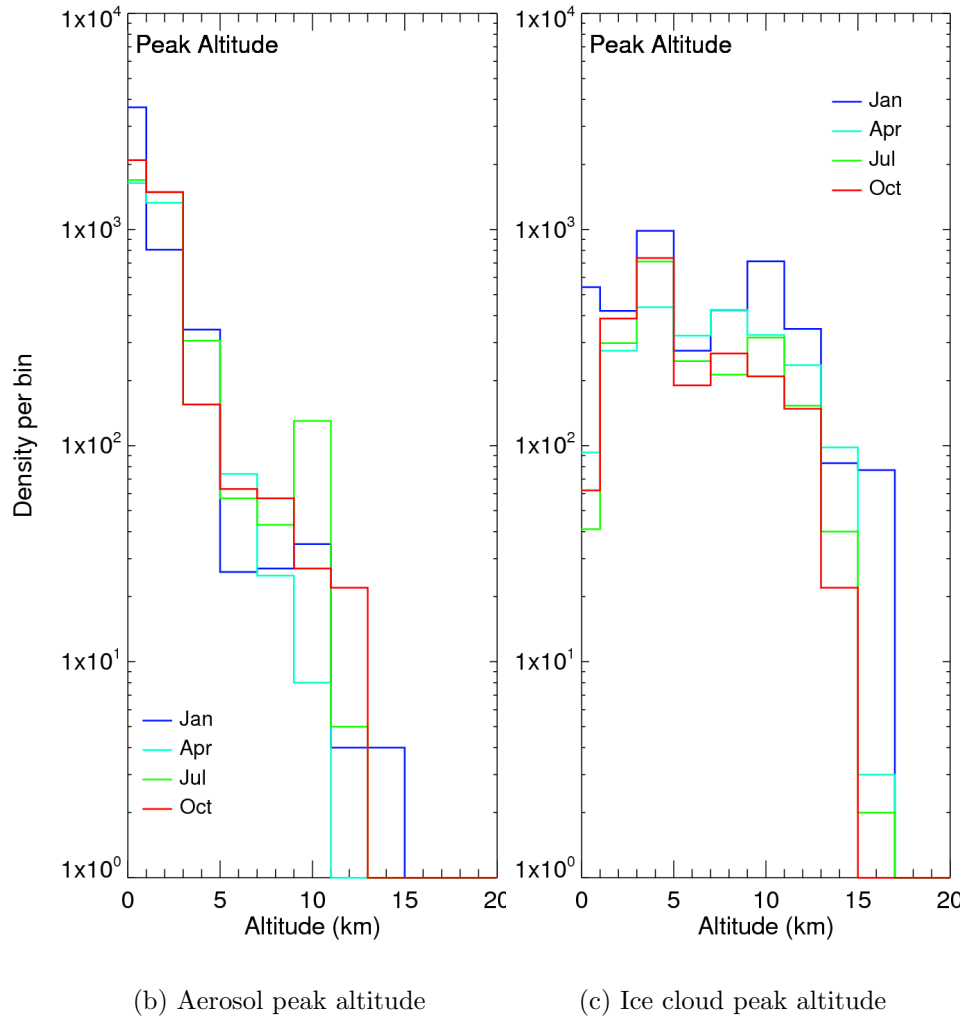


Figure 4.20: Histograms for the altitude of peak optical depth for simulated (a) aerosols and (b) ice clouds for January, April, July and October 2004 (from the combined aerosol and cirrus cloud run). Note the y-axis utilises a log scale for altitude.

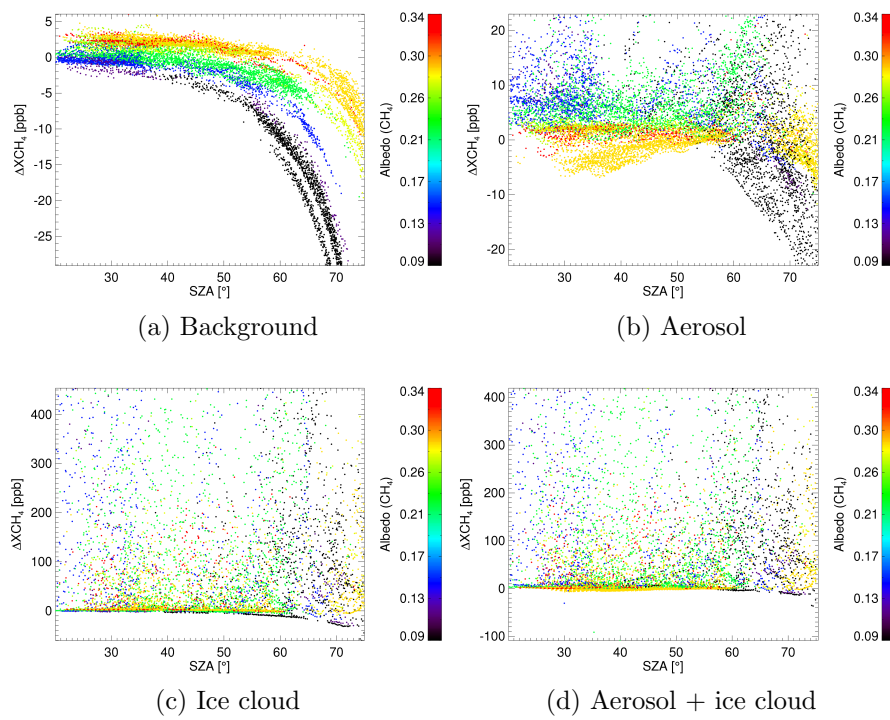


Figure 4.21: Scatter plots of ΔXCH_4 from Oct 2004 against SZA for (a) background, (b) aerosol, (c) ice cloud and (d) aerosol + ice cloud simulation scenarios.

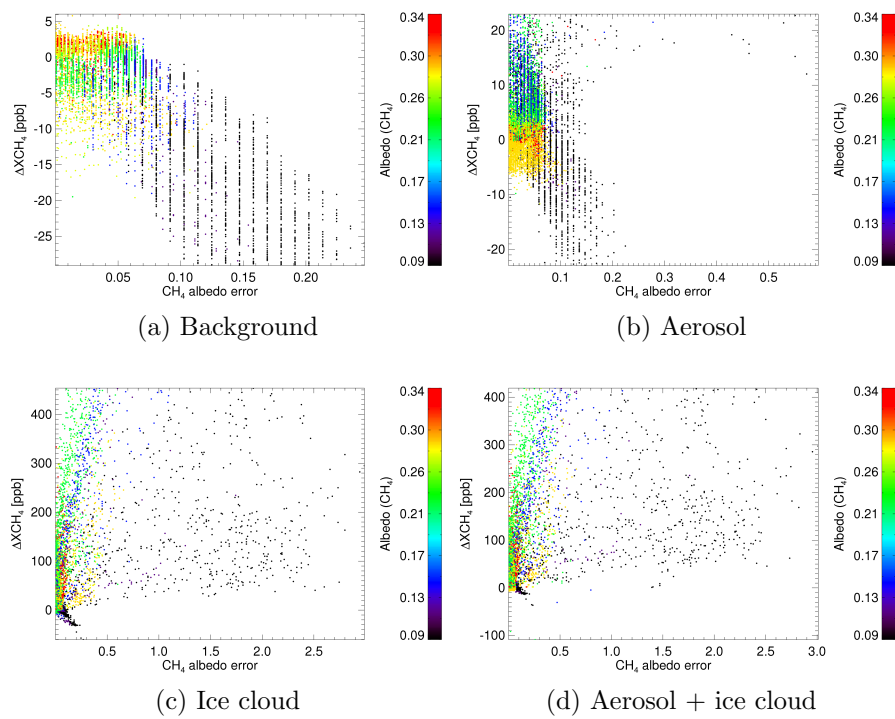


Figure 4.22: Scatter plots of ΔXCH_4 against CH_4 surface albedo estimation error for (a) background, (b) aerosol, (c) ice cloud and (d) aerosol + ice cloud simulation scenarios for Jan 2004.

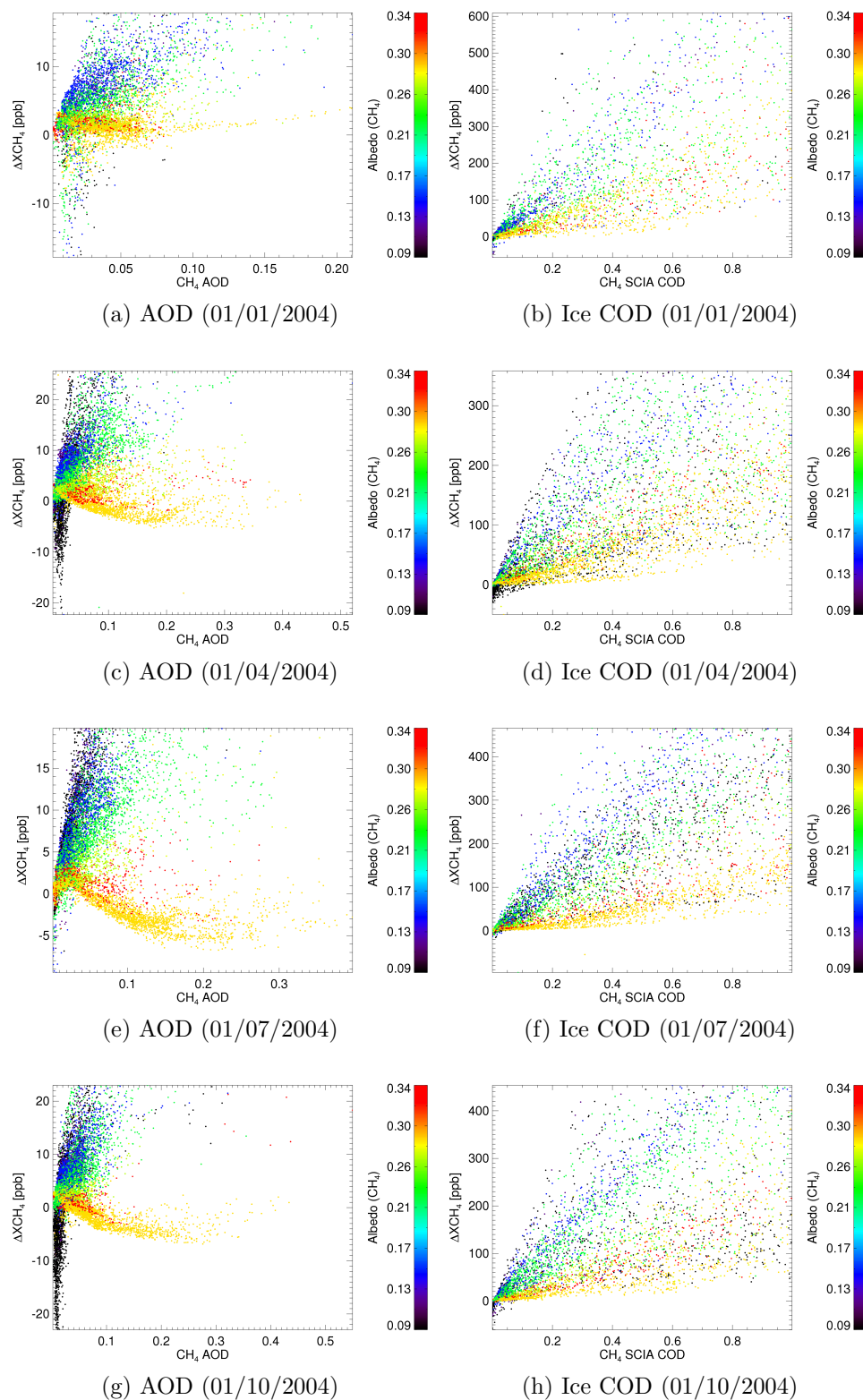


Figure 4.23: Scatter plots of ΔXCH_4 against AOD [(a), (c), (e) and (g)] and ice COD [(b), (d), (f) and (h)] for the months January, April, July and October of 2004 respectively.

Comparison with Existing Results

As mentioned in Section 3.4.5, a study into the effects of aerosol and cirrus cloud induced scattering on satellite retrievals of XCH₄ has previously been carried out by Butz et al. (2010). Although there are similarities between the study by Butz et al. (2010) and the work performed in Simulation 3, there are a number of fundamental differences in both the set-up and results of the two studies which are outlined in Table 4.4. For example, Butz et al. (2010) utilise aerosol data from the global aerosol model ECHAM5-HAM which is defined on 19 atmospheric levels and has a spatial resolution of 3° × 3° whereas GEMS data utilised in Simulation 3 is defined on 60 model levels at a spatial resolution of 1.125° × 1.125°.

Parameter	Simulation 3	Butz et al. (2010)
Retrieval method	FSI WFM-DOAS V2	Optimal estimation based
Aerosol model	GEMS (MMR)	ECHAM5-HAM (MODIS scaled)
Cloud model	GEMS (IWC)	Ray tracing model (CALIOP scaled)
Total τ range	0–1.0 (at 1.65 μm)	0–0.5 (at 1.65 μm)
Max aerosol τ	1.0 (at 1.65 μm)	0.2 (at 0.55 μm)
Max ice cloud τ	1.0 (at 1.65 μm)	0.4 (at 0.55 μm)
Max ΔXCH_4	35%	2%

Table 4.4: Comparison of the set-up of Simulation 3 detailed in this section with an existing study by Butz et al. (2010).

Figure 4.24 shows the error on XCH₄ retrievals (equivalent to ΔXCH_4 shown as a percentage) from Butz et al. (2010) obtained when using the proxy method with simulated SCIAMACHY measurements containing aerosol and cirrus cloud scattering. Retrieval errors are clearly far less than those obtained in Simulation 3 (see ΔXCH_4 in Figure 4.19). However, results from Butz et al. (2010) correspond to a smaller range of optical depths; AOD is limited to 0.2 and COD is limited to 0.4 (both at 0.55 μm). For all but the largest particles, optical depth generally decreases as wavelength changes from 0.55 μm to the centre of the CH₄ retrieval window at 1.65 μm (see Figure C1 for the wavelength dependence of AOD). As a result, the limits on AOD and COD employed by Butz et al. (2010) become even tighter at a wavelength of 1.65 μm . From Figure 4.6 it can be seen that by imposing a limit of AOD \leq 0.2 on results from Simulation 2, ΔXCH_4 is at most 5% when considering aerosols at an altitude of 3 km and SZA = 60°; for lower altitudes and SZA, ΔXCH_4 is far lower. Similarly, it can be seen from Figure 4.7 that imposing the Butz et al. (2010) limit of COD \leq 0.4 on ice clouds would result in ΔXCH_4 of up to 13% in

high surface albedo cases and 60% in very low surface albedo cases.

Taking into consideration the reduction in optical depth at $1.65 \mu\text{m}$, the lower limit of aerosol scattering induced errors found in Simulation 2 and results from the global aerosol runs in Simulation 3 are consistent with ΔXCH_4 obtained by Butz et al. (2010). Applying the same optical depth reduction at a wavelength of $1.65 \mu\text{m}$ to ice clouds, although a difference in ΔXCH_4 still exists between the two studies, its magnitude is not as severe as the upper limit discussed above (i.e. COD of 0.4 at $1.65 \mu\text{m}$) since ΔXCH_4 decreases sharply with decreasing COD.

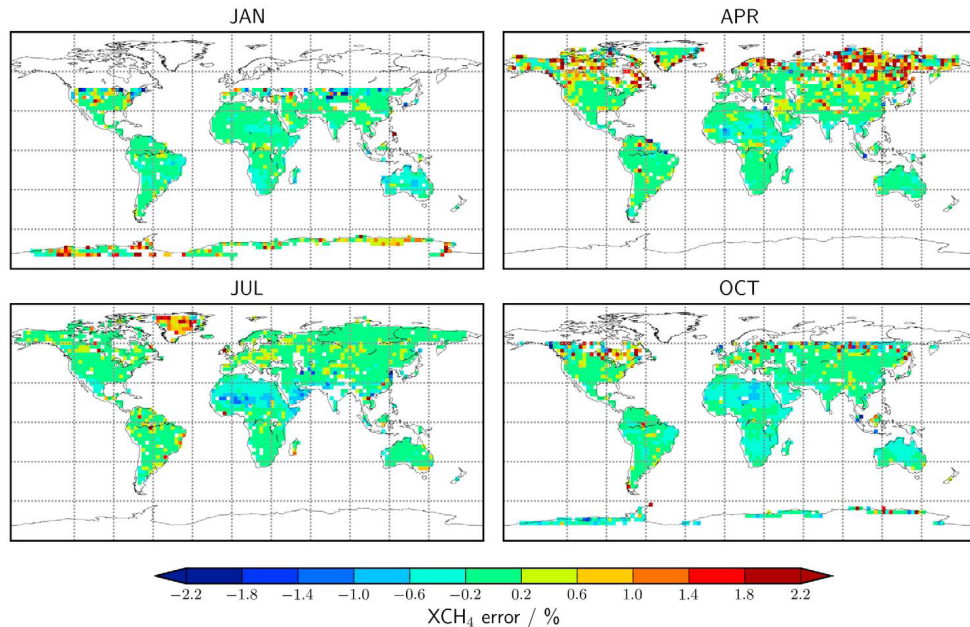


Figure 4.24: XCH_4 error [%] (equivalent to ΔXCH_4) for proxy based retrievals using simulated SCIAMACHY spectra for an ensemble of aerosol and cirrus cloud scenarios (figure taken from Butz et al. (2010)).

4.4.7 Summary of Simulation 3

Global sensitivity tests reveal that when no aerosol or ice cloud is simulated the FSI WFM-DOAS V2 retrieval algorithm performs well, with $\Delta\text{XCH}_4 < 1\%$ in the vast majority of cases. However, even though no aerosol or cirrus induced scattering is present in this case, high SZAs and low surface albedos encountered at northern latitudes result in a small number of cases where XCH_4 is underestimated by up to 1.6%. The simulation of aerosols, based on profiles of GEMS aerosol MMR, reveal

that retrieval errors of up to 1.5% are incurred at various latitudes in the four days considered, particularly in Southeast Asia and central Africa.

The simulation of ice clouds resulted in a significant reduction in the number of usable scenes due to the imposed limit of $\tau < 1$. From the remaining scenes, retrieval errors of up to around 35% were encountered, indicating that ice clouds are a far greater source of retrieval error than aerosols. As a result, ice cloud errors dominate the combined aerosol and ice cloud simulation and the errors encountered are very similar to those of the stand alone ice cloud case. The disparity in retrieval errors for aerosols and ice clouds is most likely due to the fact that simulated AOD rarely exceeded 0.3 whereas ice COD's in the region of 1 were not unusual. Furthermore, the altitude of the peak optical depth was much lower for aerosols than ice clouds (see Figure 4.20). This suggests that the interaction of radiation with ice clouds occurs higher in the atmosphere than for aerosols, thus the relative increase in error is also a manifestation of the altitude dependence of the scattering induced retrieval error identified in Simulation 2.

4.5 Summary

From the three sensitivity studies undertaken in this chapter it can be concluded that:

1. Scattering induced retrieval errors are highly dependent on the altitude at which scattering occurs.
2. For comparable altitudes and optical depths, scattering due to aerosols causes greater error than scattering due to ice clouds.
3. In reality, retrieval errors due to aerosol are far less than those due to ice clouds.
4. Retrieval errors due to scattering are amplified by high SZA and/or low surface albedo scenarios.

Sensitivity test 1 reveals that the importance of accurate aerosol a priori information increases as the optical depth of the scene increases; this is to be expected since the default low τ aerosol estimation of FSI is a close approximation of low τ scenes, but

a poor approximation of high τ scenes. As a result, greater knowledge of aerosol τ is required in future retrievals, such as the inclusion of GEMS aerosol extinction profiles as a priori information.

Although Sensitivity test 2 indicates that aerosols can cause greater retrieval errors than ice clouds for comparable optical depths and scattering altitudes, global sensitivity tests show that in reality retrieval errors due to ice clouds are far greater than those due to aerosols. This is because aerosols are typically found at low altitude (0–5 km) and AOD rarely exceeds 0.3, whereas ice clouds (particularly cirrus) reside at high altitude (up to 17 km) and can have optical depths from just above zero up to the imposed limit of 1. Since ice cloud scattering dominates retrieval errors in global sensitivity tests (with ΔX_{CH_4} up to $\sim 35\%$ in the most extreme cases) strict cloud filtering, including filtering for cirrus, is clearly still required in future FSI WFM-DOAS V2 retrievals of CH_4 , even though the proxy approach (see Sections 1.4.4 and 3.3.2) for VCD normalisation is employed. The results in this thesis can therefore provide a guide to the level of cloud filtering required in terms of cloud optical depth.

Chapter 5

FSI WFM-DOAS Retrievals of CH_4 over North America

5.1 Introduction

Sensitivity tests undertaken in Chapter 4 revealed that FSI WFM-DOAS V2 retrievals of CH_4 in the SWIR are particularly sensitive to the albedo and optical depth of an observed scene. As a result, two significant updates to the FSI WFM-DOAS V2 algorithm have been made; 1) the LUT approach previously used to estimate albedo has been replaced with albedo retrieved from the Moderate Resolution Imaging Spectroradiometer (MODIS) and 2) basic aerosol assumptions have been replaced by a realistic aerosol initialisation based on profiles of aerosol MMR from GEMS. These combined modifications were intended to result in a new version of the retrieval algorithm, FSI WFM-DOAS V3 (see Figure 5.1), however owing to time constraints the impact of MODIS and GEMS modifications have only been assessed separately thus far. This chapter therefore details retrievals of total column CH_4 over North America for the year 2004 performed using three different versions of the FSI WFM-DOAS V2 retrieval; in its original form (OFSI), modified with a priori albedo from MODIS (MFSI) and modified with aerosol extinction calculated from GEMS MMR (GFSI). The validation of satellite retrievals using FTS measurements from the TCCON (see Section 1.4.3) site at Park Falls, Wisconsin, is also presented.

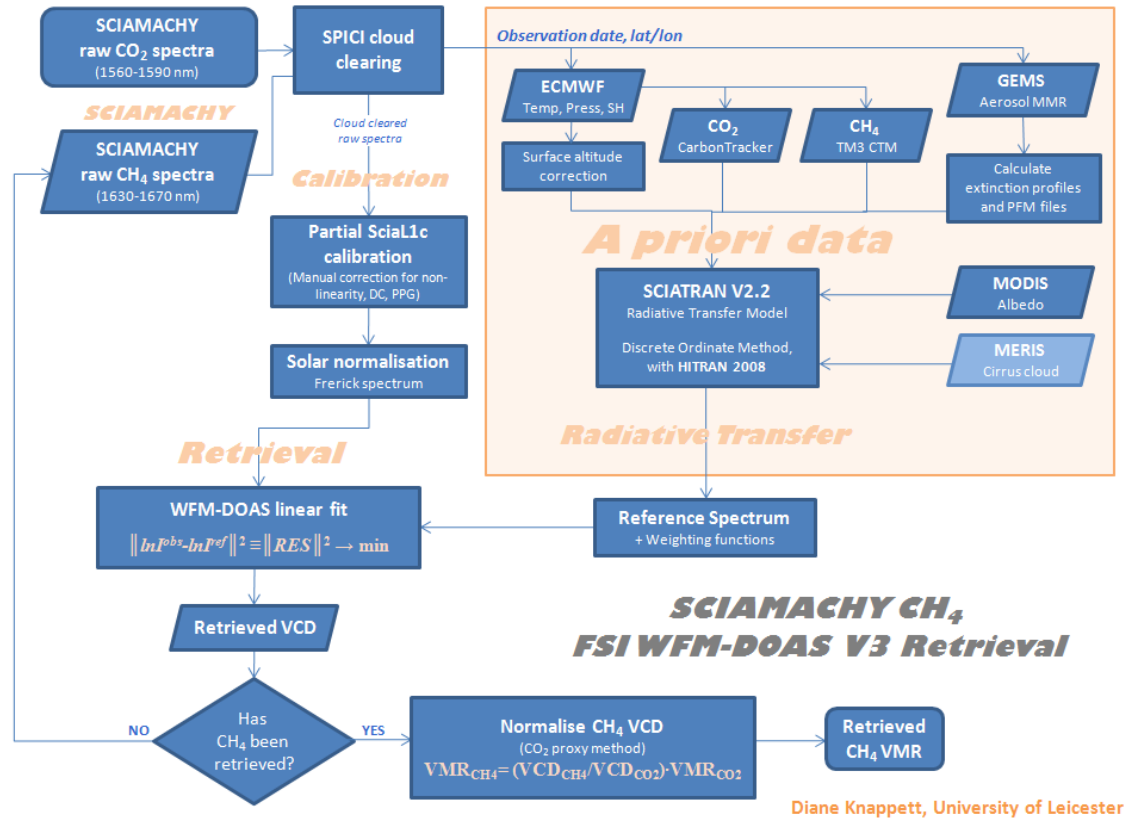


Figure 5.1: Flowchart portraying the progression of the FSI WFM-DOAS V3 retrieval algorithm. In this version aerosol extinction profiles calculated from GEMS MMR are used as a priori aerosol and a priori albedo is obtained from MODIS. Cloud flagging of cirrus clouds using data from MERIS is mentioned as a future modification.

5.1.1 MODIS Albedo Modifications

A 16 day MODIS albedo product was used to obtain an improved a priori albedo for use within the MFSI retrieval. MODIS instruments are carried onboard two separate NASA satellites and the albedo product “Albedo 16-Day L3 Global 0.05Deg CMG” used here combines data from both instruments for improved data quality. Each MODIS instrument has thirty six spectral bands, four of which are within the SWIR, however band 6 covering 1628-1652 nm is the nearest to the retrieval windows for CO₂ and CH₄.

AVIRIS albedo datasets (also used in Section 4.2 for spectral simulations) corresponding to each MODIS land cover type were interpolated to obtain albedo values corresponding to the central wavelengths of both the CO₂ and CH₄ retrieval win-

dows (denoted A_{ret}) as well as for MODIS band 6 at $1.64 \mu\text{m}$ ($A_{1.64}$). The ratio of A_{ret} to $A_{1.64}$ was taken to be a good approximation of the spectral dependence of albedo in the SWIR and was used to scale the MODIS albedo $M_{1.64}$ to the centre of each retrieval window as follows:

$$M_{\text{ret}} = \left(\frac{M_{1.64}}{A_{1.64}} \right) A_{\text{ret}}. \quad (5.1)$$

Figure 5.2 shows an example of the original MODIS global albedo along with the resulting scaled global albedo corresponding to retrieval windows at $1.57 \mu\text{m}$ and $1.65 \mu\text{m}$ in Figure 5.3.

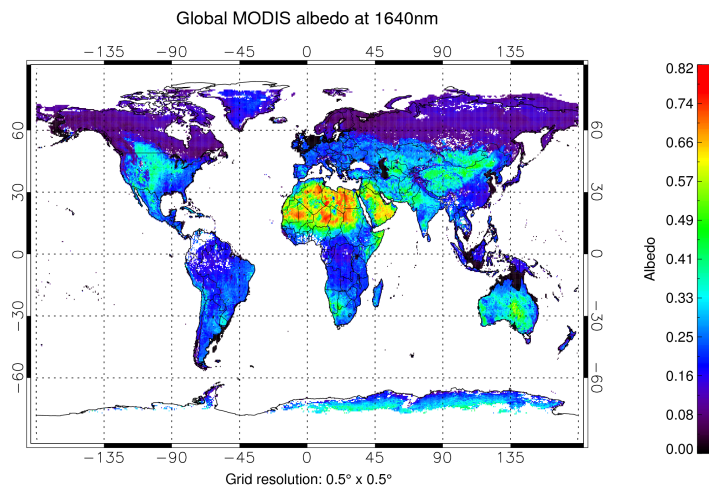


Figure 5.2: MODIS retrieved 16 day mean albedo at $1.64 \mu\text{m}$ for 01/10/2004. Black areas over land indicate consistently cloudy regions or inland water.

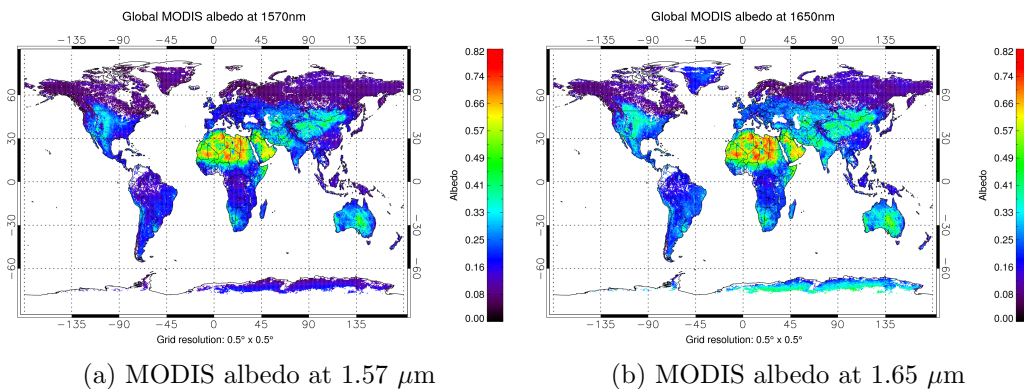


Figure 5.3: MODIS albedo scaled to the central wavelengths of retrieval windows for (a) CO_2 and (b) CH_4 at $1.57 \mu\text{m}$ and $1.65 \mu\text{m}$ respectively.

To extract an a priori albedo from the MODIS global dataset corresponding to a SCIAMACHY observed scene, firstly the nearest MODIS grid points to each corner of the SCIAMACHY footprint were identified. Since the footprint of a SCIAMACHY scene is typically at an angle with respect to lines of constant longitude, the highest and lowest latitude and longitude values were used to define a sub-grid of MODIS values that would encompass the entire SCIAMACHY footprint. The MFSI a priori albedo was then simply taken to be the mean of the MODIS albedo sub-grid, provided that the sub-grid contained at least one finite value. In the instance where the extracted MODIS sub-grid consisted entirely of non-zero values, a composite monthly average was used. If this also contained no finite albedo values then the retrieval was discarded.

5.1.2 GEMS Aerosol Modifications

A global dataset of GEMS aerosol MMR profiles covering the entirety of 2004 (four time steps per day) was converted to extinction following the same procedure as detailed in Section 4.4.1. Owing to the large volume of data, the MMR to extinction conversion was performed in a pre-processing stage to reduce the retrieval run time of GFSI. During the retrieval, the same procedure for spatial and temporal interpolation as applied to ECMWF meteorological profiles in Section 3.3.6 was used to extract profiles of aerosol extinction tailored to the time and location of each SCIAMACHY observation. Scattering weighted PFMs were calculated using the procedure described in Section 4.4.1. However, since PFM calculations had to be performed for each individual retrieval, computational time was significantly increased as a result. In general, the runtime of SCIATRAN 2.2 is dependent on the complexity of the modelled atmosphere, therefore scenes with a high aerosol extinction typically resulted in an increase of retrieval runtime by ~ 20 minutes. Unfortunately there were retrieval convergence problems with GFSI which resulted in some loss of data with respect to the OFSI and MFSI retrievals.

5.2 FSI WFM-DOAS Retrievals over North America for 2004

5.2.1 Data Filtering

Retrievals were performed for all cloud-free SCIAMACHY scenes over the continent of North America (defined by the boundaries: $10^\circ \text{ N} < \text{latitude} < 85^\circ \text{ N}$ and $170^\circ \text{ W} < \text{longitude} < 50^\circ \text{ W}$) for the year 2004. However, since a number of factors can result in retrieval errors, retrieval datasets require filtering using carefully selected statistical thresholds. Firstly, radiative transfer calculations for a plane parallel atmosphere in SCIATRAN are inaccurate for SZAs greater than 70° , therefore scenes in which the SZA exceeded 70° were discarded. Similarly, low albedo and surface ice in the northernmost regions of the continent meant that retrievals made at high latitudes were also ignored. Cases in which $\sigma_{\text{CO}_2} > 100\%$, $\sigma_{\text{CH}_4} > 1000\%$ or the a priori albedo was set to zero were discarded since these results were not written correctly to file and are clearly erroneous. The resulting thresholds for SZA, surface albedo, latitude and longitude have been summarised in Table 5.1 and will be collectively referred to as ‘Filter 1’.

Data filters
SZA $> 70^\circ$
Albedo $< 1 \times 10^5$
Latitude $> 70^\circ$
Longitude $> -53^\circ$

Table 5.1: Filter 1; thresholds for SZA, albedo, latitude and longitude used to filter out anomalous FSI WFM-DOAS V2 retrievals of CH_4 .

Despite applying Filter 1, the OFSI, MFSI and GFSAI distributions of retrieved XCH_4 and σ_{CH_4} contained a significant number of outliers, many of which were far from the mean. Figures 4.8 and 4.9 show that aerosols and ice clouds of high optical depth, or at high altitude, cause an increase in the retrieval fit error, σ_{XCH_4} . Consequently, the filtering of data with high σ_{XCH_4} is likely to remove CH_4 retrievals affected by aerosols and ice clouds with high optical depth and/or at high altitudes.

In order to reduce the influence of outliers, robust statistics can be employed in which the median and median absolute deviation (σ_{MAD}) are used to describe the

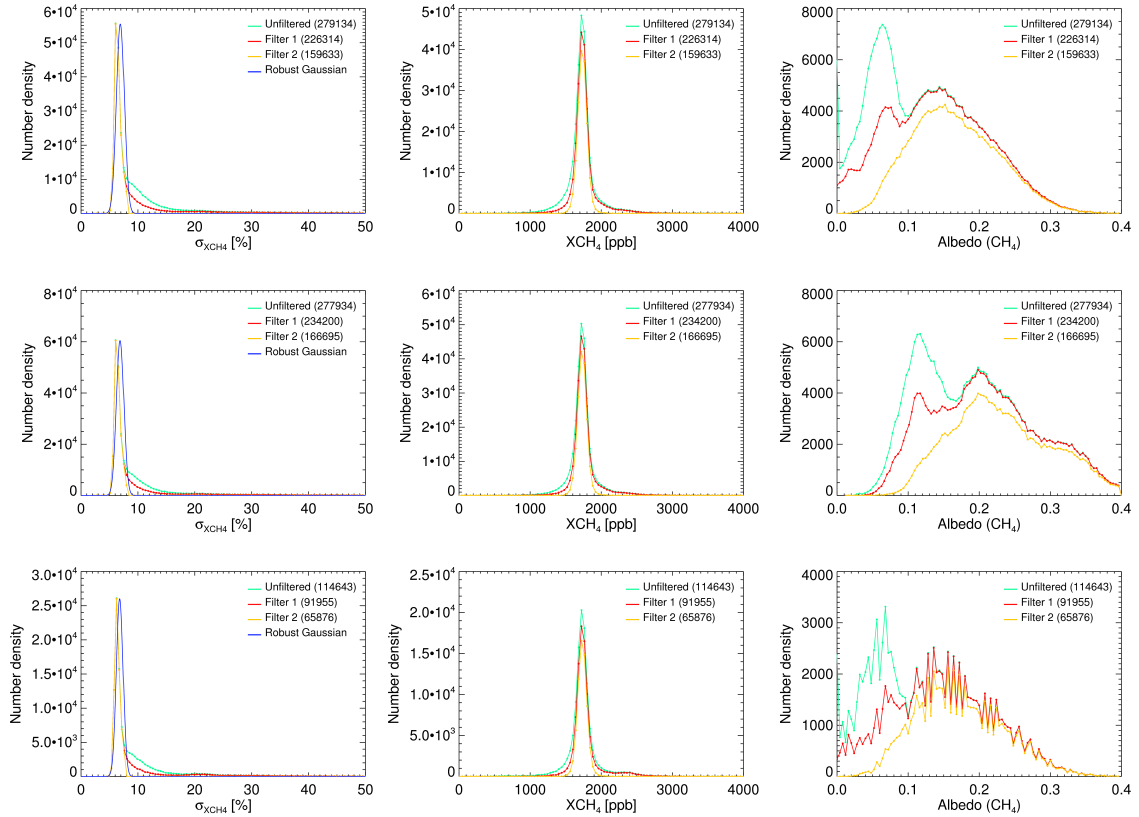


Figure 5.4: Distributions of the retrieval fit error σ_{XCH_4} , retrieved XCH_4 and a priori albedo for the OFSI (top), MFSI (centre) and GFSI (bottom) retrievals. Unfiltered data is shown in green and data filtered by Filter 1 (thresholds defined in Table 5.1) are shown in red. The median and median absolute deviation of the Filter 1 distribution of σ_{XCH_4} have been used to plot a robust gaussian (shown in blue) from which the thresholds of Filter 2 (shown in yellow) have been defined.

distribution in place of the mean and standard deviation. Figure 5.4 shows distributions of σ_{XCH_4} , XCH_4 and albedo for the OFSI, MFSI and GFSI retrievals. The original, unfiltered distribution of data is shown in green whereas data remaining after the application of Filter 1 is shown in red. Note that the highly variable nature of the albedo distribution is an artifact of employing a LUT for the estimation of surface albedo with no subsequent interpolation; the same LUT approach is used for OFSI but the effect is less prominent due to the large number of retrievals. A robust Gaussian was fitted to the σ_{XCH_4} distribution, after being filtered by Filter 1, and is shown in blue. To identify retrievals for which the WFM-DOAS fit was suitably accurate, a limit of $2\sigma_{MAD}$ from the median of the σ_{XCH_4} distribution of each retrieval version was used to filter the respective σ_{XCH_4} distributions and will be referred to as ‘Filter 2’. The distributions remaining for σ_{XCH_4} , XCH_4 , and surface

albedo after the application of Filter 2 are shown in yellow.

Figure 5.5 shows density correlation plots of retrieval fit errors (given by Equation 2.24) for unfiltered retrievals of CO₂ VCD, CH₄ VCD and XCH₄ respectively (Figures C8 and C10 show corresponding plots for MFSI and GFSI in Appendix C). For comparison, Figure 5.6 shows distributions of the same parameters after the application of both Filter 1 and Filter 2 (Figures C9 and C11 show corresponding plots for MFSI and GFSI, in Appendix C). Figure 5.6c clearly shows how the spread of σ_{XCH_4} has been significantly reduced as a result and highlights the distribution peak between 6–7%, which agrees well with the retrieval fit errors obtained from simulations of four typical cases of high/low SZA and albedo, given in Table 5.2.

SZA	Albedo (1670 nm)	σ_{CO_2} [%]	σ_{CH_4} [%]	σ_{XCH_4} [%]
26.6	0.048	2.93	6.50	7.13
28.6	0.322	1.69	6.06	6.29
28.8	0.175	1.92	5.94	6.24
68.2	0.164	1.86	6.79	7.04

Table 5.2: The error [%] incurred in CO₂ and CH₄ retrieved VCDs for SCIAMACHY scenes corresponding to low/high SZA and albedo. The resulting combined error on XCH₄, given by $\sigma_{\text{XCH}_4} = \left[\left(\frac{\sigma_{\text{CO}_2}}{\text{VCD}_{\text{CO}_2}} \right)^2 + \left(\frac{\sigma_{\text{CH}_4}}{\text{VCD}_{\text{CH}_4}} \right)^2 \right]^{\frac{1}{2}}$, is shown in the final column.

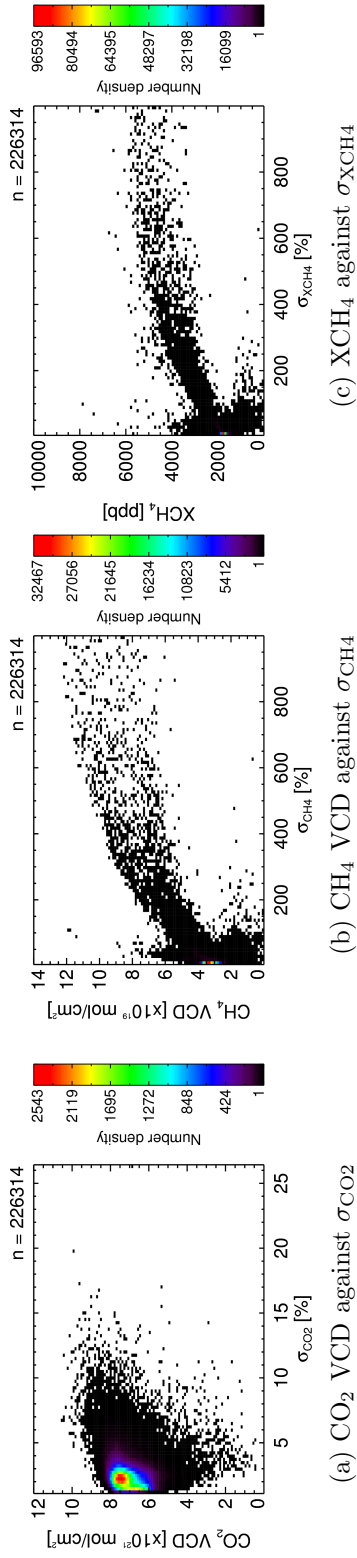


Figure 5.5: Density correlation plots of σ_{CO_2} , σ_{CH_4} and σ_{XCH_4} from the OFSI retrieval once filtered by Filter 1.

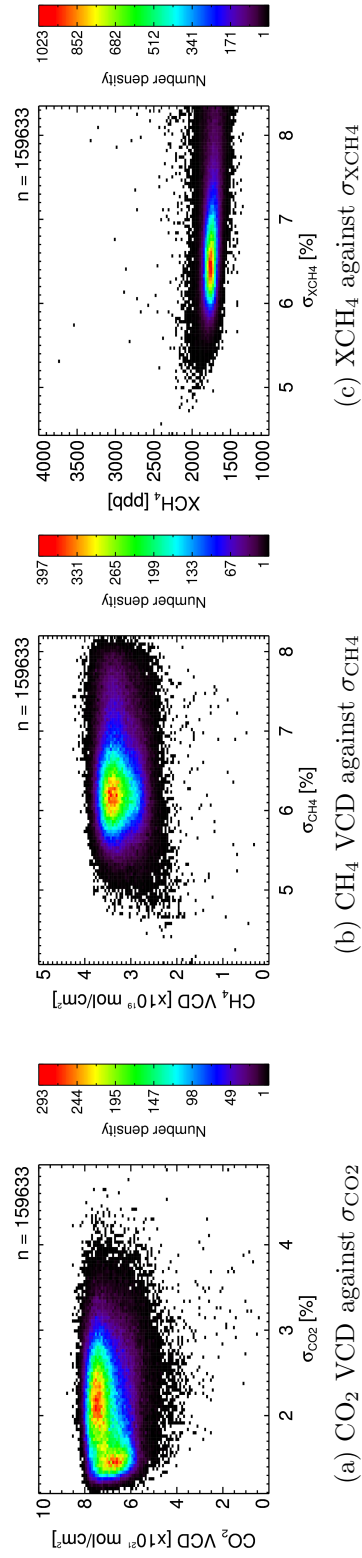


Figure 5.6: Density correlation plots of σ_{CO_2} , σ_{CH_4} and σ_{XCH_4} from the OFSI retrieval once filtered by Filter 2.

The absolute number of retrieved scenes varied between the three separate retrieval schemes because each approach resulted in different retrieval run times and imposed different criteria for skipping retrievals; the runtime of GFSI was so extensive that only alternate months of 2004 could be processed in the time available whereas for MFSI, SCIAMACHY scenes for which no corresponding MODIS albedo was available (often the case in persistently cloudy regions) were not processed.

5.2.2 Gridded Monthly Mean CH₄ over North America

Figures 5.7 and 5.8 show monthly averages of retrieved XCH₄ for 2004, from OFSI and MFSI respectively, gridded to 1°×1° over North America. Figure 5.9 shows XCH₄ retrieved by GFSI for alternate months of 2004 only (starting from January), due to the extensive runtime of this version of the retrieval. In the following discussion, results from each of the three retrieval versions (OFSI, MFSI and GFSI) will initially be considered separately and then compared at the end.

OFSI Retrieved XCH₄

Plots of monthly averaged XCH₄ retrieved using OFSI given in Figure 5.7 clearly show elevated* CH₄ concentrations around the Gulf of Mexico for the period May–September 2004. High XCH₄ over southeast USA is particularly widespread during May and June, but remains elevated for the period July to September. During the autumn/winter months (October through April) CH₄ concentrations in this region largely return to between 1700–1800 ppb. Retrieved XCH₄ over eastern Mexico generally remains > 1800 ppb throughout the year, reaching between 1850–1900 ppb in May and September, and even exceeding 1900 ppb in June. CH₄ emission estimates from Emission Database for Global Atmospheric Research (EDGAR) for the year 2005 can be seen in Figure 5.12a, and Figure 5.12b shows the increase in CH₄ emissions over the period 2000–2005. Figure 5.12a indicates the presence of large CH₄ emissions (of comparable scale) in both eastern USA and Mexico during 2005. Furthermore, Figure 5.12b implies very little change in emissions in both these regions from 2000–2005, implying emissions in these regions for 2005 are representative of the years 2000–2004 also. That being the case, EDGAR emissions data is consistent with OFSI results that XCH₄ over southeast USA and Mexico was elevated during 2004.

*With respect to the 2005 yearly global mean of 1774 ppb [Forster et al. (2007)]

For comparison with the largest observed XCH_4 enhancements in OFSI retrievals, TM3 model total column XCH_4 over North America for the first day of months May–August 2004 are shown in Figure 5.10. Model data indicates that XCH_4 is consistently high (around 1850 ppb) in eastern USA during the four month period shown, and corresponds with OFSI retrievals of heightened XCH_4 over southeast USA. However, the model shows no obvious XCH_4 enhancement over Mexico, attributing this region with lower values of XCH_4 (around 1780–1800 ppb) than locations north of 30° latitude. TM3 model XCH_4 for the entirety of 2004 can be found in Figure C12 in Appendix C.

Monthly averaged XCH_4 for May–August 2004 retrieved using the WFM-DOAS version 1.0 retrieval algorithm [Schneising et al. (2009)] is shown in Figure 5.11. WFM-DOAS v1.0 retrievals show enhanced XCH_4 over eastern USA (with respect to the west) for May 2004, however the particularly high values seen in OFSI retrievals are not replicated. Since retrievals for June 2004 are sparse, very little comparison can be made for this month. For July and August, WFM-DOAS v1.0 XCH_4 is significantly heightened (~ 1810 – 1830 ppb) across both the northern and eastern USA. WFM-DOAS v1.0 retrievals of XCH_4 for the whole of 2004 are given in Figure C13 in the Appendix.

Comparison of MFSI and OFSI Retrieved XCH_4

Monthly averaged MFSI retrievals of XCH_4 appear to be very slightly lower than those from the OFSI retrieval; this is particularly evident over eastern Mexico for the period May–September. Generally however the difference between monthly averaged retrievals is surprisingly small, despite significant difference in a priori albedo between the two retrieval versions.

Comparison of GFSI and OFSI Retrieved XCH_4

Monthly averaged GFSI retrievals of XCH_4 are consistently lower over eastern Mexico during March, May, July and September than in the OFSI retrievals. Conversely, a slight enhancement of CH_4 concentrations can be seen over eastern USA for the months May, July and September.

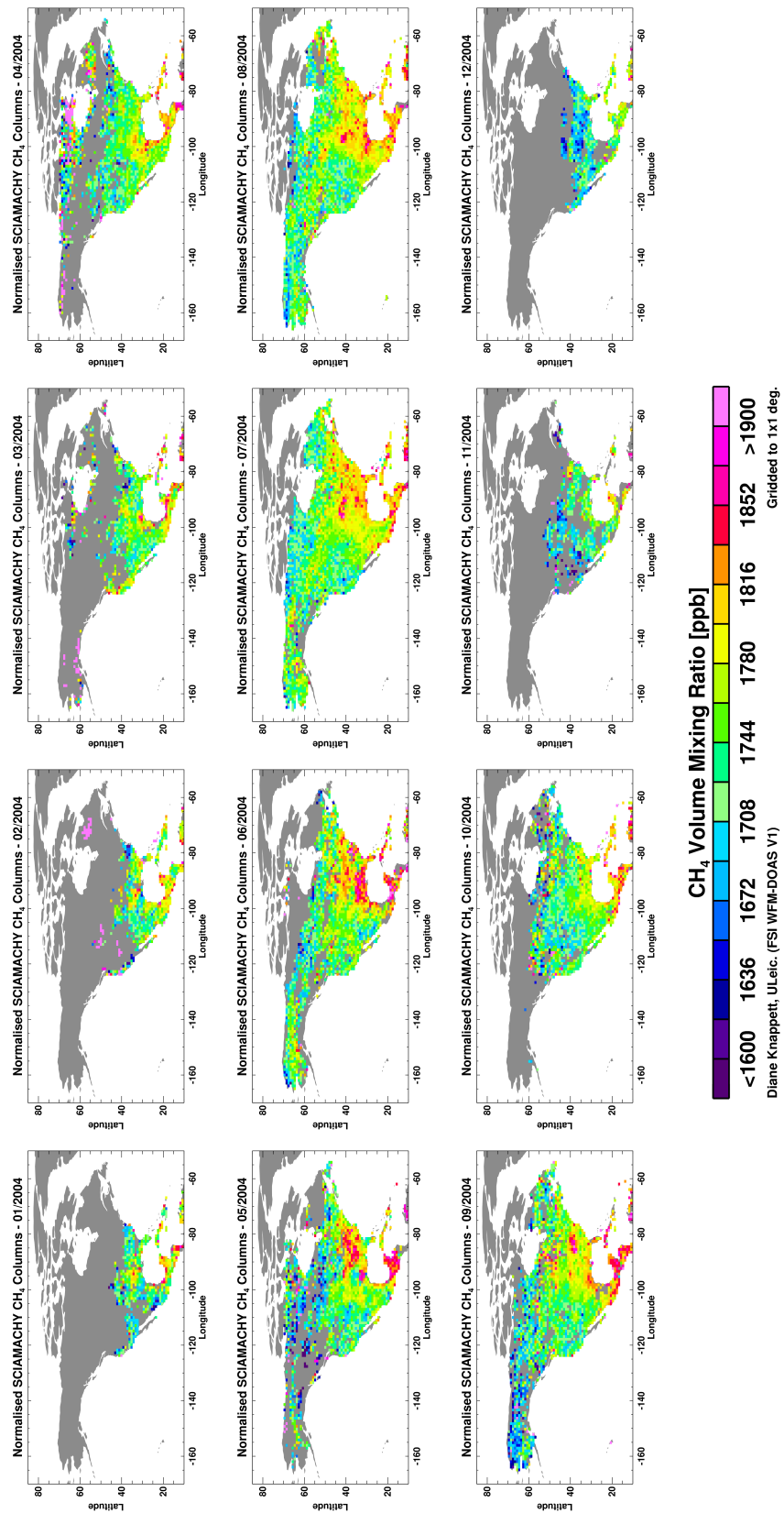


Figure 5.7: Monthly averaged OFSI retrievals of CH₄ over North America for the period Jan-Dec 2004.

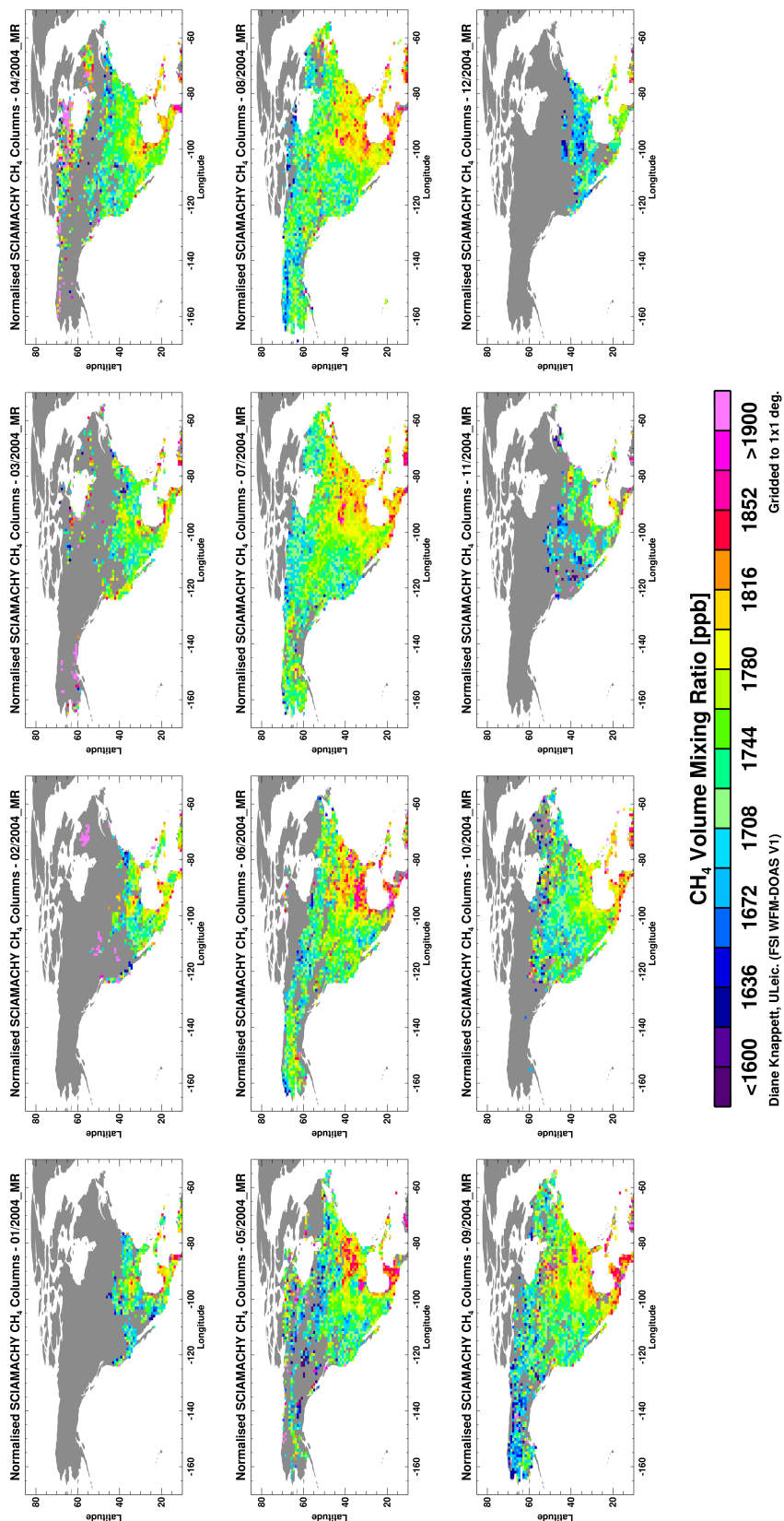


Figure 5.8: Monthly averaged MFSI retrievals of CH₄ over North America for the period Jan-Dec 2004.

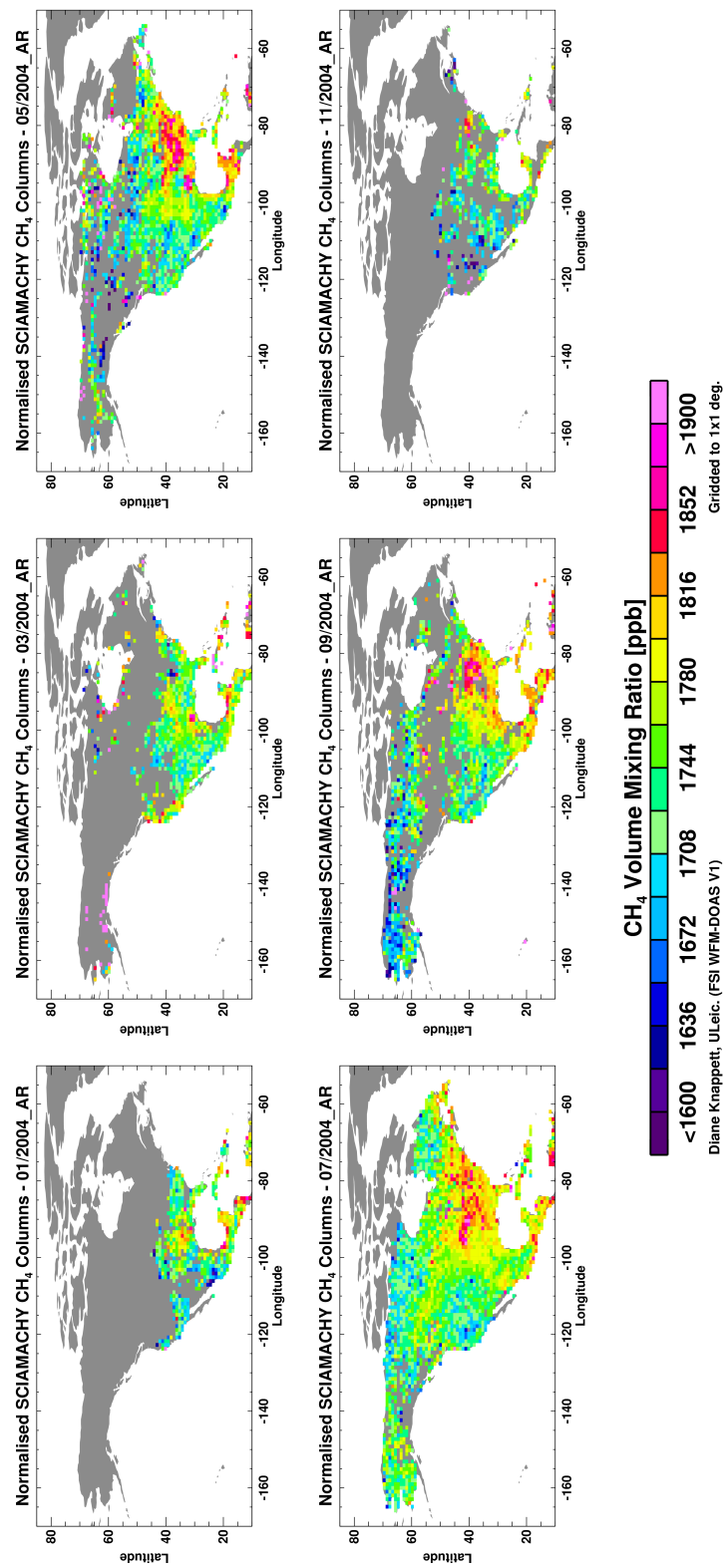


Figure 5.9: Monthly averaged GFSI retrievals of CH₄ over North America for alternate months from Jan-Nov 2004.

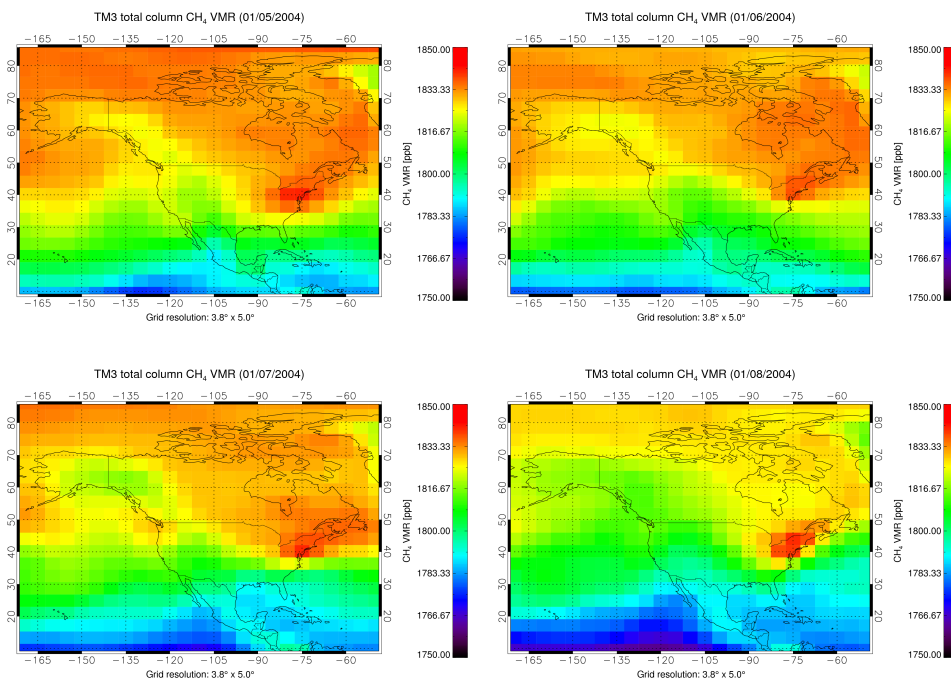


Figure 5.10: Total column XCH_4 from TM3 (used as a priori XCH_4 in the FSI WFM-DOAS V2 retrieval) for the first day of months May–August of 2004 gridded to $3.8^\circ \times 5^\circ$

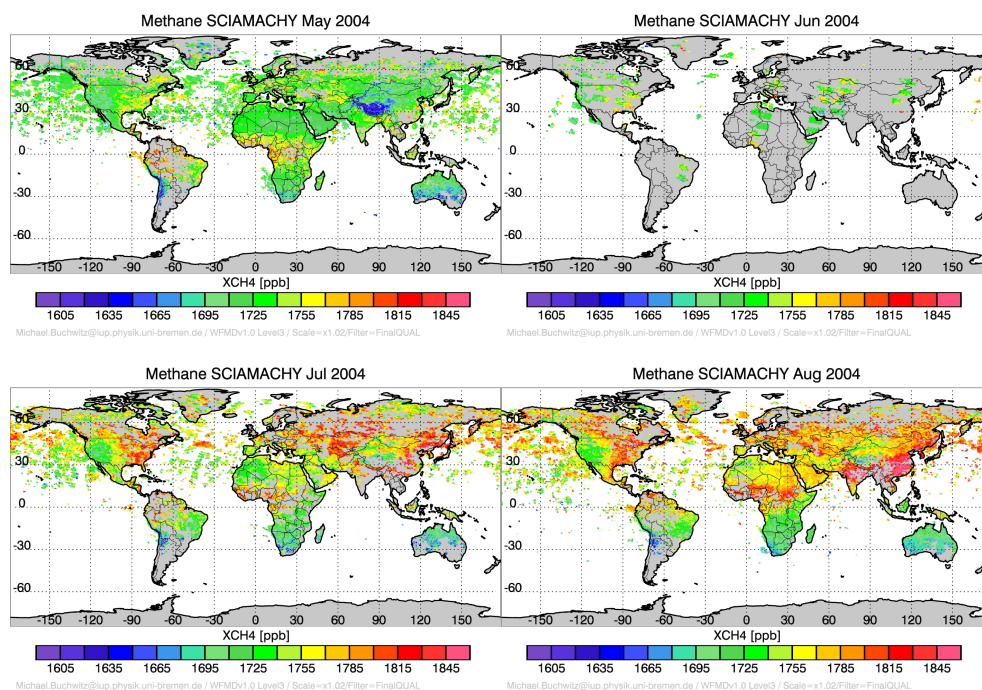


Figure 5.11: Monthly averaged XCH_4 retrieved by WFM-DOAS version 1.0, for the period May–August 2004, gridded to $1^\circ \times 10^\circ$ (figure taken from Buchwitz (2007)).

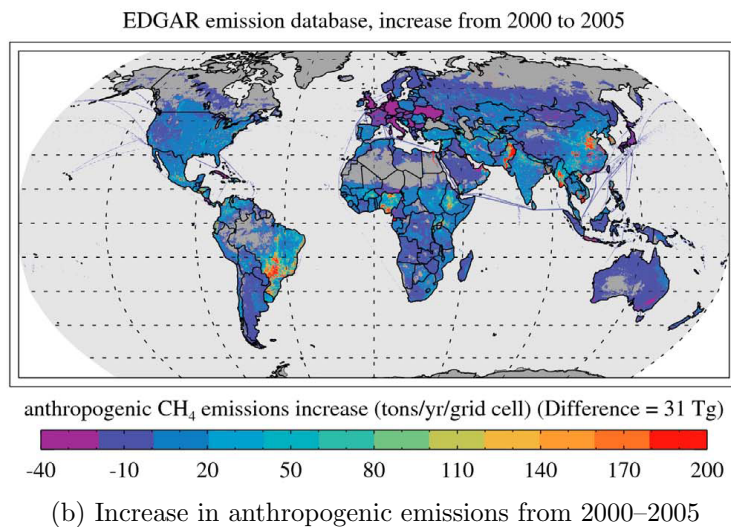
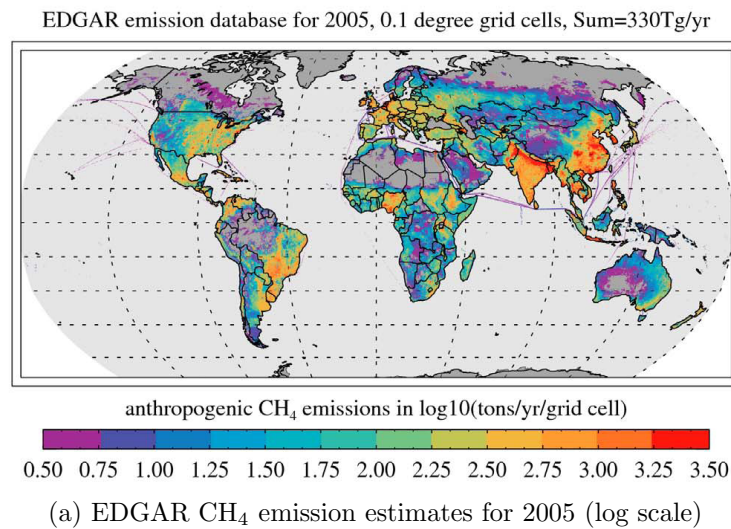


Figure 5.12: Anthropogenic CH₄ emission estimates from EDGAR for 2005 and the increase in emissions over the period 2000–2005 (both figures taken from Frankenberg et al. (2011)).

5.2.3 Monthly Mean Retrieved CH₄ Comparison

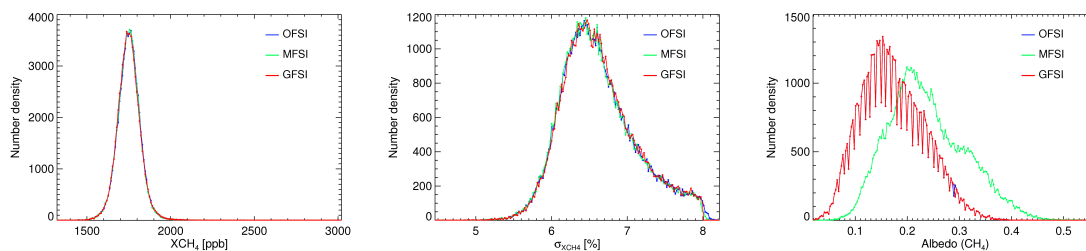


Figure 5.13: Comparison of OFSI, MFSI and GFSI distributions for matching scenes only.

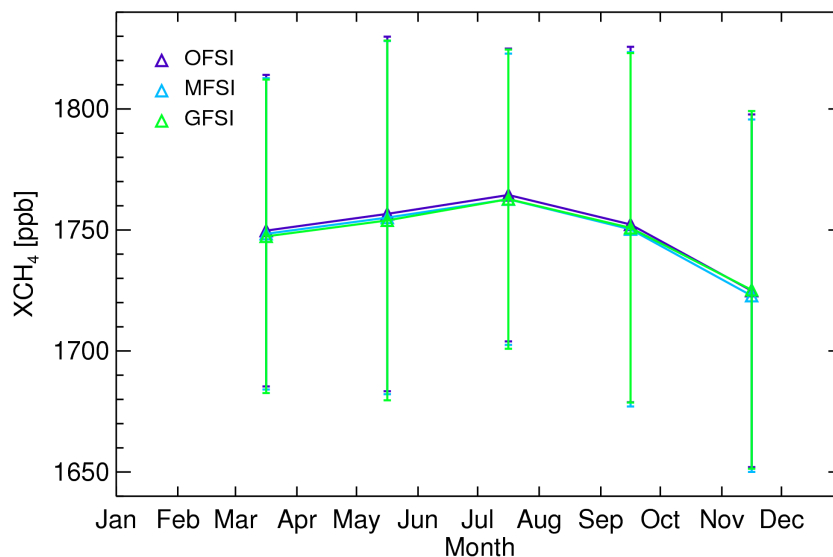


Figure 5.14: Comparison of OFSI, MFSI and GFSI monthly mean retrieved XCH₄ for matching scenes only (with 1 σ error bars).

Only retrieved XCH₄ corresponding to SCIAMACHY scenes that were processed by all three retrievals could strictly be compared. Figure 5.13 compares distributions of retrieved XCH₄, σ_{XCH_4} and a priori albedo, for matching scenes from the three separate retrievals, after the application of both Filter 1 and Filter 2. The difference in retrieved XCH₄ and σ_{XCH_4} from the three retrievals is actually quite small, despite a marked difference in the a priori albedo used in MFSI compared to the other two retrievals. Figure 5.14 shows the comparison of monthly mean retrieved XCH₄ from OFSI, MFSI and GFSI for the whole North American scene. Very little difference in the monthly mean XCH₄ between the retrieval types is observed, however both the

MFSI and GFSI retrievals appear to produce marginally lower XCH_4 than retrievals from OFSI.

GFSI is expected to produce significantly improved retrievals in regions where there is a high aerosol loading, however since aerosol concentrations over North America are not particularly high, the small difference between the retrieval schemes is not surprising. Furthermore, any localised disparity in retrieval results is likely to have been lost by averaging over such an extensive spatial region, therefore a comparison over a smaller area, or dedicated latitude bands is likely to reveal greater differences between the retrieval methods.

5.3 Validation with TCCON FTS from Park Falls

Ground based FTS retrievals of XCH_4 from the TCCON [Wunch et al. (2011)] site at Park Falls, Wisconsin, were used to validate OFSI, MFSI and GFSI retrievals. SCIAMACHY scenes were considered coincident with the TCCON site if the central latitude and longitude of the ground pixel footprint was located within a $5^\circ \times 5^\circ$ box centred on Park Falls (45.95 N, 90.27 W). Figure 5.15 compares individual XCH_4 retrievals (corresponding daily means with 1σ error bars are also shown) for OFSI (a), MFSI (b) and GFSI (c) with TCCON data. Significant spread in the data is observed even after data filtering using Filter 1 and Filter 2. However the majority of TCCON points are within the 1σ error limit of the daily means.

Figure 5.16 shows monthly mean retrieved XCH_4 (with 1σ error bars) over Park Falls from OFSI, MFSI, GFSI and TCCON for all available data points. Monthly mean XCH_4 for the OFSI and MFSI retrieval algorithms are constantly similar, with the greatest difference of ~ 15 ppb occurring in January. By comparison, monthly means from GFSI are consistently larger than those from OFSI and MFSI for the alternate months available.

In Figure 5.17 retrieved XCH_4 for GEMS matched scenes only are compared and reveals far greater agreement between the three retrieval schemes. As in Figure 5.16, monthly mean GFSI retrieved XCH_4 is consistently higher than in the OFSI and MFSI cases, with a difference of ~ 25 ppb in January, and ~ 10 – 15 ppb in May, July, September and November.

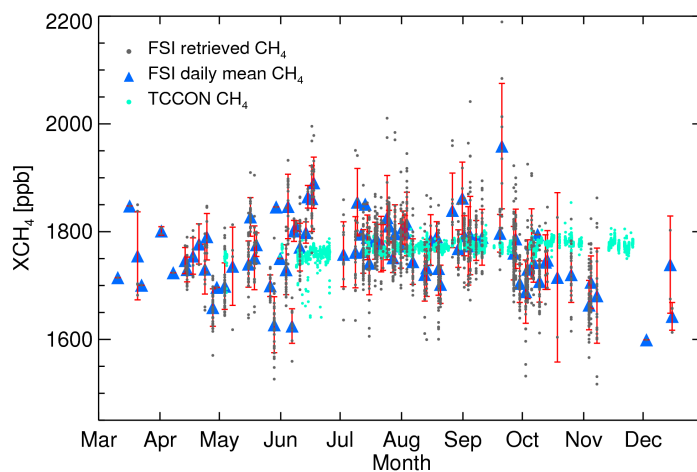
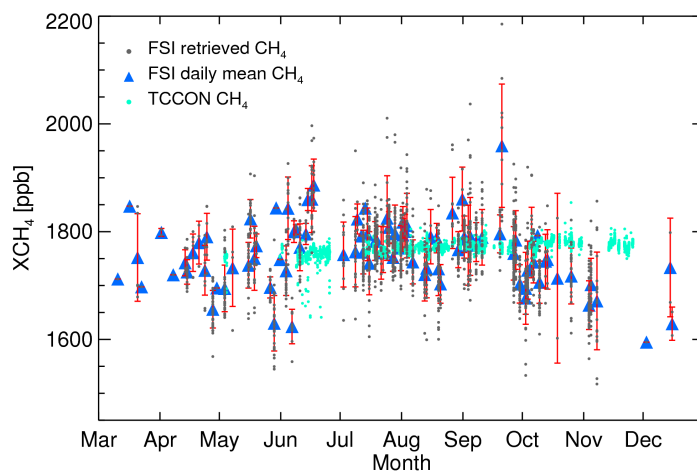
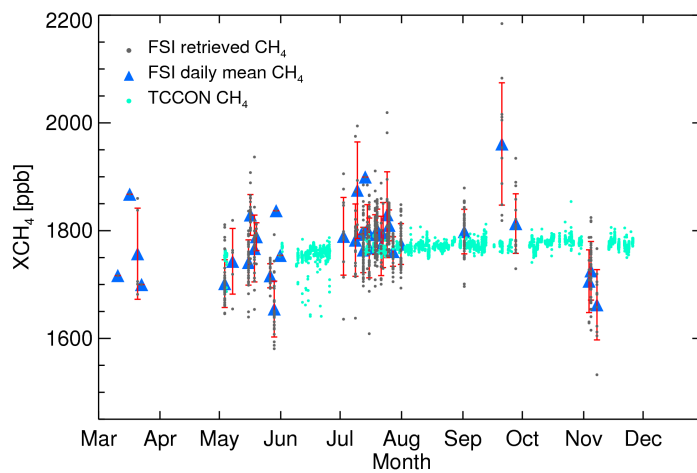
(a) TCCON XCH₄ with OFSI XCH₄(b) TCCON XCH₄ with MFSI XCH₄(c) TCCON XCH₄ with GFSI XCH₄

Figure 5.15: Comparison of TCCON FTS retrieved XCH₄ with SCIAMACHY retrieved XCH₄ over Park Falls, Wisconsin.

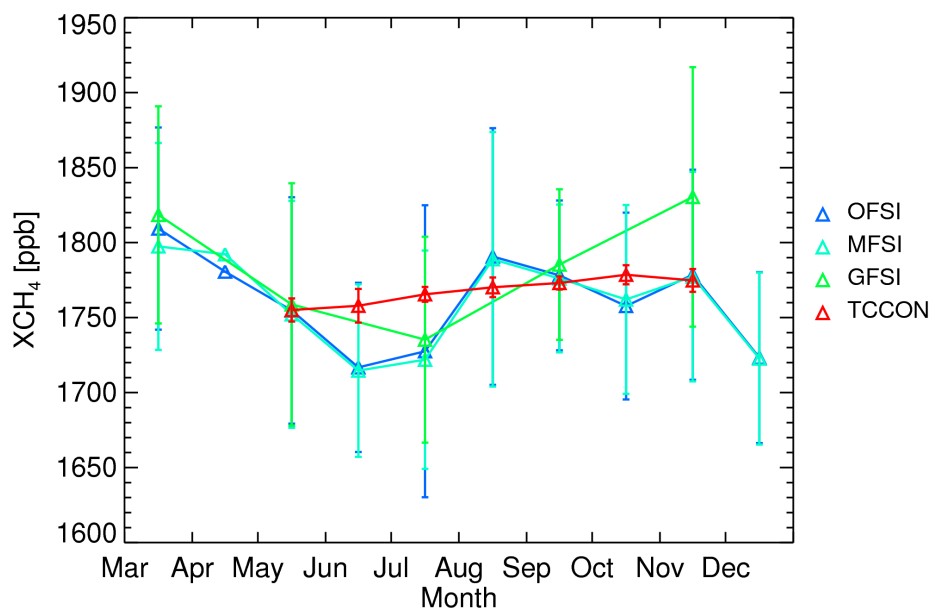


Figure 5.16: Comparison of monthly mean XCH₄ (filtered by both Filter 1 and 2) retrieved using OFSI, MFSI and GFSI with data from TCCON over Park Falls, Wisconsin.

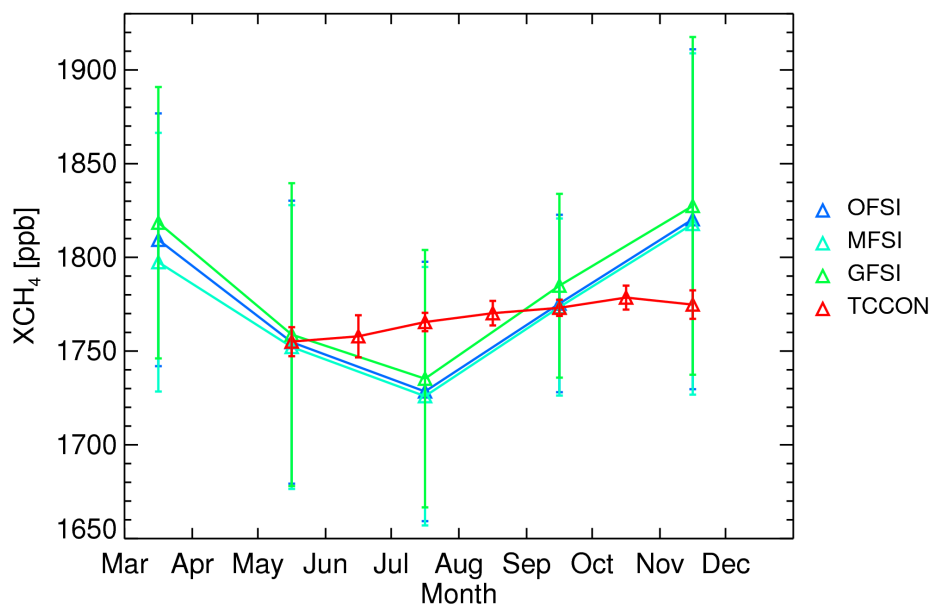


Figure 5.17: Comparison of monthly mean XCH₄ (filtered by both Filter 1 and 2) retrieved using OFSI, MFSI and GFSI with data from TCCON over Park Falls, Wisconsin, for GEMS matching scenes only.

5.4 Summary

Retrievals of XCH_4 have been performed for the year 2004 using three different versions of the FSI WFM-DOAS V2 retrieval; in its original form (OFSI), modified with a priori albedo from MODIS (MFSI) and modified with aerosol extinction calculated from GEMS MMR (GFSI). Although the number of scenes processed by each retrieval version varies due to differing methods of filtering out poor SCIAMACHY data and differences in retrieval runtime, monthly averaged XCH_4 gridded to $1^\circ \times 1^\circ$ from each of the three FSI retrievals identifies very similar areas of CH_4 enhancement. In particular, elevated XCH_4 is observed over eastern Mexico and southeast USA for the period May–September 2004. The replacement of a priori albedos from a LUT with MODIS retrieved albedo (resulting in MFSI) appears to have very little effect on the retrieved total columns. Replacement of the basic FSI WFM-DOAS V2 estimation of aerosol with detailed profiles of aerosol extinction calculated from GEMS MMR (in GFSI) appears to have noticeably reduced the monthly mean XCH_4 over eastern Mexico. However, this is likely to be an artifact of the data loss incurred by GFSI due to a large number of non-convergent runs. The similarity between retrieval results is displayed by Figure 5.14 which compares monthly mean XCH_4 from each retrieval version over the North American region. However, a better comparison may be achieved by calculating the monthly mean XCH_4 for each retrieval version over a smaller spatial extent, such as dedicated latitude bands, to avoid the loss of localised variation between individual retrievals.

In general, North America is a good region for test retrievals due to the availability of ground based measurement networks for validation purposes. However, the lack of significant aerosol contamination in this region means that it is difficult to assess the performance of aerosol a priori modifications made in GFSI. Implementation of the GFSI retrieval over areas of high AOD, such as Southeast Asia, is expected to result in significantly improved retrieval performance.

FSI WFM-DOAS V2 retrievals of XCH_4 over an area surrounding the TCCON site at Park Falls, Wisconsin, show significant scatter with respect to the TCCON XCH_4 . However, the close proximity of the Park Falls site to extensive areas of inland water (which cause insufficient light to be reflected) may account for some of the outlying results. In addition, the use of a $5^\circ \times 5^\circ$ box to classify SCIAMACHY scenes as satellite overpasses may account for some of the degree of scatter observed. SCIAMACHY retrieval results in this thesis show approximately a 3% variation

from month to month which is larger than the variation of around 1.4% apparent in TCCON data.

Chapter 6

Conclusions

6.1 Thesis Achievements

6.1.1 FSI WFM-DOAS V2 Algorithm Modifications

As outlined in Chapter 1, the aim of this thesis was to modify the FSI WFM-DOAS retrieval algorithm to perform new retrievals of CH₄ and assess the sensitivity of the new algorithm to scattering caused by aerosols and cirrus clouds. To enable the retrieval of CH₄ using FSI WFM-DOAS in the 1630–1670 nm wavelength region, the addition of an a priori CH₄ climatology and changes to the calibration of SCIAMACHY data were made. Since the main advantage of FSI is its ability to improve the linearisation of the retrieval fit by utilising a priori data tailored to each retrieval scene, the following improvements to a priori data and retrieval performance were also made:

- Updated CH₄ and H₂O spectroscopy
- New interpolation of ECMWF meteorological data
- Updated radiative transfer model (SCIATRAN 2.2) implemented
- CO₂ proxy method for CH₄ VCD normalisation implemented

The modified retrieval resulting from the combination of updates detailed above is referred to as FSI WFM-DOAS V2.

Following these initial modifications, improvements to the a priori albedo using MODIS data and the addition of a priori aerosol extinction information (derived

from GEMS MMR) were also separately implemented resulting in two additional retrieval versions; MFSI and GFSI respectively. Note: in Chapter 5, the original FSI WFM-DOAS V2 retrieval is referred to as ‘OFSI’ for ease of comparison with MFSI and GFSI.

6.1.2 Outcome and Impact of Sensitivity Tests

The three sensitivity tests undertaken in Chapter 4 reveal that:

1. Without accurate aerosol a priori information the FSI WFM-DOAS V2 retrieval produces large retrieval errors for scenes of high optical depth. Performance for low and medium aerosol scenarios was much better, but dependent on the altitude of the aerosol layer.
2. The altitude at which scattering occurs (for aerosol or ice cloud) greatly influences the magnitude of the resulting retrieval error.
3. Ice clouds result in the largest retrieval errors because of their high altitude and large optical depth.
4. High SZA and low surface albedo serve to amplify errors caused by scattering.

Large retrieval errors (ΔX_{CH_4} of up to 35%) encountered in the global sensitivity tests indicate that the proxy approach breaks down when aerosols or ice clouds, particularly of high optical depth and at high altitude, are present in a SCIAMACHY scene. Although these findings relate to the proxy approach when applied to total columns retrieved by FSI WFM-DOAS V2, the same findings are likely to apply to any retrieval method which utilises the $1.65 \mu\text{m}$ spectral region for the retrieval of CH_4 and $1.57 \mu\text{m}$ for the retrieval of CO_2 .

It should be noted that for global ice cloud simulations performed in this work, no altitude threshold was imposed on GEMS profiles of IWC, hence ice clouds were simulated for a range of altitudes between 0–20 km. Cirrus clouds generally reside between 6–18 km, therefore future simulations could ensure only clouds within this altitude range are considered in order to isolate errors due specifically to cirrus clouds.

6.1.3 FSI WFM-DOAS V2 Retrievals

Discussion of Retrieval Results

Qualitative comparison of OFSI retrievals over North America with the retrievals from WFM-DOAS version 1.0 and TM3 model CH₄ data is encouraging and shows that the elevated XCH₄ detected over southeast USA is in good agreement with existing results. Enhancements in retrieved XCH₄ observed over eastern Mexico however require further investigation. Only small differences in the retrieved XCH₄ was observed when modified albedo (MFSI) and aerosol a priori (GFSI) were used to initialise the retrieval. In the case of GFSI, this is most likely due to the lack of scenes corresponding to high AOD over North America.

The validation of retrieved XCH₄ over Park Falls, Wisconsin, shows a large degree of scatter for all retrieval versions (OFSI, MFSI and GFSI) with respect to XCH₄ retrieved from the ground based TCCON FTS. However, this was expected since the inherent precision and signal to noise ratio of SCIAMACHY measurements is far lower than for ground based FTS measurements. In general, overall agreement is apparent since TCCON measurements fall within the 1σ error bars of calculated monthly means.

Retrieval Errors

Previous retrievals have estimated the instrument noise for SCIAMACHY to be around 1.7–1.8% (see Section 3.4.1 for details). In general, the fit residual of a retrieval can be taken as a good approximation of the instrument noise since, in theory, a perfect fit should be possible if noise is not present in the measured spectrum. However, retrievals performed with OFSI, MFSI and GFSI over North America typically produce retrieval fit errors of 6–7%, pointing to an as yet undetermined fitting error. Sensitivity tests detailed in Chapter 4 involve simulated spectra which do not contain noise however analysis of σ_{XCH_4} resulting from Sensitivity Test 2 reveals that errors of up to $\sim 2\%$ are incurred in both aerosol and ice cloud simulations. This implies that the presence of scattering in a measured spectrum introduces spectral features which cannot be correctly fitted.

Figure 3.3 (third panel from top) gives an example of a typical FSI WFM-DOAS V2 fit of the $2\nu_3$ CH₄ band and reveals a clear discrepancy between the measured and modelled spectrum when fitting the Q-branch at 1666 nm. This poor fit may be the

result of neglecting line mixing since a study by Tran et al. (2010) showed that line mixing is important for CH₄ spectroscopy in the 1.67 μm spectral region. Tran et al. (2010) conclude that the use of effective line widths for the P and R branches, such as those determined by Frankenberg et al. (2008b) and implemented in FSI WFM-DOAS V2, should be adequate for the purpose of atmospheric retrievals (assuming the total pressure is less than 1 atm) for two reasons. Firstly, since SCIAMACHY measured spectra are of relatively low resolution, the use of effective line widths produces very similar retrieval residuals to those obtained when line mixing is taken into consideration (a difference of less than 0.5% is observed). Secondly, inclusion of line mixing in radiative transfer models greatly increases the computational time of the retrieval without providing significant improvement in the retrieval fit. Further work is therefore required to verify the cause of the poor spectral fit (and hence high values of σ_{XCH_4}) in FSI WFM-DOAS V2 retrievals of CH₄. However, such problems are likely to be removed by using higher spectral resolution instruments which can focus on the better understood non-Q branch lines.

Future Work

Further investigation into the source of elevated FSI WFM-DOAS V2 retrievals of XCH₄ over southeast USA and eastern Mexico is required. In particular, a more thorough comparison of retrievals with the EDGAR emissions database for 2004 would confirm whether the observed peaks in XCH₄ correspond to known CH₄ emission in these regions. In addition, a thorough comparison with independent model data from the GEOS-Chem CTM (similar to that performed by Parker et al. (2011)) would provide further validation of retrieval results.

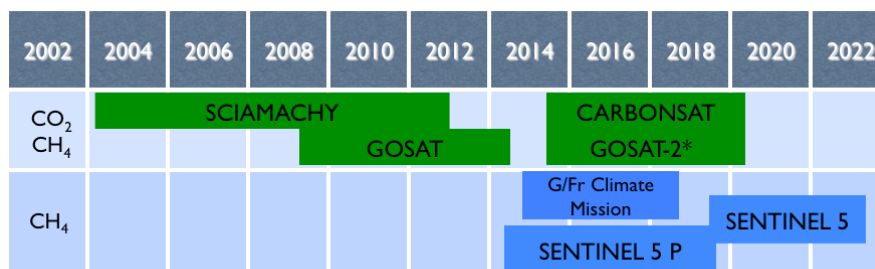
An assessment of the improvement in retrieval error owing to the inclusion of a priori GEMS aerosol could be better achieved via a comparative study of OFSI and GFSI over a region of known high AOD, such as Southeast Asia. In this case, a significant improvement in retrieval error is expected by employing GFSI. Since the impact of ice clouds has been shown to cause far greater errors than those imposed by aerosols, the identification and removal of SCIAMACHY scenes contaminated with cirrus clouds by utilising cloud data from instruments such as MERIS or the Along Track Scanning Radiometer (ATSR) is required.

Furthermore, since scattering layer altitude has been identified as an important factor in determining the magnitude of retrieval error induced, the use of lidar

measurements to provide cloud/aerosol height information would help to determine whether a scene was suitable for retrieval.

6.2 Future CH₄ Satellite Missions

Continuous global records of XCH₄ from satellite measurements are required for the analysis of long term climate trends and accurate source/sink modelling. Originally launched in 2002, SCIAMACHY's host satellite ENVISAT has now entered a period beyond its original planned lifetime and is currently executing operations in a new low-orbit configuration. Although SCIAMACHY is still operational, pixel degradation in the SWIR channel 6 post-2005 has made retrievals of CH₄ from the 1.65 μm spectral region difficult. The continuation of CH₄ measurements in the SWIR from space therefore currently relies on GOSAT's Thermal and Near-Infrared Sensor for Carbon Observation (TANSO), launched in early 2009. TANSO is comprised of two separate instruments; an FTS and the Cloud and Aerosol Imager (CAI). CO₂ and CH₄ can be retrieved from TANSO FTS Band 2 (1.56–1.72 μm) and Band 4 (5.56–14.3 μm).



*GOSAT-2 mission definition review will be in 2010, and request budget for start pre-project in 2011.

Figure 6.1: Timeline of present and planned space based missions sensitive to CH₄ in the planetary boundary layer (figure adapted from Ciais et al. (2010)). Note: CarbonSat and GOSAT-2 are currently both *proposed* missions and, only if confirmed, are likely to be launched around 2018.

Figure 6.1 shows the operational lifetimes of current and future satellite missions with sensitivity to CH₄ in the planetary boundary layer. The Sentinel 5 Precursor mission is due to be launched in 2014 and will carry the Tropospheric Monitoring Instrument (TROPOMI). TROPOMI is a UV-Vis-NIR-SWIR push-broom grating spectrometer with five targeted channels within the spectral ranges of 260–495 nm,

710–775 nm and 2314–2382 nm with spectral resolutions ranging from 0.25–1.1 nm. Retrievals of XCH₄ will be possible using the mid-infrared channel. TROPOMI will provide nadir measurements with a ground pixel size of 7×7 km² and achieve global coverage daily. CarbonSat [Bovensmann et al. (2010)] is an ESA mission, proposed to be launched in 2018, which would observe the atmosphere in nadir and sunglint modes with a footprint size of 2×2 km². CarbonSat would be able to achieve a precision of less than 2 ppb for retrievals of XCO₂ and 13 ppb for XCH₄, and also includes an imager for cloud filtering.

One of the key criteria for future satellite missions intended to observe CH₄ is that high spatial resolution is achieved in an effort to minimise cloud contamination [Ciais et al. (2010)]. In addition to reducing cloud contamination, the combination of high resolution passive measurements with high precision lidar measurements on a single space-based platform would provide an effective means of observing localised emissions and thus improving CH₄ source/sink estimates [Ciais et al. (2010)].

Appendix

A Basic Molecular Spectroscopy

The interaction of radiation with matter at the molecular level, and the exchange of energy that takes place therein, requires the use of quantum mechanics since a classical treatment is not sufficient to describe such small scale systems. In QM the position and momentum of a particle cannot be simultaneously known precisely therefore these properties are described by a wavefunction, Ψ , which effectively gives the *probability* of a particle having a given position and momentum.

The constituent electrons and nuclei of a molecule possess charge and move under the influence electrostatic forces. Since electrons are much smaller in size than nuclei, yet the magnitude of the electrostatic force acting on them is comparable, electrons are forced to move at great speed whereas the nuclei move very little and to a good approximation can be considered as fixed in space. By treating the nuclei within a molecule to be fixed with respect to the electrons, the resulting wavefunction can be separated into electronic and nuclear terms, where the nuclear term can be further split into vibrational and rotational components. The separation of a wavefunction into separate components each corresponding to processes associated with different energies is known as the Born-Oppenheimer approximation:

$$\Psi_{\text{tot}} = \Psi_e(q_e)\Psi_{\text{nuc}}(q_{\text{nuc}}) = \Psi_e(q_e)\Psi_{\text{vib}}(q_{\text{vib}})\Psi_{\text{rot}}(q_{\text{rot}}), \quad (\text{A1})$$

Since the wavefunctions can be separated, the associated energies of these processes can be separated also:

$$E_{\text{Tot}} = E_e + E_{\text{vib}} + E_{\text{rot}}. \quad (\text{A2})$$

The electronic term E_e relates to the excitation of electrons within the molecule and can be treated as independent of the nuclear behavior. Molecular vibration (E_{vib}) is the periodic change in bond length between nuclei about an equilibrium position and molecular rotation (E_{rot}) refers to the change in angular momentum of the molecule with respect to a fixed, external coordinate system. The energies associated with these three mechanisms form a distinct hierarchy; electronic transitions are the most energetic involving radiation of UV wavelengths, vibrational transitions emit radiation in the IR region of the spectrum and rotational transitions involve photons in the microwave region.

A1 Rotational Transitions

The electric dipole moment quantifies the asymmetry of charge within a molecule and must be non-zero for rotational spectroscopic transitions to occur; a rotating electric dipole moment produces the electric field necessary for interactions with electromagnetic radiation (of the same frequency) to take place. For a simple diatomic molecule the rotational energy levels are given by the simple equation $E_{\text{rot}} = BJ(J + 1)$ where B is the rotational constant and $J = 0, 1, 2, \dots$. As a molecule rotates faster due to the absorption of energy the bond length r increases due to increasing centrifugal force. Since molecular bonds behave elastically, the stretching that occurs as J increases induces an oscillation in bond length. Taking centrifugal distortion into account, the energy levels of a rotating diatomic molecule are given by the following equation:

$$E_{\text{rot}} = BJ(J + 1) - DJ^2(J + 1)^2 + HJ^3(J + 1)^3 + KJ^4(J + 1)^4 \dots, \quad (\text{A3})$$

where the second term on the right hand side of is a correction required to account for centrifugal distortion and D is the centrifugal force constant, in cm^{-1} , given by:

$$D = \frac{\hbar^3}{32\pi^4 I^2 r^2 k c}. \quad (\text{A4})$$

The second term in Equation A3 only accounts for simple harmonic oscillations induced by centrifugal distortion, therefore all additional terms allow for anharmonic oscillations of the diatomic molecular bond. The coefficients of the anharmonic correction terms (i.e. H , K , etc) are related to the geometry of the molecule but are vanishing small for a diatomic molecule when compared with D .

The rotation of a polyatomic molecule is best described by its three principle moments of inertia; I_A , I_B and I_C , corresponding to a set of perpendicular axes. CO_2 is a linear molecule, that is, its constituent atoms are connected in a straight line. For linear molecules the moment of inertia about axis A is negligible compared to that about axes B and C and can be approximated to zero. Linear molecules are therefore defined by $I_B = I_C$, $I_A = 0$ which is the same as for a simple diatomic molecule. As a result, the energy levels of a linear molecule are also described by Equation A3.

A2 Vibrational Transitions

Molecular bonds are not rigid but elastic and as a result the bond length is allowed to oscillate about a mean length during rotation. In addition to oscillations induced by centrifugal distortion, the constituent atoms of a molecule inherently vibrate about an equilibrium position. In an idealised, simple harmonic model of molecular vibration, the molecular bond can stretch indefinitely and subsequently gives rise to an infinite set of equally spaced energy levels. In reality however molecular vibration is anharmonic, therefore a bond can only be stretched a finite amount, beyond which the constituent atoms will disassociate. The energy levels relating to anharmonic oscillations, is given by:

$$E_{\text{vib}} = h\omega_e \left(\nu + \frac{1}{2} \right) - h\omega_e x_e \left(\nu + \frac{1}{2} \right)^2. \quad (\text{A5})$$

For polyatomic molecules various vibrational configurations are possible. In general, linear molecules possess $3N - 5$ normal modes of vibration and non-linear molecules possess $3N - 6$, where N is simply the number of constituent atoms.

A3 Vibration-Rotation Transitions

Using the Born-Oppenheimer approximation, the combined energy of vibration-rotation levels ($E_{J,\nu}$) is given by a sum of their separate energies;

$$E_{J,\nu} = E_{\text{vib}} + E_{\text{rot}} = BJ(J+1) + h\omega_e \left(\nu + \frac{1}{2} \right) - h\omega_e x_e \left(\nu + \frac{1}{2} \right)^2. \quad (\text{A6})$$

The energy of a transition between levels is given by the difference in energies, denoted ΔE . For an R-branch transition this is given by:

$$\begin{aligned} \Delta E[R(J)] &= \Delta E = E_1 - E_0 \\ &= \Delta E_{\text{vib}} + 2B(J+1) \end{aligned} \quad (\text{A7})$$

The equivalent P-branch transition is as follows:

$$\begin{aligned} \Delta E[P(J)] &= \Delta E = E_0 - E_1 \\ &= \Delta E_{\text{vib}} - 2BJ. \end{aligned} \quad (\text{A8})$$

B SCIATRAN 2.2

SCIATRAN is a computational software package which includes both atmospheric trace gas retrieval and radiative transfer model capabilities. SCIATRAN was created specifically for use with/ simulation of spectra from the space-borne passive UV-Vis-NIR-SWIR spectrometers GOME and SCIAMACHY covering the spectral range 240-2400nm, but can also be used for much wider applications. Within this thesis work SCIATRAN has been used solely for the simulation of SCIAMACHY-like spectra, firstly for the creation of reference spectra within FSI WFM-DOAS V2 and secondly for the creation of synthetic SCIAMACHY spectra with which to test the sensitivity of the FSI WFM-DOAS V2 retrieval to various atmospheric conditions.

The atmospheric trace gases CO₂ and CH₄ are classified as ‘line absorbers’ which means that their absorption bands are heavily dependent on ambient temperature and pressure. As a result the consideration of these gases within SCIATRAN requires absorption data from a spectral database, here obtained from HITRAN 2004 with updates for the CH₄ and H₂O spectroscopy (Frankenberg et al, 2009).

Clouds can be defined in SCIATRAN by a number of different methods however within this work the optical depth, τ was used as the defining parameter, from which all other parameters were then calculated. For a given value of τ and either a default or user supplied cloud profile $S(z)$, the vertical profile of the extinction coefficient κ_e is given by:

$$\kappa_e(z) = \frac{\tau S(z)}{\int_{h_b}^{h_t} S(z) dz}. \quad (\text{B1})$$

The corresponding profile of scattering coefficients is then calculated from κ_e and the user supplied values of single scattering albedo ω ; $\kappa_s(z) = \kappa_e(z)\omega$.

Input	Required parameters and format
Trace gas	For 'line absorbers' CO ₂ and CH ₄ Trace gas replacement file
Aerosol	<p>Aerosol control file (man_aer.inp) containing vertical profiles of: Extinction [km⁻¹] Absorption [km⁻¹]</p> <p>For each layer of the aerosol profile a file containing the aerosol phase function moments as a series of Legendre series expansion coefficients is required.</p>
Cloud	<p>Individual clouds are defined as 'cloud layers' within the cloud control file (cloud.inp). For each cloud layer the following data is required:</p> <p>Cloud base and top altitude [km]</p> <p>For 'TAU' integral input parameter: Optical depth [-]</p> <p>File containing vertical profiles of the following cloud layer parameters: Dimensionless height variable of cloud sub-layer Shape of the ice water content profile (arbitrary units)</p> <p>Cloud layer phase function file containing: Extinction coefficient Scattering coefficient Moments of the phase function</p>

Table B1: Description of specialised parameters required as input into SCIATRAN.

C Retrieval Parameters and Data

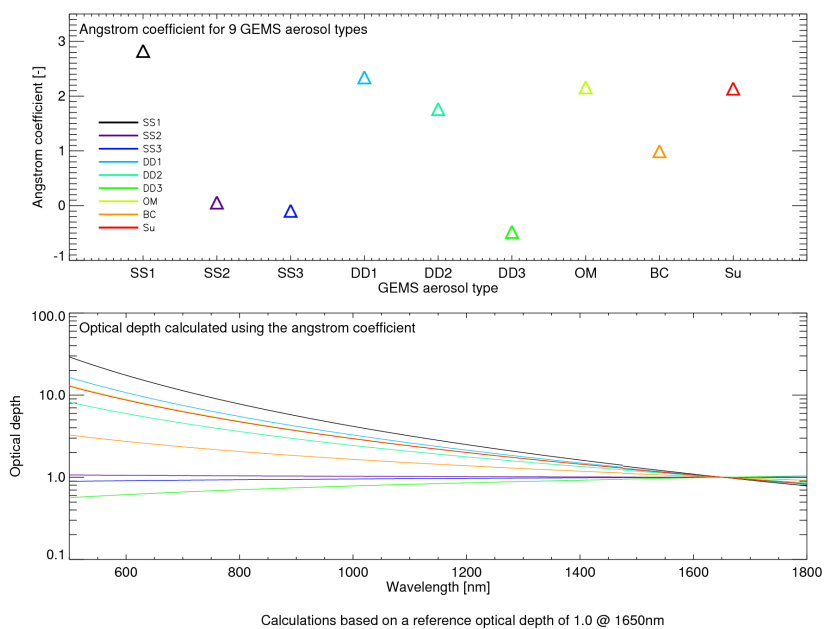


Figure C1: Value of α for 9 GEMS aerosol types computed by taking the mean of α values computed for one days worth of global GEMS data (corresponding to 01/10/2004). Calculations were based on a reference optical depth of $\tau = 1$ at 1650 nm.

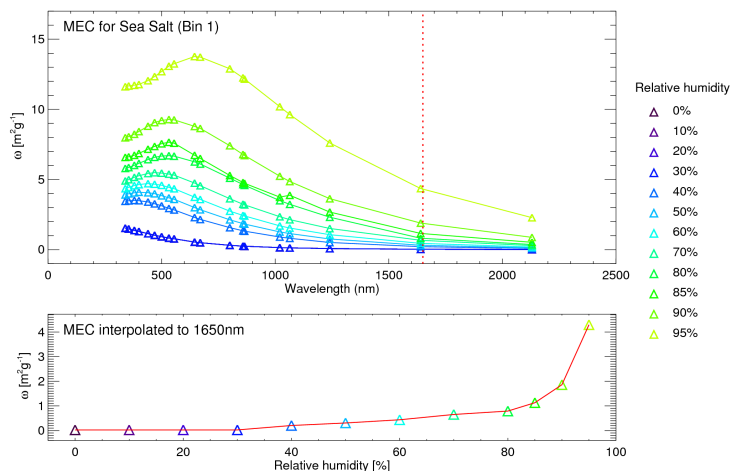


Figure C2: Mass extinction coefficients (ω) for the RH dependent GEMS sea salt particle size bin 1. The upper plot displays ω for all RH and λ values whereas the lower plot shows ω interpolated to a specific λ , for all values of RH.

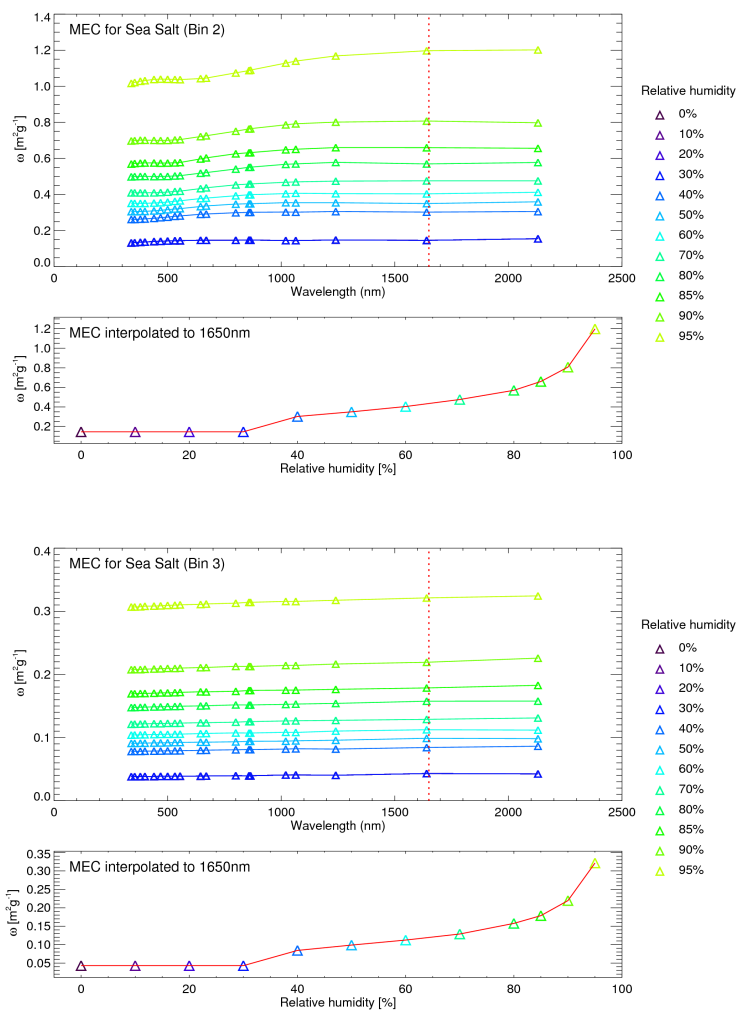


Figure C3: Mass extinction coefficients (ω) for RH dependent GEMS sea salt particle size bins 2 and 3. The upper plot in each panel displays ω for all RH and λ values; the lower plot shows ω interpolated to a specific λ , for all values of RH.

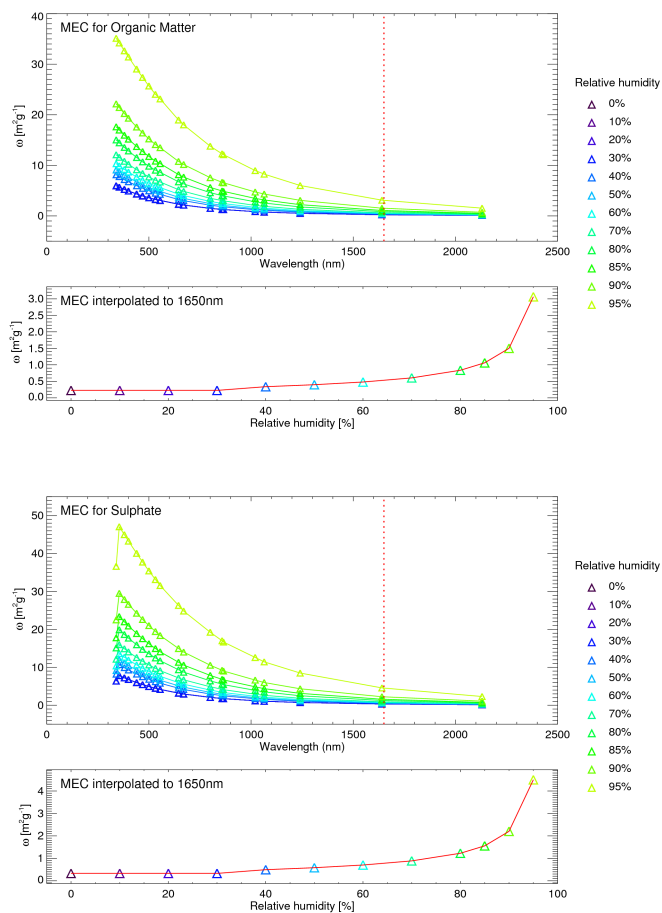


Figure C4: Mass extinction coefficients (ω) for RH dependent aerosols; organic matter (top panel), sulphate (bottom panel).

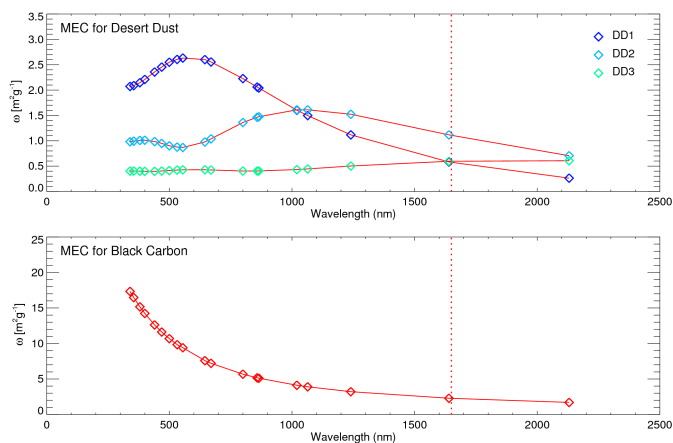


Figure C5: Mass extinction coefficients (ω) for non-RH dependent aerosols; desert dust (top) and black carbon (bottom).

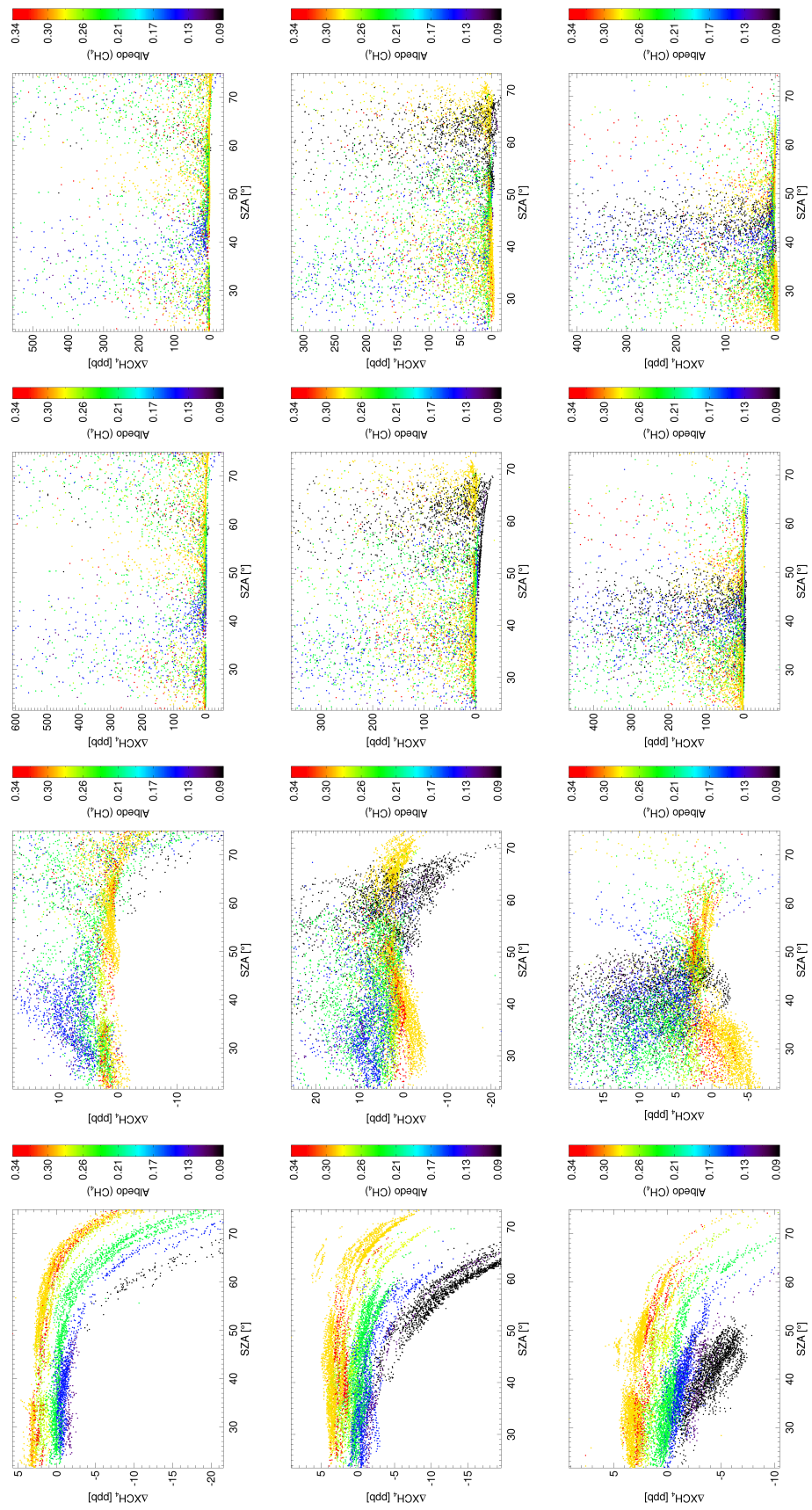


Figure C6: Scatter plots of ΔXCH_4 against SZA for all simulation cases (from top to bottom; background, cirrus, aerosol, cirrus + aerosol) in each of the four months January, April, July and October 2004 (left to right).

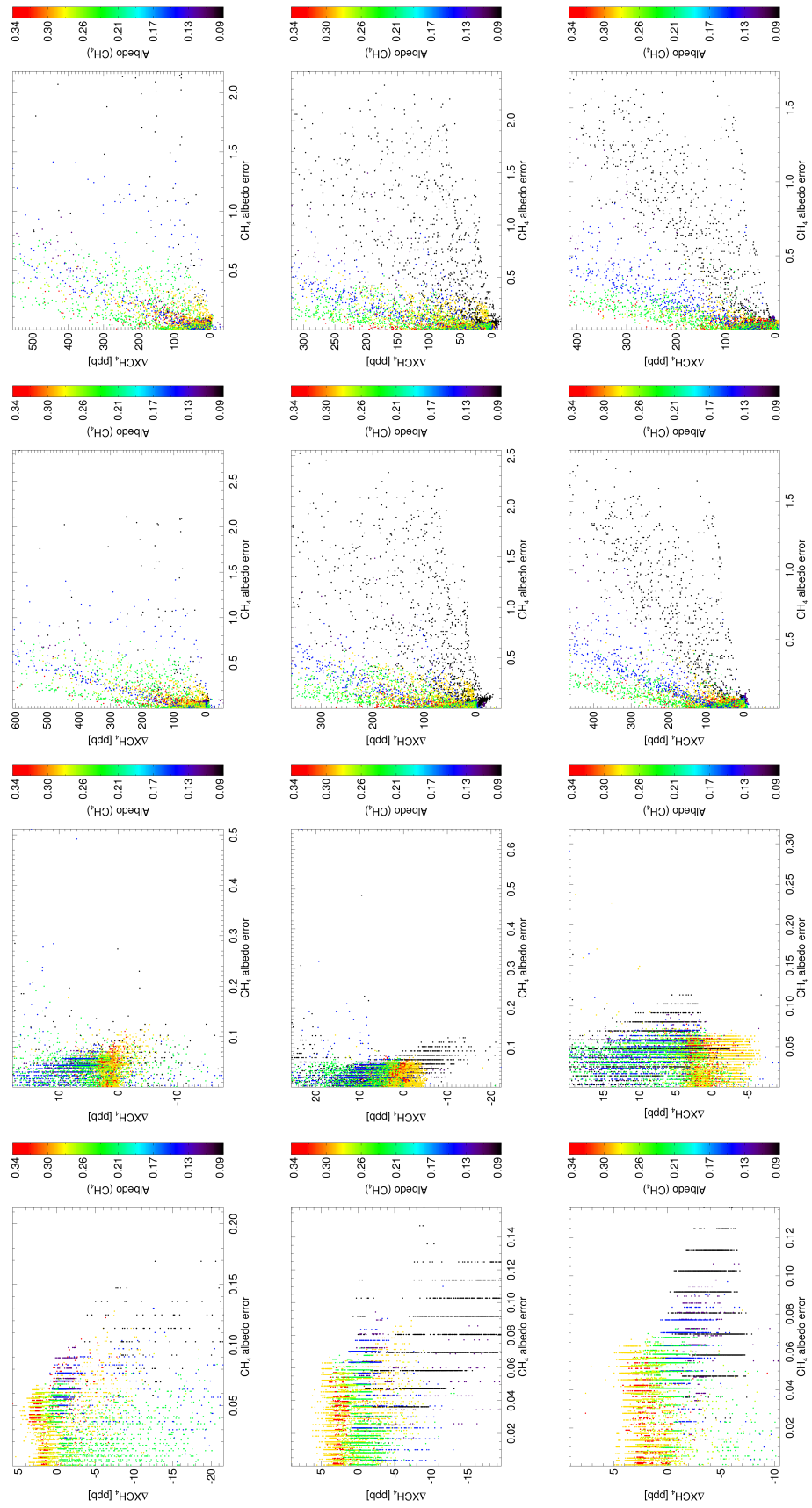


Figure C7: ALL CASES: Scatter plots of ΔXCH_4 against the error on CH_4 and CO_2 albedo estimation using the FSI look-up table method

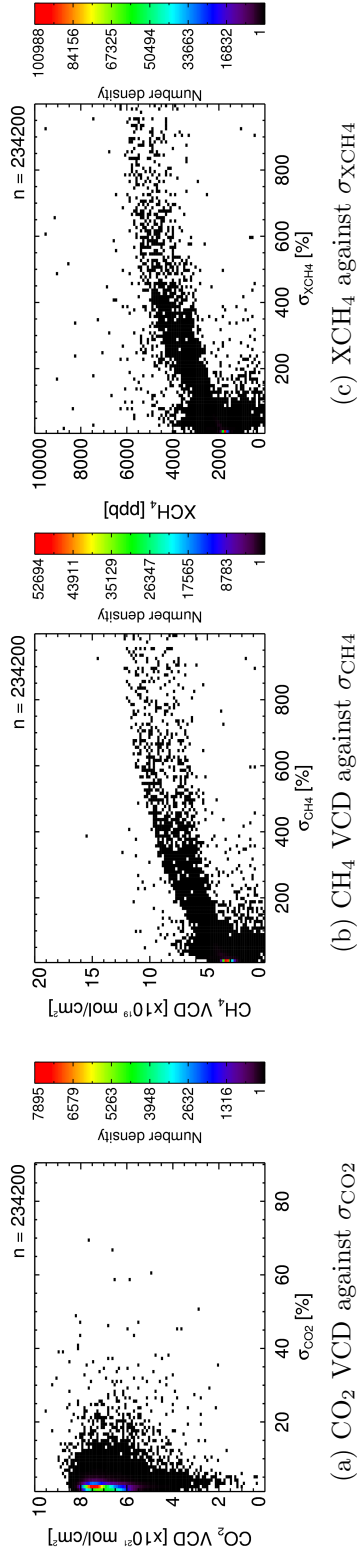


Figure C8: Density correlation plots of σ_{CO_2} , σ_{CH_4} and σ_{XCH_4} from the MFSI retrieval once filtered by Filter 1.

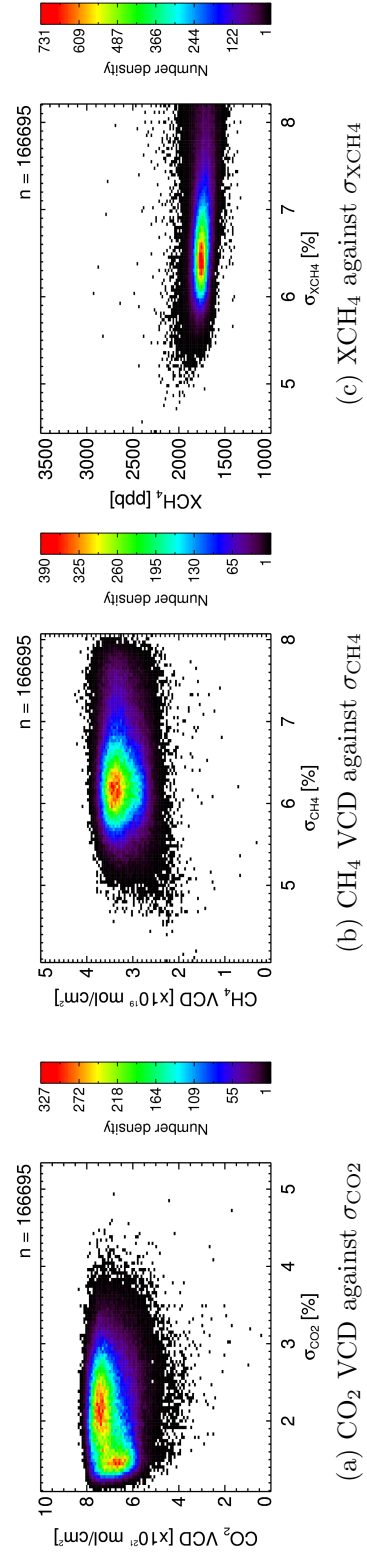


Figure C9: Density correlation plots of σ_{CO_2} , σ_{CH_4} and σ_{XCH_4} from the MFSI retrieval once filtered by Filter 2.

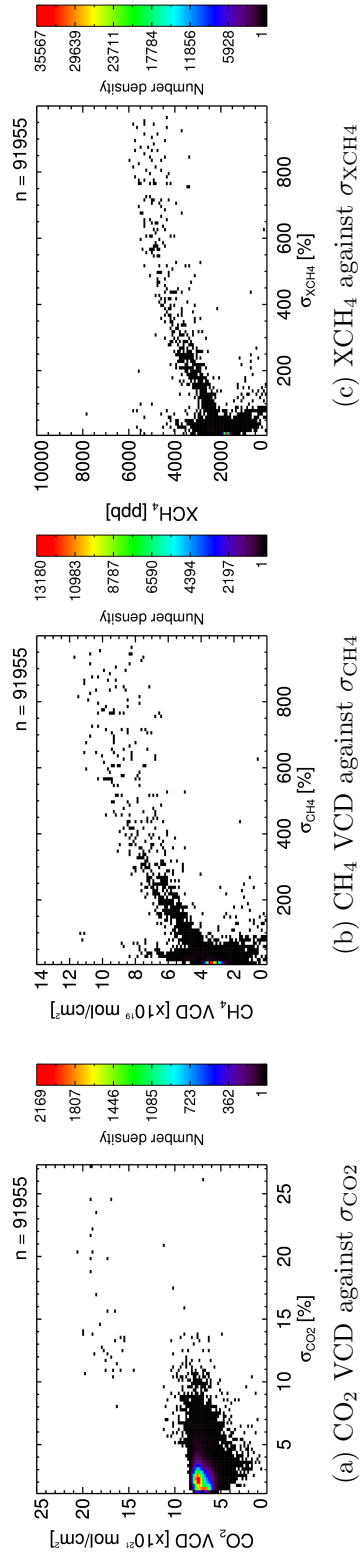


Figure C10: Density correlation plots of σ_{CO_2} , σ_{CH_4} and σ_{XCH_4} from the GFSI retrieval once filtered by Filter 1.

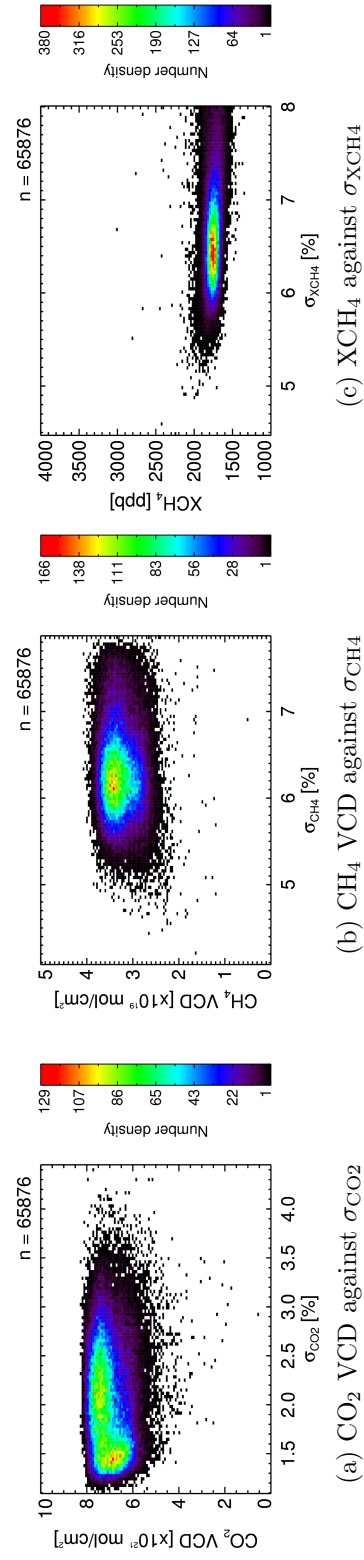


Figure C11: Density correlation plots of σ_{CO_2} , σ_{CH_4} and σ_{XCH_4} from the GFSI retrieval once filtered by Filter 2.

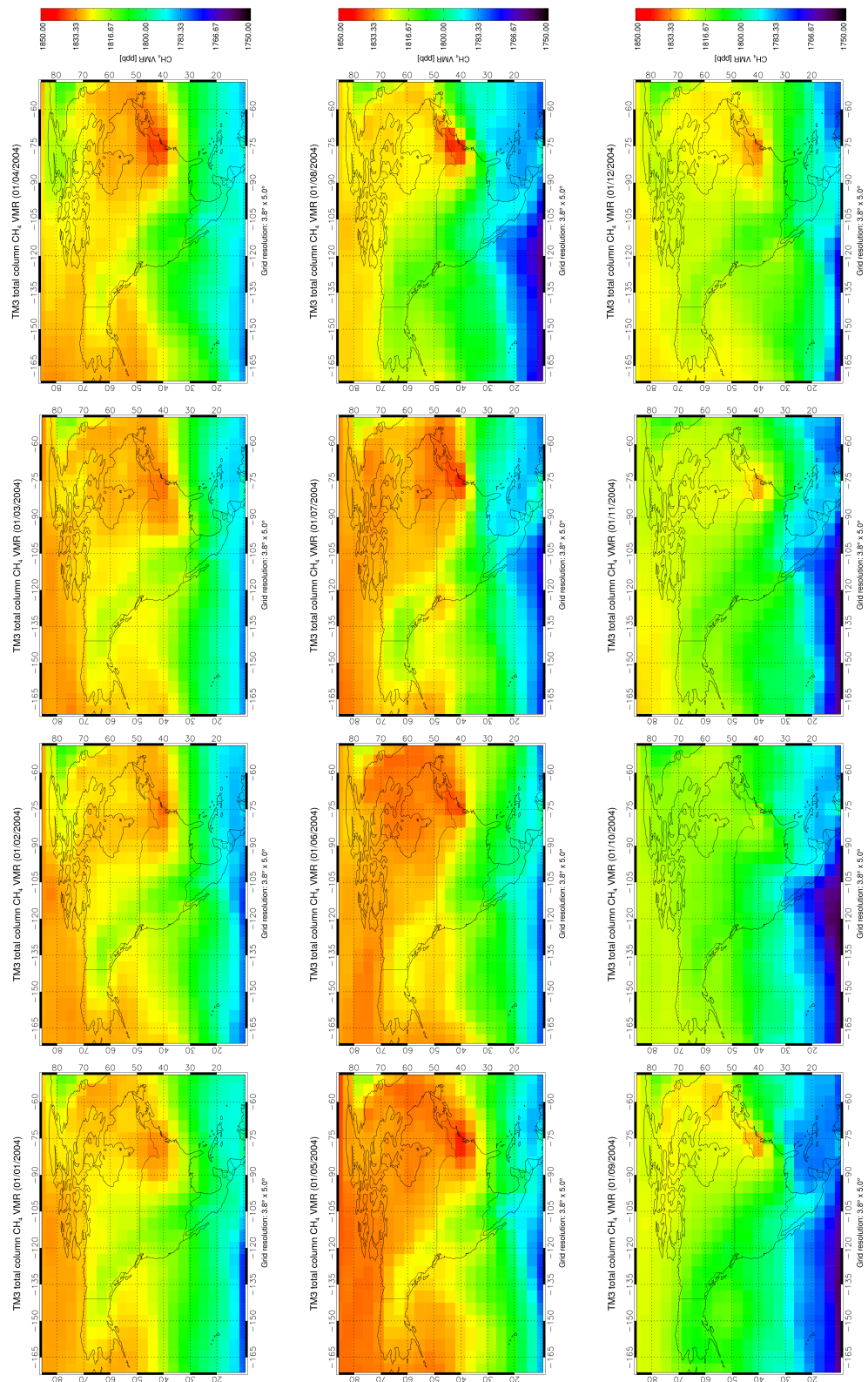


Figure C12: Total column CH₄ for the first day of each month of 2004 gridded to 3.8° × 5°

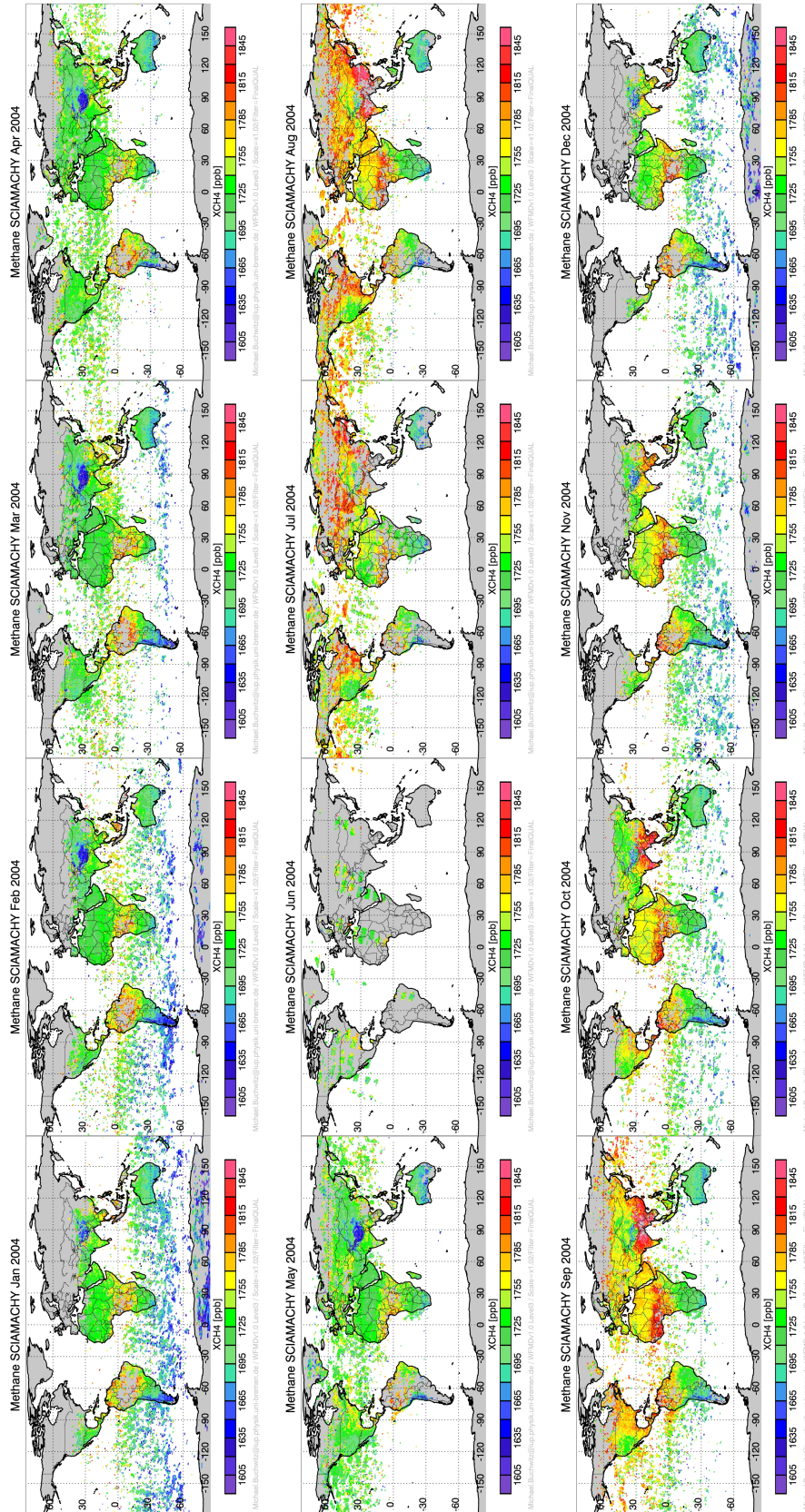


Figure C13: Monthly averaged total column CH₄ retrieved by WFM-DOAS version 1.0, gridded to 1° × 10° [Buchwitz (2007)].

References

- Andrews, D. G.: An introduction to atmospheric physics, Cambridge University Press, Cambridge, UK, 2000.
- Baede, A. P. M., Ahlonsou, E., Ding, Y., and Schimel, D.: The climate system: an overview. In: Climate change 2001: The scientific basis. Contribution of Working Group I to the Third Assessment Report of the Intergovernmental Panel on Climate Change, 2001.
- Banwell, C. N. and McCash, E. M.: Fundamentals of molecular spectroscopy, Tata McGraw-Hill Publishing Company, New Delhi, fourth edn., 1994.
- Barkley, M.: Measuring atmospheric carbon dioxide from space, PhD Thesis, 2007.
- Barkley, M. P., Frieß, U., and Monks, P. S.: Measuring atmospheric CO₂ from space using Full Spectral Initiation (FSI) WFM-DOAS, Atmospheric Chemistry and Physics, 6, 3517–3534, 2006.
- Barkley, M. P., Monks, P. S., Hewitt, A. J., Machida, T., Desai, A., Vinnichenko, N., Nakazawa, T., Arshinov, M. Y., Fedoseev, N., and Watai, T.: Assessing the near surface sensitivity of SCIAMACHY atmospheric CO₂ retrieved using (FSI) WFM-DOAS, Atmospheric Chemistry and Physics, 7, 3597–3619, 2007.
- Baum, B. A.: Ice cloud bulk scattering models in the visible (VIS) to shortwave infrared (SWIR) spectral region, http://www.ssec.wisc.edu/~baum/Cirrus/Solar_Spectral_Models.html, 2010.
- Bergamaschi, P. and Bousquet, P.: Estimating sources and sinks of methane: an atmospheric view. In: The continental-scale greenhouse gas balance of Europe, 2008.
- Bösch, H., Toon, G. C., Sen, B., Washenfelder, R. A., Wennberg, P. O., Buchwitz, M., de Beek, R., Burrows, J. P., Crisp, D., Christi, M., Connor, B. J., Natraj,

- V., and Yung, Y. L.: Space-based near-infrared CO₂ measurements: Testing the Orbiting Carbon Observatory retrieval algorithm and validation concept using SCIAMACHY observations over Park Falls, Wisconsin, *Journal of Geophysical Research*, 111, 2006.
- Bousquet, P., Ciais, P., Miller, J. B., Dlugokencky, E. J., Hauglustaine, D. A., Prigent, C., Van der Werf, G. R., Peylin, P., Brunke, E. G., Carouge, C., Langenfelds, R. L., Lathière, J., Papa, F., Ramonet, M., Schmidt, M., Steele, L. P., Tyler, S. C., and White, J.: Contribution of anthropogenic and natural sources to atmospheric methane variability, *Nature*, 443, 439–443, 2006.
- Bovensmann, H., Burrows, J. P., Buchwitz, M., Frerick, J., Noël, S., and Rozanov, V. V.: SCIAMACHY: Mission objectives and measurement modes, *Journal of the Atmospheric Sciences*, 56, 1999.
- Bovensmann, H., Buchwitz, M., Burrows, J. P., Reuter, M., Krings, T., Gerilowski, K., Schneising, O., Heymann, J., Tretner, A., and Erzinger, J.: A remote sensing technique for global monitoring of power plant CO₂ emissions from space and related applications, *Atmospheric Measurement Techniques*, 3, 781–811, 2010.
- BREMEN, I.-I.: SCIAMACHY on ENVISAT, <http://www.iup.uni-bremen.de/sciamachy/>, accessed 09/2011.
- Buchwitz, M.: Methane from SCIAMACHY: WFM-DOAS version 1.0: Year 2004, http://www.iup.uni-bremen.de/sciamachy/NIR_NADIR_WFM_DOAS/wfmd_CH4v1_figs_2004.html, accessed 09/2011, 2007.
- Buchwitz, M., Vladimir, V., Rozanov, V., and Burrows, J. P.: A near-infrared optimized DOAS method for the fast global retrieval of atmospheric CH₄, CO, CO₂, H₂O, and N₂O total column amounts from SCIAMACHY Envisat-1 nadir radiances, *Journal of Geophysical Research*, 105, 231–245, 2000.
- Buchwitz, M., de Beek, R., Burrows, J. P., Bovensmann, H., Warneke, T., Notholt, J., Meirink, J. F., Goede, A. P. H., Bergamaschi, P., Körner, S., Heimann, M., and Schulz, A.: Atmospheric methane and carbon dioxide from SCIAMACHY satellite data: Initial comparison with chemistry and transport models, *Atmospheric Chemistry and Physics*, 5, 2005a.
- Buchwitz, M., de Beek, R., Noël, S., Burrows, J. P., Bovensmann, H., Bremer, H., Bergamaschi, P., Körner, S., and Heimann, M.: Carbon monoxide, methane and

- carbon dioxide columns retrieved from SCIAMACHY by WFM-DOAS: Year 2003 initial data set, *Atmospheric Chemistry and Physics*, 5, 2005b.
- Burrows, J. P., Hölzle, E., Goede, A. P. H., Visser, H., and Fricke, W.: SCIAMACHY- Scanning Imaging Absorption Spectrometer for Atmospheric Chartography, *Acta Astronautica*, 7, 445–451, 1995.
- Butz, A., Hasekamp, O. P., Frankenberg, C., Vidot, J., and Aben, I.: CH₄ retrievals from space-based solar backscatter measurements: Performance evaluation against simulated aerosol and cirrus loaded scenes, *Journal of Geophysical Research*, 115, 2010.
- Chen, Y. H. and Prinn, R. G.: Estimation of atmospheric methane emissions between 1996 and 2001 using a three-dimensional global chemical transport model, *Journal of Geophysical Research*, 111, 2006.
- Ciais, P., Dolman, A. J., Dargaville, R., Barrie, L., Bombelli, A., Butler, J., Canadell, P., and Moriyama, T.: GEO Carbon Strategy, Technical report- version 1, Group on Earth Observations, editing by John Gash, 2010.
- Crevoisier, C., Nobileau, D., Fiore, A. M., Armante, R., Chédin, A., and Scott, N. A.: Tropospheric methane in the tropics first year from IASI hyperspectral infrared observations, *Atmospheric Chemistry and Physics*, 9, 6337–6350, 2009.
- Davies, C. N.: Size distribution of atmospheric particles, *Aerosol Science*, 5, 293–300, 1974.
- Denman, K. L., Brasseur, G., Chidthaisong, A., Ciais, P., Cox, P. M., Dickinson, R. E., Hauglustaine, D., Heinze, C., Holland, E., Jacob, D., Lohmann, U., Ramachandran, S., da Silva Dias, P. L., Wofsy, S. C., and Zhang, X.: Couplings between changes in the climate system and biogeochemistry. In: *Climate change 2007: The physical science basis. Contribution of Working Group I to the Fourth Assessment Report of the Intergovernmental Panel on Climate Change*, 2007.
- Dlugokencky, E. J., Houweling, S., Bruhwiler, L., Masarie, K. A., Lang, P. M., Miller, J. B., and Tans, P. P.: Atmospheric methane levels off: Temporary pause or a new steady state?, *Geophysical Research Letters*, 30, 2003.
- Dlugokencky, E. J., Bruhwiler, L., White, J. W. C., Emmons, L. K., Novelli, P. C., Montzka, S. A., Masarie, K. A., Lang, P. M., Crotwell, A. M., Miller, J. B., and

- Gatti, L. V.: Observational constraints on recent increases in the atmospheric CH₄ burden, *Geophysical Research Letters*, 36, 2009.
- Dueck, T. A., de Visser, R., Poorter, H., Persijn, S., Gorissen, A., de Visser, W., Schapendonk, A., Verhagen, J., Snel, J., Harren, F. J. M., Ngai, A. K. Y., Verstappen, F., Bouwmeester, H., Voesenek, L. A. C. J., and van der Werf, A.: No evidence for substantial aerobic methane emission by terrestrial plants: a ¹³C-labelling approach, *New Phytologist*, 175, 29–35, 2007.
- Ejiri, M. K., Terao, Y., Sugita, T., Nakajima, H., Yokota, T., Toon, G. C., Sen, B., Wetzel, G., Oelhaf, H., Urban, J., Murtagh, D., Irie, H., Saitoh, N., Tanaka, T., Kanzawa, H., Shiotani, M., Aoki, S., Hashida, G., Machida, T., Nakazawa, T., Kobayashi, H., and Sasano, Y.: Validation of the Improved Limb Atmospheric Spectrometer-II (ILAS-II) Version 1.4 nitrous oxide and methane profiles, *Journal of Geophysical Research*, 111, 2006.
- Forster, P. V., Ramaswamy, P., Artaxo, T., Berntsen, R., Betts, R., Fahey, D. W., Haywood, J., Lean, J., Lowe, D. C., Myhre, G., Nganga, J., Prinn, R., Raga, G., Schulz, M., and van Dorland, R.: Changes in atmospheric constituents and in radiative forcing. In: *Climate change 2007: The physical science basis. Contribution of Working Group I to the Fourth Assessment Report of the Intergovernmental Panel on Climate Change*, 2007.
- Frankenberg, C., Meirink, J. F., van Weele, M., Platt, U., and Wagner, T.: Assessing methane emissions from global space-borne observations, *Science*, 308, 1010–1014, 2005a.
- Frankenberg, C., Platt, U., and Wagner, T.: Iterative maximum a posteriori (IMAP)-DOAS for retrieval of strongly absorbing trace gases: Model studies for CH₄ and CO₂ retrieval from near infrared spectra of SCIAMACHY onboard ENVISAT, *Atmospheric Chemistry and Physics*, 5, 9–22, 2005b.
- Frankenberg, C., Meirink, J. F., Bergamaschi, P., Goede, A. P. H., Heimann, M., Körner, S., Platt, U., van Weele, M., and Wagner, T.: Satellite cartography of atmospheric methane from SCIAMACHY on board ENVISAT: Analysis of the years 2003 and 2004, *Journal of Geophysical Research*, 111, 2006.
- Frankenberg, C., Bergamaschi, P., Butz, A., Houweling, S., Meirink, J. F., Notholt, J., Petersen, A. K., Schrijver, H., Warneke, T., and Aben, I.: Tropical methane

- emissions: A revised view from SCIAMACHY onboard ENVISAT, *Geophysical Research Letters*, 35, 2008a.
- Frankenberg, C., Warneke, T., Butz, A., Aben, I., Hase, F., Spietz, P., and Brown, L. R.: Pressure broadening in the $2\nu_3$ band of methane and its implication on atmospheric retrievals, *Atmospheric Chemistry and Physics*, 8, 5061–5075, 2008b.
- Frankenberg, C., Aben, I., Bergamaschi, P., Dlugokencky, E. J., van Hees, R., Houweling, S., van der Meer, P., Snel, R., and Tol, P.: Global column-averaged methane mixing ratios from 2003 to 2009 as derived from SCIAMACHY: Trends and variability, *Journal of Geophysical Research*, 116, 2011.
- Gloudemans, A. M. S., Schrijver, H., Kleipool, Q., van den Broek, M. M. P., Straume, A. G., Lichtenberg, G., van Hees, R. M., Aben, I., and Meirink, J. F.: The impact of SCIAMACHY near-infrared instrument calibration on CH₄ and CO total columns, *Atmospheric Chemistry and Physics*, 5, 2369–2383, 2005.
- Gottwald, M., Bovensmann, H., Lichtenberg, G., Noël, S., von Bargaen, A., Slijkhuis, S., Piders, A., Hoogeveen, R., von Savigny, C., Buchwitz, M., Kokhanovsky, A., Richter, A., Rozanov, A., Holzer-Popp, T., Bramstedt, K., Lambert, J. C., Skupin, J., Wittrock, F., Schrijver, H., and Burrows, J.: SCIAMACHY, monitoring the changing Earth's atmosphere, DLR, Institut für Methodik der Fernerkundung (IMF), Germany, 2006.
- Hollas, J. M.: *Basic atomic and molecular spectroscopy*, The Royal Society of Chemistry, Cambridge, 2002.
- Hoogeveen, R. W. M., van der A, R. J., and Goede, A. P. H.: Extended wavelength InGaAs infrared (1.0–2.4 μm) detector arrays on SCIAMACHY for space-based spectrometry of the Earth atmosphere, *Infrared Physics and Technology*, 42, 1–16, 2001.
- Houweling, S., Hartmann, W., Aben, I., Schrijver, H., Skidmore, J., Roelofs, G. J., and Breon, F. M.: Evidence of systematic errors in SCIAMACHY-observed CO₂ due to aerosols, *Atmospheric Chemistry and Physics Discussions*, 5, 3313–3340, 2005.
- Jansen, E., Overpeck, J., Briffa, K. R., Duplessy, J. C., Joos, F., Masson-Delmotte, V., Olago, D., Otto-Bliesner, B., Peltier, W. R., Rahmstorf, S., Ramesh, R., Raynaud, D., Rind, D., Solomina, O., Villalba, R., and Zhang, D.: *Palaeoclimate*.

- In: Climate change 2007: The physical science basis. Contribution of Working Group I to the Fourth Assessment Report of the Intergovernmental Panel on Climate Change, 2007.
- Jenouvrier, A., Daumont, L., Règalia-Jarlot, L., Tyuterev, V. G., Carleer, M., Vandaele, A. C., Mikhailenko, S., and Fally, S.: Fourier transform measurements of water vapor line parameters in the 4200-6600 cm^{-1} region, *Journal of Quantitative Spectroscopy and Radiative Transfer*, 105, 326–355, 2007.
- Karlsson, E. and Simpson, D.: Ozone and methane- climate and environment connected. In: Air pollution and climate change: Two sides of the same coin?, 2010.
- Keppler, F., Hamilton, J. T. G., Braß, M., and Röckmann, T.: Methane emissions from terrestrial plants under aerobic conditions, *Nature*, 439, 187–191, 2006.
- Kleipool, Q. L.: SCIAMACHY SODAP; Objective 38: Leakage current versus temperature, SRON Technical Report- Version 1, 2002.
- Kleipool, Q. L.: SCIAMACHY: Recalculation of OPTEC5 non-linearity, SRON Technical Report- Version 1, 2003.
- Lichtenberg, G.: SCIAMACHY level 1 data: calibration concept and in-flight calibration, *Atmospheric Chemistry and Physics*, 6, 2006.
- Liou, K.: Influence of cirrus clouds on weather and climate processes: A global perspective, *Monthly Weather Review*, 114, 1167–1199, 1986.
- Liou, K. N.: Radiation and cloud processes in the atmosphere, Oxford University Press, Oxford, 1992.
- Liou, K. N.: McGraw-Hill yearbook of science & technology, The McGraw-Hill Companies, 2005.
- Mao, J. and Kawa, S. R.: Sensitivity studies for space-based measurement of atmospheric total column carbon dioxide by reflected sunlight, *Applied Optics*, 43, 2004.
- McFarquhar, G. M. and Heymsfield, A. J.: Parameterization of tropical cirrus ice crystal size distributions and implications for radiative transfer: Results from CEPEX, *Journal of the Atmospheric Sciences*, 54, 1997.

- Meehl, G. A., Stocker, T. F., Collins, W. D., Friedlingstein, P., Gaye, A. T., Gregory, J. M., Kitoh, A., Knutti, R., Murphy, J. M., Noda, A., Raper, S. C. B., I. G. Watterson, A. J. W., and Zhao, Z. C.: Global climate projections. In: Climate change 2007: The physical science basis. Contribution of Working Group I to the Fourth Assessment Report of the Intergovernmental Panel on Climate Change, 2007.
- Meirink, J. F., Eskes, H. J., and Goede, A. P. H.: Sensitivity analysis of methane emissions derived from SCIAMACHY observations through inverse modelling, *Atmospheric Chemistry and Physics*, 6, 1275–1292, 2006.
- Miller, J. L.: Principles of infrared technology: A practical guide to the state of the art, Springer, New York, 1994.
- Mishchenko, M. I., Travis, L. D., and Lacis, A. A.: Scattering, absorption, and emission of light by small particles, Cambridge University Press, Cambridge, 2002.
- Parker, R., Bösch, H., Cogan, A., and L. Feng, A. F., Palmer, P., Messerschmidt, J., Deutscher, N., Griffith, D. W. T., Notholt, J., Wennberg, P. O., and Wunch, D.: Methane observations from the Greenhouse Gases Observing SATellite: Comparison to ground-based TCCON data and model calculations, *Geophysical Research Letters*, 38, 2011.
- Payan, S., Camy-Peyret, C., Oelhaf, H., Wetzell, G., Maucher, G., Keim, C., Pirre, M., Huret, N., Engel, A., Volk, M. C., Kuellmann, H., Kuttippurath, J., Cortesi, U., Bianchini, G., Mencaraglia, F., Raspollini, P., Redaelli, G., Vigouroux, C., De Mazière, M., Mikuteit, S., Blumenstock, T., Velasco, V., Notholt, J., Mahieu, M., Duchatelet, P., Smale, D., Wood, S., Jones, N., Piccolo, C., Payne, V., Bracher, A., Glatthor, N., Stiller, G., Grunow, K., Jeseck, P., Te, Y., Pfeilsticker, K., and Butz, A.: Validation and data characteristics of methane and nitrous oxide profiles observed by MIPAS and processed with Version 4.61 algorithm, *Atmospheric and Chemistry Discussions*, 7, 18 043–18 111, 2007.
- Payne, V. H., Clough, S. A., Shephard, M. W., Nassar, R., and Logan, J. A.: Information-centered representation of retrievals with limited degrees of freedom for signal: Application to methane from the Tropospheric Emission Spectrometer, *Journal of Geophysical Research*, 114, 1–16, 2009.
- Peters, W., Jacobson, A. R., Sweeney, C., Andrews, A. E., Conway, T. J., Masarie, K., Miller, J. B., Bruhwiler, L. M. P., Pètron, G., Hirsch, A. I., Worthy, D. E. J.,

- van der Werf, G. R., Randerson, J. T., Wennberg, P. O., Krol, M. C., and Tans, P. P.: An atmospheric perspective on North American carbon dioxide exchange: CarbonTracker, Proceedings of the National Academy of Sciences of the United States of America, 104, 18 925–18 930, 2007.
- Ramaswamy, V., Boucher, O., Haigh, J., Hauglustaine, D., Haywood, J., Myhre, G., Nakajima, T., Shi, G. Y., and Solomon, S.: Radiative forcing of climate change. In: Climate change 2001: The scientific basis. Contribution of Working Group I to the Third Assessment Report of the Intergovernmental Panel on Climate Change, 2001.
- Razavi, A., Clerbaux, C., Wespes, C., Clarisse, L., Hurtmans, D., Payan, S., Camy-Peyret, C., and Coheur, P. F.: Characterization of methane retrievals from the IASI space-borne sounder, Atmospheric Chemistry and Physics, 9, 7889–7899, 2009.
- Reuter, M., Buchwitz, M., Schneising, O., Heymann, J., Bovensmann, H., and Burrows, J. P.: A method for improved SCIAMACHY CO₂ retrieval in the presence of optically thin clouds, Atmospheric Measurement Techniques, 3, 209–232, 2010.
- Rigby, M., Prinn, R. G., Fraser, P. J., Simmonds, P. G., Langenfelds, R. L., Huang, J., Cunnold, D. M., Steele, L. P., Krummel, P. B., Weiss, R. F., ODoherty, S., Salameh, P. K., Wang, H. J., Harth, C. M., Mühle, J., and Porter, L. W.: Renewed growth of atmospheric methane, Geophysical Research Letters, 35, 2008.
- Rodgers, C. D.: Inverse methods for atmospheric sounding: Theory and practise, World Scientific, London, 2000.
- Rothman, L. S., Jacquemart, D., Barbe, A., Benner, D. C., Birk, M., Brown, L. R., Carleer, M. R., Chackerian Jr, C., Chance, K., Coudert, L. H., Dana, V., Devi, V. M., Flaud, J. M., Gamache, R. R., Goldman, A., Hartmann, J. M., Jucks, K. W., Maki, A. G., Mandin, J. Y., Massie, S. T., Orphal, J., Perrin, A., Rinsland, C. P., Smith, M. A. H., Tennyson, J., Tolchenov, R. N., Toth, R. A., van der Auwera, J., Varanasi, P., and Wagner, G.: The HITRAN 2004 molecular spectroscopic database, Journal of Quantitative Spectroscopy and Radiative Transfer, 96, 139–204, 2005.
- Rozanov, A.: User’s guide for the software package SCIATRAN (radiative transfer model and algorithm)- Version 2.2, User guide, Institute of Remote Sensing University of Bremen, 2007.

- Rozanov, A., Rozanov, V., Buchwitz, M., Kokhanovsky, A., and Burrows, J. P.: SCIATRAN 2.0 - A new radiative transfer model for geophysical applications in the 175–2400 nm spectral region, *Advances in Space Research*, 36, 1015–1019, 2005.
- Ruth, S., Kennaugh, R., Gray, L. J., and Russell III, J. M.: Seasonal, semiannual, and interannual variability seen in measurements of methane made by the UARS Halogen Occultation Experiment, *Journal of Geophysical Research*, 102, 16 189–16 199, 1997.
- Scherbakov, D.: SCIAMACHY command line tool; SciaL1c - software user's manual, Technical report- version 2/B, DLR, ENV-SUM-DLR-SCIA-0071, 2009.
- Schmid, O.: Derivation of the density and refractive index of organic matter and elemental carbon from closure between physical and chemical aerosol properties, *Environmental Science and Technology*, 43, 2008.
- Schneising, O., Buchwitz, M., Burrows, J. P., Bovensmann, H., Bergamaschi, P., and Peters, W.: Three years of greenhouse gas column-averaged dry air mole fractions retrieved from satellite Part 2: Methane, *Atmospheric Chemistry and Physics*, 9, 2009.
- Shettle, E. P. and Fenn, R. W.: Models for the aerosols of the lower atmosphere and the effects of humidity variations on their optical properties, *Environmental Research Papers*, 676, 1979.
- Slijkhuis, S.: ENVISAT-1: SCIAMACHY level 0 to 1c processing, Algorithm theoretical basis document, DLR, ENV-ATB-DLR-SCIA-0041, 1999.
- Slingo, A. and Schrecker, H. M.: On the shortwave radiative properties of stratiform water clouds, *Quarterly Journal of the Royal Meteorological Society*, 108, 407–426, 1982.
- Stephens, G. L.: Remote sensing of the lower atmosphere, Oxford University Press, Oxford, 1994.
- Stern, N.: Stern review: The economics of climate change, http://webarchive.nationalarchives.gov.uk/+http://www.hm-treasury.gov.uk/sternreview_index.htm, accessed 09/2011, 2006.

- Sun, Z.: Reply to comments by Greg M. McFarquhar on Parametrization of effective sizes of cirrus-cloud particles and its verification against observations, *Quarterly Journal of the Royal Meteorological Society*, 127, 267–271, 2000.
- Sun, Z. and Rikus, L.: Parametrization of effective sizes of cirrus-cloud particles and its verification against observations, *Quarterly Journal of the Royal Meteorological Society*, 125, 3037–3055, 1999.
- Tobias, M. L.: Using the log-normal distribution in analyzing aerosols: the mathematical reasoning underlying the various diameters used and the plotting procedure, Technical report, Oak Ridge National Laboratory, 1993.
- Tran, H., Hartmann, J. M., Toon, G., Brown, L. R., Frankenberg, C., Warneke, T., Spietz, P., and Hase, F.: The $2\nu_3$ band of CH_4 revisited with line mixing: Consequences for spectroscopy and atmospheric retrievals at $1.67 \mu\text{m}$, *Journal of Quantitative Spectroscopy and Radiative Transfer*, pp. 1344–1356, 2010.
- UNFCCC: Kyoto Protocol to the United Nations Framework Convention on climate change, <http://unfccc.int/resource/docs/convkp/kpeng.pdf>, accessed 09/2011, 1998.
- UNFCCC: Report of the Conference of the Parties on its fifteenth session, held in Copenhagen from 7 to 19 December 2009, <http://unfccc.int/resource/docs/2009/cop15/eng/11a01.pdf>, accessed 09/2011, 2010.
- Vigano, I., van Weelden, H., Holzinger, R., Keppler, F., McLeod, A., and Röckmann, T.: Effect of UV radiation and temperature on the emission of methane from plant biomass and structural components, *Biogenosciences*, 5, 937–947, 2008.
- Walter, K. M., Smith, L. C., and Chapin, S. F.: Methane bubbling from northern lakes: present and future contributions to the global methane budget, *Philosophical Transactions of The Royal Society*, 365, 1657–1676, 2007.
- Wunch, D., Toon, G. C., Blavier, J. F. L., Washenfelder, R. A., Notholt, J., Connor, B. J., Griffith, D. W. T., Sherlock, V., and Wennberg, P. O.: The Total Carbon Column Observing Network, *Philosophical Transactions of the Royal Society*, 369, 2087–2112, 2011.
- Zender, C.: Radiative transfer in the Earth system, <http://dust.ess.uci.edu/facts/rt/rt.pdf>, accessed 09/2011, 2010.

Zimov, S. A., Davydov, S. P., Zimova, G. M., Davydova, A. I., Schuur, E. A. G., Dutta, K., and Chapin, F. S.: Permafrost carbon: Stock and decomposability of a globally significant carbon pool, *Geophysical Research Letters*, 33, 2006.